Developing a Mechatronic System Model for Self-Pierce Riveting SPR Tools

By:

Daniel Tang

A thesis submitted in partial fulfilment of the requirements for the degree of

Doctor of Philosophy

The University of Sheffield

Faculty of Engineering

Department of Mechanical Engineering

Submission Date

September 2019

Acknowledgements

To start, I would like to thank my supervisor Prof. Neil Sims, who has provided unwavering support and guidance throughout the duration of the PhD. Many thanks also to Prof. Luca Susmel for his advice and helpful discussions around the project.

I express my gratitude to the Engineering and Physical Sciences Research Council for funding this industrial CASE studentship. Furthermore, I want to thank Atlas Copco IAS UK Limited for the financial and technical assistance on the project. Special thanks to my industrial supervisor, Mike Evans, for his continued support of my work as well as his invaluable insights into the SPR system. I would also like to thank Paul Briskham for all the insightful discussions we have had around the technical and commercial implications of the work.

It goes without saying that I am grateful for the support my family has given me over the years. Their positivity was what inspired me to take up this challenge in the first place, and I have them all to thank for the immensely rewarding experiences gained along the way.

Finally, my sincere thanks to all those that I have had the pleasure of sharing an office with in Sheffield and Deeside.

Summary

Self-pierce riveting (SPR) is a complex joining process where multiple layers of material are joined by creating a mechanical interlock via the simultaneous deformation of the inserted rivet and surrounding material. Inertia-based servo SPR systems such as that illustrated in Figure 1(a) are commonly used in producing joints for automotive applications. Figure 1(b) shows a SPR system in action during the riveting of an example workpiece. The cross section of a typical joint is shown in Figure 1(c).

Due to the large number of variables which influence the resulting joint, finding the optimum process parameters has traditionally posed a challenge in the design of the process. Furthermore, there is a gap in knowledge regarding how changes made to the system may affect the produced joint.

In this thesis, a new system-level model of an inertia-based SPR system has been proposed, consisting of a physics-based model of the riveting machine and an empirically-derived model of the joint. Model predictions have been validated against extensive experimental data for multiple sets of input conditions, defined by the setting velocity, motor current limit and support frame type. High levels of accuracy have been achieved in the predicted response of the system as well as the head height of the joints.

A model-based case study has been conducted to identify changes to the system which enable either the cycle time or energy usage to be reduced. It is shown that the system configuration and parameter settings can be optimised to achieve significant savings in cost or energy consumption, without compromising the overall quality of the produced joint.

In addition, global sensitivity analysis methods have been used to identify the factors with the most influence on the joint via two distinct examples. In the first example, the Elementary Effects method is used to explore the plausible design space of the SPR system. In the second example, a variance-based method is used to understand how the variation in the outputs of a specific SPR process is affected by uncertainty in its inputs. The relative importance of three factors is highlighted: the friction in the planetary roller screw mechanism, the maximum available spring compression in the clamping mechanism, and the length of the rivet.

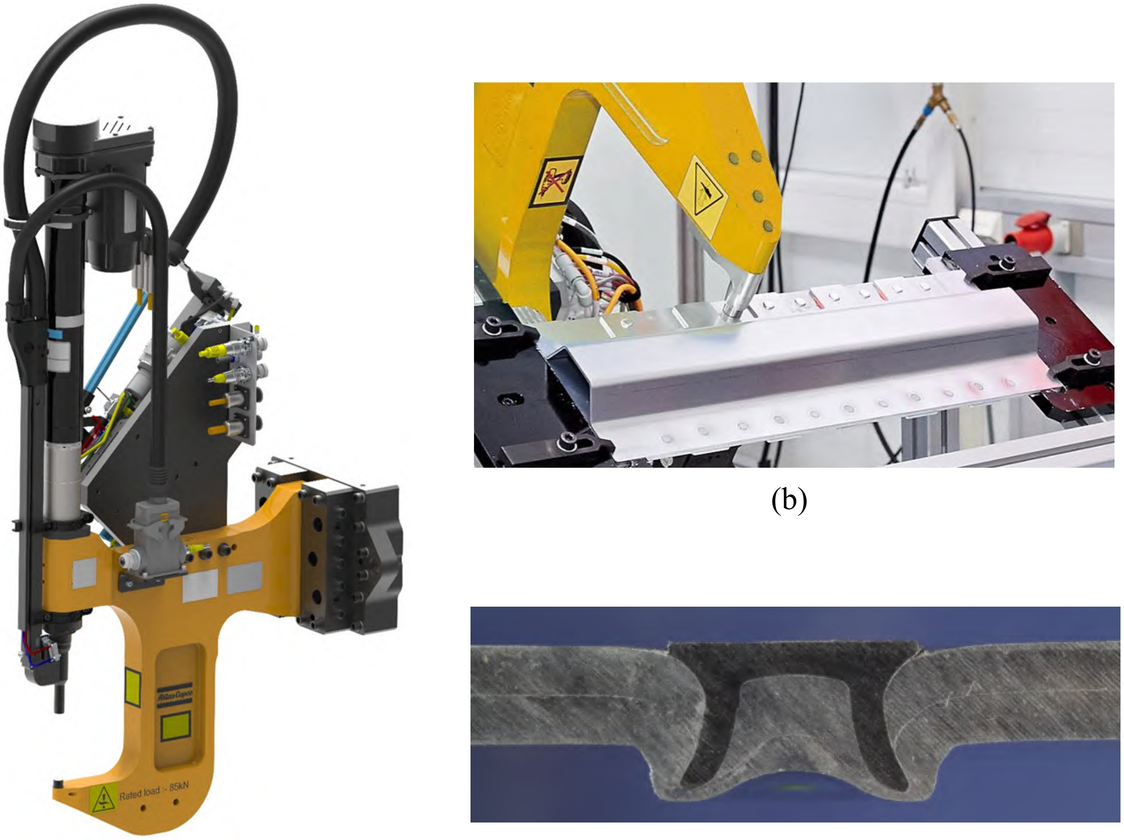

(b)

(a)

(c)

Figure 1: (a) Illustration of a servo SPR system. (Source: Atlas Copco, 2018. Image reproduced with permission). (b) Example workpiece undergoing riveting. (Source: Atlas Copco, 2017. Image reproduced with permission). (c) Cross section of a SPR joint.

The current work is the first to develop a mechatronics system-level model of the SPR process. The extensive and systematic validation of the model gives confidence to the model-base analyses performed. The examination of the effects of system-wide process factors on the produced joint via a global sensitivity analysis forms an important contribution to knowledge. The usefulness of the model is demonstrated in identifying areas of improvement for the SPR process, such as significant reductions in the cycle time or the energy usage. The predictive capabilities of the model may be further leveraged to reduce the costs involved in the design and validation of SPR systems and processes. Additionally, it may serve as a tool for exploring further avenues of research, such as co-simulation with a finite element model of the joint in order to achieve high-fidelity representation of the full riveting process.

Contents

Nomenclature

AC	Alternating current
DAQ	Data acquisition
DC	Direct current
EE	Elementary effects
EMF	Electromotive force
FE	Finite element
GSA	Global sensitivity analysis
MEI	Main effect index
OAT	One-at-a-time
PFI	Programmable function interface
PLC	Programmable logic controller
PRSM	Planetary roller screw mechanism
PWM	Pulse width modulation
NRMSE	Normalised root mean square error
RFS	Restoring force surface
SPR	Self-pierce riveting
TEI	Total effect index
TTL	Transistor-transistor logic
VSI	Voltage source inverter
B_r	Viscous friction coefficient in roller screw
C_{DC}	Capacitance of DC bus capacitor
C_2	Effective damping constant of disc spring pack
C_3	Effective damping constant of hard stop contact
C_b	Effective damping constant of belt
C_c	Effective damping constant of C-frame
C_{plpu}	Effective damping constant of plunger-punch subassembly
C_r	Effective damping constant of roller screw
D_0	Nominal diameter of roller screw nut

e_i	Vector with zeros but with a value of 1 in the ith element, used in sample generation for the Elementary Effects method
$E_{friction}$	Energy dissipated due to friction
E_{input}	Total energy input into system
E_{joint}	Energy dissipated in joint
$E_{kinetic}$	Kinetic energy of system
E_{strain}	Elastic strain energy stored in system
$E_{w.regen}$	Energy consumption of system accounting for regenerated energy
EE_i	Elementary effect of the ith input factor
f_d	Frequency of waveform
F_1	Force transmitted through the slack side of the belt
F_2	Force transmitted through the tight side of the belt
F_{c2}	Coulomb friction in disc spring pack
F_{clamp}	Clamp force
F_L	Force transmitted through central shaft of roller screw
$F_{pretension}$	Pretension in the belt
F_{punch}	Punch force
i	Motor current
i_d	Direct axis component of current
i_{err}	Motor current error
i_q	Quadrature axis component of current
i_{ref}	Motor current reference
J_M	Inertia of motor and driving pulley
J_{setter}	Inertia of flywheel, driven pulley and roller screw mechanism
k	Total number of parameters
K_1	Stiffness of the coil spring
K_2	Effective stiffness of disc spring pack
K_3	Effective stiffness of hard stop contact
K_b	Effective stiffness of belt
K_c	Effective stiffness of C-frame
K_e	Back-EMF constant
K_{mat}	Effective stiffness of material stack
K_{plpu}	Effective stiffness of plunger-punch subassembly
K_r	Effective stiffness of roller screw
K_t	Torque constant
l	Number of levels used in discretising the input parameter space

L_d	Direct axis component of inductance
L_q	Quadrature axis component of inductance
m_c	Effective mass of C-frame
m_n	Mass of clamp tube
m_{pc}	Mass of coupler
m_{plpu}	Mass of plunger and punch
N	Base sample size
P_1	Amplitude of the first peak
P_n	Amplitude of the nth peak
P_h	Lead of planetary roller screw mechanism
r	Number of trajectories in sample generation for the Elementary Effects method
r_{riv}	Restoring force of the joint at the rivet
r_{mat}	Restoring force of the joint at the material directly under clamping
R	Winding resistance
R_1	Radius of driving pulley
R_2	Radius of driven pulley
S_i	Main effect index for the ith parameter
S_{Ti}	Total effect index for the ith parameter
T	Motor current limit
T_{cr}	Static friction torque
T_e	Electromagnetic torque
T_{fric}	Friction torque
T_{p1}	Torque acting on the driving pulley due to a net elongation of the belt
T_{p2}	Torque acting on the driven pulley due to a net elongation of the belt
v	Motor voltage
v_a	Phase 1 voltage of a three-phase supply
v_b	Phase 2 voltage of a three-phase supply
v_c	Phase 3 voltage of a three-phase supply
v_d	Direct axis component of voltage
v_{DC}	DC bus voltage
v_q	Quadrature axis component of voltage
v_{ref}	Motor voltage reference
V	Setting velocity
x_d	Deflection between C-frame arms in the axial direction of the punch

x_{m1}	Displacement at the driving pulley-end of the belt span, on the slack side of the belt
x_{m2}	Displacement at the driving pulley-end of the belt span, on the tight side of the belt
x_{L1}	Displacement of the driven pulley-end of the belt span, on the slack side of the belt
x_{L2}	Displacement of the driven pulley-end of the belt span, on the tight side of the belt
x_n	Displacement of clamp tube
x_{pc}	Displacement of coupler
x_{pu}	Displacement of the punch
x_r	Axial displacement of roller assembly
X	Input factor to model
y	Relative displacement between coupler and clamp tube
Y	Model output
Z_1	Maximum distance between coupler and hard stop
Z_s	Maximum available compression of disc springs
α	Belt drive transmission ratio
δ	Logarithmic decrement
Δ_0	Value in range [0,1] used in the calculation of Δ_i
Δ_i	Change in value of the ith input factor
ζ	Damping ratio
η_{prac}	Mechanical efficiency of the planetary roller screw mechanism
η'_{prac}	Indirect mechanical efficiency of the planetary roller screw mechanism
θ_{err}	Motor angular displacement error
θ_m	Motor angular displacement
θ_L	Driven pulley angular displacement
θ_{ref}	Motor angular displacement reference
μ^*	Mean of the magnitude of the elementary effects
μ_{prac}	Coulomb friction coefficient in roller screw
σ	Standard deviation of the elementary effects
Ψ_m	Flux linkage
ω	Electric angular velocity of motor
ω_{err}	Motor angular velocity error
ω_m or $\dot{\theta}_m$	Motor angular velocity
ω_{ref}	Motor angular velocity reference

Chapter 1

Introduction

1.1 Project background

In modern times the reduction of the weight of a vehicle, or lightweighting, is a dominant trend in the automotive industry [1]. In addition to the reduction of emissions, lightweighting is also beneficial for the performance of the vehicle [2]. The body of the vehicle can weigh up to 25% of the total weight, hence is one of the primary targets for lightweighting [3]. This has led to the introduction of new materials in replacement of the mild steel traditionally used in the body structure. Materials such as high strength steels, aluminium and composites have enabled the reduction of weight without compromising the structural strength of the vehicle, but at the same time they have pushed the boundaries of existing joining technologies. The development of novel techniques that are better able to join said materials is therefore paramount to the production of next-generation vehicles. Self-pierce riveting (SPR) is one such technique.

SPR is a mechanical joining method used commonly in the assembly of panels, hoods, and structural frames. In the automotive industry, the increased substitution of steel with aluminium in vehicle bodies allowed SPR to rise to prominence as a competing technology to the more established techniques such as resistance spot welding. The Audi A8, launched in 1993, marked the first use of an aluminium space frame in a vehicle, as well the first deployment of automated SPR tools in the production process. SPR joints made up approximately 70% of the single point joints on the vehicle [4]. The Jaguar XJ (X350) in 2003, became the first high volume production car with a fully aluminium monocoque chassis, and was made with 3195 SPR joints alongside other joining methods [5]. The novel design of the body structure meant that the body in white weighed 200 kg less than its predecessor with no detrimental effects on structural strength. A more recent example is in 2015 with the launch of the first generation of the Ford F-150 pickup truck to feature an aluminium body, which contributed to a weight saving of over 300 kg in comparison with its predecessor [6]. SPR featured prominently in the production process.

1.2 Description of the SPR process

SPR is a cold process in which a semi-tubular rivet is inserted into multiple layers of material to create a permanent joint. The deformation of the stack of material and the rivet is such that a mechanical interlock is formed during the insertion process. The rivet does not penetrate through the bottom-most layer of material. The four main steps of the rivet insertion process are illustrated in Figure 1.1.

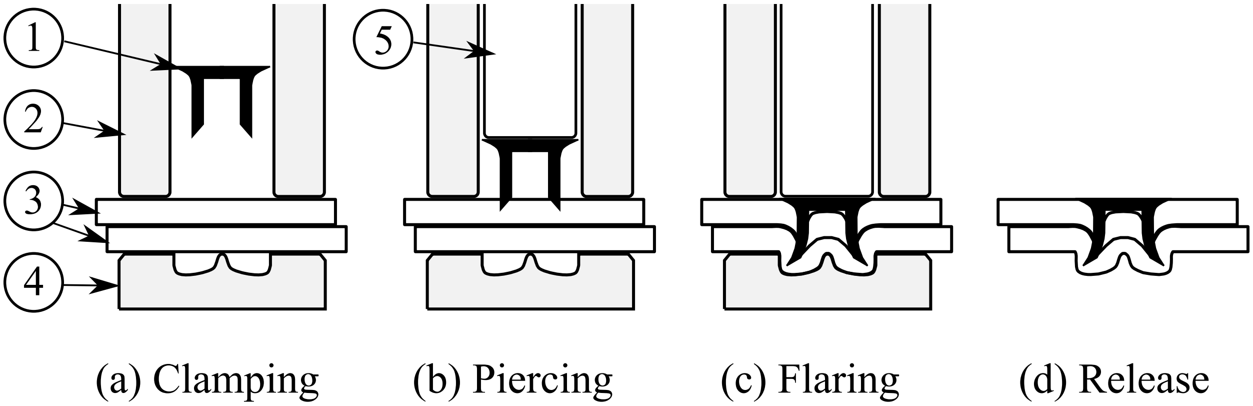

(a) Clamping (b) Piercing (c) Flaring (d) Release

Figure 1.1: A cross-section view of the stages of the SPR process: (a) clamping of the material stack, (b) piercing of the top sheet of material, (c) flaring of the rivet shank to form the interlock, (d) release of the joint. Components are numbered as follows: (1) rivet, (2) blank holder, or clamp tube, (3) stack of material, (4) die, (5) punch.

Various approaches can be used for forcing the punch against the die. One approach is via a 'squeeze' type actuation, such as in a hydraulic SPR process where the components are pressed together at relatively low speed. Another approach is an inertia-based one, where the punch is attached to a flywheel mechanism to avoid the need for high actuation forces.

The current work focuses on the inertia-based servo SPR system, an example of which is illustrated in Figure 1.2, consisting of a permanent magnet synchronous motor, belt drive, planetary roller screw mechanism (PRSM), clamping mechanism, and C-frame. The core actuated mechanical subassembly is commonly referred to as the 'rivet setter', and consists of the PRSM as well as the clamping mechanism. The motor is controlled by a drive unit with an integrated programmable logic controller (PLC), not shown in the figure.

The PRSM is actuated by the motor via the belt drive, and transforms rotary motion into linear displacement of the punch, which is shielded inside the clamping mechanism. In

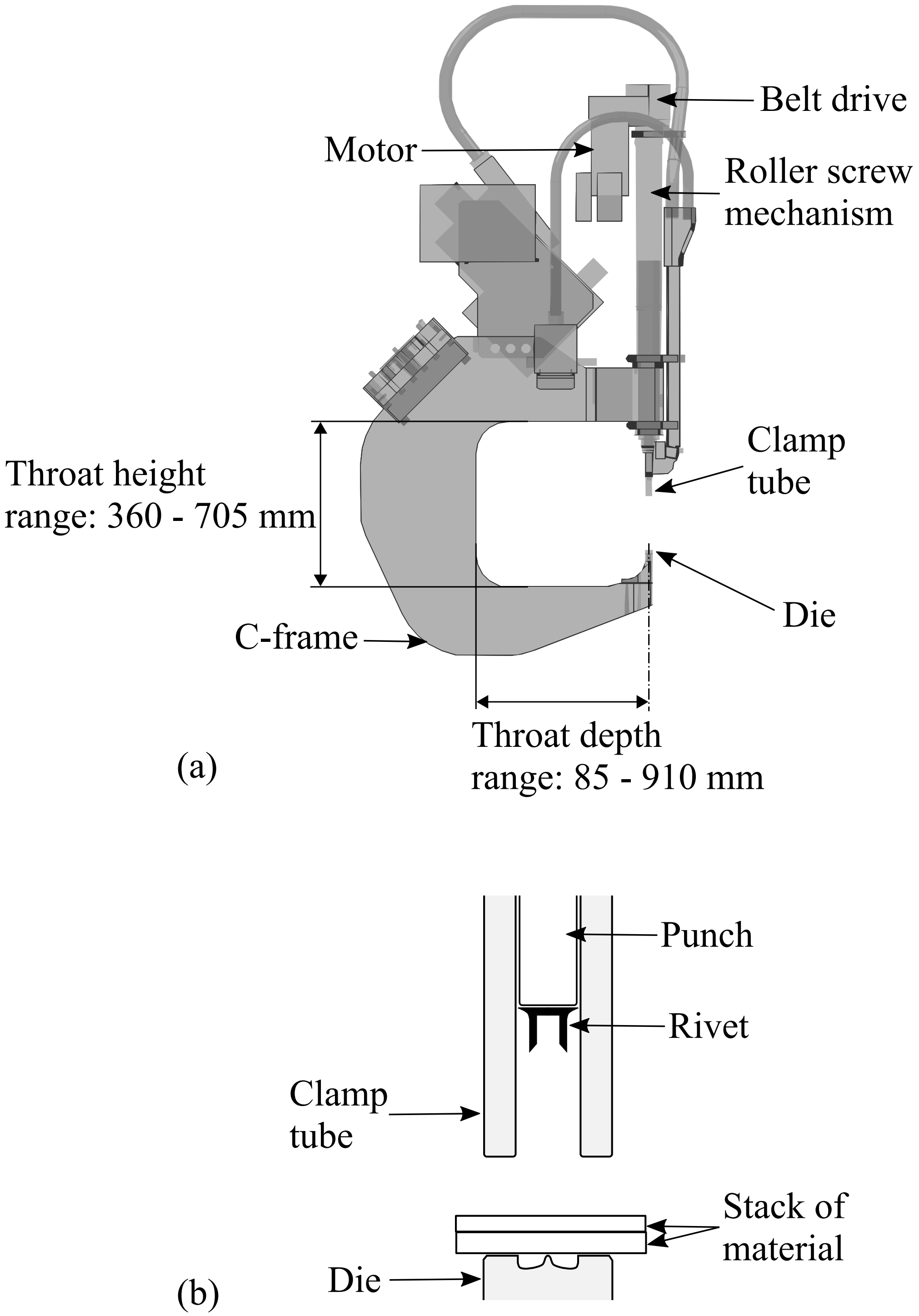

Figure 1.2: Schematic of a servo SPR system: (a) Full system. (b) Close-up of the riveting interface. Dimensions are shown for illustrative purposes only, indicating the approximate range for the height and depth of the opening between the upper and lower arms of existing C-frames. The opening affects the ability of the system to access joining locations on a structure or subassembly.

a typical riveting operation, the punch and clamping mechanism are advanced towards the die and accelerated up to a predefined velocity, which determines the kinetic energy available for the riveting operation. The clamp tube makes first contact with the material stack and holds it in place against the die. The rivet is driven into the material as the punch advances through the inside of the clamp tube. During this phase, the motor also applies a forward-driving torque to aid rivet insertion, which is determined by a predefined level for the motor current limit. When the kinetic energy of the system is reduced to zero and the punch comes to rest against the joint, the motor is reversed and the punch is retracted back to its start position. The punch and the die are in line and act on either side of the joint during rivet insertion. The C-frame provides the reaction force necessary for the forming of the joint. The geometry of the C-frame affects both access to joining locations and its ability to make certain joints.

1.3 Challenges

One of the challenges in the design of SPR processes is identifying the optimum process parameters for joining a given stack of material. For example, a key process parameter for inertia-based systems is the setting velocity, or the initial velocity with which the rivet is driven into the material. In determining the feasibility of inserting the rivet to the target depth, a trial-and-error approach is often taken, and consequently many test samples may be used and discarded before a suitable velocity is found. Further complicating the matter is that the SPR system used on the production line is unlikely to be the same as the designated test system. Differences in the type of support frame (‘C-frame’) or construction of the riveting system often mean that a different setting velocity is required to achieve the same joint quality. Additional testing would therefore need to be carried out on the actual system, potentially at the test facilities of the production plant. When the number of material combinations or system variants is large, all this can culminate in an enormous amount of testing, consumables and time.

The need for a model-based approach is evident. A robust model of the process which is able to predict the effects of changing the process inputs on the resulting joint would substantially reduce the experimental effort required, and would therefore be an important contribution to the industry.

This project is part of the Industrial CASE scheme and has been undertaken in collaboration with Atlas Copco IAS UK Limited. In reference to the EPSRC portfolio, the project ties strongly into Control Engineering and Manufacturing Technologies, both of which are areas of continuing investment and national interest. Funding of research in the areas of manufacturing continues to grow in reflection of the UK's bid to become a leader in high-value manufacturing [7]. With a view of the wider manufacturing industry, the prominence of Industry 4.0, digital twins and other related concepts is symbolic of the increasing push towards the improvement of existing processes via model-based methods.

1.4 Research objectives

Given the direct relevance of the research topic to the needs of the joining industry as well as to the interests of the funding body, the principal aims of the research were initially defined as follows:

- To characterise the behaviour and performance of the SPR system using a model-based approach.
- Use the model to investigate the effects of process parameters on the rivet insertion process.
- Use the resulting model to identify ways to enhance the productivity of the system.

Over the course of the project, the above-mentioned items were expanded into more specific aims:

- Review internal literature from the industry partner to get up to speed with historical and recent developments in the riveting technology.
- Understand the roles of the main elements of the SPR system and how they contribute to the riveting process.
- Understand the control algorithm used in the operation of the system.
- Derive equations describing the dynamic behaviour of the overall SPR system.
- Identify suitable methods to model the forming of the SPR joint.
- Assess the impact of changing key process parameters on the resulting joint.
- Identify ways to improve the energy efficiency of the process.
- Establish an experimental setup to obtain comprehensive data from during the riveting process.
- Use the acquired data to validate the model of the SPR system.

- Develop control algorithms to reduce the process variability that is attributed to fluctuations in the environmental conditions.

Considering the progress made in the current research, most of the listed objectives were achieved. However, the final aim listed was not realised in the time frame of the PhD. During the research it became clear that certain topics required more time than previously anticipated, such as the characterisation of the existing system. Nonetheless, substantial headway has been made in expanding the knowledge base on the SPR system and process.

1.5 Thesis outline

The layout of the thesis is as follows: Chapter 2 provides an overview of the published literature relating to the modelling of the SPR process and other related systems. The literature concerning the modelling and analysis techniques used in this work are reviewed in the later chapters that also address the application of these techniques. The experimental setup and measurement uncertainties are explained in Chapter 3. Chapter 4 describes the modelling of the SPR system, followed by the modelling of the joint in Chapter 5. Subsequently, model verification and validation are addressed in Chapter 6. A model-based case study is used to investigate the reduction of cycle time and also the energy consumption of the SPR process in Chapter 7. Chapter 8 delves into the sensitivity analysis of the simulated system. Chapter 9 is a discussion of the implications of the work, ideas for further work, and finally the conclusions.

Chapter 2

Literature Review

This chapter looks at the state of the art in the research on SPR, with a focus on the approaches taken in modelling as well as the insights gained from experimental methods. The gaps in the existing body of knowledge on SPR are highlighted. Furthermore, some approaches to the modelling of alternative systems from the wider literature are discussed with regards to their relevance to the current research.

2.1 Existing research on the SPR process

2.1.1 Joint quality and strength

One of the principal goals of simulations of the SPR process has been to predict the quality of the resulting joint for a given set of inputs. In a recent review of the literature on SPR [8], the need for accurate simulations was noted as one of the overarching challenges.

Joint quality is generally assessed by visual examination of the appearance of the joint, both externally and internally [9]. The key measurements taken from the produced joint are the head height, the interlock and the minimum remaining thickness of the bottom sheet of material, also known as t-min. These are illustrated in Figure 2.1.

The importance of the aforementioned measurements was established within industry [10]. They are typically mentioned in studies that refer to the cross-section of a SPR joint [11, 12, 13, 9], which suggests that such measurements have long been accepted by the research community.

The head height of the joint is used commonly as an indicator of joint quality. It is defined as the distance between the top surface of the rivet head and the plane of the undeformed

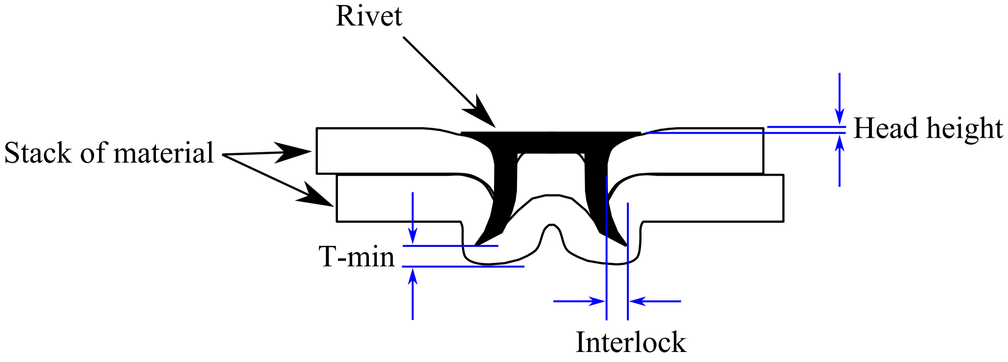

Figure 2.1: Cross section view of a joint and the measurements typically used to assess the quality of the joint: head height, interlock and minimum remaining thickness of the bottom sheet of material, also referred to as t-min.

surface of the top layer of material. A head height of zero is generally desirable in terms of the aesthetics of the joint, in particular for applications that demand a flat surface. Depending on the particular joint design, the head height may be indicative of the state of internal features of the joint such as the interlock. Inferences are typically qualitative and based on past experience.

The interlock represents the amount of material that is directly held in place by the deformed rivet shank. The larger the deformation, the larger the curvature of the shank, and also the larger the interlock. As seen from Figure 2.1, the volume of material that would have to be sheared for the rivet to be pulled out from the substrate is closely related to the magnitude of the interlock. In other words, the interlock has a large influence on the performance of the joint under loading.

The t-min represents the amount of the material remaining in the bottom sheet before the rivet penetrates through it. A non-zero t-min is an indicator of the integrity of the bottom sheet of material and therefore the water-tightness of the joint.

The cross-section image of a joint, obtainable only upon the destruction of the joint, is currently the only way to obtain measurements of the interlock and t-min.

Industry demands the accurate prediction of the static and dynamic behaviour of SPR joints. Approaching this with model-based tools is far from simple since the behaviour in question is influenced not only by the geometries of the features of the joint, but also by the residual stresses, the characteristics of material deformation under loading, the loading mode and profile, etc. Fayolle et al. [14] noted that in order to accurately predict the strength of a joint under loading, the mechanical history of the joint must be accounted for, i.e. the results from the rivet insertion process must be included in the inputs to the joint testing process. In addition, emphasis was placed on having a robust damage model to predict the failure mode of the joint.

The relation between key measurements on the joint and the strength of the joint has been approached mainly using empirical methods. Studies have shown that there is correlation between key measurements from the cross-section and the static strength of the joint; positive correlation between the interlock and the lap shear strength of the joint was presented in [15] and [16]. The results from the empirical studies suggest that the measurements of key dimensions on the joint may be considered as indicators of the performance of the joint. Therefore, the prediction of those key measurements would be a useful output from a model of the SPR process.

2.1.2 Numerical modelling

Throughout the published literature, the modelling of the SPR process has largely been undertaken using finite element (FE) methods. The scope of the simulation is typically focused on the deformation of the rivet and material during the rivet insertion process. The punch, blank holder and die are usually assumed to be rigid parts, while the other components in the riveting system are excluded from the analysis. This exclusion is perhaps motivated by the fact that the rivet and material undergo much larger deformations in comparison to the rest of the system.

A particular challenge is the simulation of the large plastic deformation in the material, which can lead to severe distortion of the element mesh, which in turn can lead to inaccuracies in the analysis. In order to prevent excessive mesh distortion, adaptive remeshing, damage models, and kill-element techniques have been used. Some earlier developments are detailed in [17, 13, 18].

FE simulation proved to be an effective tool in the optimisation of the SPR process in the work by Mori et al. [19], where numerical simulations were used to guide modifications to the shape of the die in order to improve the quality of joints made with ultra high strength steel and aluminium alloy sheets. For illustrative purposes, the key features of an example die are shown in Figure 2.2. In [19] the diameter and depth of the die cavity were increased to enable sheets of different thicknesses to be joined without quality issues. In experimental validation, defects such as excessive deformation or fracture in the shank of rivet, as well as fracture in the material sheets were prevented. Although the optimisation was achieved through trial and error, the cost of additional simulation runs was undoubtedly much lower than an equivalent empirical approach. In that sense, the study clearly demonstrated the benefits of model-based analysis of the process.

Beyond rivet insertion, Bouchard et al. [13] used the results of a riveting simulation as

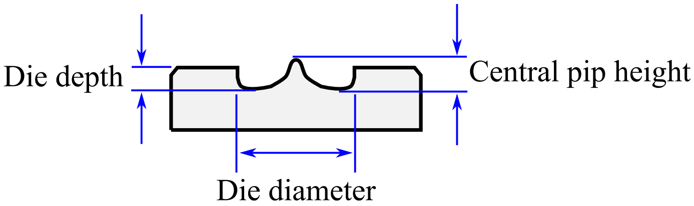

Figure 2.2: Cross section view of a profiled die with labelled key features.

inputs to a structural analysis of the simulated joint. This transfer of data encapsulating the mechanical state of the joint was noted to enable more accurate prediction of the shear strength of the joint. In [20], Atzeni et al. also performed a structural analysis on the model of a joint having first simulated the rivet insertion process in a separate model. The model used in the structural analysis was generated using the same assumptions as those made in creating the rivet insertion model. Both the predicted failure mode and shear strength were found to be in good agreement with experimental data.

More recently, Fayolle et al. [14] used simulations of the rivet insertion process followed by structural analysis of the joint to optimise the strength of the joint, via modifications to the profile of the die. In theory, the simulation could also be used to assess the effects of rivet geometry, clamping load, or other factors on the strength of the joint.

The continuity of data flow from one process to the next appears to be an important factor in the performance of the models for each process. Could simulation cover the life of a joint from the initial forging of the rivet through to the destruction of the joint in the crash test of a vehicle, i.e. from cradle to the grave? Such an endeavour may offer insights into how each process influences the next, which would certainly be of value.

Optimisation of the SPR process to achieve the desired mechanical properties in the resulting structure that contains multiple joints is an ongoing area of research. This was the motivation behind the work by Grujicic et al. [21]. In the study three separate numerical analyses were developed, consisting of: the rivet insertion process, joint testing, and the identification of constitutive equations for SPR connectors. The intention was to link together the different analyses to develop a constitutive relationship for the behaviour of the riveted joint. With complex vehicle crash simulations in mind, it was argued that including detailed models of every SPR joint in a model of a vehicle would be impractical, but replacing the individual joints with constitutive models would drastically reduce the computational expense of the problem.

The authors used simplified connector elements as a proxy for the SPR joints, using detailed simulations of joint testing to inform the properties of the connector elements. This resulted in connectors which were defined in sufficient detail to allow the computation of the elastic and plastic response under loading, but at a significantly reduced computational cost.

The referenced study demonstrated that a complex system can be suitably represented using a constitutive model, where the degree of simplification or abstraction depends on the intended analysis. Applying the same line of thought to the modelling of the SPR system, it should be possible to create proxy models of selected components to aid the simulation of the full riveting process. For example, a constitutive model of the rivet-material interaction may be appropriate for the purposes of evaluating the dynamics of the overall system and its effects on the joint.

In [21] the authors also alluded to the possibility of conducting an optimisation analysis regarding the performance of SPR joints using the proposed approach. This would rely on how well the model is able to capture the effects of process parameters on the produced joint. Although some progress has been made in this regard in the existing literature, the current understanding of how all the inputs to the SPR process influence the resulting joint remains limited.

2.1.3 Process sensitivity

The effect of the process parameters on the produced joint is a topic of continuing interest. The number of process inputs that are known to influence the quality of the resulting joint is extensive, as illustrated in Figure 2.3. This is a major source of complexity for both the design and the modelling of the process.

Although the influence of process inputs on the SPR joint is not a new topic, existing work has tended to focus on either a single factor such as the riveting velocity [10, 22, 23, 15], or a group of factors relating to the properties of the rivet, material and die [24, 25, 26].

2.1.3.1 Effect of rivet, material and die

Part of a study by Abe et al. [27] experimentally investigated the effects of geometric ratios on the quality of the joints. R_l was defined as the ratio of the thickness of the lower sheet of material to the total thickness of the material stack, and R_{rl} was defined as ratio of the rivet length to the total thickness of the material stack. It was found that small values of R_l or R_{rl} led to insufficient flaring of the rivet. Rupture in the bottom sheet of material occurred in cases where the value of R_{rl} was too large. Via experimentation at different ratios, a process window was identified for which the resulting joint was of an acceptable quality.

The identification of process windows provides an intuitive way to visualise the effects of changing two process parameters on the resulting joint. In the broader parameter space of the full SPR system, the number of process parameters would not be limited to two, and

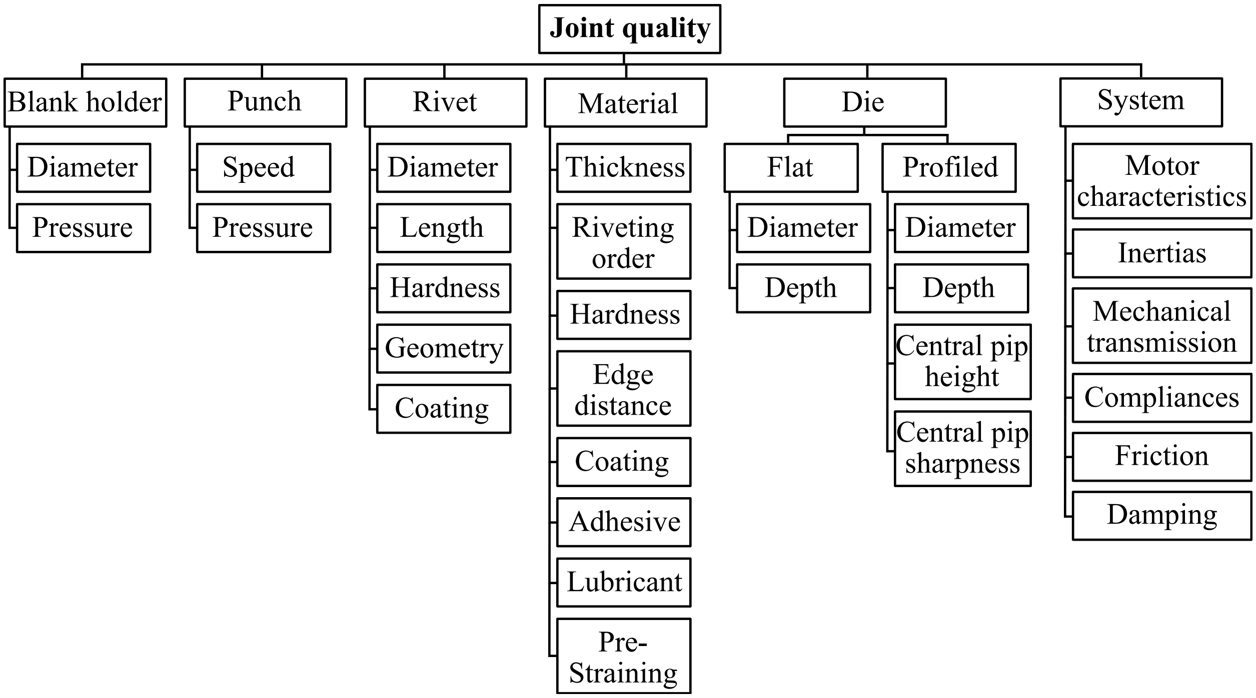

Figure 2.3: Factors that affect the SPR process, based on [9]

thus a model-based method would be required to determine the process window.

Detailed process windows were presented in the paper by Ma et al. [16], where experimental riveting results across seven different rivet and die combinations were analysed with consideration of the die-to-rivet volume ratio, rivet hardness, rivet length, die diameter and central pip height. The authors argued that a die-to-rivet volume ratio of larger than 1 was necessary to avoid the occurrence of cracking in the bottom sheet of material. Furthermore, it was noted that longer rivets and smaller dies improved the joint strength at the expense of the rivetability range, while softer rivets and larger dies improved the rivetability range with compromise on the joint strength.

Despite the extensiveness of the study, the process inputs considered were still a subset of all the factors of influence. This links back to the point about the complexity of the SPR process; with so many input factors, it would be impractical to investigate all of them in a single study, yet that is what the gap in knowledge demands in order to identify the factors with the most influence as well as any potential interaction effects between process variables. A model-based approach would be crucial in bridging that gap.

Papers that have studied the sensitivity of the process via a model-based approach are few in number. In [26] a numerical sensitivity study was used to investigate the effect of the die profile on the interlock in the joint. The depth of the die was found to have the largest influence on the interlock, followed by the diameter of the die to a smaller extent.

Based on this, a movable die concept was proposed, with hints at adaptive control to achieve consistent joint quality by optimising the die depth.

Similarly in [28], FE simulation was used to examine the effects of the die geometry on the features of the cross-section of the resulting joint. It was noted that reducing the depth of the die and reducing the height of the central cone, or pip, resulted in an increase in the interlock as well as the bottom layer thickness measurements. The author stated that appropriate selection of the die could help to lower the process forces and minimise the diameter of the flash on the bottom of the joint, both of which would be desirable developments for SPR applications.

What is interesting is that with the exception of [26], the idea of controlling the system to improve the quality of the produced joint is seldom mentioned in the broader literature on SPR. This would be a worthwhile avenue to pursue, especially considering the scope of all the factors that affect the joint.

The aforementioned papers highlight the importance of the die design in the SPR process. The geometry of the die is a common design parameter for model-based optimisation. This may be attributed to the sensitivity of the SPR process to the die profile, as well as the relative ease with which different dies can be changed on real operating systems. These factors make the die a prime candidate for modification. However, aside from the die, detailed investigations are also needed to examine the impact of the other key components of the system.

In the full scope of the SPR system, one must account for the characteristics of the motor or actuator, the inertias of the system, the properties of the mechanical transmission, the compliances within the system, friction, damping, etc. While past studies have shown that that the properties of the rivet and die play a significant role in the forming of the joint, these are only one part of the bigger picture. Little has been published in the way of a formal study on how the SPR system affects the produced joint, either experimental or model-based. The behaviour of the riveting machine and its influence on the joint is not well understood, and this is a persisting gap in the SPR knowledge base.

2.1.3.2 Effect of setting velocity

Multiple papers have investigated the effects of setting velocity on the appearance and mechanical properties of the joint.

A study into the impact of setting velocity on the mechanical strength of the joint was carried out by Han et al. [10]. By incrementing the setting velocity, notable changes to the appearance of the cross section of the joint were observed. Three key geometric measurements from the joint: head height, interlock and remaining material thickness, were considered with regards to the mechanical performance of the joint. Experimental results indicated a positive correlation between setting velocity and interlock, which was said to govern the strength of the joint in both shear and peel loading.

A more comprehensive investigation by Li et al. [15] also found that the head height and the interlock of the SPR joint were significantly affected by the setting velocity. Correlation was noted between the extent of the formed interlock and the lap shear strength of the joint, as well as between the head height and the T-peel strength.

Wang et al. [23] investigated an alternative SPR technique where gunpowder was used to actuate the punch, achieving setting velocities of over 5 m/s. Differences between the cross-sections of joints made via this technique and a hydraulic SPR system were noted. The former was said to exhibit less variability and better lap-shear strength in contrast to the latter. A study by Hahn et al. [22] compared an even wider range of setting velocities of 0.01, 10 and 100 m/s, in which a reduction in cycle time and tool wear were observed for SPR joints made at higher velocities.

Work by Jäckel et al. [29] addressed riveting with self-piercing solid-rivets. It was suggested that at elevated tool velocities of 5 to 10 m/s, higher strain rates would lead to larger flow stresses. Strain rate-dependent hardening and temperature-dependent softening were considered as interacting phenomena in the process.

Although the published literature on SPR suggests that the setting velocity can have significant effects on the form of the produced joint and its performance under load, one must keep in mind that the setting velocity of an inertia-based system largely determines the energy input into the joining process. Without controlling for the total energy input or the extent of rivet insertion, a meaningful study of the effects of strain rate on the SPR process cannot be realised. For a typical servo SPR system the lowest and highest achievable strain rates are unlikely to be as wide-ranging as those used in [23] or [22], hence it remains to be seen if the typical range of strain rates seen on servo SPR systems have a significant impact on the quality of the produced joint.

A broader narrative of the effects of tool velocity on cutting and forming processes is provided in [30]. In shearing processes, the strain rate in the cutting zone has a direct impact on the behaviour of the material, in terms of the stresses as well as the cutting force. The former can determine the quality of the cut, while the latter directly influences the life of the tooling. Cutting forces may also have implications for the quality of the process if the dynamic response of the tooling is significantly affected by the process forces.

In forming processes, strain rate affects stresses in the workpiece and forming forces. Furthermore, tool velocity is noted to affect tribological interactions between tooling and the workpiece. Although the authors in [30] were referring to the dynamic viscosity of lubricants between the tooling and the workpiece, velocity also comes into play regarding the dynamic properties of the lubricants used in the mechanical transmission of the machine.

SPR can be considered as a combination of shearing and forming processes. The shank of the rivet shears through all but the bottom-most layer of material while the material slug is left in the cavity of the semi-tubular rivet. The forming aspect of the process consists of the deformation of the rivet and material such that an interlock is created to hold the separate layers of material together. Unlike conventional cutting and forming processes, the rivet acts as a deformable extension to the tooling which is left behind in the workpiece as part of the SPR process. Being a combination of the said processes, SPR is subject to all the associated physical phenomena: strain-rate dependency of the material, thermal expansion of the tool, temperature-dependent behaviour of the material, heat transfer between the joint and the tooling, etc. The simultaneous occurrence of shearing and forming undoubtedly leads to interactions between the aforementioned phenomena. In view of the importance of strain rate, it is logical that the rivet setting velocity would play an major role in the outcome of the process. From a modelling point of view, the influence of setting velocity on both the joint as well as the riveting system must be characterised.

2.1.4 Analytical and empirical approaches

In order to fully understand the riveting process, the final state of the joint must be related to the physics of what happens during rivet insertion. One approach has been to make a series of joints under progressively higher setting velocities or pressures such that the head height for each joint is lower than the previous. The collection of cross sections provide insight into the stages in the forming of the joint, which are discussed in detail in [31] and [32].

Haque et al. [31] studied the force-displacement curve of the process in parallel with the cross-sections of partially inserted joints. The correlation between the features on the curve and the cross-section images suggested that for a hydraulically-actuated SPR process and a specific joint configuration, there exists a master force-displacement curve which is characteristic of the process.

That particular work was significant in that it laid out a procedure for identifying a characteristic of the SPR process. In simulation, the characteristic force-displacement curve serves as a checkpoint en route to the final goal, which is to accurately predict the profile of the resulting joint. The modelling effort can be facilitated by the availability of more checkpoints or data against which the model can be validated.

The force-displacement curve, such as that shown in Figure 2.4, is a common reference

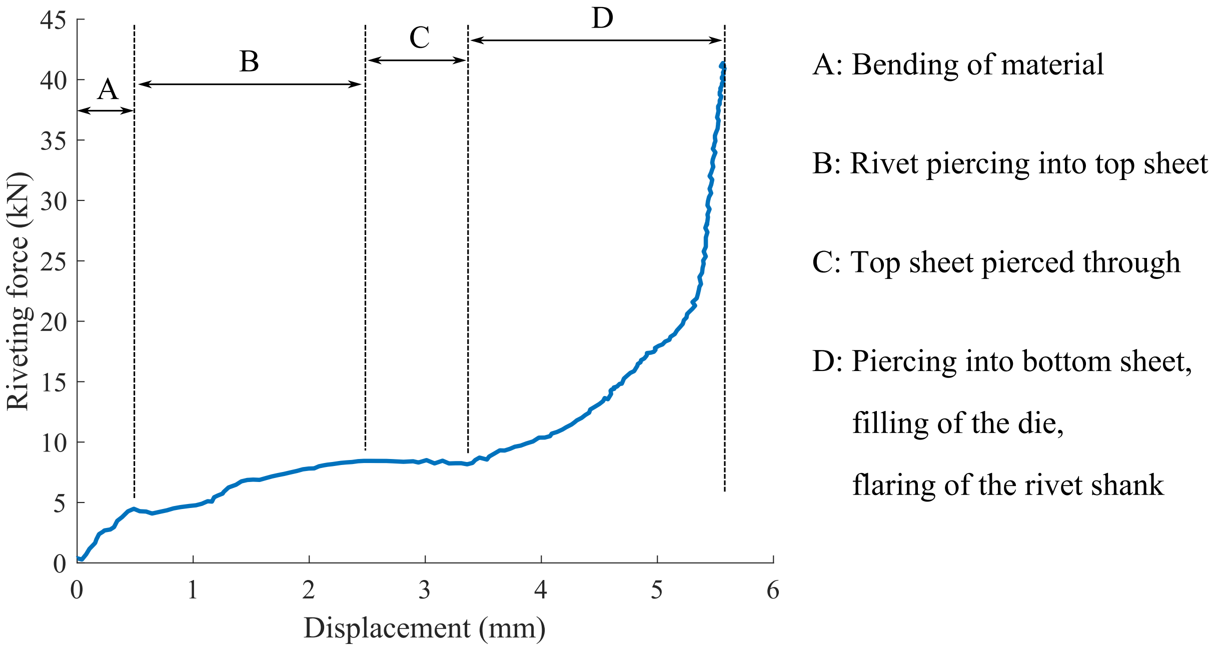

Figure 2.4: Example force-displacement data for a SPR operation with labelled stages. The curve corresponds to the loading phase of rivet insertion.

point for studies on both FE and analytical modelling of the SPR process. In his thesis, King [11] recognised the force-displacement curve as an indicator of repeatability and joint quality. A detailed interpretation of the curve was provided by Haque in [33], alongside a preliminary assessment of the effects of certain parameters on the shape of the curve, such as rivet hardness, material hardness and material thickness. It was demonstrated that the deformation characteristics of a joint could be ascertained via examination of the force-displacement curve.

In [34], the force-displacement data from a riveting operation was used to estimate the quality of the resulting joint. Cross sections of joints were interrupted at various stages during the joining process, and used to generate an empirical equation for the flaring of the rivet during insertion. This allowed the flaring to be predicted given the corresponding force-displacement curve, material thickness, and geometrical values for the die and undeformed rivet. The work was taken a step further when Haque et al. [35] integrated the equation with the analytical joint strength estimator derived by Sun et al. [12]. Whereas certain inputs to the strength estimator equation were previously only obtainable by cross sectioning the joint, the integrated solution was able to approximate these inputs to give an adapted strength estimator, which predicted the joint strength without the need to destroy the joint. For the configurations used in the study, the results showed promise with predictions lying within 10% of the measured joint strengths.

2.1.5 Discussion

The referenced articles in Section 2.1.4 represent a small subgroup in the published literature, which attempts to characterise specific stages of the rivet insertion using analytical and empirical approaches. The force-displacement curve plays a critical part, meaning that a certain reliance on experimental data is inevitable.

There appear to have been no previous attempts to combine a system model of the riveting machine with a model of the joint. Far from being irrelevant, such a model of the SPR process would offer a more complete picture of how the dynamics of the riveting system influence the quality of the joint. However, while it would be possible to run a full FE model of the joint in parallel with a model of the SPR system via co-simulation, the computational effort would be higher still than that of the simulation of the joint alone, which would certainly hinder the realisation of model-based analyses such as sensitivity studies. It may be more practical to represent the joint using a proxy model, such as a reduced-order representation of the full FE model or an empirical model identified from the real riveting process.

It remains to be seen if anything short of a full FE model would be appropriate for capturing the dynamics of the rivet insertion. From a system modelling perspective, a simplified model for the rivet-material-die interaction may serve as a valid alternative to complex FE models. Empirical models in particular, may be run at negligible computational cost. The suitability of such a model would depend on whether the inputs and outputs of the model allow sufficient interaction with the simulated riveting system to be of value. Interactions may be in the form of a force, a displacement, or some other variable. The desired level of detail would be such that some indication about the final state of the joint is obtained from the simulation, such as the head height, since this would enable a model-based study of how the process parameters of the full riveting system can affect the quality of the joint.

2.2 Modelling of alternative systems

In the existing body of work on SPR the effects of changes made to the riveting system (i.e. changes to the hardware, software, or process parameters) and the resulting joint is an understudied area. Looking further afield, the effects of the system on the workpiece is a more established topic in the simulation of forming, forging and press systems. This section examines some of the modelling approaches taken to simulate said systems, and discusses the relevance of the techniques to the modelling of the SPR process.

2.2.1 Simulation approaches

In their review of the topic of process-machine interaction, Brecher et al. [36] distinguished between two main approaches to the modelling of such interactions: model integration and co-simulation.

Model integration is where both the model of the machine and that of the process are modelled in the same simulation environment. An example of this is [37] in which Behrens et al. introduced an algorithm to compute the tool wear and subsequently update the tool geometry in the simulation of a forging process. The process was simulated using a nonlinear implicit FE-solver in Simufact.

Another example is the work by Swidergal et al. [38], in which a combined rigid multibody and FE simulation approach was taken to study the vibrations in a forming tool, more specifically the blankholder. The authors noted that FE modelling would be a computationally inefficient way of modelling press systems in their entirety, but that this could be supplemented by the use of rigid multibody simulation. Coupling between the two methods was realised by including the rigid multibody equations in the FE code to be solved by the FE solver. The multibody model consisted of the press, tool and blankholder, i.e. three subsystems. A FE model of the blankholder was imported into the model to provide higher-fidelity representation of the component of interest. Analytical equations were used to define the dynamics of the components in the system, and were parameterised based on experimental data. e.g. dampers and gas springs were characterised using force-displacement data. The forces of the forming process were generated from a separate numerical simulation, and were applied in the multibody model as a force vector between the relevant bodies. This appeared to be a black-box representation of the forces from a given process, defined as a function of the forming slide position. Through a dynamic analysis, the model of the system was found to perform to a good level of accuracy. The coupling of multibody and FE models afforded the advantage of better stress estimations in the blankholder.

It is noted that valuable insights can be gained into a process without the need for high-fidelity models of each constituent part. By selectively defining the complexity of individual subsystems or components in the system according to the areas of interest, the computational expense may be reduced without detriment to the predictive accuracy of the model.

In contrast to model integration, co-simulation refers to the computation of separate models in their respective simulation environments with synchronised data exchange between them. This would be useful in the case of a large complex model, where the individual sub-models may be coded using different programming tools. Via co-simulation, different simulation tools are linked via a common platform and therefore the strengths of each tool can be leveraged.

In their study of a rolling process, Franzke et al. [39] performed the simulation of the tooling and the process separately in a co-simulation setup, with bi-directional data exchange between the two FE simulations. The coupling of the models was realised using a mapping table or interaction model, which updated the geometry in both models based on the contact forces and stresses. In contrast to the simulation of the full system and process using a single FE model, the approach taken was said to be able to better handle contact conditions and allowed a smaller stiffness matrix to be defined.

Brecher et al. [40] used co-simulation to consider the interactions between a multi-stage forging process and the forging press. In the data exchange between the FE simulations of the process and the machine, process loads on the die, the forging load, and tool displacements were transferred. The FE mesh on the tool was updated at every simulation step in order to adequately account for the interactions between the press and the workpiece. It was noted that more realistic results could be obtained via the coupled simulations in comparison to a conventional approach that assumed an ideal, rigid machine.

2.2.2 Compliances in systems

A common motivation behind the co-simulation setup in [39] and [40] was to account for the elastic deformation in the machine during the process. In the simulation of forming processes, the need to accurately model the dynamics of the equipment is noted as one of the requirements for achieving better predictions of the process outputs [41, 36, 42].

In [42], the stiffnesses of a cold forging press and its tooling were included in the FE process simulation as linear spring elements. Groche et al. [43] used a compliance matrix in the modelling of a multipoint servo press, to describe the position-dependent compliances of the system. Schenke et al. [44] studied the dynamics of a servo-screw press used in metal forming. The system was considered as a series of interconnected stiffnesses to account for the compliance in the power train, the frame, the press table, etc. Analysis using the model included the effect of direct and indirect position measurement and the effects of different powertrain configurations.

Each of the aforementioned works acknowledged the need to account for the compliances in the machine in order to obtain accurate simulation results. The same point equally applies to the SPR system, where the accuracy of the simulated outputs would also depend on the characterisation and inclusion of the compliances in the full system, alongside other factors of influence.

2.2.3 Discussion

2.2.3.1 System considerations

The structure and level of detail of a model should reflect the intended analysis. One of the application areas for a model of the SPR process would be to evaluate the optimisation of the input parameters to the process to reach a desired outcome. Several objectives would be of interest, such as achieving a consistent joint quality for any system variant, minimisation of cycle time, minimisation of the energy usage of the system, etc. From these objectives, it is clear that the model of the system must adequately capture the dynamic behaviour of the machine itself, its interactions with the joint during the riveting process, as well as the control structure and motion logic which drive the actuation of the system.

The compliances and damping in the system should be identified and included in the model, since this will allow better characterisation of the dynamic response of the system, which in turn will enhance the accuracy of the simulated process.

2.2.3.2 Process model

Having seen the capabilities of FE modelling in capturing complex process dynamics, it may seem logical to choose a numerical approach to model the workpiece. However, there already exists a collection of work regarding the numerical modelling of the SPR process, hence an alternative technique would offer a novel viewpoint from which the problem can be addressed.

It is possible to reduce a complex process down to a simplified representation that is adequate for a specific goal or analysis. The complexity of the rivet-material interaction may be simplified via a proxy model which is governed by well-defined relationships between a set of specific inputs and outputs. Such a model may be in the form of a non-parametric or black-box model, which may not necessarily have a physical-basis, but the predictive accuracy may be sufficient for the intended analysis.

Among the gaps in knowledge regarding SPR, the sensitivity of the process to its input parameters has been noted to be one of the principal areas of interest. In order to address this gap via a sensitivity analysis, a fundamental requirement would be the accurate prediction of a meaningful output from the SPR process. This output should be related to the quality of the joint since that is the core product of the process. An option could be the head height of the joint, as this is easily measurable without the need to destroy the joint.

Taking an alternative approach instead of FE modelling of the joining process would put co-simulation outside the immediate scope of the project. The option of model integration where a proxy model of the process is directly implemented in the same simulation environment as the model of the system would be much more practical and computationally efficient.

On the other hand, combining a high-fidelity numerical model of the joint with a systems model may be considered a potential future development, and measures can be taken to facilitate the future adaptation of the model for the purposes of co-simulation. The usage of a versatile simulation environment such as MATLAB/Simulink facilitates the transition to a co-simulation setup. The modularisation of the model into physically meaningful subsystems makes it easier to change any component of the system and keep track of such changes. Moreover, a model with a strong physical basis can be shared and intuitively reconfigured by users with differing backgrounds. All of these points would contribute to the ease with which the developed model can be improved for further analyses going forward.

2.3 Summary

On the whole, publications in the existing literature have dealt with the modelling of the riveting process on a component level, focusing on the rivet-material-die interactions, without addressing the dynamics of the riveting machine and its effects on the joint. Consideration of the full system dynamics is a necessary step towards improving the accuracy of the simulation and expanding the overall understanding of the SPR technique. Characterisation of the full system would also facilitate the optimisation of its design via effective model-based analyses and therefore better serve the needs of the industry.

The general trend in the automotive industry is pointed towards the use of novel materials which are of low ductility and high strength, as well as multi-material stacks featuring combinations of different lightweight materials. This places increasing pressure on the SPR system to be able to reliably deliver the higher riveting forces required without compromising the consistency of the joints. Such demands motivate the further development of the SPR technique via model-based methods.

The present work adopts a systems approach to the modelling of the SPR process in order to reduce the computational cost (compared to FE methods), and to account for the mechanical, electrical, and digital domains of the system. The premise of this work is that the developed model would enable the exploration of new ideas and ways to improve the SPR technique, which would lead to better process repeatability as well as the capability to join more advanced and novel materials. Given the extensive usage of SPR in automotive assembly, the advancement of the joining technique will have a direct impact on the production and performance of the next generation of vehicles.

In the next chapter, details on the test system used for model identification as well as data acquisition from the riveting process are presented.

Chapter 3

Experimental Method

3.1 Introduction

The purpose of the experimental work is twofold: one, to gain a deeper understanding of the behaviour of the SPR system, and two, to acquire data for model identification.

The core SPR system is composed of the following components: the motor, the rivet setter, the C-frame, as well as the control panel. SPR joints are made by driving a rivet into a stack of material using a punch and a die, as illustrated in Figure 1.1. The punch is actuated by the motor whose rotary output is converted into linear motion via a roller screw mechanism in the rivet setter. The C-frame provides the reaction force necessary in forming the joint. The control panel powers the motor such that the desired motion profile of the rivet setter is achieved. The role of each component in the riveting process is explained in depth in Section 3.3.

The experimental work carried out in the project was based on a core SPR system, with adaptations and additional instrumentation such as load cells and a high speed camera, in order to obtain the data required to characterise the dynamic behaviour of the system as well as the joint during the rivet insertion process. Figure 3.1 provides an illustration of the experimental setup used. Details of the experimental setup are elaborated in Section 3.4.

Two key challenges of the experimental study are: (a) the inherent variability associated with SPR testing, and (b) the extensive range of parameters that could be modified (i.e. controlled) during experiments.

To address these challenges, the chapter begins by reviewing the generic literature concerning design of experiments, in order to ensure that the planned tests give rise to valid and useful experimental data. Then, for completeness, the operational capabilities of a standard industrial SPR machine are described. This paves the way for a description of the experimental SPR system that formed the basis of the present research. This experimental facility

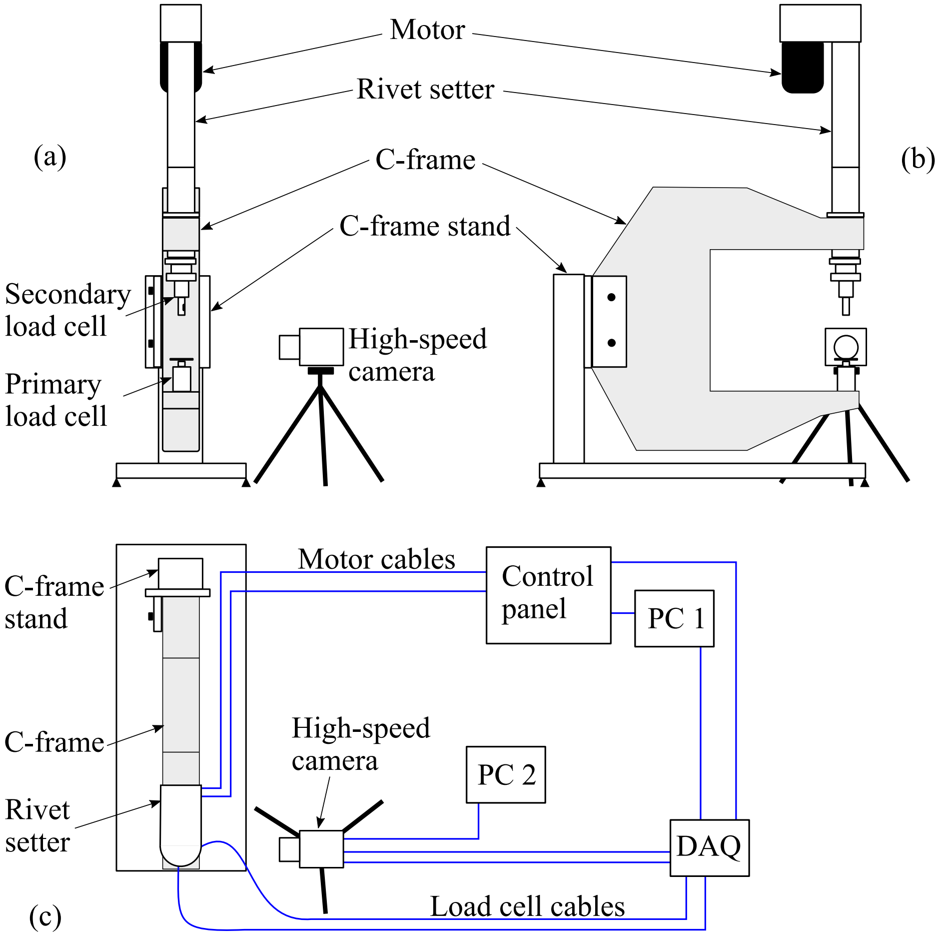

Figure 3.1: Front (a), side (b) and top down (c) views of the full experimental setup. Among the key data acquired during the testing were the total process force, the clamp force, and the relative displacement between the punch and the die.

was pre-existing but was extensively modified to meet the requirements of the project. Typical experimental data from the modified test facility is presented. Finally, the uncertainty budgets associated with the key measurements of the experiments are provided.

3.2 Theoretical basis: design of experiments

3.2.1 Overview

Design of experiments (DOE) is a methodology for structuring an experiment such that the data obtained gives the most amount of insight into the system or process of interest, for a given number of experimental runs.

Key definitions used in DOE are as follows:

- Unit - the target system or process under investigation. (If the unit is a human being, the alternative term used is ‘subject’)
- Factors - variables in an experiment
- Level - specific value of a factor
- Treatment - specific conditions applied to the unit, i.e. a combination of levels for the factors

Table 3.1 shows an example experiment design consisting of two factors, two levels per variable (i.e. high and low), and four treatments.

Table 3.1: Example experiment design to illustrate DOE definitions.

Treatment	Factor 1	Factor 2
1	High level	High level
2	Low level	High level
3	High level	Low level
4	Low level	Low level

The aim of an experiment is often to identify the influence of each variable on the result (i.e. main effects), as well as any interacting influences between the variables (i.e. joint effects). In order to realise this, the conditions of the experiment must be changed systematically. Changing the value of each variable one at a time can lead to many experimental runs and can be expensive or impractical. Furthermore, joint effects cannot be revealed this way. Another risk is that over the course of the experiment, unmeasured or uncontrolled changes to the conditions of the experiment may affect the outcomes. DOE provides a framework for maximising the useful information obtained for a given amount of effort, and for mitigating the effects of unknown variations. In that sense, it is an efficient approach to carrying out experimental work. With regards to industrial processes, DOE can be used to improve the understanding of how process inputs affect outputs, increase productivity, and reduce operational costs [45].

In the published literature DOE methods have been applied to a wide-range of areas. Here, selected examples relating to joining and forming processes are mentioned to illustrate the relevance of DOE to the study of industrial systems.

In [46] Elangovan et al. examined the influence of welding parameters in an ultrasonic metal welding process via DOE methods. The chosen experiment design was essentially a full factorial design with three factors each at three levels, which enabled the study of main as well as interaction effects. Via analysis of variance, the percentage contributions of parameters and interactions were obtained, and the combination of parameter levels for maximising the weld strength was determined.

DOE techniques have also been used to study the resistance spot welding process. One such work is that of Pashazadeh et al. [47], in which a full factorial design was used to investigate the effects of the welding time, current and pressure on the geometry of the resulting weld nugget. The choice of input parameters was based on their known importance to the resulting weld. While the authors did not discuss the decision behind the use of the full factorial design, the small number of design variables would have undoubtedly been a contributing factor.

Jäckel et al. [26] used DOE to design a series of numerical simulation cases in a study of how the die geometry influenced the SPR joint. The importance of five features of the die geometry was determined with respect to their influence on the interlock of the produced joint, the t-min measurement, the joining force, etc. The results were used to construct a response surface or metamodel relating the interlock of the joint and the die depth and diameter. Similarly the influence of the properties of the material on the joint was also studied. The authors used an advanced latin hypercube sampling design, the reason behind which was not explained, but in other literature it has been shown to be a more efficient design than simple random sampling [48].

The work by Moroni et al. [49] compared the mechanical performances of simple and hybrid joints using DOE. Hybrid joints consisted of joints made with adhesive in combination with welding, clinching or riveting, while simple joints referred to joints involving a single joining technique only. The strength, stiffness and energy absorption were chosen as output variables of the process. Six process factors were considered in the analysis. A fractional factorial experiment design was used to keep the number of test runs to a practical number. The results of the DOE provided insights into the effects of each process factor, which meant that tailored joint designs could be proposed to suit an application. The example given showed how selection of the pitch and material thickness levels would make a notable difference to the stiffness, strength and energy absorption of a joint in contrast to a nominal traditional design.

Faria Neto et al. [50] examined the effects of two process parameters on the outcomes of a heat staking process, where a heated metal insert is pushed into a thermoplastic part. In the first stage of the work, the authors used a two level factorial design augmented with five replicates at the centre point to study the two main input factors: the heating temperature and the insertion time. In the second stage, a three level factorial design with five replicates for each treatment was carried out. The transition to three levels was motivated by the need to identify quadratic relationships which were inadequately represented via the linear model resulting from the two level factorial design. From the generated response surface, the operating point of process could be adjusted to optimise for either the productivity or the energy consumption of the process.

In the field of metal forming, Allam et al. [51] conducted a model-based study on the effects of process parameter variations on the output part of a hot forging process. The runs were set up using DOE with three parameters and three levels. Simulated results indicated that temperature was a key contributor to the geometric variations of the product, hence it could be concluded that monitoring of billet temperature was crucial to ensuring that the thickness of the produced part did not deviate beyond the acceptable bounds.

Kim et al. [52] studied the effects of the forming velocity on a precision forging process, using a combination of FE modelling and DOE. The design variables were chosen to be the stroke of the first stage (i.e. the upsetting stage) and also the forming speed of the upper and lower sleeves in the second stage of the process. By examining the forming load variation the authors found that it was possible to optimise the motion profile of the press system to minimise the forming load and achieve the desired quality of process outputs.

As part of the study in [53], Gao et al. used DOE to carry out a model-based evaluation of the sensitivities of a deep drawing process. More specifically, the effects of the five main process parameters on the energy consumption were examined. The contribution of each parameter was quantified through the analysis of variance. It was concluded that the process energy could be more effectively reduced via material selection and optimising the die profile, rather than changing the operating parameters of the system such as drawing velocity and blankholder force.

The work by Muñoz-Escalona and Maropoulos [54] used an orthogonal array design to determine the impact of input parameters on a milling process, with three parameters at three levels. Orthogonal arrays have the property of being balanced in the sense that all parameter levels are weighted equally. The chosen design belonged to the family of Taguchi designs, which are particularly effective in identifying main effects in a relatively small number of experiment runs. In the study the authors identified the optimal parameter values which would produce the longest tool life. In addition, an alternative set of parameter values were determined which would give the lowest surface roughness on the machined surface.

In the work by Oudjene and Ben-Ayed [55], a numerical study of the influence of tool geometry on a clinching process was carried out. Via the Taguchi method, the effects of eight geometrical parameters were explored using results from eighteen simulation runs. Response variables of interest were the clinch lock, nick thickness and the maximum separation force of the joint. The study offered a broad overview of the main effects of the parameters, thus it can be said that the chosen design served well for the purposes of screening.

Another numerical study of the clinching process was presented in the paper by Wang et al. [56], in which several analyses were realised in sequence. First, the authors conducted a parameter study to screen out the insignificant variables based on their main effects with respect to the process output. Of the initial thirteen variables evaluated, nine were found to be important and were subsequently included in a Box-Behnken design, which is one of the classical quadratic designs used in response surface modelling [57]. Then, a multi-objective optimisation was conducted to maximise the neck, interlock and tensile strength of the clinched joint while satisfying constraints on the neck and thinning rates of the material sheets.

Cipriano et al. [58] employed a central composite experiment design, which is also a response surface design, in their study of a friction-riveting process. The experiment design consisted of a fractional factorial design with a set of central and axial points. Five factors and two levels were chosen. The construction of response surface models enabled further understanding of the individual impact of process parameters as well as their interactions with respect to the physical features of the produced joints. Moreover, in part two of the work [59], a relationship was obtained which determined the parameter levels that would maximise the mechanical strength of the joint while minimising the energy input into the process.

In summary, the various examples from the published literature demonstrate that valuable insights into complex processes can be obtained using DOE methods. The scope of the DOE is defined with consideration of the cost and time required for experimentation or simulation, and factors are generally chosen based on some prior knowledge of their effects on the outputs of the process. With respect to the choice of experiment design, full factorial designs are preferable if the experimental cost is manageable, since these provide the most information about the effects of factors. Fractional factorial, or alternatively Taguchi designs allow significant reductions in the size and cost of the experiment, but offer limited information about interactions, as noted in [60] and [57].

In the present work, the aim is not to obtain empirical relationships between input factors and response variables, but rather to use DOE as a robust framework in which adequate data can be obtained for the validation of the model of the SPR system. By comparing the simulated results with those from the real process, the performance of the model may be quantitatively assessed and the modelling assumptions may be verified. The use of DOE is motivated by the presence of influences on the response of the real system which are of a stochastic nature. Due to material variations, fluctuations in environmental conditions, changes in system behaviour with age, etc., there are numerous uncontrolled contributors to the variability in the SPR process. This variability should be minimised to mitigate potential interference with the effects of interest (i.e. those relating to the controlled changes made to the system). DOE is highly appropriate for addressing this as it provides a systematic way to reduce the impact of uncontrolled factors. The three principles of DOE that help to achieve this are described in the next subsection.

3.2.2 Principles

Three principles of DOE can be implemented to reduce experiment bias and increase the efficiency of an experiment: replication, randomisation and blocking.

3.2.2.1 Replication

Replication is the repeating of experimental runs with specific conditions. Results from repeat runs can provide an estimate of the experimental error, as well as more accurate estimates of the main and joint effects associated with each parameter. Repetition and replication are two distinct concepts. In DOE terminology, repetition refers to performing a treatment multiple times before moving onto another treatment. Replication on the other hand signifies repeating a treatment multiple times where the runs are interspersed with runs of other treatments in a random sequence. The advantages of replication over repetition are explained by the principle of randomisation.

3.2.2.2 Randomisation

Any experiment is subject to the influence of factors which are either difficult or impossible to control, such as human error, fluctuation of environmental conditions, etc. These factors can have unexpected influences on the outcome of the trials. Randomisation can help to reduce the experimental bias by averaging out the effects of said factors. By randomising the experimental runs, the probability of each run being affected by these factors is equal across all the runs, whereas without randomisation certain runs may be more severely affected than others, which may give rise to misleading results.

3.2.2.3 Blocking

Running a completely randomised experiment may be costly or impractical. Limitations in terms of availability of units, difficulties in configuring the levels specified by a treatment, or other challenges mean that it might make more sense to collect similar units together into a group or block. This is referred to as blocking or block design. Blocks are typically defined to contain runs with a common experimental condition, such as a specific unit, material batch, day, or other conditions which may be difficult to control.

Although blocking disrupts the complete randomisation of an experiment, randomisation can still be realised within each block. The results can be interpreted to give separate conclusions for each block.

3.2.3 Workflow and experiment designs

The workflow of carrying out a DOE for an industrial process starts with the planning stage, which can be summarised into the following steps:

1. Formulate the problem
2. Choose a response variable, or a measure of process quality
3. Select the process variables
4. Classify process variables into two groups: controllable, or uncontrollable. The former is for variables that are controllable by the operator of the system, the latter is for variables which are difficult to control, such as ambient temperature variations.
5. Define levels for each process variable
6. List interactions and decide which ones are of interest, i.e. which to include in the study

Next is the designing stage, where the decisions made in the planning stage are used to guide the design of the experiment. Common experiment designs can be categorised into three groups: screening designs, full factorial designs and fractional factorial designs.

- Screening - the aim of screening is to reduce the number of factors to only those that have a significant effect on the process. Hence, the screening design is oriented towards examining as many factors as possible with as few runs as necessary. The Plackett-Burman design [61] is an efficient screening design for cases where only the main effects are of interest. The number of runs is a multiple of four, and the maximum number of factors (k) that can be studied is:

  $$k = \frac{N-1}{L-1} \tag{3.1}$$

  Where N is the number of runs, and L is the number of levels. Alternatively, for a given number of factors, the minimum number of runs required is:

  $$N = k(L-1) + 1 \tag{3.2}$$

- Full factorial - full factorial designs allow the study of main and interaction effects between all factors, as they contain all possible combinations of levels for the factors. The notation used to describe a full factorial design is L^k, e.g. a 2^3 full factorial design is one with three factors, each with two levels. The number of runs required is equal to L^k. Table 3.1 showed a 2^2 full factorial design, with four runs in total.

- Fractional factorial - a fractional factorial design is a fraction or subset of a full factorial design. This is useful in cases where higher order interactions between the factors of a given process are not of interest, and a tailored design that allows the computation of the main effects and selected interaction effects would be more efficient than a full factorial design. Further details on fractional factorial designs can be found in [57].

The output of the design stage is a design matrix that describes all the factors and levels included in the experiment, as well as the sequence of runs. The experiment can then be carried out according to the design matrix.

The implementation of DOE in the current study will be described in Section 3.6. Alongside the aforementioned principles of DOE, effective experiment design also requires a good understanding of the capabilities of the SPR system, particularly regarding the selection of factors and levels. In relation to this, the details of a standard servo SPR system are presented in the next section to explain its capabilities and the functions of its main components.

3.3 Production system

3.3.1 Overview

As explained in Section 1.2, the system of interest in the current study is the inertia-based servo SPR system. The configuration of a production system previously illustrated in Figure 1.2(a) serves as a starting point for an in-depth look at the interactions in the system as well as the functions of each main component.

A simplified schematic of the lumped-parameter representation of the system is shown in Figure 3.2. The arrows within the control structure (i.e. the left side of the diagram) denote the signal flow. The riveting machine is represented as a six degree of freedom system composed of inertias, masses, stiffnesses, dashpots and other elements. The joint is represented using two nonlinear elements (i.e. boxes with crossed lines), which will be explained in Chapter 5. The illustrated state of the system in Figure 3.2 corresponds to an instant during rivet insertion, with the clamping tube and the punch both in contact with the joint.

The following subsections delve into the key components of the system.

3.3.2 Drive control

3.3.2.1 Software interface

IndraWorks is the main software tool used to communicate with the drive via a user PC. The software provides a graphical user interface through which the drive can be configured, for example: the adjustment of the control gains of the system, the assignment of signals on the input and output ports on the drive, as well as limited parameterisation of the motion profile. As such, IndraWorks plays an important role in the commissioning and diagnosis of the production system.

The software IndraLogic is used to load and modify the code in the PLC, which determines the control signals that would actuate the SPR system. The code is developed in the CODESYS programming environment, in which a combination of five programming languages is used: sequential flow chart, ladder diagram, function block diagram, structured text, and instruction list. All said languages are defined in the international standard IEC 61131-3 [62].

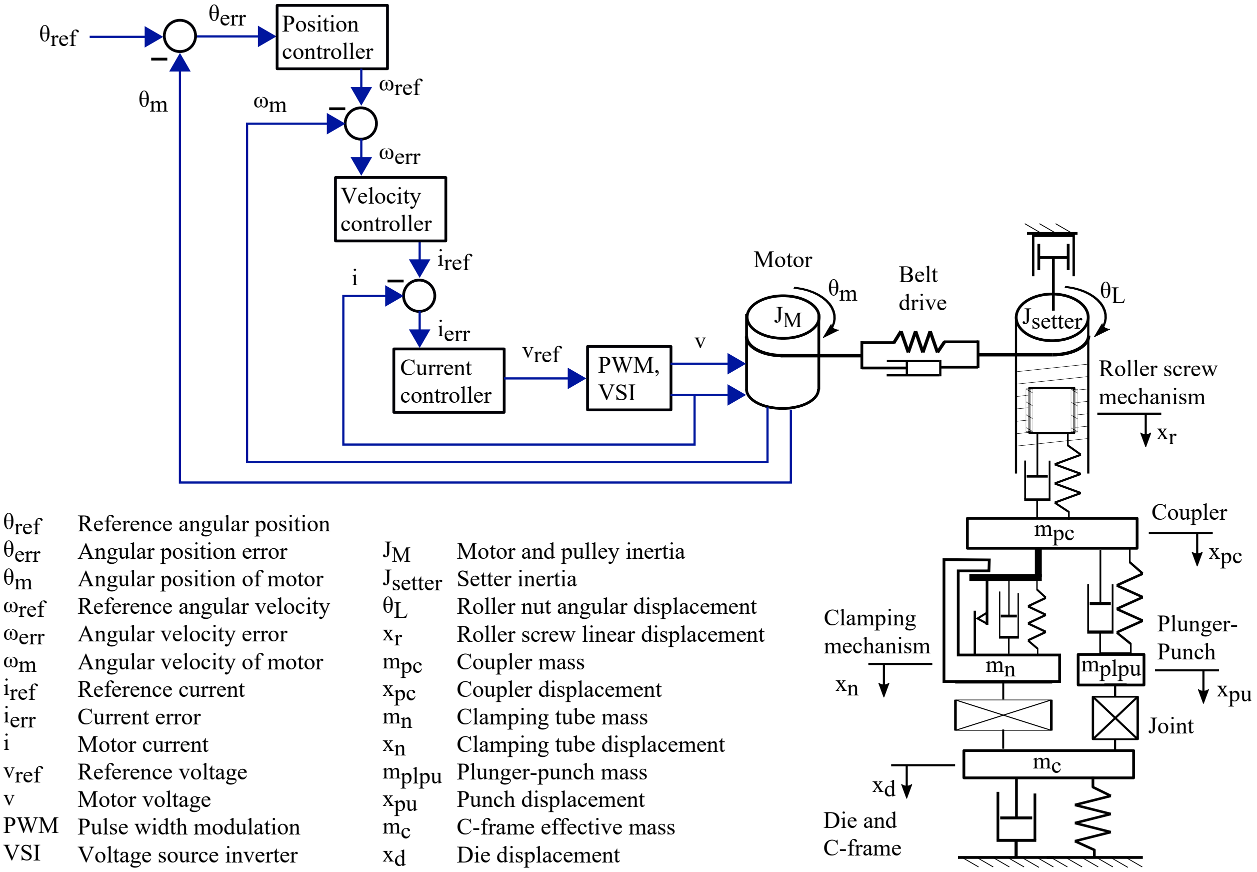

θ_{ref}	Reference angular position
θ_{err}	Angular position error
θ_m	Angular position of motor
ω_{ref}	Reference angular velocity
ω_{err}	Angular velocity error
ω_m	Angular velocity of motor
i_{ref}	Reference current
i_{err}	Current error
i	Motor current
v_{ref}	Reference voltage
v	Motor voltage
PWM	Pulse width modulation
VSI	Voltage source inverter

J_M	Motor and pulley inertia
J_{setter}	Setter inertia
θ_L	Roller nut angular displacement
x_r	Roller screw linear displacement
m_{pc}	Coupler mass
x_{pc}	Coupler displacement
m_n	Clamping tube mass
x_n	Clamping tube displacement
m_{plpu}	Plunger-punch mass
x_{pu}	Punch displacement
m_c	C-frame effective mass
x_d	Die displacement

Figure 3.2: Lumped-parameter representation of the system. The control structure is shown on the left side of the diagram, where arrows indicate direction of signal flow. The mechanical system is shown on the right side.

3.3.2.2 Motion sequence

The motion logic determines the sequence of action of the riveting process and is implemented via the PLC code. In a typical riveting process, the cycle begins with forward motoring as the punch is accelerated towards the material to be joined, up to a predefined setting velocity. During the rivet insertion phase a specified limit is imposed on the amount of current that can be drawn by the motor (i.e. motor current limit) in order to achieve a consistent torque output from the motor, as well to prevent it from overheating. Throughout rivet insertion, the C-frame undergoes deflection under the insertion force. After rivet insertion, the C-frame springs back into its unloaded position while simultaneously pushing the punch backwards. The motor is then driven in reverse to bring the punch back to rest at the initial home position.

3.3.2.3 Power electronics

The physical hardware which provides electrical power to the system is housed within the control panel. More specifically, the control and power sections of the drive unit. The power section is made up of three main components: a converter which rectifies the AC line voltage into a DC voltage, a DC bus which stores the power rectified by the converter via capacitors and also acts as a DC voltage source, and lastly a voltage source inverter which produces the desired AC voltage from the DC bus.

The primary purpose of the voltage source inverter is to try to supply the desired voltage control signals to the motor, which are three-phase with variable-amplitude and variable-frequency. This is achieved by switching on and off six power switches at specific durations and frequencies. The timing of the action of each switch is determined via pulse width modulation, which generates pulses from comparing the reference three-phase voltage signal with a triangular wave.

The layout of a three-phase voltage source inverter is shown in Figure 3.3. It consists of three legs each with two Insulated-Gate Bipolar Transistor switches and diode pairs: S_a and $\overline{S_a}$, S_b and $\overline{S_b}$, S_c and $\overline{S_c}$. The motor terminals are connected to the mid-point of the legs in between each pair. Only one switch out of each pair is permitted to switch on at any instant to avoid a short circuit. In total there are 8 possible switching states, which are used to output a pulse waveform for each of the three-phases. The widths of the pulses in the waveforms are determined by the timing of the switches and contain a sinusoidal fundamental component that matches closely the reference three-phase voltage signal.

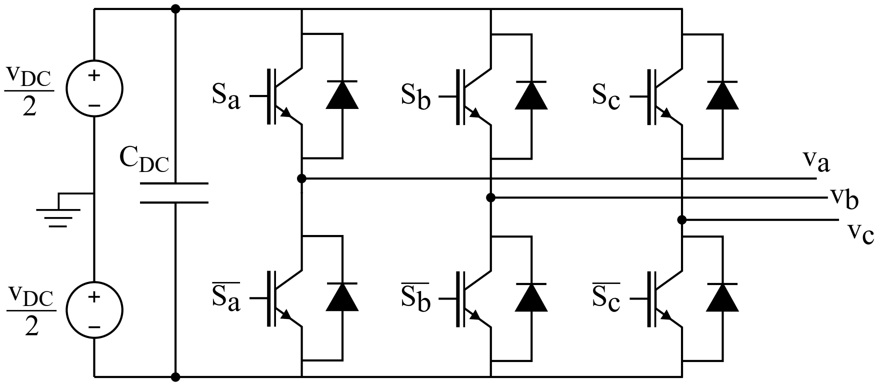

Figure 3.3: Diagram of a three-phase voltage source inverter.

3.3.3 Motor

The motor is a three-phase permanent magnet synchronous motor, consisting of armature windings on the stator and permanent magnets on the rotor. Electromagnetic torque is generated by the interaction between the three winding currents in the stator and the magnetic field of the rotor. The motor is controlled via a technique known as field oriented control, which will be explained in Section 4.2.1.

Relative position and velocity are measured by an incremental optical encoder coupled to the back of the motor. The nature of the incremental encoder means that a datum position must be established before operation.

3.3.4 Belt drive

Power is transmitted from the motor to the roller screw mechanism via a pulley and belt drive. The pulleys are equal in pitch diameter to provide a drive ratio of one. The belt itself consists of Neoprene backing and teeth, Nylon facing and helically wound fibreglass tensile members.

3.3.5 Planetary roller screw mechanism

The PRSM converts rotary motion into linear movement of the punch. In a standard PRSM the screw shaft is surrounded by equally spaced rollers which are contained inside a threaded nut. The rollers transfer the rotation of the nut to the screw shaft. One revolution of the screw results in an axial displacement equivalent to its lead. The helix angle of the rollers is the same as that of the internal threads on the nut. If the nut is restricted from rotating, the subsequent rotation of the screw will result in the axial displacement of the nut by one lead of the screw per full turn. If instead, the screw is restricted from rotating, the PRSM is said to be inverted, and the rotation of the nut would then result in the axial displacement of the screw by one lead relative to the nut per full turn. Both the standard and inverted types are used in the production systems in the field.

3.3.6 Clamping mechanism

The clamping mechanism is a mechanical subassembly in which a substantial clamping force is generated and exerted onto an area of the material immediately surrounding the location of rivet insertion.

The magnitude of the force generated is dependent on the position of the punch relative to the end of the clamp tube. In a typical cycle, initial compression of a coil spring causes a force of approximately 300 N to be applied by the clamp tube on the material stack, which serves to hold it in place in preparation for rivet insertion. When the punch is almost flush with the end of the clamp tube, a stack of disc springs is engaged, causing a force in the region of 8 kN to be applied on the material by the clamp tube. This serves to flatten and reduce distortion in the surrounding material. Further details regarding the generation of the clamp force are provided in Sections 4.2.4 and 4.2.5.

3.3.7 C-frame

The reaction force generated between the upper and lower arms of the C-frame is the force transmitted through the joint. During the riveting process the upper and lower arms undergo deflection, the extent of which depends on the transmitted load as well as the stiffness of the C-frame. Hence the mechanical properties of the structure play a critical role in the forming of the joint.

C-frames are also designed with accessibility in mind. The throat opening of the C-shape allows material or parts to be supplied from the front and sides of the C-frame for joining. Alternatively, robot-mounted C-frames may be manoeuvred into place for making joints on larger structures, such as the body-in-white of a vehicle.

In automated robotic applications, the payload capacity of the robot is a limiting factor. Special C-frames were developed to minimise the weight of the riveting equipment for cases where long throat reach and weight were desired [24]. Via the use of Aligned C-frame technology, licensed to the partner company by C-Power technologies AB, the design introduced hollowed out sections into the body of the C-frame to allowed a weight reduction of up to 40% in comparison to conventional C-frames. A further distinction is that the Aligned C-frame does not exhibit angular deflection like the conventional C-frame, hence better axial alignment between the punch and the die is achieved during the riveting process.

3.4 Experimental system

3.4.1 Test system

In the facilities at Atlas Copco IAS UK Limited, existing test systems consisted of a rivet setter and C-frame mounted on a stand, powered via a control panel, as shown in Figure 3.4. Typical data acquired included the total process force, the angular displacement and velocity of the motor, as well as the motor current.

For the current project, the model of the joint was a key component of the overall model of the SPR process. Identification of a model for the joint required the relevant measurements to be obtained from the riveting event, such as the extent and rate of rivet insertion, the forces transmitted through the clamping mechanism as well as that transmitted through the

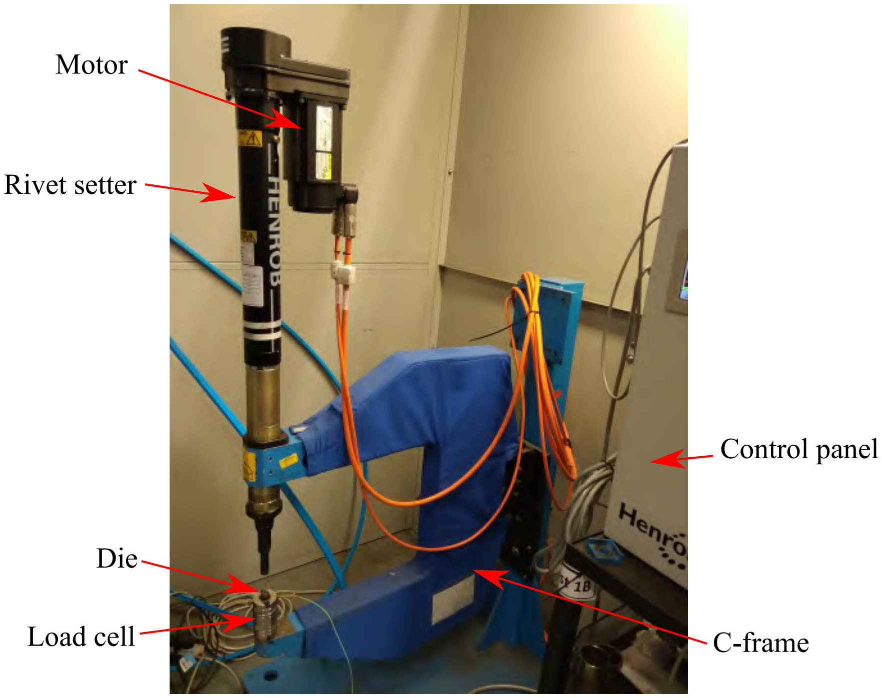

Figure 3.4: Picture of the original SPR test system.

punch. The existing test setup was not able to provide all the required data, hence changes had to be made to the test rig design.

The clamping of the material stack and punching of the rivet represented two distinct forces acting on different parts of a joint: the clamp force and the punch force. Two load cells were used to obtain the individual components of the total process force. The total force was measured using the primary load cell located under the die. The clamp force was measured using a secondary load cell which was part of an adapted clamping mechanism. The punch force was estimated by subtracting the clamp force from the total force.

The load cells used were Kistler piezoelectric sensors, each containing a quartz element which produced an electric charge according to the compressive load applied across the sensor. A charge amplifier was necessary to convert the generated charge to a voltage that could be practicably measured. Each load cell had a specific sensitivity value which described the amount of charge produced per unit force, as noted in Table 3.2. The sensitivities values were manually entered and downloaded to the charge amplifier via the Manuware software. The configuration screens in Manuware are shown in Appendix A.

Table 3.2: Specifications of the load cells used in testing.

Load cell	Type	Measuring range (kN)	Sensitivity (pC/N)
Primary	9363A	0 ... 120	3.882
Secondary	9343A	0 ... 70	4.029

In order to gain a closer observation of the rivet insertion, a high-speed camera was used to record the process. The rivet was not directly visible since it was shielded inside the clamping mechanism, hence the clamp tube was redesigned with a slot to allow visibility of the punch, and the displacement of the rivet was inferred from the motion of the punch instead. This was done by making a mark on the punch such that between the start of rivet insertion (Figure 3.5(a)) and when the rivet is fully inserted (Figure 3.5(b)), the mark would remain visible via the open slot on the clamp tube. Thus, the displacement of the punch relative to the die was used to estimate the extent of rivet insertion into the material. Figures 3.5(c) and (d) show the cutaway views corresponding to Figures 3.5(a) and (b) respectively. Figures 3.5(e) and (f) are photographs of the actual setup corresponding to Figures 3.5(a) and (b) respectively.

The necessary data was acquired using the test rig illustrated in Figure 3.1. Details of the data acquisition setup are given in Section 3.4.2.

3.4.2 Data acquisition setup

A detailed view of the wired connections and relevant signals in the test setup is provided in Figure 3.6. Data acquisition (DAQ) was performed on the following data loggers at a sampling rate of 4 kHz. The full data acquisition system involved three main components:

- National Instruments (NI) chassis and DAQ modules
- Bosch drive, housed inside the control panel
- Photron FASTCAM Mini UX100 high-speed camera

Additionally, the setup required two computers. PC 1 was a computer connected directly to the Bosch drive via an Ethernet cable, through which the drive was configured. PC 1 was also connected to the NI DAQ system via a USB cable for transfer of the total force, clamp force, motor temperature and encoder position data. PC 2 was a dedicated computer for operating the high-speed camera and saving the video data via an Ethernet connection.

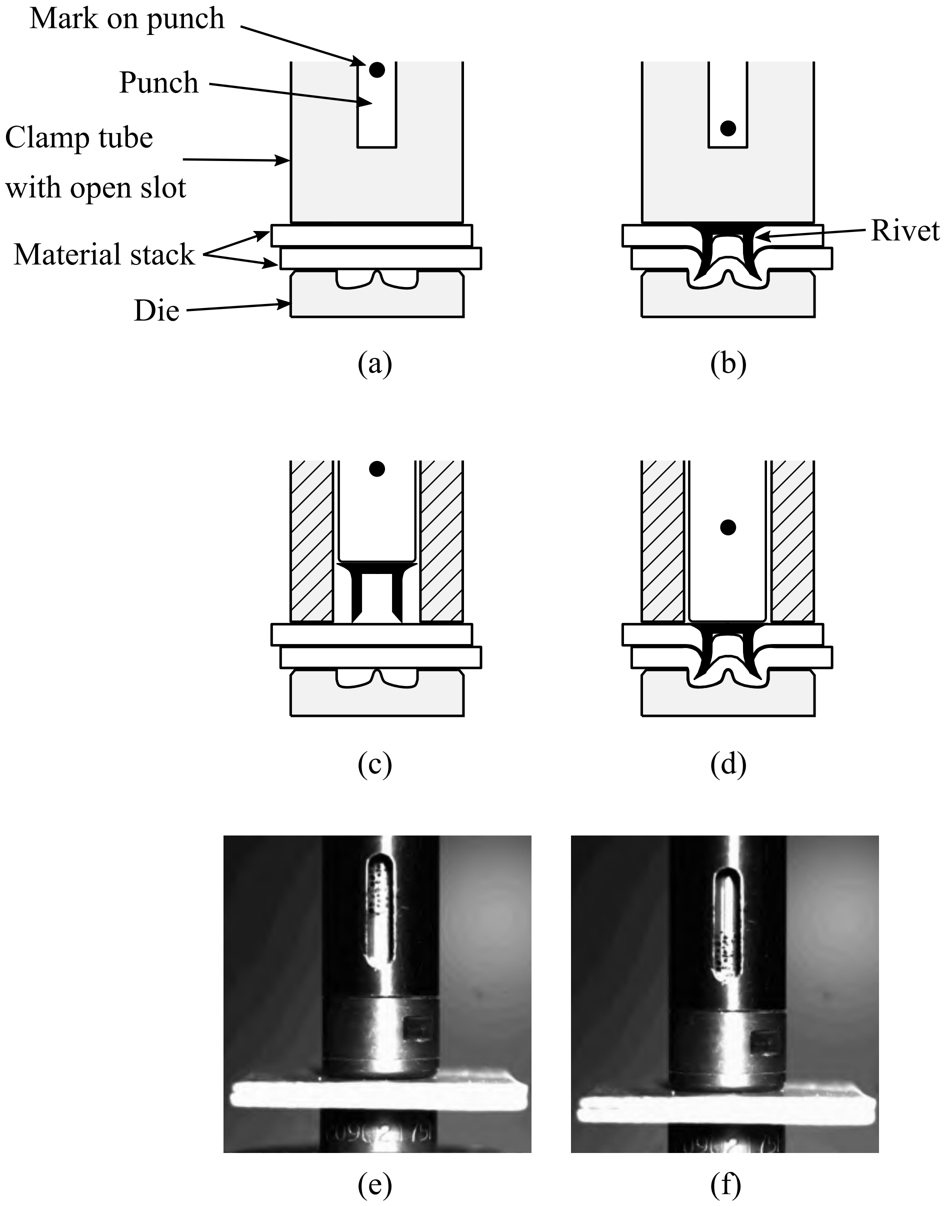

Figure 3.5: Illustration of the relative motion between the punch and the die during rivet insertion. (a) External view of the clamp tube with no direct visibility of the rivet, just before rivet insertion. (b) External view of the clamp tube once rivet is fully inserted. (c) Cutaway view of the clamp tube, just before rivet insertion. (d) Cutaway view of the clamp tube, once the rivet is fully inserted. (e) Photograph of the setup, just before rivet insertion. (f) Photograph of the setup, once the rivet is fully inserted.

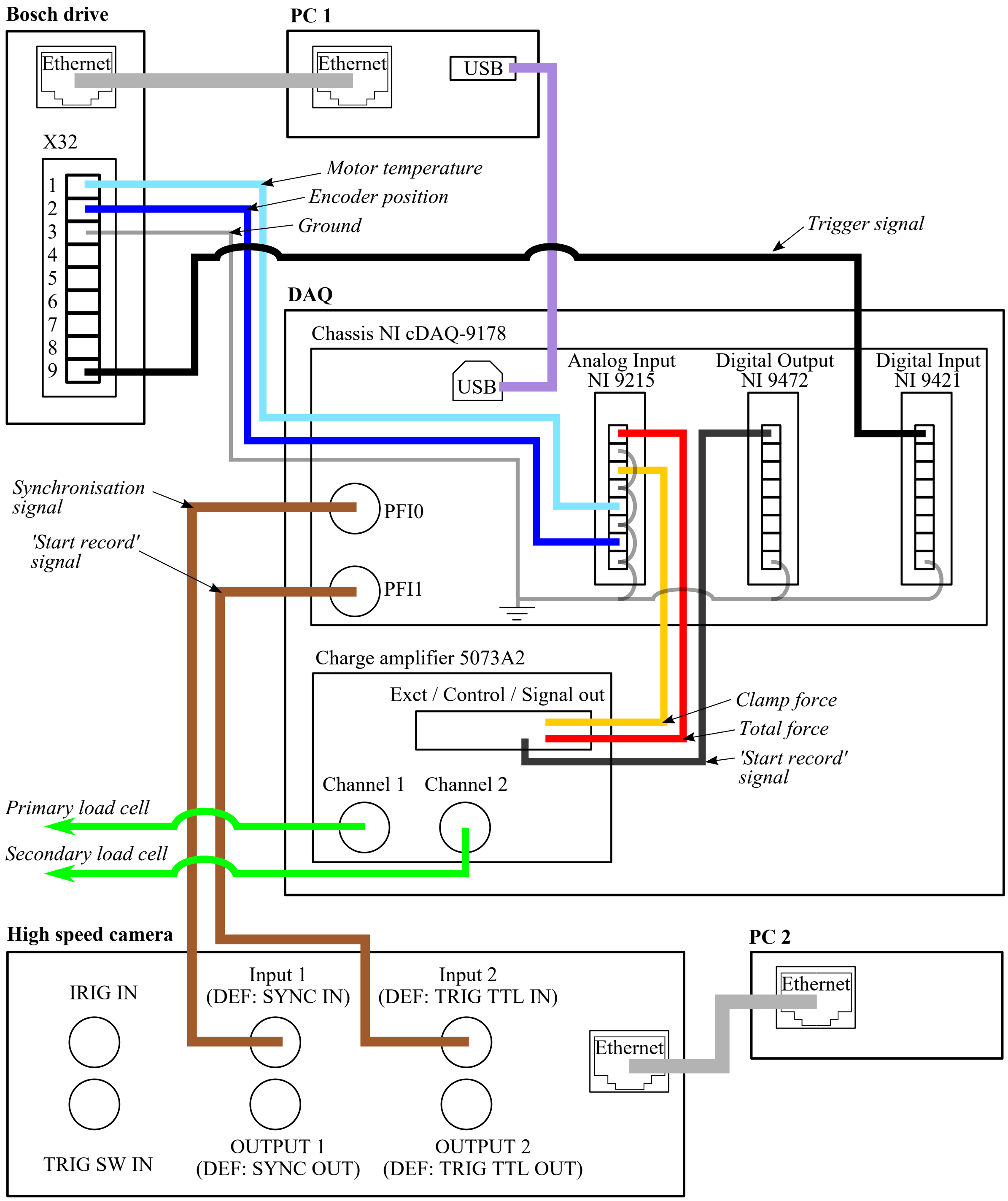

Figure 3.6: Wired connections between data loggers in the test system.

3.4.2.1 National Instruments chassis and modules

The data recorded using the three separate data loggers needed to be synchronised. To realise this, the NI DAQ system was designated as the master system. The NI DAQ system was responsible for recording the force signal from the load cell, as well as generating the synchronisation and the trigger signal for the camera. The constituent parts of the system are described as follows:

- NI cDAQ-9178: Chassis. This provided power and signal routing for the installed modules. Ports PFI0 and PFI1 were used to output digital signals to the camera; PFI0 and PFI1 were connected to the SYNC IN and TRIG TTL IN ports on the camera respectively, using BNC cables.

- NI 9215: Analog Input module. This read the signal output from the charge amplifier to obtain the force measurement, as well as the position analog signal from the Bosch drive.

- NI 9472: Digital Output module. This produced a trigger signal used to start the measurement on the charge amplifier. The same start trigger signal was exported to PFI1 port on the chassis (via internal wiring in the chassis) to start the recording on the camera. The module also generated a digital pulse train which was exported to the PFI0 port on the chassis to be used as the synchronisation signal for the camera.

- NI 9421: Digital Input module. This detected a position-based trigger signal from the Bosch drive, such that the NI DAQ system would start the chain of data acquisition tasks only when the punch had reached a specified position before rivet insertion.

- 5073A2: Kistler charge amplifier. This conditioned the signal from the load cell to provide a voltage proportional to the force acting on the load cell. The output signal was routed to the NI Analog Input module.

A tailored LabVIEW programme was written to deal with the following tasks:

- Detection of the position-based trigger signal from the Bosch drive

- Generation of the synchronisation signal for the camera

- Generation of the ‘start record’ signal for the camera and charge amplifier

- Acquisition of the total force, clamp force, motor temperature and encoder position data via the analog input module

The synchronisation signal for the camera was a pulse train generated at a specified frequency, such that the camera would acquire frames at that frequency once triggered.

The ‘start record’ signal sent from the NI DAQ system to the camera was a rising edge, generated at the same instant as the start trigger of the Analog Input task, meaning that the image acquisition on the camera and data acquisition on the analog input would start simultaneously.

The synchronisation between the NI DAQ system and the Bosch drive was done in post-processing, where a common signal shared between the two data loggers was used to perform the synchronisation. On the Bosch drive, the position signal was processed from the motor encoder measurements and recorded to file. This signal was also exported from the drive via the analog output port and routed to the analog input module of the NI DAQ system. MATLAB code was developed to postprocess and synchronise the data from the drive to that acquired on the NI DAQ system based on this common position signal.

3.4.2.2 Bosch drive

The configuration of the Bosch drive was carried out using the IndraWorks software interface. In reference to Figure 3.6, the motor temperature and encoder position signals were exported as analog signals via ports 1 and 2 of the X32 interface, and routed to the Analog Input module in the NI DAQ chassis. A trigger signal based on the encoder position was exported via port 9 to the Digital Input module on the NI DAQ chassis, which served as a flag for the NI DAQ system to initiate the chain of acquisition tasks.

3.4.2.3 High-speed camera

Positioning and alignment As indicated in Figure 3.1(a), the camera was mounted on a tripod and positioned to the side of the C-frame. The rotational alignment of the camera was adjusted using the bubble spirit levels on the tripod and the three-way head as follows:

- The forward/backward tilt angle (pitch) was set to 0 degrees.
- The left/right swivel angle (yaw) was set such that the camera lens pointed in the direction normal to the side plane of the C-frame, alignment by eye was considered adequate for the requirements of the tests.
- The side to side pivot angle (roll) was set to 0 degrees.

Regarding the translational degrees of freedom of the camera, the following steps were performed:

- To configure the elevation of the camera, the tripod legs were opened up to put the camera at the appropriate elevation. The legs were kept at their minimum extensions to help minimise compliance in the tripod. The height of the central rod supporting the camera was adjusted until the lens of the camera was approximately level with the die on the riveting system.
- The position along the left/right direction was set such that the camera pointed directly at the load cell.
- The position in the forward/backward direction was set such that the camera was approximately 0.3 m away from the C-frame.

Wired connections made to the camera were: Ethernet cable, SYNC IN, and TRIG TTL IN. The Ethernet cable served as the communication and data transfer channel between the PC and the camera. The SYNC IN and the TRIG TTL IN ports were input channels for an external synchronisation signal and trigger signal respectively. These were connected to ports PFI0 and PFI1 respectively on the NI chassis.

Once powered up, the Photron FASTCAM Viewer software was used to examine the live images from the camera, based on which the position, alignment and focus of the camera were fine-tuned. This was necessary as the C-frame was not perfectly vertical in its mounting on its stand. Fine-tuning was carried out by adjusting the side to side pivot angle of the camera until the clamping tube of the setter could be seen to be aligned with the reference vertical lines of the on-screen grid. The aforementioned measures also facilitated motion tracking during the post-processing stages.

Calibration The relation between the pixels in the camera image and physical lengths needed to be established in order to extract any meaningful measurements from the high-speed video data. Calibration of the camera was done via the following steps:

1. A die was installed in the primary load cell, which is labelled in Figure 3.1(a).
2. The rivet setter was operated so that the clamping tube and the die were both visible in the live image of the camera, as shown in Figure 3.7.
3. The position of a distinctive feature on the clamping tube was noted in terms of pixels from the top edge of the live image, as measured using Photron FASTCAM Viewer.
4. A Vernier caliper was used to manually measure the distance between the bottom of the clamping tube and the flat surface of the die.

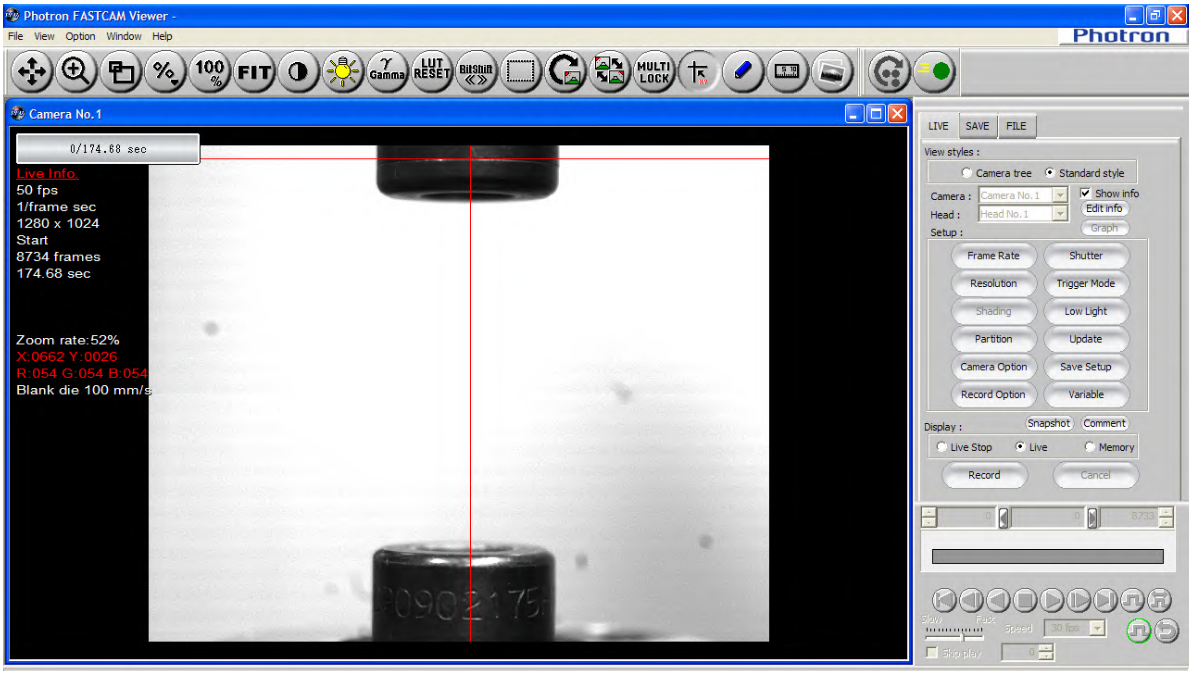

0/174.88 sec
Live Info.
50 fps
1/frame sec
1280 x 1024
Start
8734 frames
174.68 sec
Zoom rate:52%
X:0662 Y:0026
R:054 G:054 B:054
Blank die 100 mm/s

Figure 3.7: View of the camera image at the start of the calibration process.

5. The setter was operated to move the clamping tube by approximately 5 mm towards the die.

6. Steps 3 to 5 were repeated until the clamping tube was too close to the die to allow caliper measurements.

Figure 3.8 illustrates the measurements taken during the calibration process. Each time the setter was operated, the change in the position of the clamping tube relative to a fixed object (i.e. $d_1 - d_2$) was obtained. This displacement was divided by the number of pixels traversed by the tracked feature on the clamping tube (i.e. d_{pix}), to give a scaling factor in units of mm/pixel. Multiple repeats allowed an average scaling factor to be determined. The average value was used in the post-processing of camera data to convert pixel measurements into meaningful displacement values.

The data from the calibration process is shown in Figure 3.9, where the scaling factor was estimated as 0.0476 mm/pixel. Dotted lines correspond to a 95% confidence interval. Calculation of the measurement uncertainties and their potential impact on the model are explored in Section 3.8.

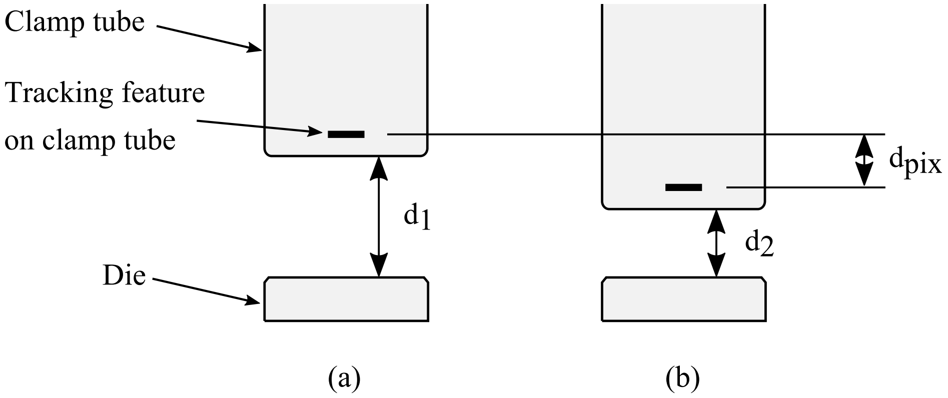

Figure 3.8: Illustration of the measurements taken in calibrating the camera. (a) First measurement. (b) Second measurement, after the clamp tube is advanced towards the die. The change in the distance between the clamp tube and the die ($d_2 - d_1$) is physically measured and related to the corresponding number of pixels from the camera image (d_{pix}).

3.5 Experiments for parameter identification

It will be seen later (Section 4.2.7) that the mechanical properties of the C-frame are important characteristics of the SPR system that need to be experimentally identified. This was done using the following approach.

The effective mass, stiffness and damping of the C-frame were estimated from data obtained using the same test setup as that shown in Figure 3.1, with the exception that a blank die (i.e. a die with a flat surface) was fitted to the primary load cell on the lower arm of the C-frame.

3.5.1 Effective stiffness

The effective stiffness was identified by loading the C-frame with a known force and measuring the relative displacement or deflection between the upper and lower arms of the C-frame. The measurement was taken by using the high-speed camera. Only the deflection in the axial direction of the rivet setter was of interest.

The loading was provided by the rivet setter, which was operated to drive against the blank die. Three runs were performed on C-frame 1 with impact velocities of 280 mm/s. The deflection of the C-frame was measured using the high-speed camera, i.e. it was determined from the relative displacement between the upper and lower arms of the C-frame along the axis of the punch travel. The effective stiffness was estimated from the average gradient of the force vs. deflection profiles shown in Figure 3.10.

The results in Figure 3.10 suggest that the response of the C-frame was predominantly

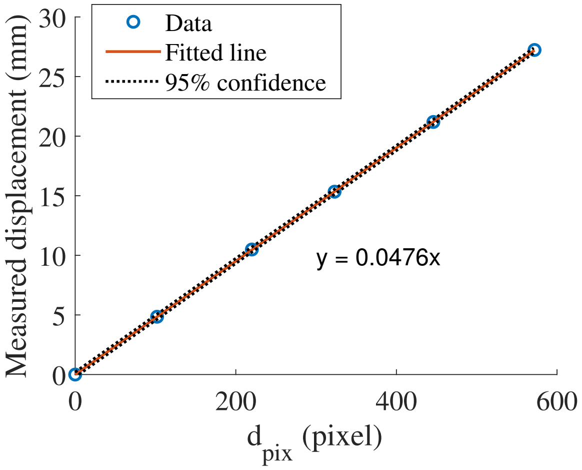

Figure 3.9: Measured displacement between the clamp tube and the die vs. number of pixels from the camera image (d_{pix}).

elastic, with relatively little damping; the area contained within the hysteresis is small. The stiffness of C-frame 1 was estimated to be in the region of 14 kN/mm, which was within 2.5% of the result of the FE analysis performed by the industry partner. This validated the effective stiffness estimations obtained via FE analysis.

The effective stiffness of C-frame 2 was obtained from FE analysis.

3.5.2 Effective mass and damping

Hammer impact tests were performed to obtain the dynamic properties of the C-frame. An impact was delivered to the lower arm of the C-frame and the response of the upper and lower arms of the C-frame was recorded using the high-speed camera. The period of oscillation as well as the decrement in the amplitude of the oscillations were used to estimate the effective mass and damping of the C-frame.

Figure 3.11(a) shows the relative displacement between the upper and lower arms of C-frame 1, which is clearly characteristic of an underdamped system. The first four peaks of the oscillations and the reduction in amplitude over time can be observed. An exponentially decreasing sine function could be fitted to the data, from which the parameters of the C-frame were estimated using the logarithmic decrement method. Likewise, Figure 3.11(b) shows the response for C-frame 2. Due to the larger effective stiffness of this C-frame, the period of oscillation was comparably shorter.

The logarithmic decrement δ is defined as:

$$\delta = \frac{1}{n}\ln(\frac{P_1}{P_{n+1}}) \tag{3.3}$$

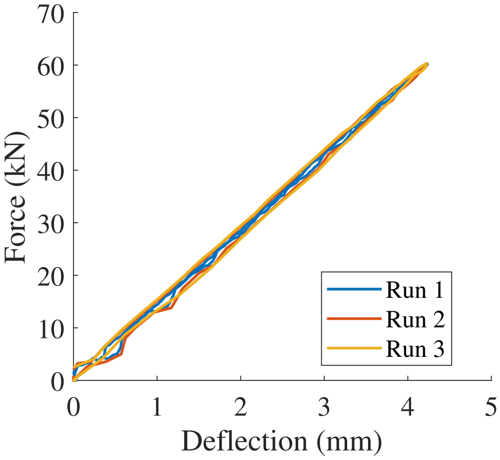

Figure 3.10: Force vs. deflection between the upper and lower arms of C-frame 1. Results are for three repeat tests.

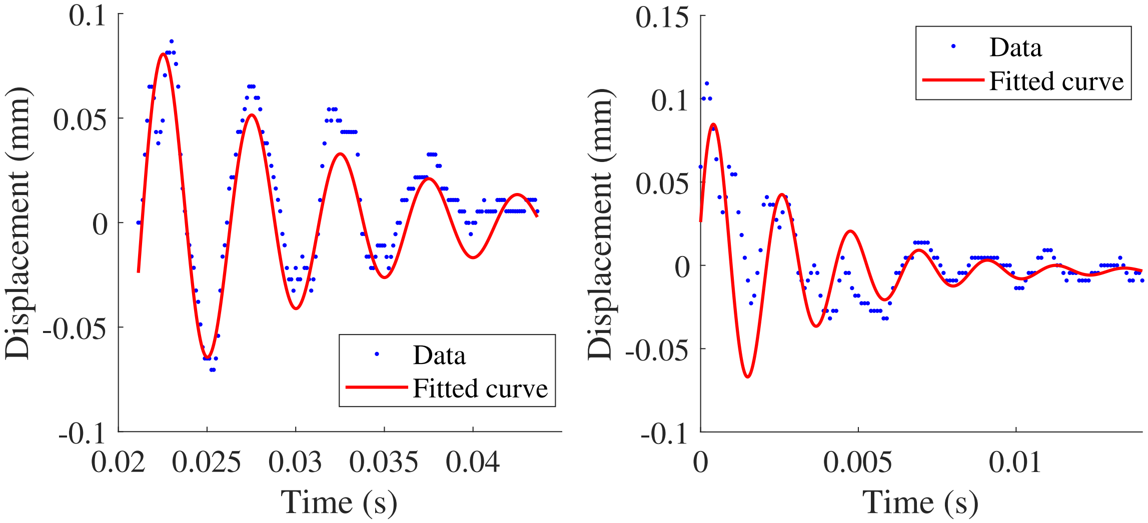

(a)

(b)

Figure 3.11: Relative displacement between the upper and lower arms of the C-frame following hammer impact. (a) Data for C-frame 1. (b) Data for C-frame 2.

Where P_1 is the amplitude of the first peak of the sine wave, P_{n+1} is the amplitude of the $(n+1)$th peak, and n is the number of cycles between the first and the $(n+1)$th peak.

The damping ratio ζ is then calculated as:

$$\zeta = \frac{\delta}{\sqrt{4\pi^2 + \delta^2}} \tag{3.4}$$

Using ζ the effective mass of the C-frame m_c is calculated via:

$$m_c = K_c \frac{1 - \zeta^2}{4\pi^2 f_d} \tag{3.5}$$

Where K_c is the effective stiffness of the C-frame, and f_d is the frequency (Hz) of the sine wave. Subsequently the effective damping constant C_c of the C-frame can be determined using:

$$C_c = 2\zeta\sqrt{m_c K_c} \tag{3.6}$$

Table 3.3 shows a summary of the parameters of C-frames 1 and 2.

Table 3.3: Estimated C-frame parameters.

C-frame type	m_c (kg)	K_c (kN/mm)	C_c (N/(m/s))
1	8.6	14.0	1500
2	3.3	28.7	2700

While approximate values for the effective mechanical properties of the C-frame could be obtained, the acquired data were susceptible to noise due to the small amplitudes of the oscillations, which could have led to potential errors in the estimated parameters. The accuracy of the displacement measurement was dependent on the resolution of the camera data, which was limited by the number of pixels in the recorded images as well as the level of zoom or magnification. Furthermore, the features used in motion tracking must all be visible within the image frame, which restricted the location and zoom setting of the camera.

More precise estimates may be obtainable using accelerometers. Accelerometers have the advantage of being attachable to a wide range of locations regardless of visibility. In addition, a triaxial accelerometer would be able to obtain data in three-dimensions in contrast to the two-dimensional data contained in a camera image. This would enable the construction and validation of a higher-fidelity model of the C-frame.

3.6 Design of experiments for joint identification

In consideration of the aims of the experiment and Section 3.2, DOE was considered a necessary approach for obtaining data that could be used to construct and validate the model of the joint.

Since the number of variables in the SPR process was extensive, a realistic plan was to select the factors which were known to have an influence over the riveting process and which were typically modified in the design and commissioning of real production systems. The chosen process variables were the setting velocity, the motor current limit and the C-frame type.

In the real process, the setting velocity was the most commonly adjusted parameter on a given system. The motor current limit was also an easily modified parameter used in the control of the process. The C-frame type was a third variable, in the sense that multiple types could be installed on a single production line. Furthermore, the C-frame was known to influence the setting velocity required to form an adequate joint. These variables could be thought of as being the main factors of interest with regards to their effects on the resulting joint. Thus, a DOE incorporating these factors would provide industry-relevant cases for the validation of the model, as well as offer insights into the variability of the process.

Needless to say, the joint configuration would have significant influence over the output of the process. However, this was not considered a variable since the material to be joined was typically predefined and outside the control of the designers of SPR systems, and the rivet and die profiles were beyond the scope of the current project.

3.6.1 Definition of joint configurations

Two joint configurations were included in the experiment to assess the suitability of the modelling approach to different types of joints. The selection was limited to two joint configurations to keep the experimental runs to a reasonable number. For convenience, the joint configurations are referred to as joint A and joint B from here onwards. The rivet, material and die which constitute each configuration are shown in Figure 3.12. Detailed information of the joint configurations are confidential and therefore not included here.

These particular joint configurations were chosen based on the fact that they were two of the most commonly made joints in production applications, hence the resulting model would offer direct insights into existing SPR processes. All material stacks were prepared with square coupons of the indicated material measuring 40 × 40 mm in length and width. Two coupons were used per riveting cycle.

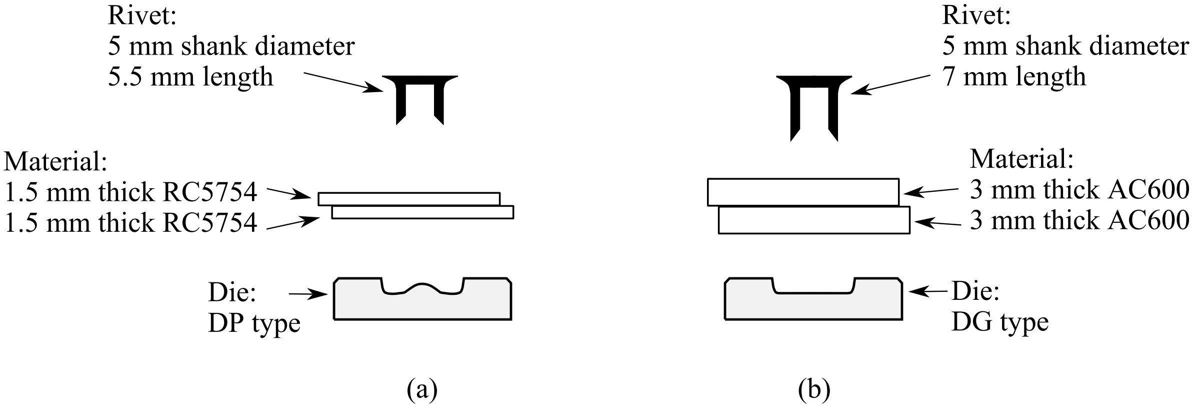

Figure 3.12: Details of the joint configurations used in testing. (a) Joint A. (b) Joint B. Joint configuration is defined by the unique combination of rivet type, material stack, and die type.

3.6.2 Experiment design

A randomised two-level full factorial experiment design was carried out to investigate the effects of three factors on the joint: C-frame type, setting velocity and motor current limit. Two levels were defined per factor, resulting in eight unique combinations of factor settings (i.e. ‘treatments’). To get an idea of the variability in the process, five replicate runs were designated for each treatment, therefore the eight treatments equated to 40 runs. Table 3.4 shows the details of each treatment. All eight treatments were carried out for each joint configuration, resulting in a total of 80 runs. To minimise the manual effort required to switch between C-frames, the runs were organised into two blocks of 40 corresponding to the two C-frames, such that the switch only had to be performed once. C-frame type 1 and 2 refer to the two types of C-frames used in the current study, the key dimensions of which are noted in the table. The C-frames were also different in that C-frame 1 was an Aligned C-frame type (as described in Section 3.3.7) and C-frame 2 was a conventional type.

Table 3.4: Treatments used in testing for a given joint configuration. Five replicates were applied for each treatment.

Treatment	C-frame type	Setting velocity V (mm/s)	Motor current limit T (%)
1	1 (throat height: 400 mm, throat depth: 450 mm)	150	100
2	1 (throat height: 400 mm, throat depth: 450 mm)	150	150
3	1 (throat height: 400 mm, throat depth: 450 mm)	250	100
4	1 (throat height: 400 mm, throat depth: 450 mm)	250	150
5	2 (throat height: 360 mm, throat depth: 300 mm)	150	100
6	2 (throat height: 360 mm, throat depth: 300 mm)	150	150
7	2 (throat height: 360 mm, throat depth: 300 mm)	250	100
8	2 (throat height: 360 mm, throat depth: 300 mm)	250	150

The experiments were run under laboratory conditions. The system was operated according to the predefined motion sequence described in Section 3.3.2.2, consisting of: advance, rivet insertion, and retraction. The measurements taken during the rivet insertion event included the process forces, angular position and velocity of the motor, relative displacement and velocity between the punch and the die, relative displacement between the clamp tube and the die, and the motor current. After each riveting cycle, the head height of the joint, or the protrusion of the rivet head relative to the top surface of the top layer of material, was measured using a Mitutoyo absolute digimatic indicator. Figure 3.13 illustrates the head height measurement.

3.7 Results for joint identification

This section presents a selection of results obtained from the tests described in Section 3.6. For details of all the results from the experiment, the reader is referred to Appendix B.

3.7.1 Joint A

A closer look is taken at the results for treatments 4 and 8. The choice of these two treatments is motivated by the higher setting velocities and forces associated with the runs, which place

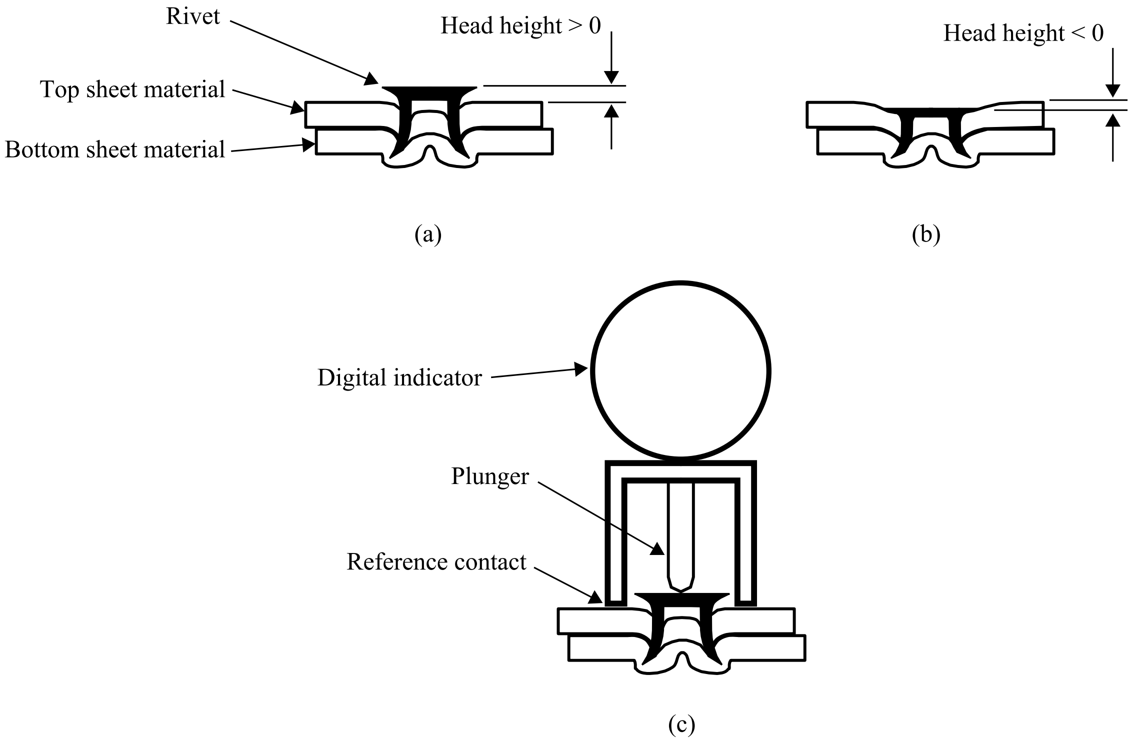

Figure 3.13: (a) In the case of a protruded rivet the head height measurement is positive. (b) For the case where the rivet head is below the surface of the top sheet of material, the head height measurement is negative. (c) Indicator used to measure head height. In industry a typical requirement is for head height to be in the range between 0.3 mm and -0.5 mm [10].

more demand on the system.

Since five replicate runs were performed for each treatment, the mean μ and sample standard deviation σ of each time-based signal could be obtained; at any given time step, the corresponding five values from the five datasets in the chosen treatment were used to calculate the mean and standard deviation at that time step. Doing this across the entire time history generates a mean curve as well as standard deviation curves. These serve as indicators of the variability of the process. In the following figures, three curves are plotted for each signal: μ, $\mu + 3\sigma$ and $\mu - 3\sigma$.

Results for treatment 4 suggest that the process was quite repeatable; little variability is noted in the forces and the camera-measured relative displacement, shown in Figure 3.14(a) and (b) respectively. Figure 3.14(c) exhibits larger variation due to the noise resulting from the numerical differentiation performed on the relative displacement signal.

In contrast, results for treatment 8 are distinguished by the apparent increase in the variability of the force signals around the region of the peak force, as shown in Figure 3.15(a). This was believed to be attributed to a combination of factors. Firstly, a mechanical change in the system had been incurred over the course of the 80 runs which led to a change in the

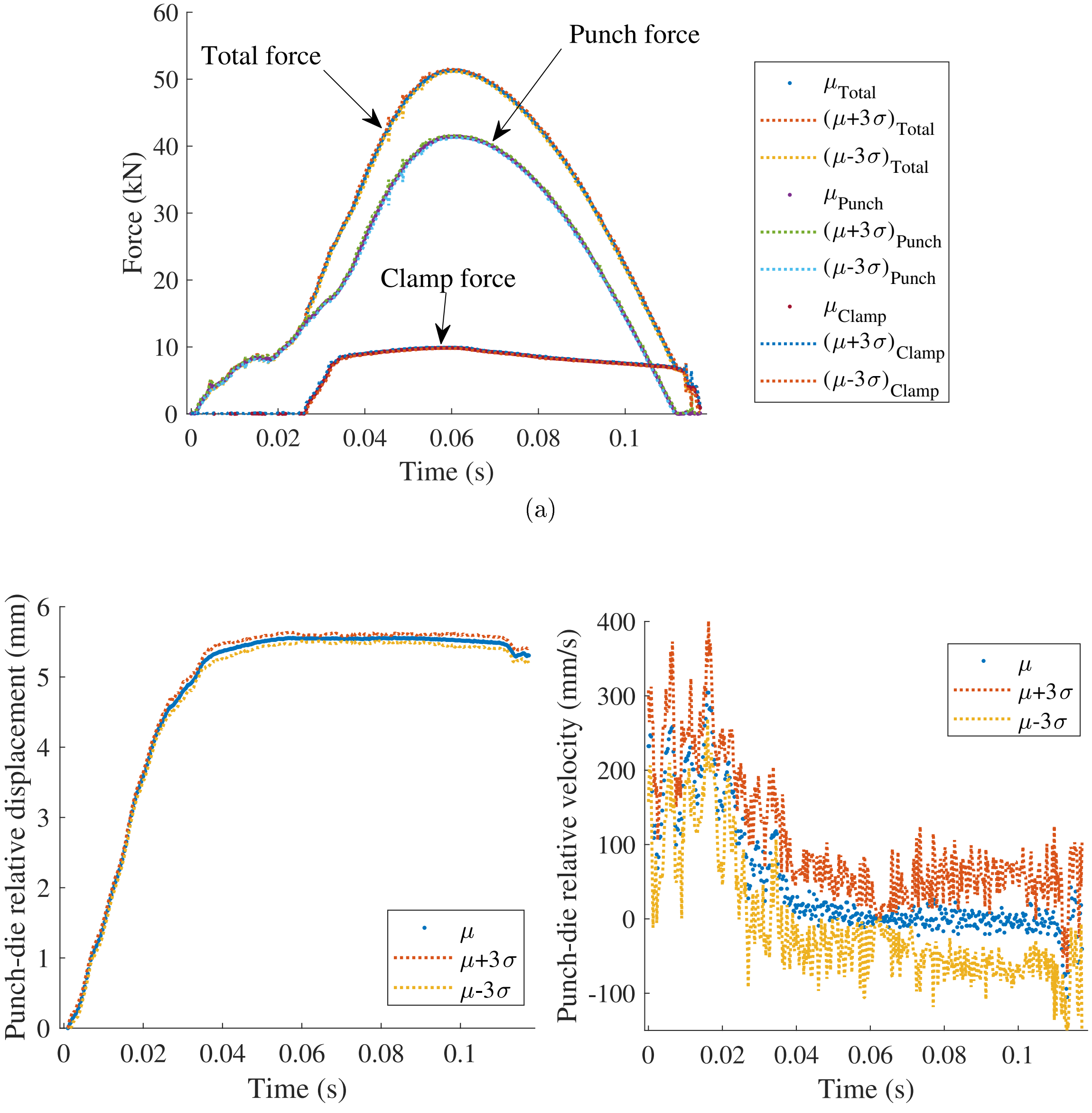

(a)

(b) (c)

Figure 3.14: Joint A, treatment 4: (a) Force vs. time. (b) Relative displacement between the punch and the die vs. time. (c) Relative velocity between the punch and the die vs. time. μ and σ represent the means and sample standard deviation respectively, which were calculated at each time step for the five datasets within the chosen treatment.

timing and magnitude of the clamp force. The change was a singular event rather than a gradual one and could be pinpointed to runs 65 and 66, between which there appeared to have been a permanent shift in the clamp force profile. The second factor was that under the conditions of treatment 8, the hard stop within the clamping mechanism was just engaged near the end of the loading phase of rivet insertion. The aforementioned change had likely resulted in a firmer contact with the hard stop which in turn caused a notable increase in the transmitted clamp force. The knock-on effects on the punch force and therefore the total force were as expected.

By nature of the design, the profile of the generated clamp force was highly sensitive to the dimensions and offsets between the internal components in the clamping mechanism. However, while the noted change in the behaviour of the system could be considered as a deviation or even a minor form of damage, the integrity of the system was not compromised, nor was it detrimental to the quality of the produced joints. The fact that this change occurred during testing suggests that it could also happen in the field, hence it was decided to include the data from all the runs in subsequent analyses.

Figures 3.15(b) and (c) suggest that despite the apparent variability in the force profiles, the relative displacement between the punch and the die was not significantly affected. This may be indicative of the robustness of the process to small changes in the clamping behaviour.

3.7.2 Joint B

For joint B, the results also indicate a repeatable process. Figure 3.16(a) shows force vs. time for treatment 4. Figures 3.16(b) and (c) show the punch-die relative displacement and velocity vs. time. The level of repeatability appears to be on par with those for joint A.

Figure 3.17(a) shows the results for treatment 8, which were also affected by the aforementioned change in the clamping mechanism. The impact is most notable in the timing of the initial rise of the clamp force. Aside from this, the punch-die relative displacement and velocity shown in Figures 3.17(b) and (c) respectively appear to be fairly repeatable.

3.7.3 Quality check

The quality of the data depended heavily on the calibration of the high-speed camera as the system was reconfigured over the course of the experiment. Figure 3.18 serves as a overall quality check of the camera data, by comparing the head height of the joints as measured using the digimatic indicator (see Figure 3.13) against the rivet distance which was estimated from the camera data. Figures 3.18(a) and (b) correspond to joint configurations A and B respectively. The linear correlation is logical, since a rivet which is inserted further into the

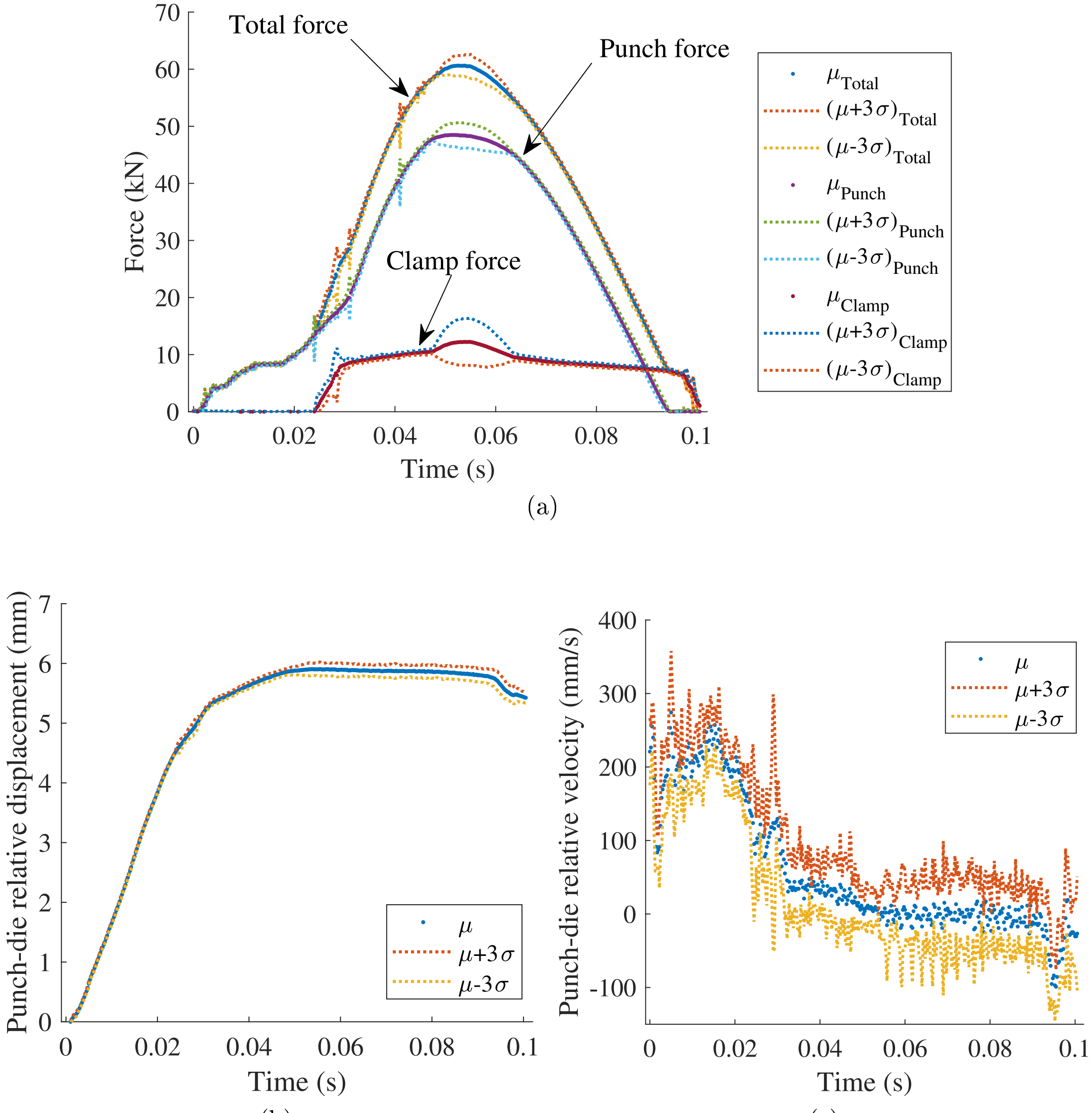

(a)

(b)

(c)

Figure 3.15: Joint A, treatment 8: (a) Force vs. time. (b) Relative displacement between the punch and the die vs. time. (c) Relative velocity between the punch and the die vs. time. μ and σ represent the means and sample standard deviation respectively, which were calculated at each time step for the five datasets within the chosen treatment.

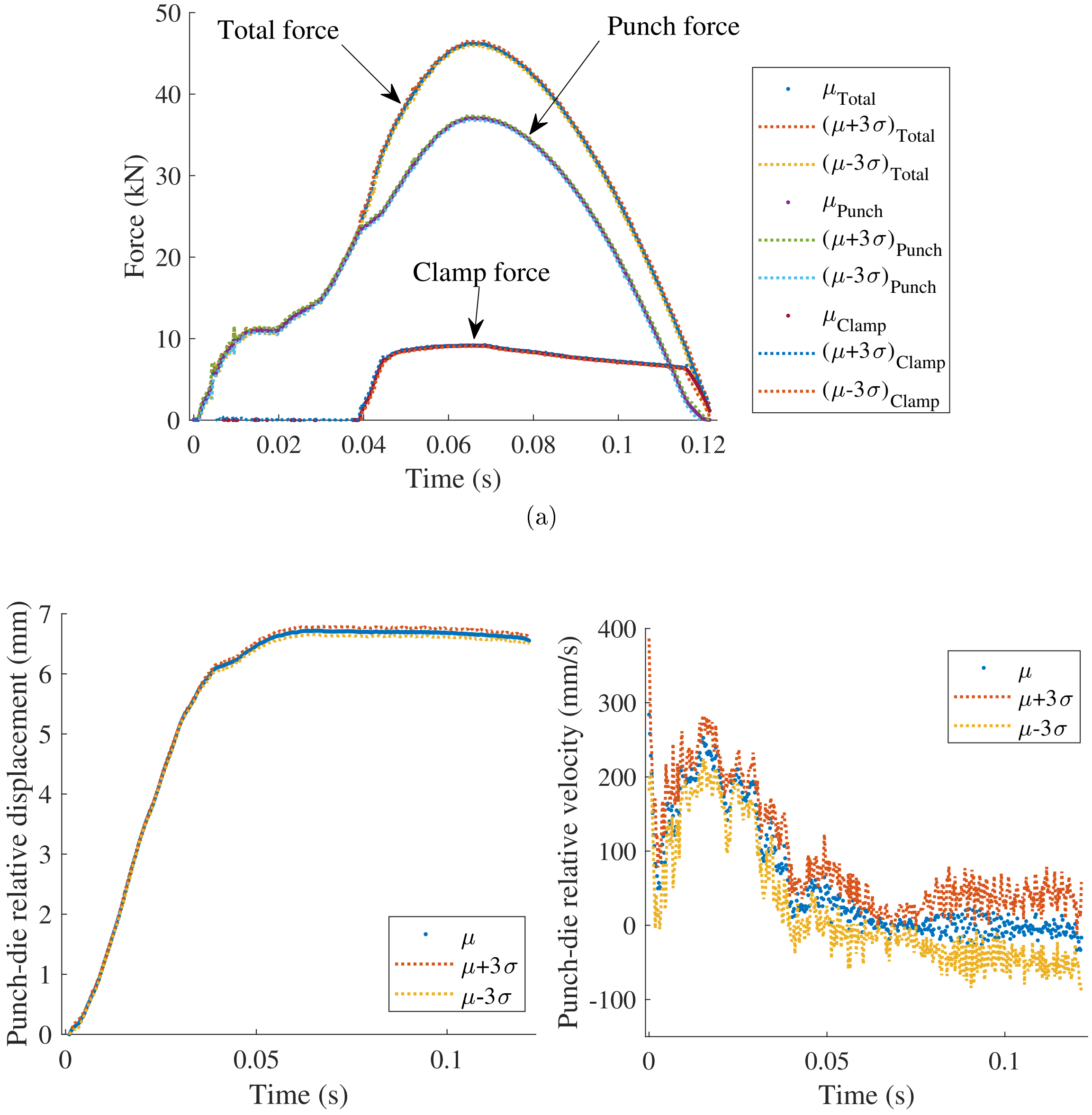

(a)

(b)

(c)

Figure 3.16: Joint B, treatment 4: (a) Force vs. time. (b) Relative displacement between the punch and the die vs. time. (c) Relative velocity between the punch and the die vs. time. μ and σ represent the means and sample standard deviation respectively, which were calculated at each time step for the five datasets within the chosen treatment.

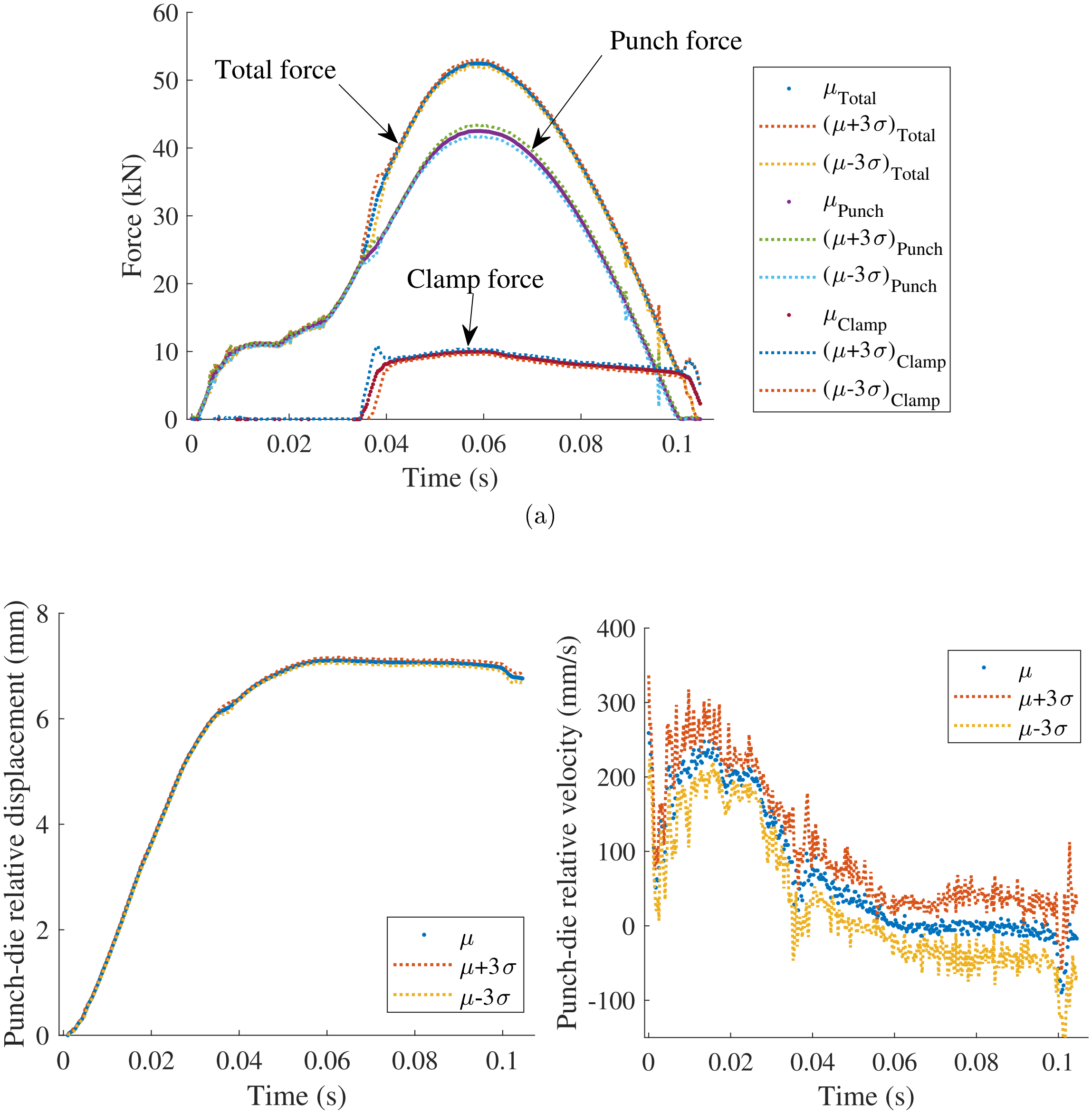

(a)

(b)

(c)

Figure 3.17: Joint B, treatment 8: (a) Force vs. time. (b) Relative displacement between the punch and the die vs. time. (c) Relative velocity between the punch and the die vs. time. μ and σ represent the means and sample standard deviation respectively, which were calculated at each time step for the five datasets within the chosen treatment.

material stack has a lower head height. A fully inserted rivet has a head height of 0 mm. It is noted that the rivet insertion distances corresponding to a 0 mm head height are 5.5 and 7 mm for joint A and B respectively, which match the nominal lengths of the rivet types for both joint configurations. The results show that the camera-measured displacements were able to capture the rivet insertion event to a fine resolution.

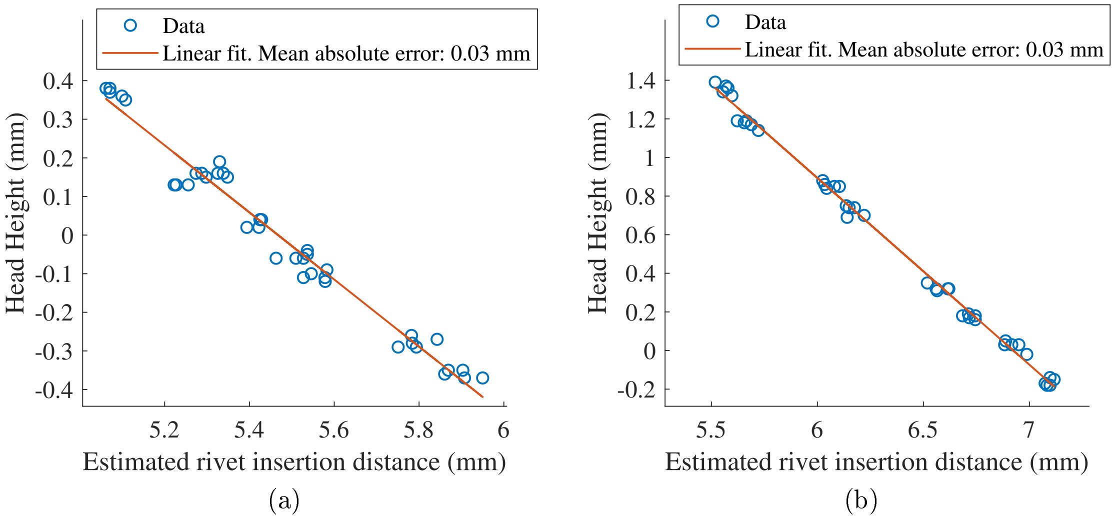

Figure 3.18: Head height measured using a digimatic indicator vs. rivet insertion distance estimated from high-speed camera data. (a) Joint A. (b) Joint B.

3.8 Measurement uncertainties

3.8.1 Background

The true value of any quantity is unobtainable, since any attempt of measuring a quantity is affected by errors associated with the measuring instrument. Consequently, without knowing the true value of a quantity, the accuracy of a measurement cannot be determined. Measurement uncertainty serves as a quantitative indicator of the possible error in a measurement [63], where the measurement itself can be considered as the best estimate of the true value of a quantity.

Uncertainty is expressed as a range in which the true value lies. The calculations to determine this range account for both systematic and random effects which may influence the measurement of interest. Systematic effects cause each measurement to be different from the true value by the same amount, in terms of direction and magnitude. Random effects cause each measurement to differ from the true value in a random and unpredictable manner. Ultimately, the combination of different uncertainties is done using the same method regardless of whether they are systematic or random.

Since a given measurement may be subject to multiple sources of uncertainties, the different uncertainties must be combined to arrive at an overall uncertainty associated with the measurement. Information on different sources of uncertainty may be provided on data sheets or calibration certificates, but they may be expressed in different mathematical forms, and therefore must be converted to a standard form before they can be combined. The standard form is standard deviation; a component of uncertainty which is expressed as such is referred to as a standard uncertainty (i.e. standard uncertainty is equivalent to standard deviation). Importantly, the standard uncertainty for any uncertainty component has the same units as the measurement itself.

The standard uncertainty u for a given source of uncertainty is calculated via:

$$u = Value/Divisor * Sensitivity\,coefficient \tag{3.7}$$

Where $Value$ is the uncertainty value stated on the datasheet regarding either a measurement or an uncertainty component. The $Divisor$ is associated with the probability distribution of a given uncertainty source, and determines how said distribution contributes to the combined uncertainty. The $Sensitivity\,coefficient$ defines how uncertainties expressed in different units contribute to the combined uncertainty.

The propagation of uncertainty through an equation consisting of multiple variables depends on how the variables interact. If all the variables are summed up, a simple estimation for the combined uncertainty would be to add up the standard uncertainty terms associated with each variable. However, this would lead to a pessimistic estimate (i.e. overestimate) as it would imply that the maximum value of uncertainty for all uncertainty sources occur simultaneously, which is less likely than some uncertainty components being high and others being low, assuming that the variables are random and independent [64].

An alternative, less conservative method is to combine the individual standard uncertainties statistically. Assuming that the uncertainty in a calculated value y is of interest, where $y = x_1 \pm x_2$, with x_1 and x_2 denoting variables each with its associated uncertainty, then the overall combined uncertainty (u_y) in y is calculated as:

$$u_y = \sqrt{\sum_{i=1}^{n} u_{x_i}^2} \tag{3.8}$$

Where n is the number of variables.

If $y = x_1 * x_2$ or $y = x_1/x_2$, then the relevant rule of uncertainty propagation is:

$$u_y = y\sqrt{\sum_{i=1}^{n}(u_{x_i}/x_i)^2} \tag{3.9}$$

If $y = a * x_1$, where a is a constant, then the uncertainty is propagated as follows:

$$u_y = au_{x_1} \tag{3.10}$$

Note that the aforementioned rules apply when considering the propagation of uncertainties through any equation, whether the equation describes the calculation of a quantity from multiple measured values, or the output of a single measurement device which may be subject to one or more sources of uncertainty. In the latter case, the independent variables would represent the sources of uncertainty.

Once the combined uncertainty is obtained, the expanded uncertainty u_E for a coverage factor k is determined by:

$$u_E = ku_y \tag{3.11}$$

Assuming that the combined uncertainty has a normal probability distribution, a coverage factor of one would correspond to a confidence of approximately 68%, and a coverage factor of two to a confidence of 95%, i.e. 95% confidence that the true value of the quantity of interest lies within the expanded uncertainty either side of the measured value. The latter was considered appropriate for the current study.

3.8.2 Head height

For the head height measurement, uncertainties associated with calibration and resolution as provided on the datasheet of the measurement device were included in the analysis. The effects of the uncertainties on the measurement were assumed to be additive. Table 3.5 shows the uncertainties in the head height measurement. Here, the sensitivity coefficient is set to one for all sources of uncertainty since they are of the same units as the measurement itself. The probability distributions for both uncertainty sources are assumed to be rectangular (or uniform), as this suitably represents the errors that may result from converting an analog signal into a digital reading in the measurement device. The standard uncertainties were calculated using Equation 3.7, and the combined uncertainty was determined using Equation 3.8.

For practical reasons, the uncertainties should be interpreted in consideration of the required accuracy of a measurement. Regarding head height, typical industry practice specifies

Table 3.5: Uncertainty calculations for the head height measurement.

Source of uncertainty	Value	Units	Probability distribution	Divisor	Sensitivity coefficient	Standard uncertainty
Calibration	0.02	mm	Rectangular	$\sqrt{3}$	1	0.012
Resolution	0.01	mm	Rectangular	$\sqrt{3}$	1	0.006
					Combined uncertainty:	0.013 mm
					Expanded uncertainty (coverage factor = 2):	0.026 mm

that the typical range of accepted head heights should be between -0.5 and +0.3 mm [10]. This implies that measuring head height to the nearest single decimal place would be adequate, i.e. an uncertainty of less than 0.05 mm at a confidence level of 95% would suffice. Here, the estimated uncertainty of 0.026 mm at a confidence level of 95% clearly satisfies the required accuracy.

3.8.3 Force

Regarding the force measurement, the signal flow was as follows:

1. Force is applied on the load cell, causing charge to be generated in the piezo-electric crystal inside the load cell.

2. The charge amplifier generates a voltage proportional to the charge.

3. This voltage is sampled by the Analog Input module (i.e. NI 9215), and is converted to digital data.

There are uncertainties at each stage: the calibration uncertainty of the load cell, the deviation in the charge amplifier, the gain and offset errors of the Analog Input module, etc. By propagating the uncertainties through all the stages of the data acquisition, the overall uncertainty then serves as an indicator of how far the true force could be from the measured value.

Due to the use of multiple devices and stages in signal handling, multiple tables are required to describe the calculation of the combined uncertainty. To simplify the calculations, the uncertainties are determined for a nominal 50 kN load on the primary load cell, and 10 kN on the secondary load cell. Under said loads, the charge produced by the primary and secondary load cells would be in the region of 194,000 and 40,300 pC respectively.

Table 3.6 shows the uncertainties in the total force (F_1) measurement for the primary load cell. Note that uncertainty values were based on information provided in calibration certificates; the calibration uncertainty of each load cell was 0.5% with a coverage factor of two, implying that a normal distribution would be a suitable representation of the uncertainty. The charge amplifier output was associated with a maximum deviation uncertainty of 0.01 V. Since the deviation may be pertinent at any point within the output range of the charge amplifier, a rectangular distribution was assumed.

The standard uncertainties were calculated using Equation 3.7, following which the overall uncertainty at the output of the charge amplifier was determined by propagating the uncertainties through Equation 3.12.

$$V_{CA} = q\alpha + \delta \tag{3.12}$$

Where V_{CA} is the output voltage of the charge amplifier, q is the charge produced by the load cell, α is the sensitivity coefficient, and δ is the deviation in the charge amplifier output.

Following that, the uncertainty in the NI-9215 module due to gain and offset errors as well as noise was accounted for in estimating the uncertainty in the acquired voltage V_{acq}. The uncertainty in the NI-9215 module depended on the input voltage [65, 66], hence it was not independent from the output of the charge amplifier and therefore the standard uncertainties were directly added to obtain the combined uncertainty of 0.017 V for V_{acq}. The 0-10 V output range of the charge amplifier corresponded to 0-120 kN, hence the measured voltage was converted to a force value using Equation 3.13. The uncertainty in the measured force equated to 0.20 kN, or an expanded uncertainty of 0.41 kN with a coverage factor of two.

$$F_1 = 12V_{acq} \tag{3.13}$$

The uncertainties associated with each step of signal generation, acquisition and processing were propagated according to Equations 3.8, 3.9 and 3.10.

Table 3.7 shows the calculation of the uncertainty in the clamp force (F_2) measurement involving the secondary load cell. Like with the primary load cell, the uncertainty in the charge amplifier output was calculated by propagating the uncertainties through Equation 3.12. Unlike the primary load cell, the measurement range of the secondary load cell was 0-70 kN; Equation 3.14 was used to convert the charge amplifier output to a force value. For a coverage factor of two, the expanded uncertainty in the clamp force measurement was 0.24 kN.

$$F_2 = 7V_{acq} \tag{3.14}$$

Table 3.8 shows the uncertainties in the calculated punch force, by taking the difference

Table 3.6: Uncertainty propagation for the total force measurement.

Device	Variable	Value	Uncertainty	Units	Probability distribution	Divisor	Sensitivity coefficient	Standard uncertainty
Primary load cell	q	194,000	1,164	pC	Normal (k=2)	2	$2.15 * 10^{-5}$	0.13
Charge amplifier	δ		0.01	V	Rectangular	$\sqrt{3}$	1	0.0058
Charge amplifier	V_{CA}	4.12		V				0.014 V
NI-9215	Error and noise		0.0033	V				0.0033 V
NI-9215	V_{acq}	4.12		V				0.017 V
PC	F_1	50		kN				
							Combined uncertainty:	0.20 kN
							Expanded uncertainty (coverage factor = 2):	0.41 kN

Table 3.7: Uncertainty calculations for the clamp force measurement.

Device	Variable	Value	Uncertainty	Units	Probability distribution	Divisor	Sensitivity coefficient	Standard uncertainty
Secondary load cell	q	40,300	706	pC	Normal (k=2)	2	$3.5 * 10^{-5}$	0.13
Charge amplifier	δ		0.01	V	Rectangular	$\sqrt{3}$	1	0.0058
Charge amplifier	V_{CA}	1.43		V				0.014 V
NI-9215	Error and noise		0.0033	V				0.0033 V
NI-9215	V_{acq}	1.43		V				0.017 V
PC	F_2	10		kN				
							Combined uncertainty:	0.12 kN
							Expanded uncertainty (coverage factor = 2):	0.24 kN

between the total and clamp forces, i.e. $F_{punch} = F_1 - F_2$. The combined uncertainty was determined using Equation 3.8.

Table 3.8: Uncertainty calculations for the calculated punch force.

Variable	Value	Units	Standard uncertainty
F_1	50	kN	0.20
F_2	10	kN	0.12
F_{punch}	40	kN	
		Combined uncertainty:	0.24 kN
Expanded uncertainty (coverage factor = 2):			0.47 kN

The required accuracy in the punch force measurement should be within ±2.5 kN. This is based on one of the process monitoring limits used in certain applications in the industry. From Figure 3.19 it is seen that the expanded uncertainties corresponding to coverage factor of two (i.e. a confidence level of 95%) do not exceed ±2.5 kN, and are therefore considered acceptable. If it were desirable to reduce the measurement uncertainty, one option would be to use a lower rated load cell to measure the total process force below the die. Uncertainty calculations in Table 3.6 indicate that the load cell with a calibrated range of 70 kN has a lower standard uncertainty than that with a range of 120 kN.

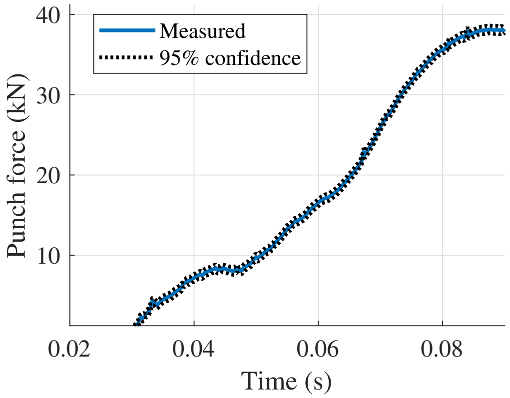

Figure 3.19: Punch force data from treatment 3. Dotted lines indicate 95% confidence interval.

3.8.4 Displacement

Obtaining the camera-measured displacement involved firstly 'calibrating' the image to determine the physical distance corresponding to a given number of pixels (i.e. identifying the mm/pixel scaling factor), then recording a video of the event of interest, followed by motion tracking analysis in which software was used to track a selected feature in the video and output the number of pixels through which that feature moved, and ultimately converting the displacement values from pixels to millimetres. More specifically, the displacement in pixels (x_{pix}) and the image scaling factor (s) were multiplied to give displacement in millimetres, as described in Equation 3.15.

$$displacement = x_{pix}s \tag{3.15}$$

The mm/pixel scaling factor was therefore a key component of the calculation process. Uncertainty in the scaling factor was considered to be the main contributor to the overall uncertainty in the displacement data. While other uncertainties such as those associated with the camera alignment were also relevant, their effects were assumed to be negligible in comparison to the uncertainty associated with the aforementioned scaling factor.

The uncertainty calculation is realised in three stages: first, the uncertainty associated with the Vernier caliper measurement is determined (Table 3.9), then the uncertainty in the scaling factor is calculated, as shown in Table 3.10. Finally, the overall uncertainty in the camera-measured displacement is obtained by propagating the uncertainties through Equation 3.15. It is clear that the uncertainty in the calculated result would increase with increasing displacement (i.e. over the course of rivet insertion); the uncertainty in the displacement would be smallest at the start of rivet insertion, and largest at the furthest insertion depth reached.

The combined uncertainty in Table 3.9 was determined using Equation 3.8.

In Table 3.10 the combined uncertainties for A and B were calculated using Equation 3.8, whereas that for the scaling factor s was calculated via Equation 3.9.

Table 3.9: Uncertainty calculations for the Vernier caliper measurement, based on [67].

Source of uncertainty	Value	Units	Probability distribution	Divisor	Sensitivity coefficient	Standard uncertainty
Calibration	0.01	mm	Normal (k=2)	2	1	0.005
Resolution	0.005	mm	Triangular	$\sqrt{6}$	1	0.002
Cosine	3	deg	Rectangular	$\sqrt{3}$	0.046	0.080
Temperature	2	degC	Rectangular	$\sqrt{3}$	0.0023	0.003
Repeatability	0.02	mm	Normal (k=1)	1	1	0.020
					Combined uncertainty:	0.082 mm
					Expanded uncertainty (coverage factor = 2):	0.165 mm

Table 3.10: Uncertainty calculations for the image scaling factor.

Variable	Value	Uncertainty	Units	Probability distribution	Divisor	Sensitivity coefficient	Standard uncertainty
d_1	64.90	0.082	mm	Normal	1	1	0.082
d_2	37.67	0.082	mm	Normal	1	1	0.082
d_{pix1}	25	1	pix	Rectangular	$\sqrt{3}$	1	0.577
d_{pix2}	597	1	pix	Rectangular	$\sqrt{3}$	1	0.577
$A = \|d_1 - d_2\|$	27.23		mm				0.116
$B = \|d_{pix1} - d_{pix2}\|$	572		pix				0.816
$s = A/B$	0.0476		mm/pix				
					Relative standard uncertainty:	0.00451	
					Absolute standard uncertainty:	0.0002 mm/pix	
					Expanded uncertainty (coverage factor = 2):	0.0004 mm/pix	

Figure 3.20 shows camera-measured displacement data from treatment 3, as well the expanded uncertainty. A coverage factor of two is chosen, i.e. the bounds are defined such that there is a 95% confidence level that the true values of the quantity of interest lie between the upper and lower bounds.

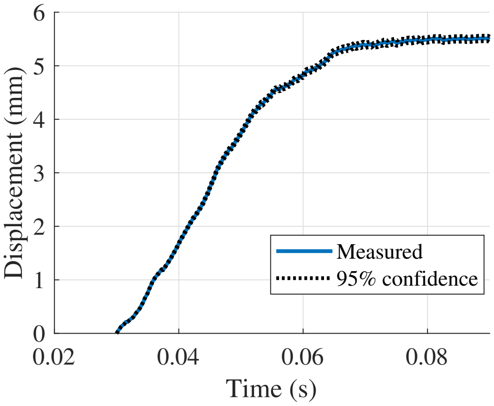

Figure 3.20: Camera-measured displacement data from treatment 3. Dotted lines indicate 95% confidence interval.

The uncertainty in the displacement data is directly related to the uncertainty in the image scaling factor which was obtained during the setting up of the high-speed camera. Due to the multiplicative operation to obtain displacement, the uncertainty at any given displacement value is proportional to the measured value, i.e. uncertainty increases with increasing displacement. The estimated uncertainty would contribute to the uncertainty in the identified force vs. displacement curve which is used in generating the model for a given joint configuration.

Note that when calculating the overall uncertainty of the displacement data, the uncertainties relating to the tracking software were not included. Judging by its outputs, the software clearly performed sub-pixel tracking, but the lack of transparency to the algorithm prevented any further understanding of the associated uncertainties. Consequently, by ignoring the uncertainties for this component of the data acquisition process, the overall uncertainty may be somewhat underestimated.

The maximum expanded uncertainties in Figure 3.20 as well as those for the datasets from the other treatments are in the region of ±0.07 mm. Relating this to the insertion depth of the rivet, for which a measurement uncertainty of ±0.05 mm is considered acceptable, the expanded uncertainty clearly exceeds the limit. This means that if the camera-measured displacement is used to estimate the head height of the resulting joint, the estimated head height would not be as accurate as the value directly measured using the Mitutoyo absolute digimatic indicator. That being said, the camera-measured displacement is still a critical component of creating the model of the joint, as will be discussed in Chapter 5. The significance of the uncertainty in the displacement must be assessed together with the uncertainty in the force measurement.

3.8.5 Force vs. displacement

The force vs. displacement curve is of key importance to the modelling of the joint. The uncertainty associated with a given curve can be visualised as upper and lower bounds either side of the measured trace in Figure 3.21, which shows the uncertainty in the force vs. displacement curve for joint A, for a 95% confidence level.

Uncertainty in the force or the displacement would equate to uncertainty in the model of the joint. However, from an energy balance perspective, the energy dissipated in the joint is a key part of the process but it is a relatively small portion of the total input energy into the riveting machine, which can be in the region of 1000 J per riveting cycle (see Chapter 7). The energy dissipated in the joint can be calculated from the area under the curve; using the measured data the energy is 52 J, the curves corresponding to the upper and lower limits of the confidence interval are 54 J and 50 J respectively, or 104% and 96% of the energy calculated from the measured curve. These differences are not considered to be significant in view of the overall energy consumption of the riveting process and hence, the uncertainties

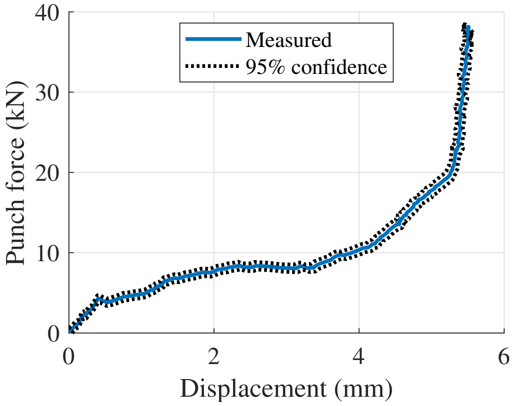

Figure 3.21: Punch force vs. punch-die relative displacement data from treatment 3. Dotted lines indicate 95% confidence interval.

in the force vs. displacement data are not significant with regards to the modelling of the process.

3.8.6 Discussion

The fidelity of a model of the SPR system to the physical system is inevitably affected by the accuracy of the experimental measurements, since the identification of certain parameters and the validation of the model are dependent on this data. The calculated uncertainties indicate how far the measured values may be from the true value for a given confidence level. In the case of large measurement uncertainties, a possible risk would be that of identifying parameter values or even model structures which may be a poor characterisation of the real system. In the current work, the uncertainty budgets for the head height, force and displacement measurements indicate that the level of uncertainty for each was within the acceptable bounds, and therefore would be adequate for use in further steps such as model training and validation.

The approach taken to produce the uncertainty budget was a ‘bottom-up’ approach, where the overall uncertainty was expressed as an equation composed of the uncertainties of all relevant factors that could affect the measurement. This method is not always straightforward as it requires the uncertainty associated with each individual factor to be determined. Furthermore, it assumes knowledge of the equation describing how all the factors influence the measurement result. An alternative method would be the ‘top-down’ approach, where the overall uncertainty is instead calculated from the variation in the measured results. This requires estimates for precision and method bias, while other effects are determined from test data.

The former approach was chosen for the current work since the equations relating the influence of factors to the measurement result were fairly well understood. Moreover, it did not rely on evaluating the method bias, which would have been challenging for the force measurement given that there was no readily available way to apply a consistent reference force representative of the riveting loads (i.e. the forces achieved on each riveting cycle was inherently slightly different due to variations in the performance of the machine as well as in the rivet and material).

The estimated uncertainties can be useful in the analysis of different experimental datasets, because they help in distinguishing whether a discrepancy between two datasets is significant enough to imply an actual difference in the physical process being measured, or no more significant than the measurement uncertainty. Likewise, when it comes to comparing simulated outputs of the SPR model with experimental data, knowing the measurement uncertainty would facilitate the assessment of how significant the errors in the simulated results are.

Having quantified the uncertainties in key measurements from the process, it is possible to include these uncertainties in the model (e.g. in the form of parameter uncertainties via Monte Carlo methods). However, this was considered unnecessary since the focus was to explore the effects of broader system-level changes to the SPR process, for which a deterministic modelling approach was adequate.

3.9 Summary

In this chapter, background on DOE methods and the capabilities of a typical industrial SPR system have been provided to give context to the experimental study.

Furthermore, the experimental setup has been presented. The setup was specifically designed to provide the required data for examining the behaviour of the system as well as identifying the models of the joints shown in Figure 3.12. Using a modified clamping mechanism and a high-speed camera, it was possible to measure the displacement of the punch towards the die during the riveting process, from which the rivet insertion distance could be inferred.

It has been shown via an evaluation of the measurement uncertainties that the experimental data acquired was within the desired level of accuracy. This was crucial to the modelling of the process and validation of the model, covered in the following chapters.

Chapter 4

Modelling of the System

4.1 Introduction

Having discussed the need for model-based analyses in Chapter 2, the model of the SPR system must satisfy the following conditions to be of significant value:

- The dynamics of the system must be adequately characterised in terms of the behaviour of the main components in the system as well as their interactions.
- The model must be able to produce useful and accurate predictions about the outputs of the SPR process, at minimal computational expense.

A system-level approach was considered the most suitable. The riveting system was treated as two main subsystems: the control unit and the rivet setter. The former consisted of the control logic and power electronics used to drive the motor, while the latter consisted of the motor, the belt drive, the PRSM, the clamping mechanism and the C-frame. Submodels corresponding to each component were established via a lumped-parameter approach, which could effectively characterise the key dynamics without incurring high computation costs.

Aside from the fact that such an approach to the modelling of the SPR system had not been realised before, the scope of the model was also more extensive than those in the existing body of work since it brought together the digital, electrical, and mechanical domains of the system into a single simulation. This would open up opportunities to explore the sensitivities of the process to a much wider range of input factors than those previously studied in the published literature. The system-level approach would also be beneficial to the future-users of the model; representation of the system in terms of clearly defined subsystems and equations was inherently intuitive to the practising engineers within the partner company.

Derivation of the model was based on detailed analysis of the physical system as well as the extensive internal documentation at Atlas Copco IAS UK Limited, including technical reports, PLC code, and engineering drawings. The model was coded in MATLAB/Simulink. Significant efforts were made to modularise the code such that the underlying equations would be contained within the associated subsystems. This was to facilitate the evaluation of model variants and the effects of changes made to the system.

This chapter explains the governing physics and the chosen model structures for the various components in the SPR system.

4.2 Equations of motion

The model of the electro-mechanical system was developed from first principles. Values of parameters were either obtained from datasheets or experimentally identified. The equations of motion were derived by considering each subsystem in turn.

4.2.1 Motor

As mentioned in Section 3.3, the motor is operated via the field-oriented control technique. This involves the vector control of currents and voltages to achieve four quadrant torque control. Field-oriented control is based on resolving the axes of the three-phase stator windings into a two-axes rotating reference frame. The three-phase winding can be represented by an equivalent orthogonal two phase winding defined in the α-β reference frame (Figure 4.1(a)). In turn the α-β axes can be transformed into a rotating reference frame where one axis is always aligned with the rotating flux of the permanent magnet rotor. This is the d-q reference frame with the d axis chosen to be coincident with the flux (Figure 4.1(b)). The details of each transformation are available in [68].

The complete transformation is summarised in Equation 4.1.

$$\begin{bmatrix} x_d \\ x_q \end{bmatrix} = \frac{2}{3} \begin{bmatrix} \cos(\theta) & \cos(\theta - \frac{2\pi}{3}) & \cos(\theta + \frac{2\pi}{3}) \\ -\sin(\theta) & -\sin(\theta - \frac{2\pi}{3}) & -\sin(\theta + \frac{2\pi}{3}) \end{bmatrix} \begin{bmatrix} x_a \\ x_b \\ x_c \end{bmatrix} \tag{4.1}$$

Where θ is the electric angle of the rotor, and x can be the current, voltage, flux, magnetic motive force, etc. Subscripts of x denote the axes of the reference frames.

The dynamics of the motor are governed by the following equations:

$$L_d \frac{di_d}{dt} + Ri_d = v_d + \omega L_q i_q \tag{4.2}$$

$$L_q \frac{di_q}{dt} + Ri_q = v_q - \omega L_d i_d - K_e \omega_m \tag{4.3}$$

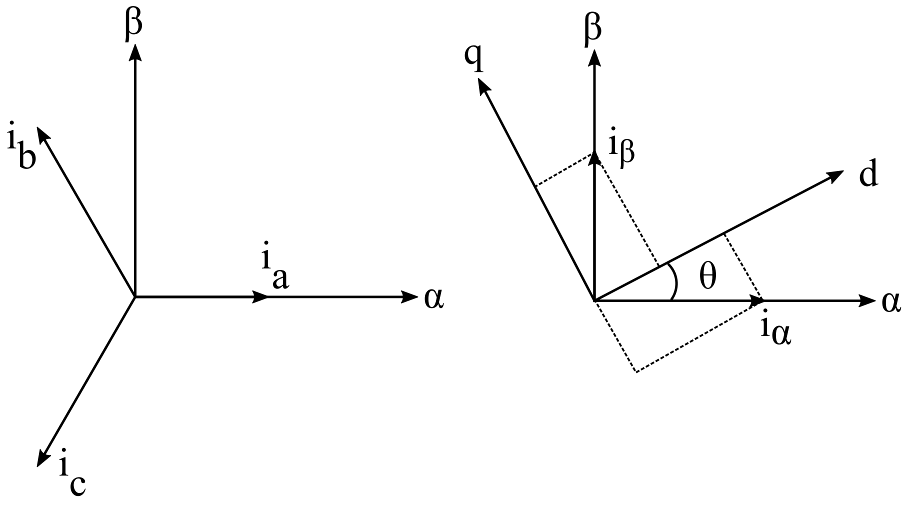

(a) (b)

Figure 4.1: (a) Representation of three-phase (i.e. a, b and c) windings using two axes (i.e. α and β). (b) Transformation of the α-β axes into the d-q rotating reference frame.

Where L_d and L_q, i_d and i_q, v_d and v_q are the d and q components of the inductance, current and voltage respectively, R is the winding resistance, K_e is the back-EMF constant, ω is the electric angular velocity and ω_m is the mechanical angular velocity.

It can be noted that the second term on the right hand side of both Equations 4.2 and 4.3 gives rise to a coupling effect; changes in i_d affect i_q, and vice versa. This is undesirable, so a decoupling term is added in v_d and v_q to cancel out the coupling effect:

$$v_d = v_d' - \omega L_q i_q \tag{4.4}$$

$$v_q = v_q' + \omega L_d i_d \tag{4.5}$$

Substituting Equations 4.4 and 4.5 into Equations 4.2 and 4.3 respectively gives:

$$L_d \frac{di_d}{dt} + R i_d = v_d' \tag{4.6}$$

$$L_q \frac{di_q}{dt} + R i_q = v_q' - K_e \omega_m \tag{4.7}$$

The electromagnetic torque T_e is obtained by considering the portion of electrical power converted into mechanical power. Readers are referred to [69] for the full details of the derivation. In the scope of the current work it suffices to know that the expression for T_e is given as:

$$T_e = \frac{3p}{2}[\Psi_m i_q + (L_d - L_q) i_d i_q] \tag{4.8}$$

Where p is the number of pole pairs and Ψ_m is the flux linkage.

For a non-salient motor where $L_d = L_q$, the equation becomes:

$$T_e = K_t i_q \tag{4.9}$$

Where $K_t = \frac{3p}{2}\Psi_m$.

The aim of field-oriented control is to control the torque-generating current i_q based on the torque demand and keep the magnetic field-generating component i_d at zero, since the latter does not contribute to the torque generated.

In the actual process i_d would be controlled to be near-zero, and the magnitude of the second term in Equation 4.8 would be much smaller in comparison to the first term, i.e. $(L_d - L_q)i_d i_q \ll \Psi_m i_q$. This suggested that the second term could be neglected without noticeable impact on the modelled dynamics, hence Equation 4.9 was used to approximate the torque generated in the motor.

4.2.2 Belt drive

The forces acting on the pulley coupled to the motor (i.e. the driving pulley) are shown in Figure 4.2. It was assumed that any internal friction in the motor was negligible.

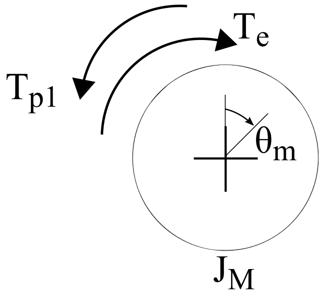

Figure 4.2: Forces acting on the motor pulley. T_{p1} is the load torque on the motor pulley, T_e is the electromagnetic torque generated by the motor, J_M is the coupled inertia of the motor and the motor pulley. θ_m is the angular displacement of the motor.

The power from the motor is transmitted to the rivet setter via the belt drive. To understand the load torque acting on the motor pulley (T_{p1}), the dynamics of the belt drive must be considered.

The belt drive can be broken down into three component groups: the driving pulley, the belt span sections and the driven pulley. The forces acting on these components are shown in Figure 4.3(a), (b), and (c) respectively. The belt span sections, or the stretches of the belt which are not meshing with the teeth in the pulley, are represented using a stiffness and damping element in parallel. This was to capture the elastic and dissipatory response as the belt tension varied during operation.

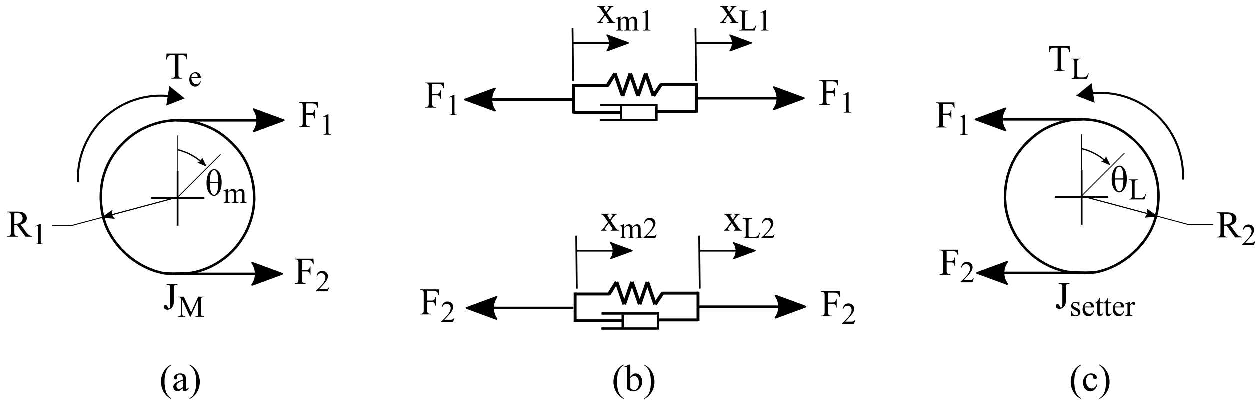

Figure 4.3: Forces acting on the components in the belt drive: (a) driving pulley, (b) belt span, (c) driven pulley. R_1 and R_2 are the pitch radii of the motor and driven pulleys respectively. x_{m1} and x_{L1} are the displacements of the ends of the belt span on one side of the belt, x_{m2} and x_{L2} are the equivalent displacements for the opposite belt span. F_1 and F_2 are the forces transmitted in the belt. T_L is the load torque, and θ_L is the angular displacement of the driven pulley.

Toothed belts are typically installed with pretension, which is necessary to ensure that the teeth of the belt and pulleys mesh properly. It also prevents sagging of the slack side of the belt. Torque transmission between the driving and driven pulleys relies on a net change in the belt tension from the nominal pretension value, i.e. it is dependent on the net stretch or elongation in the belt. Stretch in the belt occurs in the span sections not meshing with the pulleys.

Here, the variables associated with the slack side of the belt are denoted with subscript 1, and those associated with the tight side of the belt are denoted with subscript 2. The net elongation of the slack side of the belt can therefore be written as:

$$elongation_1 = x_{m1} - x_{L1} \tag{4.10}$$

x_{m1} is the displacement of the end of the belt span at the motor pulley side, and can also be expressed in terms of the angular displacement of the driving pulley (θ_m). x_{L1} is the displacement of the end of the belt span at the driven pulley side and can be written in terms of the angular displacement of the driven pulley (θ_L):

$$x_{m1} = R_1\theta_m \tag{4.11}$$

$$x_{L1} = R_2\theta_L \tag{4.12}$$

Equation 4.10 can therefore be written as:

$$elongation_1 = R_1\theta_m - R_2\theta_L \tag{4.13}$$

Each span of the belt is assumed to behave as a spring and damper arranged in parallel, characterised by the spring stiffness K_b and the damping constant C_b. The forces transmitted in the slack and tight sides of the belt are expressed as F_1 and F_2 respectively:

$$F_1 = F_{pretension} - K_b(R_1\theta_m - R_2\theta_L) - C_b(R_1\dot{\theta}_m - R_2\dot{\theta}_L) \tag{4.14}$$

$$F_2 = F_{pretension} + K_b(R_1\theta_m - R_2\theta_L) + C_b(R_1\dot{\theta}_m - R_2\dot{\theta}_L) \tag{4.15}$$

Where $F_{pretension}$ is the pretension of the belt.

To simplify the analysis, the power transmission is assumed to be realised only on the tight side of the belt. In other words the net change in tension in the slack side of the belt is assumed to be much less than that of the tight side, and can be neglected. So the force in the slack side of the belt F_1 simplifies to:

$$F_1 = F_{pretension} \tag{4.16}$$

It follows that the resulting torque on the motor pulley (T_{p1}) due to the net elongation of the belt can be expressed as:

$$T_{p1} = R_1(F_2 - F_1) \tag{4.17}$$

Which expands out as:

$$T_{p1} = R_1^2(K_b(\theta_m - \alpha\theta_L) + C_b(\dot{\theta}_m - \alpha\dot{\theta}_L)) \tag{4.18}$$

Where $\alpha = R_2/R_1$. The torque seen by the driven pulley (T_{p2}) due to the net elongation of the belt is described by:

$$T_{p2} = R_2(F_2 - F_1) = \alpha T_{P1} \tag{4.19}$$

All the terms are in place for deriving the equation of motion for the motor and the coupled pulley. Considering the forces shown in Figure 4.2, the following expression is obtained:

$$T_e - T_{p1} = J_M \ddot{\theta}_m \tag{4.20}$$

Where J_M is the total inertia of the motor and coupled pulley. Equation 4.18 can be substituted into Equation 4.20 to give a more complete expression:

$$J_M \ddot{\theta}_m = T_e - R_1^2 (K_b(\theta_m - \alpha\theta_L) - C_b(\dot{\theta}_m - \alpha\dot{\theta}_L)) \tag{4.21}$$

4.2.3 Planetary roller screw mechanism (PRSM)

Figure 4.4(a) shows the relevant torques acting on the PRSM: the torque transmitted via the driven pulley T_{P2}, and a load torque T_L. Figure 4.4(b) shows an alternative view of the lumped parameter model of the PRSM, where the load torque is represented in terms of its main contributors: a friction torque T_{fric} acting on the nut of the PRSM and also a linear load force F_L acting on the roller assembly.

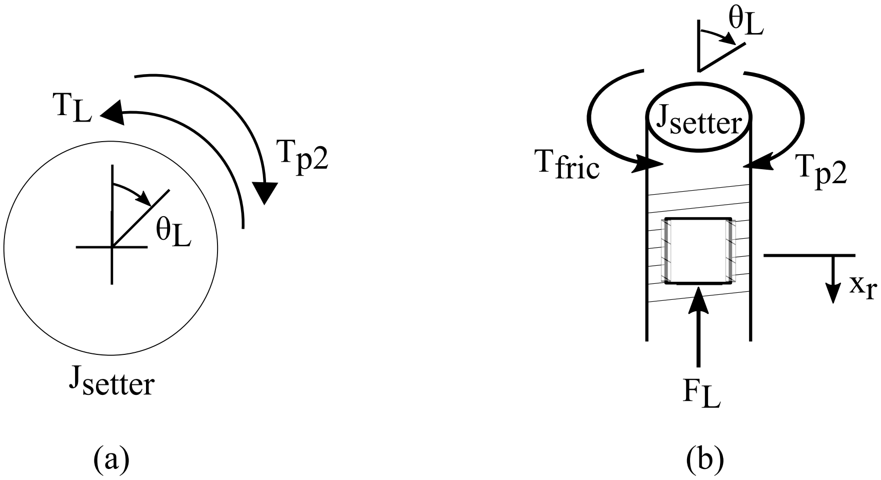

Figure 4.4: (a) Torques acting on the lumped parameter representation of the PRSM. (b) Alternative view of the PRSM including the roller assembly.

4.2.3.1 Load torque

In the theoretical case of a 100% efficient PRSM, the load torque T_L would derive entirely from the linear-rotational transformation of the process forces, i.e. it would be the torque transmitted to the nut of the PRSM due to the riveting and clamping forces acting through the central shaft of the roller screw, expressed as:

$$T_L = F_L \frac{P_h}{2\pi} \tag{4.22}$$

Where P_h is the lead of the roller screw which defines the linear displacement of the PRSM shaft per revolution of the nut.

However, real systems have friction and thus the load torque can be considered as the combination of the transformed axial force and a friction torque T_{fric}, as illustrated in Figure 4.4(b).

$$T_L = F_L \frac{P_h}{2\pi} + T_{fric} \tag{4.23}$$

The friction torque derives largely from friction in the PRSM. While existing test data from internal archives had clearly indicated a dependence of the friction on the velocity of travel, a purely viscous characteristic was insufficient to capture the complex friction profile which was also affected by the load, the temperature and quadrant of operation. A more detailed discussion of these influences can be found in [70].

Temperature effects on the behaviour of the system were beyond the scope of the project, hence focus was directed at characterising the dependency of friction on the transmitted load and quadrant of operation.

The load dependence of the friction in a PRSM is described in the equations in [71]. The mechanical efficiency η_{prac} is used as an independent variable in the expression for the load torque T_L, which is also a function of the axial load F_L on the shaft of the PRSM.

$$T_L = \frac{F_L P_h}{2\pi\eta_{prac}} \tag{4.24}$$

In [71] the definition of η_{prac} is given as:

$$\eta_{prac} = \frac{1}{1 + \frac{\pi D_0}{P_h}\mu_{prac}} \tag{4.25}$$

Where D_0 is the nominal nut diameter, and μ_{prac} is the practical coefficient of friction. μ_{prac} is determined from an empirical function of the helix angle [71].

A more physically meaningful expression for the load torque can be obtained by substituting Equation 4.25 into Equation 4.24, which gives the following:

$$T_L = \frac{F_L P_h}{2\pi} + \frac{F_L D_0}{2}\mu_{prac} \tag{4.26}$$

The first term on the right hand side of Equation 4.26 is the torque required on the nut to generate the axial load F on the shaft in an ideal frictionless PRSM. The second term is the additional torque required to overcome friction, i.e. the friction torque.

Next, regarding the dependency of friction on the quadrant of operation, Equation 4.26 describes the mechanical power transformation in the direct sense. Conversely, in the indirect sense, an indirect efficiency η'_{prac} is defined for the axial load on the shaft required to generate a torque T_{Lb} on the nut. η'_{prac} is given in [71] as:

$$\eta'_{prac} = 2 - 1/\eta_{prac} \tag{4.27}$$

The indirect efficiency does not equal the direct efficiency. This is a phenomenon which is observed during backdriving, when the shaft of the PRSM is pushed in reverse motion against the forward driving torque of the motor, which occurs in the inertia-based servo riveting process due to the springback of the C-frame following rivet insertion. The equation for T_{Lb} is given by:

$$T_{Lb} = \frac{F_L P_h \eta'_{prac}}{2\pi} \tag{4.28}$$

Equation 4.28 can be expressed into a more familiar form by substituting Equations 4.27 and 4.25 into it.

$$T_{Lb} = \frac{F_L P_h}{2\pi}(2 - 1/\eta_{prac})$$

$$T_{Lb} = \frac{F_L P_h}{2\pi} - \frac{F_L D_0}{2}\mu_{prac} \tag{4.29}$$

The first term on the right hand side of Equation 4.29 describes the torque generated on the nut by an axial load F_L acting on the shaft of an ideal frictionless PRSM, and the second term represents the friction torque which takes away from the resulting torque. Together with Equation 4.24, it can be seen that the second term in both equations is essentially a Coulomb friction term which acts to oppose the axial travel of the roller within the PRSM. To neaten the expressions for the purposes of modelling, a single equation can be written:

$$T_L = \frac{F_L P_h}{2\pi} + \text{sign}(\dot{\theta}_L)\frac{F_L D_0}{2}\mu_{prac} \tag{4.30}$$

Where $\dot{\theta}_L$ is the angular velocity of the nut of the PRSM.

Alongside the load-dependent component of friction in Equation 4.30, a further term representing the velocity-dependent component of the friction profile is needed. Viscous friction effects are related to the lubrication used in the PRSM. Additionally, internal test data indicate that in the absence of a riveting load and at very low travelling velocities, there is still a non-zero component of friction. This is suggestive of the presence of internal static friction in the system. Hence a further Coulomb friction term is introduced to account for this. The full expression for the load torque is written as:

$$T_L = \frac{F_L P_h}{2\pi} + \text{sign}(\dot{\theta}_L)\frac{F_L D_0}{2}\mu_{prac} + \text{sign}(\dot{\theta}_L)T_{cr} + B_r\dot{\theta}_L \tag{4.31}$$

Where T_{cr} is the static friction torque that is independent of the load and B_r is the viscous friction coefficient. Relevant test data and the identification of the parameter values are detailed in Appendix C.

4.2.3.2 Equation of motion

Considering Figure 4.4(a), the equation of motion for the PRSM can be written as:

$$J_{setter}\ddot{\theta}_L = T_{p2} - T_L \tag{4.32}$$

Where J_{setter} is the inertia of the rivet setter which includes the inertia of the PRSM as well as that of the driven pulley and coupled flywheel.

Having determined the expression for the load torque, Equation 4.32 can be expressed in terms of its basic components:

$$\begin{aligned} J_{setter}\ddot{\theta}_L = {} & R_1R_2K_b(\theta_m - \alpha\theta_L) + R_1R_2C_b(\dot{\theta}_m - \alpha\dot{\theta}_L) \\ & - (\frac{F_L P_h}{2\pi} + \text{sign}(\dot{\theta}_L)\frac{F_L D_0}{2}\mu_{prac} + \text{sign}(\dot{\theta}_L)T_{cr} + B_r\dot{\theta}_L) \end{aligned} \tag{4.33}$$

The force F_L which is transmitted axially through the central shaft of the roller screw is described in terms of the effective stiffness (K_r) and damping (C_r) of the roller screw, the axial displacement of the roller assembly (x_r) and also that of the coupler (x_{pc}):

$$F_L = K_r(x_r - x_{pc}) + C_r(\dot{x}_r - \dot{x}_{pc}) \tag{4.34}$$

Figure 4.5 shows the components of the force F_L.

4.2.4 Coupler

The coupler is a part which links the output shaft of the PRSM to the punch, and serves as a critical component in the generation of the clamp force. The design of the part is such that up to three different contact surfaces are enlisted in the clamping process. Figure 4.6(a) illustrates the geometry of the coupler with labels indicating each of the three contact surfaces:

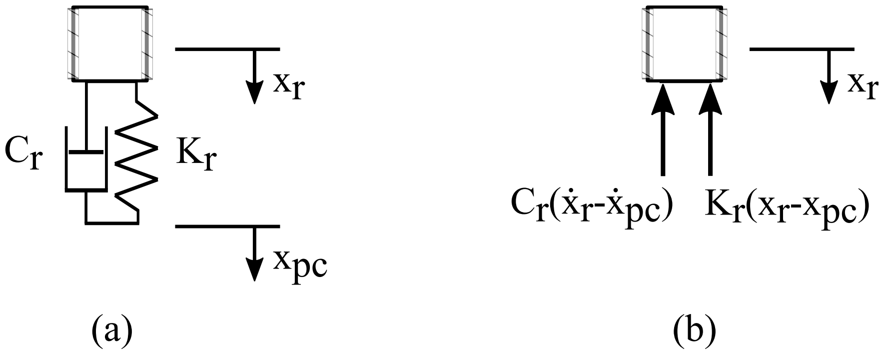

Figure 4.5: (a) Lumped parameter representation of the roller assembly and the roller screw shaft. (b) Components of the force F_L which act on the roller assembly. For clarity, the forces resulting from the transformation of the torques acting on the nut of the PRSM are not shown in the visualisation.

1. The upper surface is engaged in cases where the travel of the punch has reached an upper limit, and acts as a hard stop to restrict further travel of the punch.

2. The intermediate surface determines the compression of the coil spring which generates a relatively low force to hold the material stack in place in preparation for rivet insertion.

3. The lower surface determines the compression of the disc spring pack which generates the bulk of the clamping force during rivet insertion.

The relative distances between the contact surfaces define the sequence and timing of the different contact events, which in turn determine the profile of the clamping force. Figure 4.6(b) illustrates the forces acting on the component.

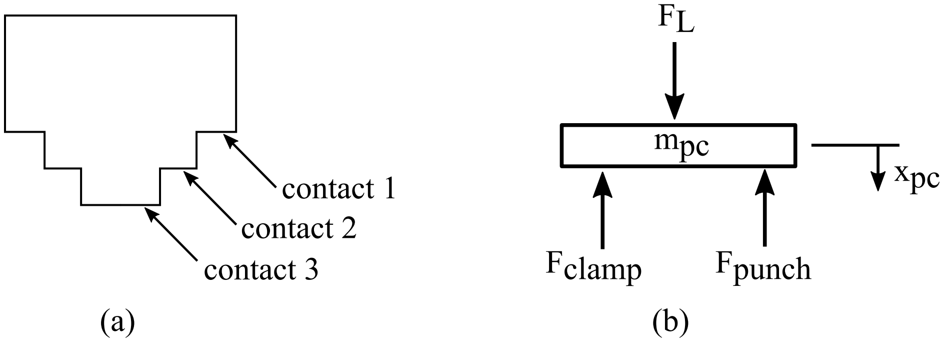

Figure 4.6: (a) Illustration of the geometry of the coupler. The generation of the clamp force involves three different contact surfaces denoted by contact 1, 2, and 3, which interact with the hard stop, the coil spring, and the disc spring pack respectively. (b) Forces acting on the lumped parameter representation of the coupler.

Its governing equation is expressed in terms of the mass of the coupler (m_{pc}), the force transmitted through the punch (F_{punch}), and the clamp force exerted by the clamp tube on the stack of material (F_{clamp}):

$$m_{pc}\ddot{x}_{pc} = F_L - F_{punch} - F_{clamp} \tag{4.35}$$

F_{punch} can be written as a function of the relative motion between the coupler (x_{pc}) and the end of the punch (x_{pu}), the effective stiffness (K_{plpu}) and damping (C_{plpu}) of the plunger-punch subassembly:

$$F_{punch} = K_{plpu}(x_{pc} - x_{pu}) + C_{plpu}(\dot{x}_{pc} - \dot{x}_{pu}) \tag{4.36}$$

To obtain an expression for F_{clamp}, the forces generated within the clamping mechanism must be considered.

4.2.5 Clamp tube

Due to nonlinearities within the clamping mechanism such as the preloaded spring pack and hard stop, F_{clamp} is dependent on the relative motion between the coupler and the clamp tube, or $x_{pc} - x_n$. Letting $y = x_{pc} - x_n$, the clamping-related events in a typical riveting cycle can be separated into distinct ranges of y, as illustrated in Figure 4.7. In stage one, the clamp tube has yet to come into contact with the material stack to be riveted, hence no clamping force is generated (Figure 4.7(a)). In stage two, initial contact between the clamp tube and the material stack leads to compression of the coil spring, which generates a relatively low force designed to hold the material stack in place (Figure 4.7(b)). In the next stage, the disc springs are engaged, leading to a significant rise in the clamping force with the purpose of eliminating any gaps between the layers of material (Figure 4.7(c)). Finally, in the event of further displacement of the coupler towards the clamp tube, the hard stop comes into contact which effectively limits any further compression of the springs as well as the extent of rivet insertion (Figure 4.7(d)).

The expression for F_{clamp} involves the stiffness (K_1) of the coil spring, the maximum distance between the coupler and hard stop (Z_1), the maximum available compression of the disc springs (Z_s), the stiffness (K_2) and damping (C_2) of the disc spring pack, the Coulomb friction in the disc spring pack (F_{c2}), the effective stiffness (K_3) and damping (C_3) of the hard stop contact:

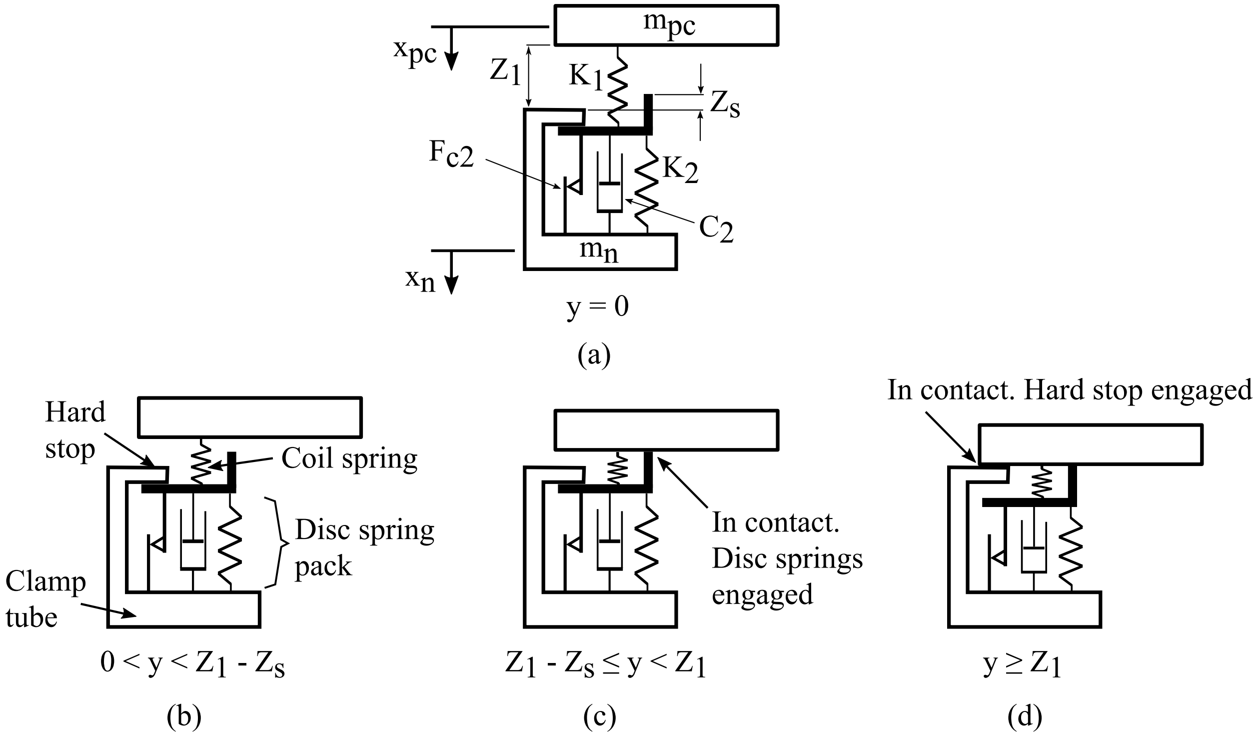

Figure 4.7: State of the internal components within the clamping mechanism at different stages of the rivet insertion: (a) Before clamp tube comes into contact with the material stack. (b) The clamp tube is in contact with material stack and the coil spring undergoes compression. (c) The disc springs are engaged, generating a significant clamping force. (d) The hard stop is engaged, preventing further compression of the disc springs.

$$F_{clamp} = \begin{cases} 0 & if\, y = 0 \\ K_1 y & if\, 0 < y < Z_1 - Z_s \\ F_1 + K_2(y - (Z_1 - Z_s)) + C_2\dot{y} + F_{c2}\text{sign}(\dot{y}) & if\, Z_1 - Z_s \leq y < Z_1 \\ F_1 + K_2 Z_s + K_3(y - Z_1) + C_3\dot{y} & if\, y \geq Z_1 \end{cases} \tag{4.37}$$

Where $F_1 = K_1(Z_1 - Z_s)$.

The four rows of Equation 4.37 correspond to the four stages labelled in 4.7.

The overall forces acting on the clamp tube are shown in Figure 4.8.

The equation of motion for the clamping tube is summarised as:

$$m_n \ddot{x}_n = F_{clamp} - r_{mat} \tag{4.38}$$

Where m_n is the mass of the clamp tube, $\ddot{x}_n$ is its acceleration, and r_{mat} is the restoring force generated by the material stack under compression. Details on the definition of r_{mat}

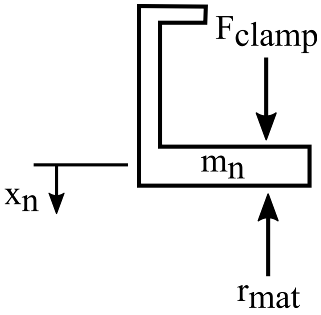

Figure 4.8: Forces acting on the clamp tube.

are provided in Chapter 5.

4.2.6 Plunger-punch

The plunger and punch are considered as a single component because they are directly coupled together and the same axial forces are transmitted through both parts. Figures 4.9(a) and (b) show the lumped parameter model of the component and the forces acting on it respectively.

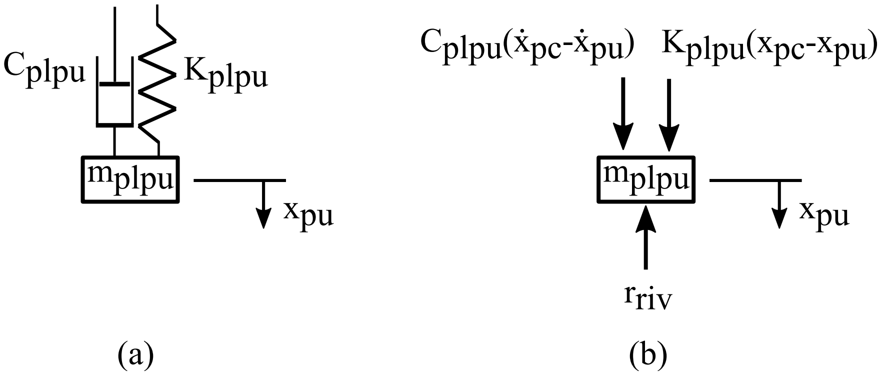

Figure 4.9: (a) Lumped parameter representation of the plunger-punch subassembly. (b) Forces acting on the effective mass of the plunger-punch subassembly.

The riveting force r_{riv} is transmitted through the plunger-punch subassembly, the governing equation of which is expressed as:

$$m_{plpu}\ddot{x}_{pu} = K_{plpu}(x_{pc} - x_{pu}) + C_{plpu}(\dot{x}_{pc} - \dot{x}_{pu}) - r_{riv} \tag{4.39}$$

Here, m_{plpu} is the mass of the plunger-punch subassembly. Details on the definition of r_{riv} are given in Chapter 5.

4.2.7 C-frame

The C-frame is modelled as single degree of freedom (SDOF) system consisting of an ideal mass-spring-damper arrangement. The C-frame and rivet setter are considered as two separate subsystems which interact only via the SPR joint. Figure 4.10(a) shows the lumped parameter model of the C-frame, the relevant forces acting on which are shown in Figure 4.10(b).

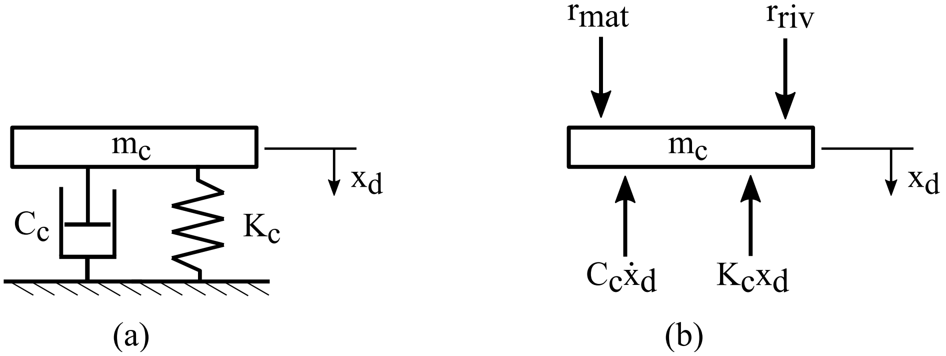

Figure 4.10: (a) Lumped parameter model of the C-frame. (b) Forces acting on the effective mass of the C-frame.

The dynamics of the C-frame are described in terms of the deflection between its upper and lower arms (x_d) and the restoring forces generated by the joint:

$$m_c\ddot{x}_d = r_{riv} + r_{mat} - K_c x_d - C_c\dot{x}_d \tag{4.40}$$

Where m_c, K_c and C_c are the effective mass, stiffness and damping of the C-frame respectively. The identification of the parameter values was described in Section 3.5.

4.3 Drive control

In reference to the details of the typical production system in Section 3.3, the model of the control structure was constructed according to the block diagram shown in Figure 3.2.

The core control logic was modelled with the Stateflow library in Simulink using Chart programming tools. The model was purposely structured to resemble the Sequential Function Chart language used in the PLC code, such that the layout would be familiar and easy to interpret by the controls engineers at the partner company.

To simplify the power electronics side of the modelling, the DC bus was modelled as a DC voltage source, and the voltage source inverter was modelled using a Universal Bridge block from the Simulink library, configured with three bridge arms to give a three phase voltage output. The pulse width modulation generator was modelled using the PWM Generator (2-Level) block from the Simulink library, configured for a three-phase bridge.

The linear motion of the punch is controlled based on the encoder signals taken at the motor shaft, hence the drive-estimated displacement of the punch ($x_{pu\,enc}$) is calculated via Equation 4.41.

$$x_{pu\,enc} = \theta_m \frac{R_1}{R_2} \frac{P_h}{2\pi} \tag{4.41}$$

The model parameter *veloSet* defines the desired linear speed of the punch at the start of rivet insertion. The velocity command profile is generated with this parameter to ensure that this velocity is reached prior to rivet insertion.

The role of the motor current limit is described in Section 3.3.2.2. In the actual system, the motor current is expressed as a percentage of a specific reference value and percentage-based control is implemented. To mirror this in the model, the model parameter *torqueLimRivet* is used to represent the percentage-based motor current limit.

Due to confidentiality, further details of the drive control have not been included here.

4.4 Discussion

The modelling of the C-frame as a SDOF or a mass-spring-damper system was a simplified representation of the structure, and was motivated by the need to minimise the complexity of the model without significant compromise to the accuracy of its dynamic behaviour. Whereas in the real system the rivet setter was held in the top arm of the C-frame and the C-frame itself was held on a stand via bolt holes on the spine of the C-shape, the assumptions in the model implied that the rivet setter was instead fixed in space, and that the base of the SDOF system representing the C-frame was attached to the ground.

This apparent difference between the real and modelled boundary conditions of the rivet setter did not pose an issue. A single fixed reference point was defined on the rivet setter relative to which all displacements would be considered. Therefore the relative movement between the upper and lower arms of the C-frame could be suitably considered as the motion of an effective mass relative to the rivet setter. The model was thus quite capable of capturing the effective dynamic response between the C-frame arms, provided that the deflection of the C-frame was predominantly in the axial direction of the punch.

The way in which C-frames undergo deflection depend on their design. Figure 4.11 illustrates the behaviour at the riveting interface for different forms of C-frame deflection. As shown in Figures 4.11(a) and (b), the axial alignment between the punch and the die

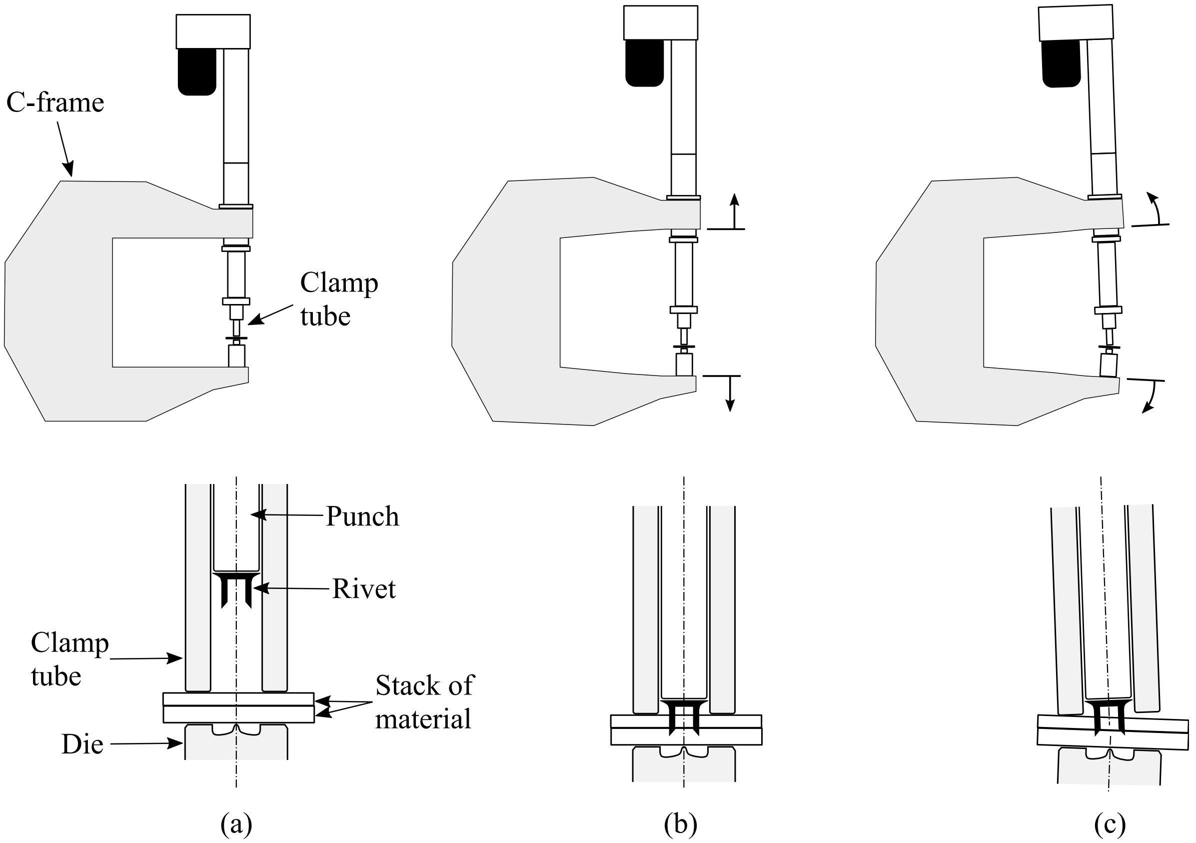

Figure 4.11: Illustration of the effects of C-frame deflection on the riveting interface. (a) No C-frame deflection. (b) Axial deflection. (c) Axial and angular deflection.

is maintained for a C-frame which only exhibits deflection in the axial direction. Figure 4.11(c) shows the case for a C-frame which additionally exhibits an angular component of deflection when under load. In certain C-frame designs, there is a non-uniform widening of the distance between the upper and lower arms of the C-frame such that the punch and the die do not remain on the same axis during the riveting process, i.e. the punch and die bend away from the throat of the C-frame. Consequently the punch and die can move out of alignment which can lead to a non-straight rivet insertion path as well as inadequate clamping of the material. The phenomenon can result in a visible slant in the profile of the rivet head relative to the surface of the top layer of the joined material. The strength of the rivet may be compromised if the misalignment is excessive.

While the model of the C-frame was defined to handle axial deflection, it did not account for angular deflection. There was a possibility that the model may not perform as well for particular C-frame types which exhibited angular deflection under load. In order to assess the consequences of the modelling assumptions, two distinctive C-frame types were included in the model validation stages of the study: one which underwent axial deflection and another which exhibited angular deflection. Further discussion on this point is elaborated in Chapter 6 with the support of experimental observations.

4.5 Summary

The governing equations of the SPR system and their derivation from first principles have been described in this chapter. The rivet setter was broken down into its constituent subsystems, and the underlying physics was expressed in terms of lumped parameters such as inertias, stiffnesses, damping terms, etc.

The work in the next chapter addresses the modelling of the SPR joint, which then completes the modelling of the SPR process. Chapters 4 and 5 serve as prerequisites to the validation of the model presented in Chapter 6.

Chapter 5

Modelling of the Joint

5.1 Introduction

As explained in Section 3.6, the key components of a joint configuration consisted of the rivet, material and type of die used in the joining process. The primary goal for the modelling of the SPR joint was to represent the rivet-material-die interactions in such a way that enabled prediction of the resulting joint quality as well as the response of the SPR system during the riveting process. Just as the model of the riveting system was expressed via a series of equations and lumped parameters in Chapter 4, the forming of the SPR joint may also be characterised using a simplified representation to satisfy this goal.

System identification techniques are relevant to the problem at hand. There are two main approaches to system identification, parametric and nonparametric. The former determines the parameter values for a predefined model structure (e.g. one that is expressed using mass, stiffness, damping or other elements), while the latter represents unknown properties of a system using functions [72]. For both approaches, access to empirical data for the inputs and response of the system is imperative.

Provided that the assumed model structure has a strong physical basis, models produced via parametric identification can be physically meaningful. However, a potential drawback of parametric system identification is that the assumed model may not be an adequate representation of the system, which can lead to inaccurate results.

Nonparametric or black-box methods offer an alternative way to address a modelling problem. Via a black-box approach, the model of a system is identified from observations of its inputs and outputs only, with no requirement of prior knowledge of the system and no consideration given to the underlying physics. The model structure is typically flexible in the sense that it can be parameterised to approximate any response or function. While such a model lacks physical significance, the input-output relationship captured in the model can be an adequate approximation of the real system, provided that the subsequent usage of the model is limited to evaluating inputs within the range of the original input data used to train the model. In contrast to a white-box or grey-box model [73], a black-box model may be less susceptible to the potential errors that could arise due to a misrepresentation of the physics of the system. On the other hand, black-box models cannot be used in extrapolation (i.e. to evaluate inputs outside of the data used in training the model), since the behaviour of the model in this region of the input space is essentially unknown.

In this chapter, a review of the literature on selected system identification techniques is undertaken, followed by a discussion of their relevance to the SPR process. From this the suitability of the restoring force surface method will be discussed. Subsequently, details are given regarding the adaptation of the restoring force surface method for the purposes of modelling the SPR joint. Finally, some preliminary results using the adapted method to identify the model of a joint are provided to demonstrate the applicability of the method.

5.2 Literature review: system identification

The SPR joint, through the various stages of its formation, is by all means a nonlinear system; the physical phenomena of piercing, cutting, shearing, forming give rise to nonlinear responses in terms of the observed state of the joint as well as the process forces. From the review papers by Kerschen et al. [74] and Noël et al. [75] it is evident that the field of structural dynamics has seen wide-ranging application of system identification techniques. Methods which deal with the identification of nonlinear systems may be relevant to the modelling of joining processes.

The process of nonlinear system identification can be summarised in three steps [74]:

1. Detect the presence of nonlinearity
2. Characterise the nonlinearity in terms of its location, type and mathematical expression
3. Determine the parameter value corresponding to the nonlinearity

In the context of SPR, the presence of nonlinearity is a given, but it is steps two and three of the identification process which pose a challenge. The complexities of the rivet-material interaction as well the large number of process variables present difficulties for the derivation of an analytical expression for the process. However, taking a macroscopic view of the rivet insertion process, a joint being formed may be considered as an evolving structure with dissipative characteristics that are largely determined by the plastic deformation of a nonlinear material (i.e. the material stack being riveted).

5.2.1 Constitutive models

Constitutive models are employed in the study of materials that exhibit nonlinear behaviour when subjected to loading. Common constitutive models in the literature such as the Kelvin-Voigt, Maxwell, Bingham model, etc. make use of different arrangements of springs, dashpots and frictional elements which enable a variety of material responses to be represented [76]. Figure 5.1 shows the structures of four common constitutive models.

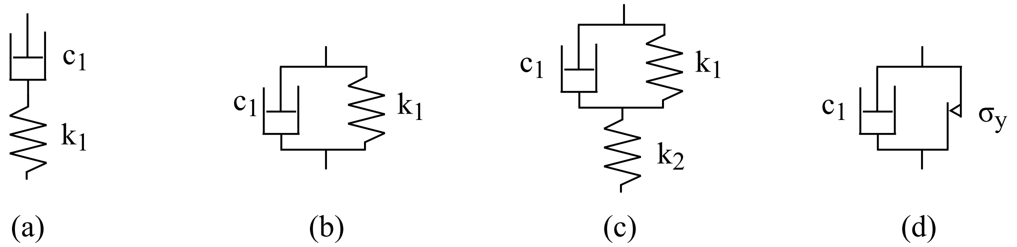

Figure 5.1: Constitutive models. (a) Maxwell model. (b) Kelvin-Voigt model. (c) Zener model, or Standard Linear Solid model. (d) Bingham model. k denotes linear stiffness, c is the viscous damping constant, σ_y represents the yield stress.

An example of system identification using constitutive models is the work by Yukawa et al. [77], where impact tests of varying intensities were performed to identify the parameters for a nonlinear Kelvin-Voigt model, in the characterisation of synthetic turf.

The study by Kulisiewicz [78] dealt with the characterisation of a nonlinear material using an extended Zener model. The model form was defined with elastic-viscoplastic materials in mind, and it was argued that with the inclusion of dry friction, damping, nonlinear stiffness and nonlinear dissipative elements, the model would be suitable for characterising a variety of materials. The identification of polyurea samples was used to demonstrate the approach. The parameter values and nonlinear functions were determined via a combination of tests with quasistatic as well as dynamic loading conditions.

In [79], Naraghi and Nobari identified the behaviour of an adhesive joint. The adhesive, Sikaflex-252 was a nonlinear viscoelastic material whose stiffness was dependent on the excitation frequency. The authors created a linear system at each specific excitation level using the optimum equivalent linear frequency response function concept [80]. The inverse eigensensitivity model updating method was used to iteratively update the physical parameters in the FE model. As part of the same study, a constitutive model for the adhesive was created using the Standard Linear Solid model (also known as Zener model) as a basis. Parameter values were determined using the model updating results previously obtained. Validation against test results suggested that the constitutive model performed well. The choice of the Standard Linear Solid model was based on the known viscoelastic nature of the adhesive.

Relating back to the SPR process, although the use of constitutive models can provide adequate representations of nonlinear materials, rivet insertion is a more complex problem in that the rivet as well as the substrate material undergo deformation. Unlike the subject of the aforementioned studies, the joint undergoing riveting is a changing system; its dynamic behaviour permanently changes with the progression of the rivet insertion. This complicates the choice of a constitutive model as well as parameter identification.

In the work by Jamroziak [81], the response of a substrate material to impact by a ballistic projectile was examined. The proposed model structure was that of a rheological model composed of a specific arrangement of stiffnesses with viscous damping and dry friction elements. The material damage was considered as two stages: firstly reversible or elastic deformation, then permanent deformation. The dry friction represented a force threshold which determined the transition from the first stage to the second stage of the material damage, in other words, the yielding of the material. Although not validated with experimental data, the proposed model showed that a lumped-parameter model could be constructed to capture distinctive physical phenomenon occurring in a piercing process, perhaps not dissimilar to the piercing of the material in the SPR process.

A challenge with the use of constitutive models is that some prior knowledge about the system is necessary when choosing the structure of the model. While the inclusion of more nonlinear elements, stiffnesses, and damping terms may allow the observed response of a system to be more accurately modelled, the contribution of each term as well as the physical significance of the model can quickly become unclear and unintuitive with an increasing number of terms. In FE models constitutive relationships are used to describe the change in the mechanical state of materials in forming and joining processes [82, 83, 84, 85, 86], but outside of the FE simulation environment, the use of constitutive models may only provide a coarse approximation to the complexities of the SPR process.

5.2.2 Restoring force surface

The restoring force surface (RFS) method, developed by Masri and Caughey [87], presented a way of identifying the unknown restoring force of a single degree of freedom system in terms of the displacement and velocity of the system. A mathematical function of the restoring force surface is obtained by fitting a multi-order Chebyshev polynomial series. Details of the method are provided in Section 5.3.

RFS has become an established technique used commonly in the identification of nonlinear systems. In [88], an updated approach by Masri et al. based on the original RFS method was applied to a Duffing oscillator, noisy Duffing-Van der Pol oscillator and a system with hysteretic behaviour governed by the Bouc-Wen model. The model of a shock absorber was the subject of study by Surace et al. [89], in which the RFS method was used together with theoretical modelling to obtain an improved model.

In the work by Ehrgott and Masri [90], three different methods including the RFS method were used to identify electrorheological materials. A model was generated with the restoring force as a function of acceleration and velocity. It was suggested that the acceleration may be better suited to capturing the yielding of the material given that it was more sensitive than the displacement. Using this model an improved force-velocity plot was obtained. Further development of this work was undertaken by Masri et al. [91] for semi-active and active structural control applications. Based on the instantaneous mechanical state of the nonlinear element representing an electrorheological device, the optimum instantaneous restoring force could be calculated. In turn the voltage required to deliver the equivalent damping force could be determined.

In their paper on modelling the nonlinear behaviour of electrorheological dampers, Gavin et al. [92] expressed the restoring force as a function of the electric field in addition to displacement and velocity, i.e. in a three-dimensional domain.

An alternative to the RFS method is force state mapping (FSM). Developed by Crawley and Aubert [93], FSM can be considered as a variant of the RFS technique. The fundamental difference between them is that ordinary polynomials are used in the curve fitting stage of FSM instead of Chebyshev polynomials. In a study by Al-Hadid and Wright [94] the fitting process with ordinary polynomials was found to be much faster than with Chebyshev polynomials.

The FSM method was originally proposed for determining the structural characteristics of space truss joints [93]. Since then, the technique has been used to investigate multi-element truss with joints [95], pinned joints with and without restricting sleeve [96], and single strut with a single clevis-tang pinned joint [97]. Joints represented good candidates for evaluating the identification method since they exhibited nonlinearities such as dead bands, friction, impact, etc.

In [98], an adapted FSM method was used to model an automotive shock absorber, with particular focus on the effect of using different state variables. The first state variable was chosen to be velocity, while the second was switched between displacement and acceleration.

The majority of publications for RFS or FSM were related to the identification of systems subjected to loading in the elastic region. To the author's knowledge, these methods have not been applied to any kind of mechanical joining or forming process where the mechanical properties of the system are irreversibly changing due to plastic deformation. Application of the RFS method would be to assume that the restoring force of the joint is a function of the deformation and rate of deformation undergone by the joint. Since the inertia-based SPR process involves a single loading and unloading stroke of the punch, the restoring force profile for a single riveting operation can be considered as that of an equivalent nonlinear system subjected to a single cycle of excitation. It should be possible to identify this system using multiple cycles at different input settings, i.e. different levels of excitation.

Regarding the use of polynomials in the RFS or FSM method, visibility of the identified restoring force function may shed some light on the physics of the system of interest, even though the methods belong to the family of nonparametric identification. On the other hand, Kerschen et al. [74] cautioned that polynomials only serve as approximations for when no prior knowledge is available for the system of interest. The restoring force of a structure may not necessarily be governed by an ordinary polynomial series, in other words, polynomial expansions may be a poor representation of certain physical phenomena. A point to consider is the risk of overfitting when high order polynomials are used.

The need for synchronised displacement, velocity, acceleration and force data at each measurement point can be a potential drawback of the RFS method. An alternative could be the use of numerical differentiation or integration to compute the necessary signals from an acquired signal, but errors may arise due to measurement noise.

5.2.3 Artificial neural networks

Artificial neural networks (ANNs) are used in nonparametric identification in which the input space of past observations are mapped to the outputs of a system. As well as system identification, ANNs can also handle a range of problems including classification, signal reconstruction, and novelty detection. The structure of an ANN is made up of an input layer and an output layer, with one or more hidden layers in between. Each layer contains one of more neurons which serve as processing elements. Neurons between adjacent layers are linked via connections with adjustable weights. Data is passed via these connections from the output of one neuron to the input of another. The weights essentially scale the inputs of each neuron, and through the model training process the weights are adjusted such that the overall output of the ANN approaches the desired results for a given set of inputs. Further background on ANNs can be found in [99].

In [100], Masri et al. used a three-layer feed-forward ANN to identify the internal restoring force in a Duffing oscillator. The network was trained using a back-propagation algorithm on input vectors consisting of the displacement and velocity of the system, as well as the output vector consisting of the measured restoring force. The advantage of the approach was that no prior assumptions were made about the model of the system, and that the network was noted to be inherently robust due to its distributed nature. Conversely, this distributed representation also meant that the model was not fully transparent for the purposes of physical interpretation. Any such interpretation would be limited to a qualitative assessment of the weight connected to the inputs.

ANNs have also been used in the modelling of metal forming processes. One such work was that of Kim and Kim [101], in which two examples were used to demonstrate the application of ANNs to forging processes. In one example, an ANN was used to predict the initial size of the billet of material that would fully fill the die cavity with minimum wastage. In the other, an ANN was used to determine the geometry of the die that would produce the desired product quality in a cold forging operation. The training and validation data was prepared using FE simulations of the forging process.

The study by Teti and D'Addona [102] used ANNs to predict the flow stress-strain characteristics for mild steel under hot forming conditions. Multiple back-propagation ANNs were trained and validated against experimental data, each with a three-layer configuration and differing layout of nodes.

The work by Sztangret et al. [103] dealt with the modelling of a uniaxial compression test. With material-related parameters, temperature and strain rate as inputs, the load profile of the compression test was predicted using ten ANNs, each corresponding to a specific time interval of the compression process.

In [104] an ANN was created to predict the required punch force in a hot extrusion process based on four process inputs: the punch velocity, material temperature, friction between the billet and die, and the inclination angle of the die. The network was trained on samples from FE simulations with the process inputs configured at specific levels.

From the published literature it is clear that ANNs can be highly useful for the identification of nonlinear relationships or processes. One of the main advantages is that there is no need for any prior knowledge of the system of interest, which makes it a versatile technique for the modelling of complex systems using data alone. Although powerful, the model structure of ANN can be unintuitive and does not offer insights into the physics of the problem. Another potential limitation is that the training of the model can be computationally intensive for large networks handling a large quantity of data.

5.2.4 Discussion

There exists a large number of techniques for the identification of nonlinear systems, only a subset of which has been mentioned in the current work based on their relevance to the modelling of the SPR process. For a comprehensive review of system identification methods, the reader is referred to [74] and [75].

Returning to the point on the modelling of the SPR joint, the following were considered to be necessary features of the model: it must contain a relationship linking the process forces and the mechanical state of the joint, it must capture the dissipative nature of the process, and the model structure must be general enough to be applicable to any joint configuration. In addition, accuracy and interpretability of the model were also important.

Of the methods mentioned, the RFS method was considered to be the most suitable for identifying the model of the joint. The model would consist of a functional polynomial relationship between the mechanical states of the modelled system and the restoring force, which may provide some insight into the physics of the rivet-material interaction, in contrast to other black-box modelling methods such as ANNs. The RFS method would offer a highly visual approach to system identification. Furthermore, the model itself would also be easy to code in any modelling environment.

The SPR joint was an unconventional system in comparison to those considered in the existing RFS literature. In the next section, the adaptation of the original RFS method for the current project is presented.

5.3 Theoretical basis: the restoring force method

5.3.1 Original method

In the RFS method originally developed by Masri and Caughey [87], a restoring force is defined as the force generated by a system for a given displacement and velocity undergone by that system. It can be visualised as a surface plotted over the displacement-velocity plane. The shape of the surface is indicative of the linear and nonlinear structural characteristics of the system.

Consider a SDOF nonlinear system as shown in Figure 5.2, the equation of motion can be expressed as follows:

$$F(t) - F_R(x, \dot{x}) = m\ddot{x} \tag{5.1}$$

Where $F_R(x, \dot{x})$ is an unknown restoring force which is a function of the displacement x and the velocity $\dot{x}$, or the state variables of the system. $F(t)$ is the applied or excitation force, m is the mass of the system, and $\ddot{x}$ is the acceleration.

To identify the mathematical function of $F_R(x, \dot{x})$, experimental data for x, $\dot{x}$, $\ddot{x}$ and $F(t)$ are required at the same sampling steps in time. $\ddot{x}$ and $F(t)$ are experimentally measured. x and $\dot{x}$ may be measured or obtained from the integration of $\ddot{x}$. Additionally, the mass m

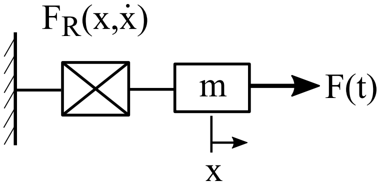

Figure 5.2: Sketch of a nonlinear SDOF system.

needs to be known or accurately estimated. Any excitation which reveals the non-linearity in the system can be used, be it random or periodic. Once the data is obtained, a curve fitting method is used to fit a model that approximates the restoring force.

The approximate restoring force function is expressed using two dimensional Chebyshev polynomials. Chebyshev polynomials have the property of orthogonality, meaning that when the polynomial order is changed or when the number of terms in series is changed, it would not be necessary to calculate all the coefficients given that the earlier coefficients remain valid, i.e. only those for the additional terms would have to be determined.

5.3.2 Adapted method

In the current project, changes to the original RFS method were necessary for the purpose of modelling the rivet insertion event. The adapted method revolves around the idea of defining a nonlinear element which outputs a restoring force as a function of the compression of that element. By drawing a bounding box around a rivet and material stack, the contents within the box may be considered as a nonlinear element, and the forces generated in rivet insertion are considered as a function of the compression of the element, i.e. the extent and rate of rivet insertion.

In contrast to the original RFS method, the definition of the system to be identified (i.e. the joint) consisted only of a nonlinear element without a mass term. This was motivated by the fact that the mass of the joint was negligible in comparison to that of the riveting system, to have included an effective mass term for the joint would have made little impact to the dynamics of the overall system, and it would have also required the definition of a contact model between the punch and the rivet which would have further increased model complexity.

With the chosen model structure, assumptions were made that the punch and rivet remained coupled together throughout the rivet insertion process, which was a valid assumption considering the continuous profile of the typical punch force vs. time curve as shown previously in Section 3.7.

Regarding the identification of the restoring force, measurements of the restoring force, as well as the state variables (i.e. displacement and velocity) had to be obtained. Although the RFS method suggested that any form of excitation could be used for system identification, the type of excitation that could be practicably applied to a joint was limited to that which could be delivered as part of the rivet insertion process. In the inertia-based riveting process, the type of loading applied to form a joint can be seen as a predominantly impulse-type excitation. Through the progression of the rivet insertion, the evolution in the behaviour of the system can be considered as being a characteristic of the system, provided that it is repeatable under the same loading conditions. Preliminary test data suggested that the response of the joint in terms of the force vs. displacement profile was also repeatable for the same loading conditions (i.e. the same setting velocity, on the same physical setup). Hence, it could be argued that the system in question could be suitably identified using data from the rivet insertion event, more specifically:

- The displacement across the system, or the extent of rivet insertion into the material stack
- The velocity across the system, or the rate of rivet insertion
- The restoring force, or the process force

The joint was represented as two distinct black-box models. This was necessary to distinguish the dynamics of the rivet-material interaction and that of the material stack under clamping, away from the immediate rivet insertion zone. The simplification of the rivet insertion process is illustrated in Figure 5.3. Figure 5.3(a) shows a partially formed joint with components of the system that are in direct contact with the joint. The forces (i.e. r_{riv} and r_{mat}) acting on the joint are noted in Figure 5.3(b). In Figure 5.3(c) the joint is visualised as two separate nonlinear elements: one representing the material stack under compression by the clamp tube, and the other serving as a proxy for the rivet and the material into which it is inserted.

The rivet-material interactions are encapsulated in the expression for r_{riv}, and the behaviour of the material stack in r_{mat}. Compression of the material stack is represented by the relative displacement between the clamp tube and the die: $x_n - x_d$. Displacement of the rivet into the material is represented by the relative displacement between the punch and the die: $x_{pu} - x_d$.

Given the findings in [94], ordinary polynomials rather than Chebyshev polynomials were used to identify the restoring force function.

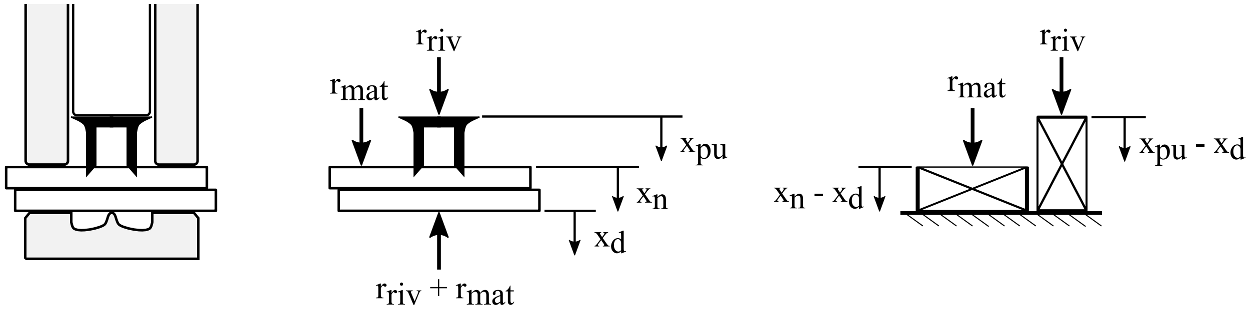

(a) (b) (c)

Figure 5.3: (a) Cross section view of the components in direct contact with a partially formed joint. (b) Cross section view of the joint with labelled forces. (c) Simplified representation of the joint.

5.4 Model identification

5.4.1 Preliminary results

Important insights into the behaviour of the joint were gained from preliminary tests performed using C-frame 1 and joint A. Figure 5.4(a) shows the cross-section images of the joints made at various setting velocities. These were obtained by cutting through the centre of the joints using a circular saw. With increasing setting velocity the progressive nature of the rivet insertion and deformation can be clearly noted.

Figure 5.4(b) shows the corresponding curves for the total process force vs. punch-die relative displacement, where punch-die relative displacement represents the extent of rivet insertion. Each curve corresponds to a different setting velocity. The loading phases of the individual curves appear to overlap, and can be said to lie on a common master curve, which suggests that the chosen joint configuration was not sensitive to the range of strain rates seen in the test. It was therefore assumed that the joint could be characterised as a nonlinear stiffness using the observed force-displacement relationship.

By characterising the joint in this way, key components of the conventional RFS method were essentially excluded, namely the mass element and the velocity component of the restoring force described in Section 5.2.2. This was equivalent to the characterisation of a nonlinear system with negligible mass and no velocity-dependence, hence the approach was considered a valid adaptation of the RFS method.

The modelling of the joint required the characterisation of the force-displacement relationships for both the punch and clamp forces (r_{riv} and r_{mat}). Example data in Figure 5.5(a) shows the punch force vs. punch-die relative displacement, and Figure 5.5(b) shows the clamp force vs. clamp tube-die relative displacement. For the loading phase, the function for r_{riv} was obtained via a polynomial fit to the loading part of the punch force vs. relative displacement data. The general form of r_{riv} during the loading phase is given by:

$$r_{riv} = f(x_{pu} - x_d) \tag{5.2}$$

For the unloading phase, the joint was modelled as a constant stiffness, which was a reasonable approximation to the true behaviour illustrated in Figure 5.5(a). The unloading curve differs from the loading profile due to the plastic deformation undergone by the rivet and material during the joining process. The area enclosed within the loading and unloading curves is indicative of the amount of energy dissipated in the joint. In order to implement this in the model, the loading and unloading phases were separately characterised using two different expressions, and the behaviour of the model was switched from one expression to the other in the transition from loading to unloading.

In Figure 5.5(b), example data illustrates the behaviour of the material stack under clamping. The relative displacement between the clamp tube and the die represents the compression of the material stack during the riveting process. The observed negative relative displacement is indicative of a ‘pushback’ effect, where during the initial rivet insertion the centre of the material stack is pushed into the die cavity and its outer edges bend up away from the die due to reaction forces at the rim of the die. The bending material pushes the clamp tube away from the joint shortly before the activation of the clamp force and the consequent flattening of the material stack. This is illustrated by the negative to positive transition of the relative displacement during the loading phase.

The hysteresis in the force profile suggests that some energy is dissipated in the plastic deformation of the material stack due to clamping. However, this is less than 3% of the energy dissipated in the rivet-material interaction, and was thus considered negligible in order to simplify the model. Accordingly, the material stack was assumed to behave as a linear stiffness in both loading and unloading. r_{mat} was defined as:

$$r_{mat} = K_{mat}(x_n - x_d) \tag{5.3}$$

Where K_{mat} is the effective stiffness of the material, x_n is the displacement of the clamp tube, and x_d is the displacement of the die.

The effective stiffness K_{mat} was estimated from the unloading part of the clamp force vs. clamp tube-die relative displacement data.

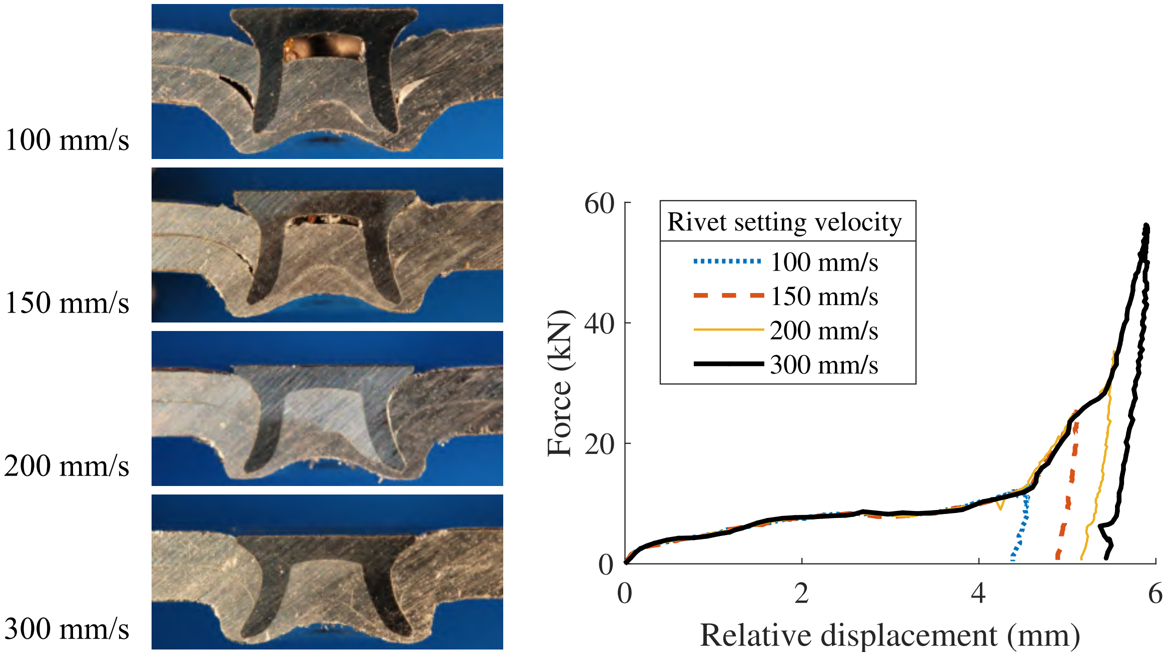

(a) (b)

Figure 5.4: (a) Cross sections images of joint A, made at the indicated setting velocities. (b) Total process force vs. relative displacement between the punch and the die. Relative displacement represents the rivet insertion distance.

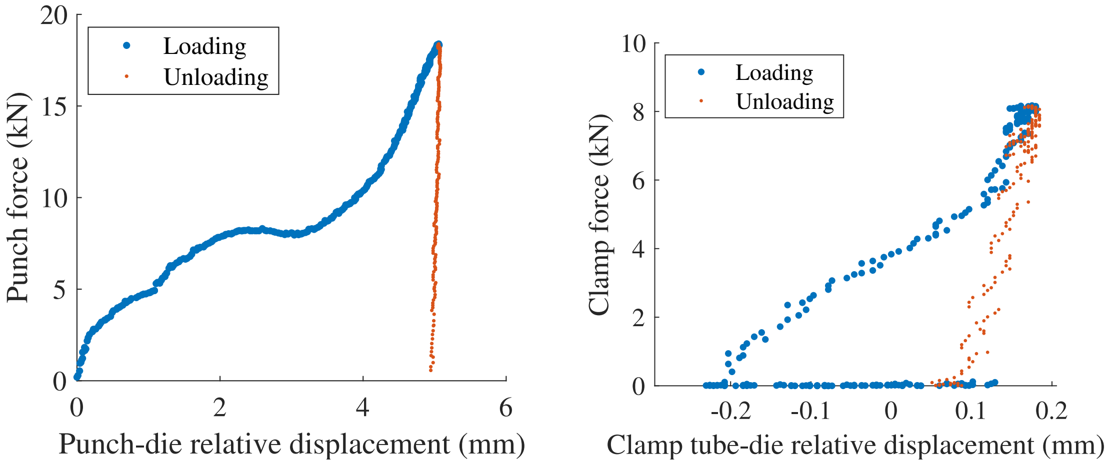

(a) (b)

Figure 5.5: Preliminary test data to illustrate the characteristic curves of an example joint. (a) Punch force vs. relative displacement between the punch and the die. (b) Clamp force vs. relative displacement between the clamp tube and the die.

5.5 Discussion

Via the chosen modelling approach, the interactions at the machine-joint interface were expressed as the transfer of forces. During rivet insertion, the punch force acts through the rivet, the clamp force acts through the material stack and the sum of the process forces acts on the C-frame. Consistent contact at said interfaces was assumed throughout rivet insertion. In comparison to the FE models of the SPR process in the existing literature, the current work represented a substantial reduction in the complexity of the problem. Not only did this significantly lower the computational effort of each simulation, but it also offered an alternative and physically meaningful way to account for the rivet insertion distance; the head height (i.e. a commonly used measure of joint quality in industry) could be predicted based on the relative displacement between the punch and the die.

In contrast to the physics-based modelling of the riveting machine, the definition of the restoring forces for the model of the joint was based entirely on empirical data. An associated disadvantage was that the model was only valid for a specific joint configuration. Each unique combination of rivet, material or die would constitute a new joint configuration and thus a new set of experiments would need to be carried out in order to identify the model. This would be a constraining factor on the number of joint configurations that can be practicably identified. On the other hand, the empirical model served as an effective representation of the joint, in providing the necessary data exchange between the subsystems within the full model to enable predictions of the response of the system.

5.6 Summary

In this chapter the modelling of the SPR joint was presented. The approach was based on the RFS method, using two separate black-box models to represent the rivet-material interaction and the clamp tube-material interaction respectively. The functions that characterise these interactions were defined using empirical data, namely force vs. displacement traces obtained from riveting cycles. The resulting model was specific to a given joint configuration, meaning that each unique rivet-material-die combination would need to be identified empirically.

The model of the joint completes the full model of the SPR process. Model training and the evaluation of the model's predictive accuracy is described in the next chapter.

Chapter 6

Model Verification and Validation

6.1 Introduction

Model verification checks whether the underlying mathematical relationships and assumptions that define the model are implemented correctly in the simulation software. Model validation evaluates whether the model is an accurate enough representation of the real system, with regards to the intended usage of the model. Validation does not imply verification, or vice versa. Both are critical processes in the overall assessment of the model.

When experimental data is available and used to assess the simulated responses, prediction errors falling within an acceptable bound would imply that the model serves as an adequate representation of the system, provided that the model has been verified. Without verification, possible mathematical errors could also produce seemingly accurate simulation results which would paint a misleading picture of the validity of the model [105].

In the current work, model verification is performed by checking that the simulated behaviour of the model matches the intended behaviour of the model. For validation, model performance is quantified by comparing selected simulation outputs to the experimental results. Furthermore, this chapter also explores how the data used in generating the model of the joint can impact the performance of the full system model.

This chapter explains:

- The approach taken to verify the model.
- The definition of a criteria against which the performance of the model can be evaluated during the validation process.
- The significance of the errors between the simulated and experimental results.
- The shortcomings of the model.

6.2 Model verification

The process of developing a numerical model of a system starts with a mathematical model of that system, which is discretised in time and space and implemented into software that solves the numerical model. Errors can arise throughout this process: in the discretisation as well as the techniques used to solve the model, not to mention potential coding errors in creating the numerical model [106]. The verification process should identify and quantify these errors in order to increase the confidence in the accuracy of any new predictions made using the model [107].

Model verification consists of checking whether the model behaves as expected with regards to the intentions of the modeller and the underlying mathematical model [108]. Verification can be considered as two categories: code verification, and solution verification. Code verification seeks to address coding errors via the execution of benchmark problems, i.e. simulation of cases for simplified models where the exact or an accurate estimate of the solution is known. Solution verification is done after code verification, and assesses discretisation errors, iterative convergence and computer round-off errors [109]. For complex models an exact or analytical solution may not be obtainable. Complete verification is only possible for simple mathematical models, for more complex and other types of models the aim should be sufficient verification, i.e. the scope of the verification should be focused only on the intended use of the model and its key outputs of interest. Techniques such as modular programming, checking the intermediate outputs of a large simulation, comparing model outputs to known analytical solutions, and animations all contribute to the verification process [110].

The outputs of interest in the SPR process were the process forces and the resulting head height of the joint. Based on the equations of motion presented in Chapter 4 and 5, every subsystem played a role in the outcome of the simulated riveting process. Therefore, the verification process aimed to evaluate each subsystem as well as their interactions, mainly by examining the intermediate outputs of the simulation. Custom simulation cases were used for this purpose, as described below:

1. Motion control, motor and setter: the SPR system was driven through a typical riveting motion profile consisting of constant acceleration, constant velocity and deceleration, in both advance and reverse directions. The sequence of events was evaluated against the expected sequence. Furthermore, the simulated velocity, displacement and motor current traces were examined in relation to the target motion profile.

2. C-frame: the setter was driven against a blank die, and the deflection of the C-frame was verified against the theoretical values.

3. Clamping mechanism: the setter was driven against a hollow die (i.e. a die where the punch is allowed to protrude beyond the end of the clamp tube). This was used to assess the timing and magnitude of the clamp forces against the expected behaviour.

4. Temporal discretisation: simulations of the riveting process were evaluated at various time step sizes to check the convergence of the solution.

6.2.1 Code verification

6.2.1.1 Motion control, motor and setter

Since the control logic of the modelled system was implemented using the Stateflow library in Simulink, the active stage of the control was automatically highlighted throughout model execution. This highlighting was monitored to ensure that the simulated process transitioned between each stage under the correct conditions. Additionally, event flags or checkpoints were set up in the model and visualised during simulation via the dashboard display shown in Figure 6.1(a), in which distinct control-related and mechanical-related events could be monitored. An example time history of these events generated in a simulated riveting cycle is shown in Figure 6.1(b). Knowledge of the real physical process was drawn upon to verify that the expected events occured in the expected sequence.

As well as logic-based evaluations of the model, time histories of simulated feedback signals were also used to examine the dynamic behaviour of the model when driven to a target motion profile. An example of this is shown in Figure 6.2, in which the velocity feedback, position feedback and motor current traces for a simulated blank die scenario are plotted; the simulated setter was driven directly against a flat die with no joint in between. The two data series (100 mm/s and 400 mm/s) correspond to setting velocities at the lower and higher ends of the typical process configuration, and thus also the range for intended model usage. It is seen that for both data series, the target setting velocity is reached after a period of constant acceleration. During the impact phase, the velocity of the setter falls sharply under the reaction load generated in the C-frame, while the motor current is maintained at the predefined level governed by the motor current limit. Throughout the cycle, the transients in the motor current reflect the changes needed to actuate the setter to complete the motion. All observed features agree with the expected behaviour of the mathematical model.

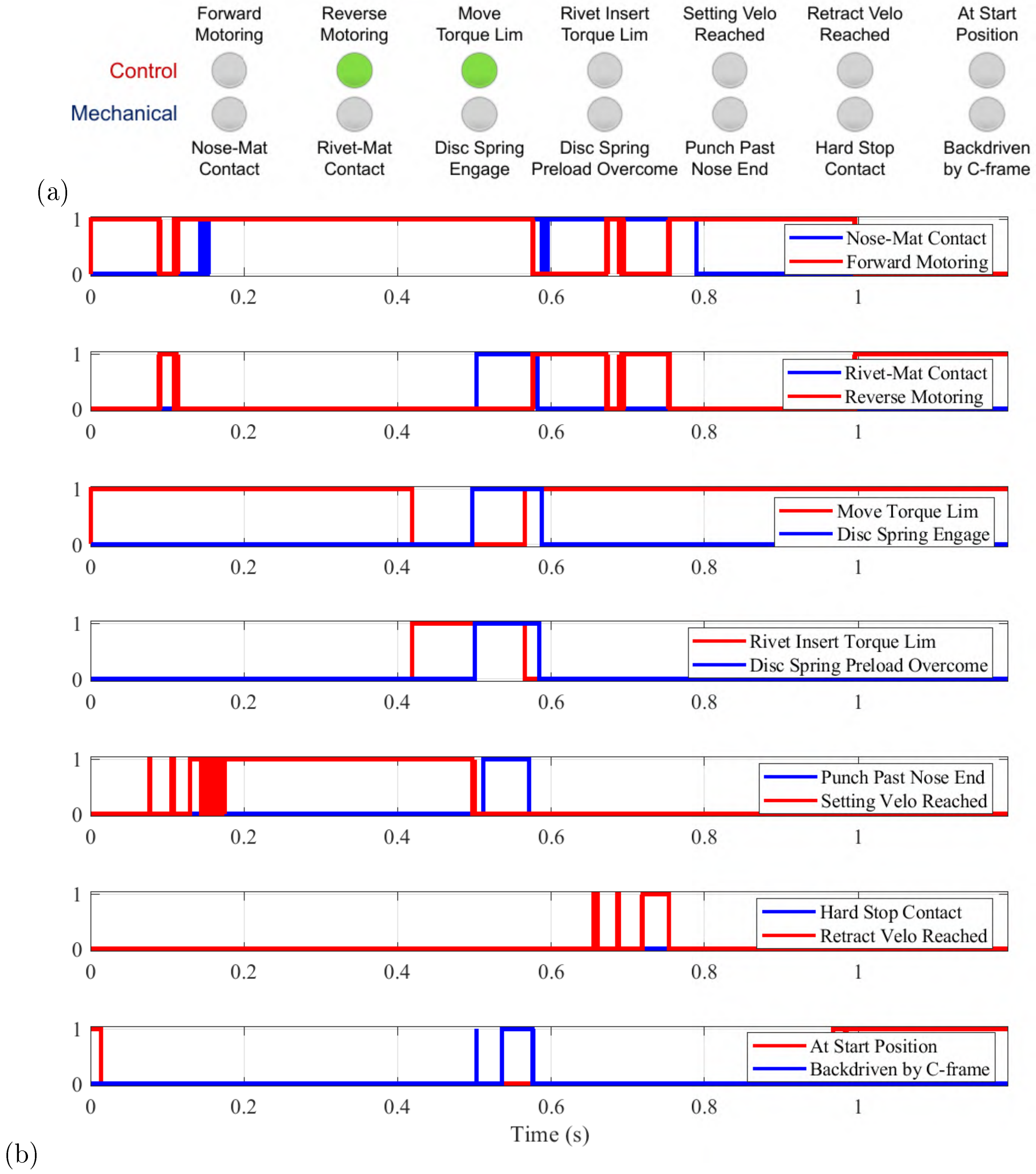

Figure 6.1: (a) Dashboard display in Simulink used to monitor the sequence of key process events during simulation. (b) Time history of said events in a simulated riveting cycle.

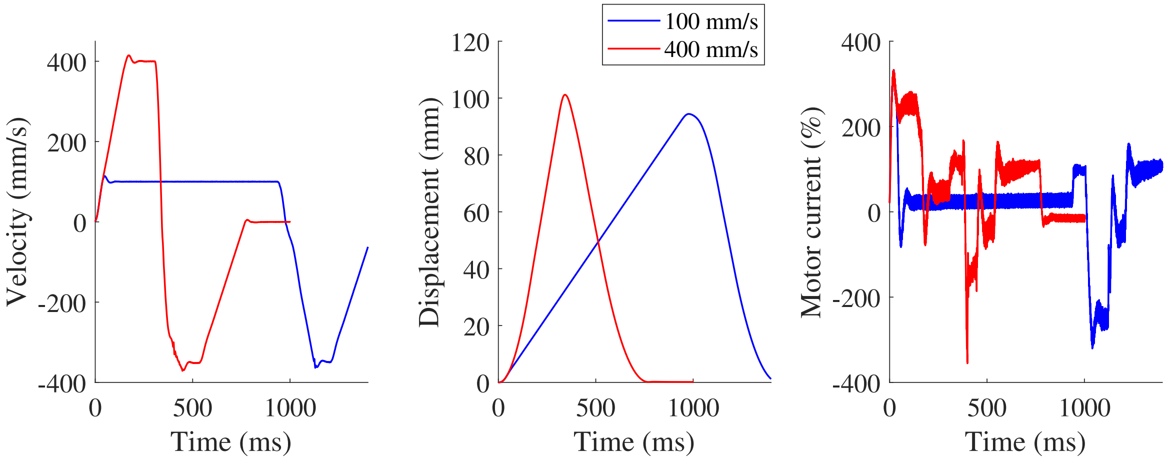

Figure 6.2: Example traces of velocity, displacement and motor current signals generated from the model.

6.2.1.2 C-frame

Focusing more closely on the events surrounding the impact phase of the cycle, in particular the response of the C-frame under load, three different stiffness values were assigned for three separate simulation runs to verify the behaviour of the C-frame model. Figure 6.3 shows the force vs. deflection profile generated from these simulations. The effective stiffnesses are identified from the gradient of the simulated results, and do not differ from the assigned stiffness values, as shown in Table 6.1. This provides evidence that the mathematical model of the C-frame was correctly implemented.

Table 6.1: Comparison of the assigned values for the C-frame stiffness and those identified from the simulated results.

Assigned stiffness (kN/mm)	Identified stiffness (kN/mm)
10	10
20	20
50	50

6.2.1.3 Clamping mechanism

In order the verify the model of the clamping mechanism, the model was executed with said component being loaded through the full range of displacement of its internal parts (i.e. relative displacement between the coupler and the clamp tube), thereby producing a clamp force vs. displacement profile, as shown in Figure 6.4. Here zero displacement is defined as the start of compression of the disc spring pack. The labelled features on the plot and

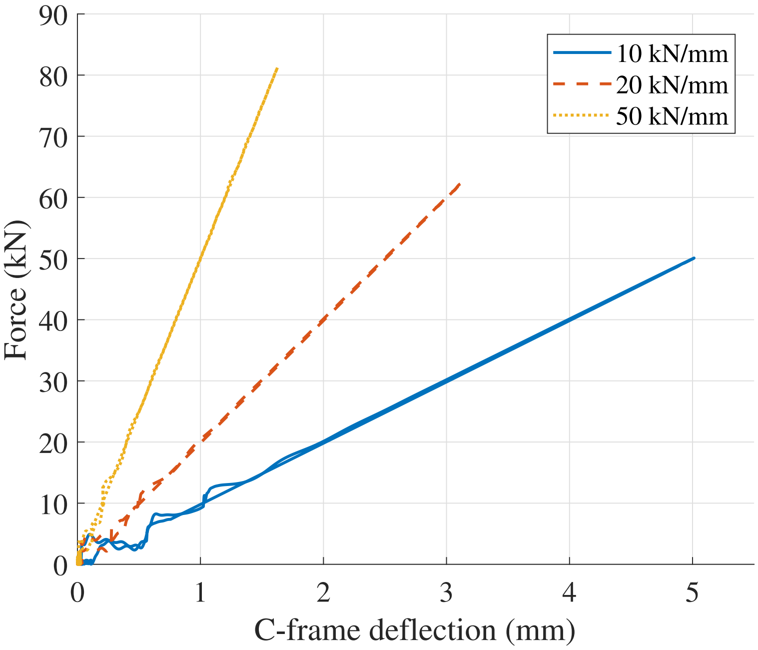

Figure 6.3: Simulated results for total process force vs. C-frame deflection, using three different C-frame stiffnesses: 10, 20 and 50 kN/mm.

corresponding values mirror the assigned values of the associated parameters in the model, i.e. the observed response reflects the intended behaviour in terms of both the magnitude and timing of the various stages of clamp engagement, therefore demonstrating that the mathematical model was correctly implemented in Simulink.

6.2.2 Solution verification

Time convergence forms another important part of the verification process. The equations of motion were solved in Simulink using the fixed-step continuous solver 'ode3' and a time step size of 10^{-5} s. An explanation for these choices is provided below.

6.2.2.1 Solver choice

The state of a system encapsulates the history of the system's response, such that this history can be used with the current inputs into the system in order to determine the current response. State variables are variables which describe the system at a given instant in time. The nature of states in a system can be categorised as 'continuous' or 'discrete'. A continuous system has state variables which change continuously in time, whereas a discrete system has state variables which change instantaneously at discrete points in time. Many systems contain a combination of continuous and discrete states, and are therefore referred

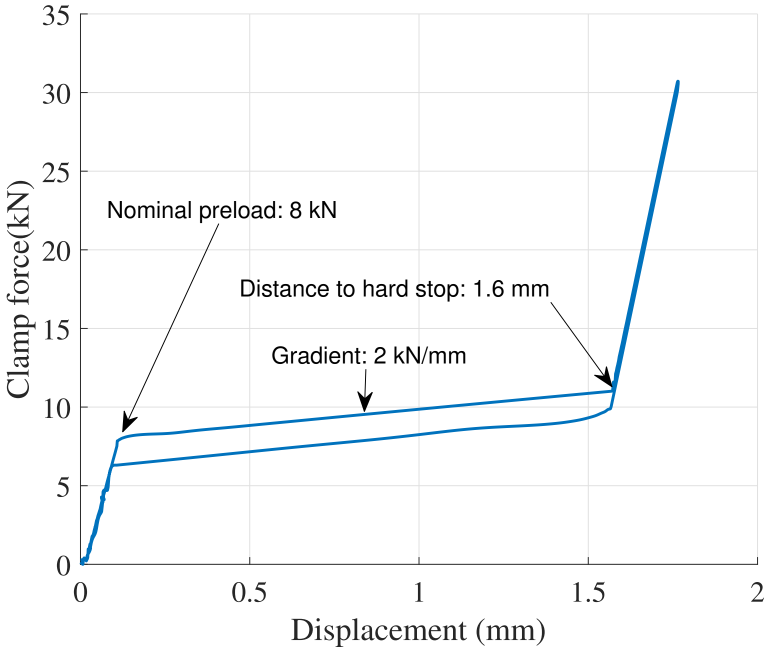

Figure 6.4: Simulated clamp force vs. displacement, where displacement refers to the relative motion between the coupler and the clamp tube, with zero defined as the start of the compression of the disc spring pack.

to as hybrid systems. For example, the SPR system is a hybrid system containing continuous state variables such as the position of the punch, as well as discrete state variables such as the output signal of the PWM generator.

In the Simulink environment, a system is modelled using a set of differential equations. Solving the model involves determining the states of the model at each time step, hence numerical integration methods are employed via solvers, which calculate the outputs of the system at the next time step given the current state and inputs. A solver defines the numerical method used to solve the ordinary differential equations which govern the dynamics of the model. A suitable solver is one which is able to solve the model to the desired level of accuracy as well as within an acceptable time.

The presence of continuous states in the model of the SPR system meant that a discrete solver was not suitable. A variable-step solver would be better suited to a fully continuous model, which the current model was not due to the discrete states of the switches in VSI. The VSI consisted of a power electronics circuit in which a PWM signal was used to operate transistor gates, or switches, at high frequencies. Given that the switches had discrete states, a fixed-step solver was necessary. Consequently fixed-step continuous solvers were deemed most appropriate. The simulations were run to the desired level of accuracy with the ‘ode3’ solver, which uses the Bogacki-Shampine formula [111] to perform the numerical integrations.

6.2.2.2 Time step size

The size of the time step determines how closely a discrete-time solution can approach the exact solution of the differential equations in the model. The error in the approximate solution is also referred to as the discretisation error. As the time step is decreased, a reduction can be expected in the discretisation error, i.e. a more accurate approximation can be obtained. However, accuracy comes at the expense of computational effort.

A convergence check was realised to determine the appropriate size of the time step that would yield an accurate enough solution. The model was parameterised according to the conditions of treatment 3 in Table 3.4, for joint A. A series of simulations were run using different time step sizes. The maximum time step size evaluated was 2.3×10^{-5} s since larger values were not suitable for solving the dynamics of the modelled system and led to early termination of the simulation.

Figure 6.5 shows the model-predicted head height vs. time step size. The values of the head height are seen to be stable across the range of time step sizes; the differences in the values were less than 0.01 mm (i.e. less than the resolution of the experimentally measured head height) and were therefore considered negligible. This indicates that the results have converged in each case. A time step size of 10^{-5} s was noted to be an adequate choice.

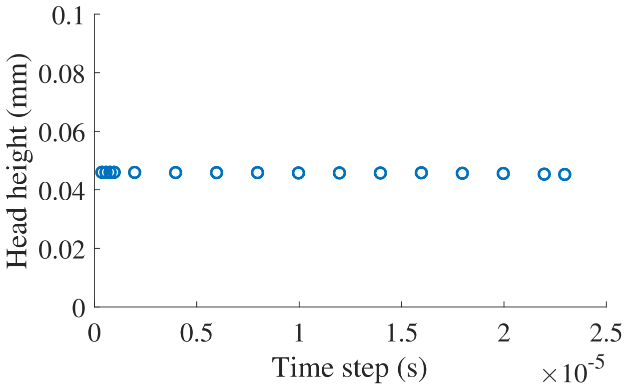

Figure 6.5: Predicted head height vs. time step size.

In summary, performing each of the aforementioned simulation cases served to verify the software implementation of the control logic as well as the mathematical equations that described the dynamics of the riveting system. This was considered sufficient verification for the intended use of the model. Following verification, the next section delves into the approach taken to train the model of the SPR joint on experimental data, and subsequently assessing the accuracy of the full model of the SPR process via validation.

6.3 Training and validation

6.3.1 Training steps

Here, model training refers to the process of generating a black box model that represents the rivet-material-die interactions for a given joint configuration, from a given dataset. Being a key component of the full model of the SPR process, the model of the joint inevitably affects the performance of the wider model. Therefore, the choice of training dataset and its effect on the overall predictive performance was of particular interest.

In order to formally assess the predictive performance of the full model, the acquired datasets corresponding to the eight treatments in Table 3.4 were divided into training and validation groups. Here, training refers to the process of generating a model of the joint from selected force vs. relative displacement data.

The process of training the model of the joint is described in Figure 6.6. Firstly, a treatment was chosen to serve as the training dataset (Figure 6.6(a)). Recall from Section 3.6 that each treatment contained five replicates, meaning that five individual datasets were available. Using all five datasets from the given treatment, the punch force vs. punch-die relative displacement curves from each dataset were overlaid (i.e. all five datasets were concatenated) and a polynomial of a predefined order was fitted to the data. The problem could be expressed as a system of linear equations in the form $\mathbf{A}\mathbf{c} = \mathbf{B}$, where $\mathbf{A}$ is a matrix constructed from the punch-die relative displacement (x) raised to powers up to the predefined polynomial order (k), $\mathbf{c}$ is an array of coefficient values, and $\mathbf{B}$ is the array of punch force (F) values, as shown in Equation 6.1. There are as many rows in each of the matrices $\mathbf{A}$ and $\mathbf{B}$ as the total number of samples (n) in all five datasets from the chosen treatment.

$$\begin{bmatrix} x_1 & x_1^2 & \dots & x_1^k \\ x_2 & x_2^2 & \dots & x_2^k \\ x_3 & x_3^2 & \dots & x_3^k \\ \vdots & \vdots & \ddots & \vdots \\ x_n & x_n^2 & \cdots & x_n^k \end{bmatrix} \begin{bmatrix} c_1 \\ c_2 \\ \vdots \\ c_k \end{bmatrix} = \begin{bmatrix} F_1 \\ F_2 \\ F_3 \\ \vdots \\ F_n \end{bmatrix} \tag{6.1}$$

The system of equations was overdetermined as there were more equations than unknowns, hence a least squares solution was obtained for the coefficients in $\mathbf{c}$.

The above steps were subsequently repeated using different polynomial orders, and the regression errors were collected and visualised in relation to the polynomial order, as illustrated in Figure 6.6(b). While a low regression error was desireable, the complexity of the model and how well it was able to capture the more nonlinear parts of the force profile were also considered when it came to model selection. Once a suitable polynomial order (i.e. model equation) was chosen, the selected model was used in subsequent simulations in the form of a polynomial equation. An example of a fitted model is visualised in Figure 6.6(c).

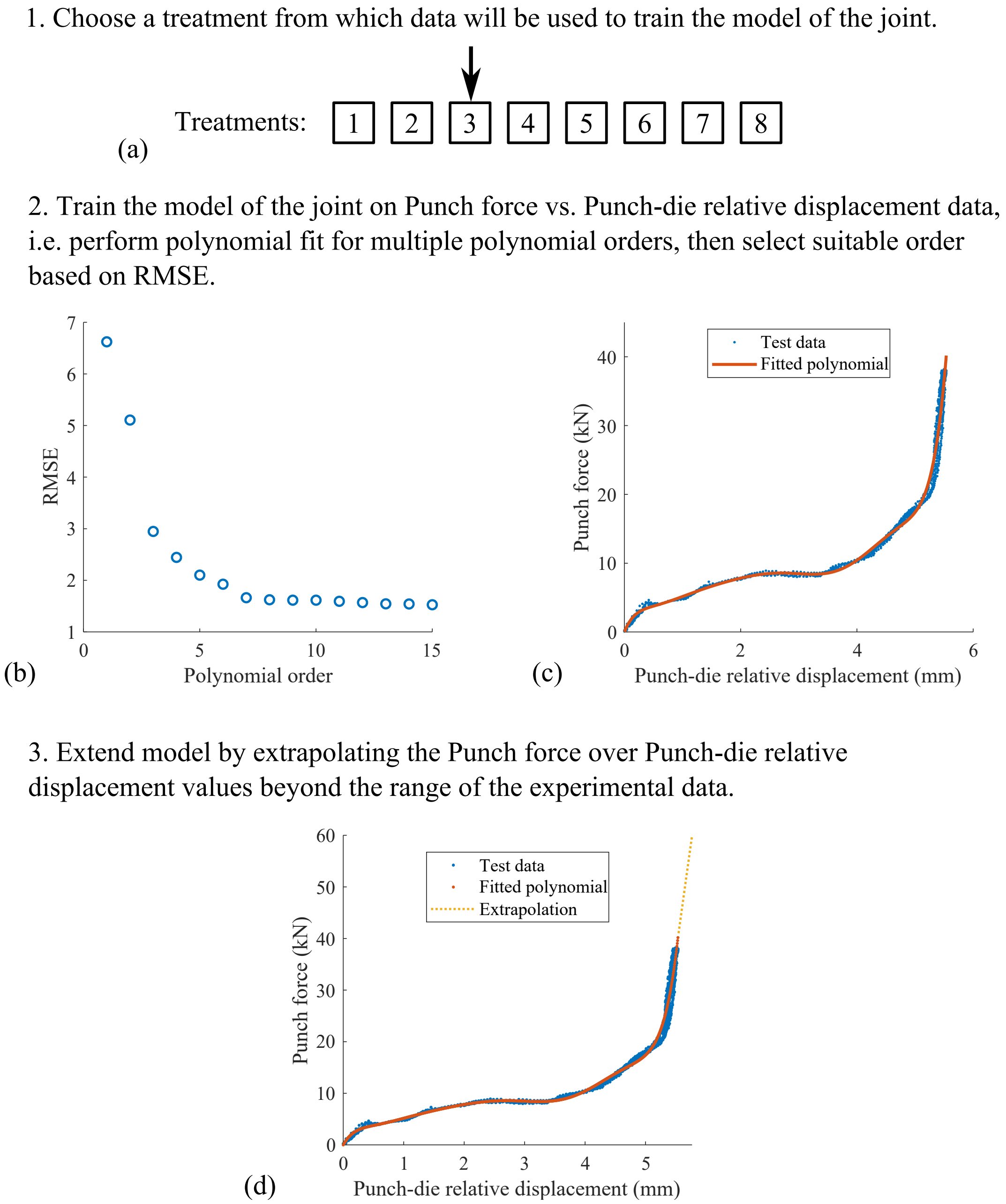

1. Choose a treatment from which data will be used to train the model of the joint.

2. Train the model of the joint on Punch force vs. Punch-die relative displacement data, i.e. perform polynomial fit for multiple polynomial orders, then select suitable order based on RMSE.

3. Extend model by extrapolating the Punch force over Punch-die relative displacement values beyond the range of the experimental data.

Figure 6.6: Workflow explaining the training process used in the current study.

A limitation of using experimental data to generate the model of the joint was that the behaviour of model was only defined up to the point of maximum force and punch-die relative displacement. Beyond the range of the experimental data points, the behaviour of the polynomial fit may be unstable. However, a stable definition of the model response in this region was needed to allow the simulation of cases where the rivet may be inserted further than the point of maximum insertion observed experimentally. Therefore, behaviour of the model over this region of further rivet insertion was manually defined, as shown in Figure 6.6(d). This linear line extrapolation of the force curve was based on the assumption that the restoring force acting on the rivet would continue to increase with further rivet insertion and that the effective stiffness of the joint would remain constant over this region. While the inaccuracy of the extrapolated region relative to the real behaviour of the joint can be expected to grow with increasing extrapolation beyond the maximum experimental data point, for the purposes of validating the model it is considered adequate since the training and validation datasets can be chosen such that the model would not be operated at points inside the extrapolated region.

As expected, the resulting model of the joint would depend on the choice of treatment (i.e. the experimental datasets). Treatment choice was guided by the test configurations associated with each treatment. With setting velocity, motor torque limit and C-frame stiffness as the main variables in the test, the combination of settings which led to the most complete punch force vs. punch-die relative displacement curve was considered the best candidate for use in model fitting. The reasons for this are elaborated in Section 6.3.3.

6.3.2 Validation steps

Validation aims to assess whether the model is a good enough representation of the real system. This requires the predictive accuracy of the model to be quantified and evaluated against predefined levels of adequacy. The steps involved in the validation of the full system model are shown in Figure 6.7. For a given treatment, each of the five component datasets were individually compared to the simulated data, namely for the following signals and metrics:

- Punch force – force transmitted directly through the rivet
- Clamp force – force transmitted through the material surrounding the rivet
- Relative displacement – extent of rivet insertion
- Relative velocity – rate of rivet insertion
- Head height – final state of the produced joint

Figure 6.7(a) illustrates the comparison between the measured and simulated punch force signals for each replicate in treatment 1.

For each signal, the normalised root mean square error (NRMSE) values across the five datasets within the treatment were averaged to obtain the mean NRMSE associated with the treatment. This was done for all eight treatments, and the mean NRMSEs were collected as shown in Figure 6.7(b). Regarding the head height, given that this was a scalar measurement rather than a signal in time, the measured values were averaged to give a mean value for each treatment and were compared to the simulated head heights, as shown in Figure 6.7(c).

The discrepancy between the simulated and experimental results was quantified using the NRMSE. The root mean square error represents the average deviation of the simulated results from the experimental data. It is associated with the variance of the error, hence larger errors have more weight in their contribution to the final value of the root mean square error, meaning that larger errors are penalised more heavily [112]. This is considered a desirable trait since the current study seeks to critically distinguish between the performances of multiple model variants. Furthermore, interpretation of the error measure is fairly intuitive given that its units are the same as the signal of interest. The NRMSE was obtained by dividing the root mean square error by the range of the experimentally observed values of the associated signal. Normalisation was necessary to enable comparisons between the performances of the different model variants of the joint, i.e. models trained on different datasets.

The evaluation of cases where the model is extrapolated would inevitably lead to larger prediction errors. Hence, not all training and validation allocations would give meaningful results. In those cases where the training data provide sufficient definition of the punch force characteristic curve such that subsequent validation cases can be handled without extrapolation, the simulated results may be considered as the best estimation of the process outputs. On the other hand, for those cases where the punch force characteristic curve must be extrapolated, additional uncertainty is introduced into the simulation inputs which would also be reflected in the outputs. The choice of validation datasets was based on the test configurations associated with each treatment, the combination of settings which led to punch force vs. punch-die relative displacement curves within the range of the training dataset was considered suitable. The reasons for this are elaborated in Section 6.3.3.

Selected validation cases for joint A and joint B are presented in this chapter. Descriptions for each joint were provided in Figure 3.12.

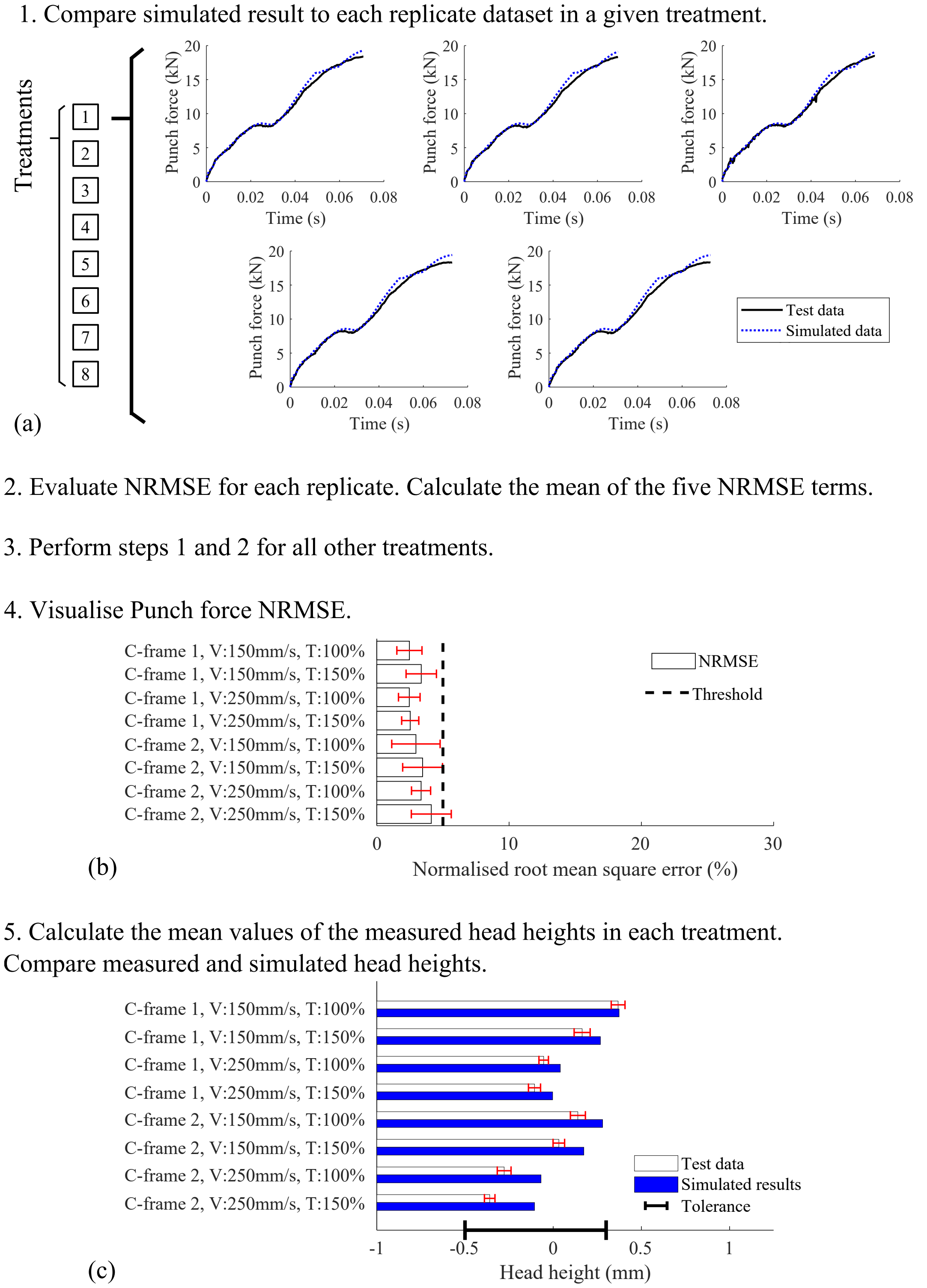

Figure 6.7: Workflow explaining the validation process used in the current study.

6.3.3 Joint A

6.3.3.1 Choice of training dataset

As mentioned in Section 6.3.1, the choice of training dataset and the regression method determine the model of the joint.

The input data for modelling the joint was the punch force and the punch-die relative displacement. Having established in Section 5.4.1 that the joint configuration in question was not sensitive to the strain rates seen in typical inertia-based SPR processes, the changing of the setting velocity, motor current limit and C-frame type was therefore expected to only affect the extent of rivet insertion and peak forces rather than the master profile of the punch force vs. punch-die relative displacement.

Figure 6.8(a) compares the punch force vs. punch-die relative displacement data from treatments of contrasting setting velocities. The most notable effect is that the curve extends further for the higher setting velocity as more energy is delivered to the joint. It can be said that a larger part of the characteristic curve is mapped out when using higher setting velocities.

The influence of different motor current limit levels on the punch force vs. punch-die relative displacement curve is compared in Figure 6.8(b). The increase in motor current limit led to further rivet insertion and higher forces, which was due to the higher level of torque output from the motor during rivet insertion.

Figure 6.8(c) compares the effect of using different C-frame types on the punch force vs. punch-die relative displacement curve. For the C-frame with the higher effective stiffness (i.e. C-frame 2), the rivet was inserted further for the same setting velocity and motor current limit. This is because under a given load the strain energy stored in a stiffer system is less than that of a more compliant one, hence for the same total input energy, a larger proportion of the input energy would be delivered to the joint in the stiffer system.

The above observations make sense from an energy perspective. Considering solely the process during the rivet insertion itself, the kinetic energy of the system and the work done by the motor torque make up the total energy input into the process, which will be partly dissipated in the joint, partly stored as strain energy in the system, and partly dissipated as heat due to friction in the setter. Any increase in the total input energy or reduction in the strain energy would result in more energy being delivered to the joint.

Further rivet insertion provides a more complete characteristic punch force curve, which would expand the range of model inputs over which the punch force can be predicted. With a view to maximise the mapping of the punch force curve, it is clear that tests performed using higher setting velocities coupled with a higher motor current limit and a stiffer C-

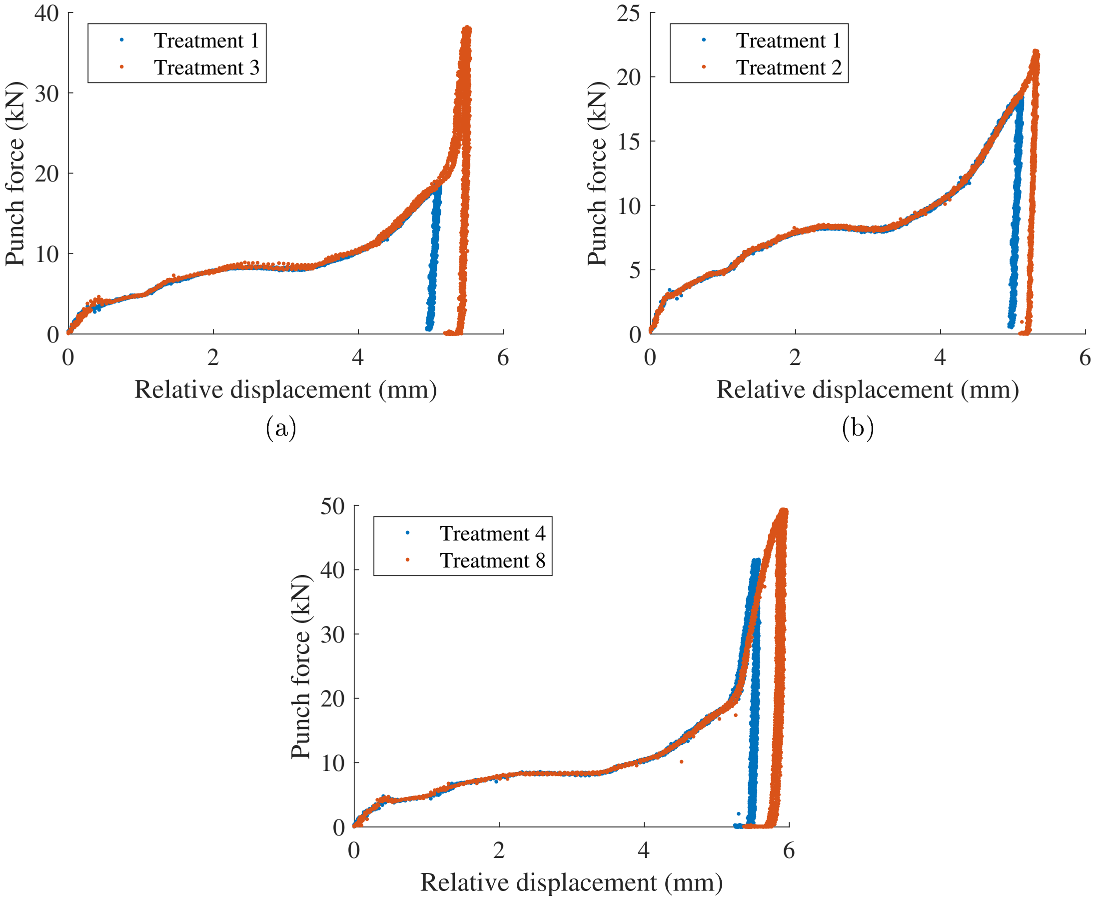

(a) (b) (c)

Figure 6.8: Joint A, punch force vs. punch-die relative displacement data from various treatments. (a) Comparing treatments 1 and 3 (i.e. setting velocities 150 and 250 mm/s respectively). (b) Comparing treatments 1 and 2 (i.e. motor current limits 100 and 150% respectively). (c) Comparing treatments 4 and 8 (i.e. C-frame types 1 and 2 respectively). Data from all five replicates for each treatment are overlaid in the figures.

frame would be more appropriate. However, something to note in Figure 6.8(c) is that at larger relative displacement (i.e. deeper rivet insertion) the punch force profiles for the two treatments do not quite overlay; in comparison to treatment 8, data from treatment 4 suggest that more force is required to insert the rivet by a specific distance above 5.5 mm. This may be related to the differences in the C-frames used since all other process settings were kept the same between the two treatments. Additionally, it places doubt on the idea that a single master curve can be used to characterise a joint. Further exploration of the potential effects of the C-frame on the joint behaviour is detailed in Section 6.3.3.3.

Of the experimental results, treatment 4 and 8 were deemed as the most suitable training datasets, given that they corresponded to the higher level of setting velocity, motor current limit. Subsequent sections explore the performance of the model trained on the associated datasets from each treatment.

6.3.3.2 Model evaluation

A model of the joint was identified first using the five replicates from treatment 4. Figure 6.9(a) shows the reduction in regression error with increasing model complexity (i.e. polynomial order). A polynomial of order 10 was chosen as a suitable compromise between model accuracy and complexity. Lower orders did not capture the nonlinear features of the force profile as well, while higher orders did not offer any noticeable improvements in terms of regression error. The fitted force curve for the chosen model is visualised in Figure 6.9(b), together with the experimental data.

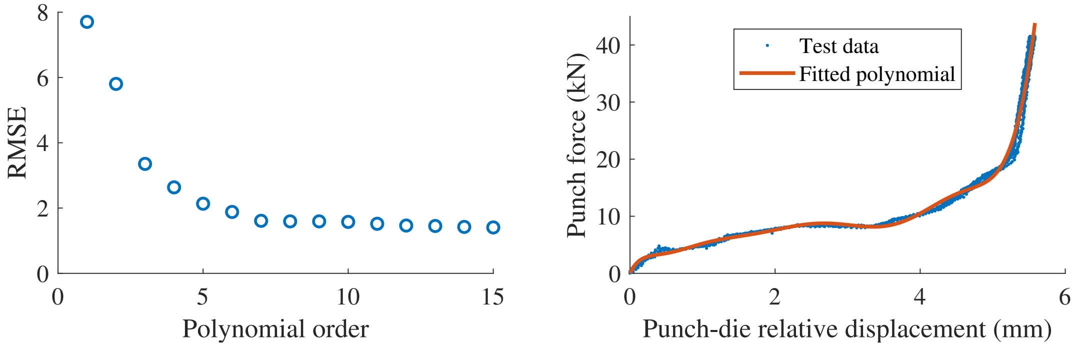

(a) (b)

Figure 6.9: Training of the model of joint A on data from treatment 4. (a) Regression errors for models defined using each polynomial order. (b) Punch force vs. punch-die relative displacement, model of polynomial order 10. Fitted function: $y = -0.006x^{10} + 0.175x^9 - 2.080x^8 + 13.669x^7 - 54.278x^6 + 134.283x^5 - 206.099x^4 + 189.342x^3 - 96.701x^2 + 26.909x$, where y and x represent the punch force and punch-die relative displacement respectively.

To study the behaviour of the model, a nominal case is examined; the model is validated against the results from treatment 1. The results of the riveting simulation and validation on treatment 1 are shown in Figure 6.10. Excellent agreement is noted for the process forces shown in Figure 6.10(a) and (b). The predicted relative displacement and relative velocity signals also match closely to the experimental data in Figure 6.10(c) and (d) respectively. Small discrepancies in Figure 6.10(a), (c) and (d) from 0.04 s onwards are believed to be related to the assumptions made in modelling the material stack. The approximation of the material under clamping as a linear spring essentially neglected the 'pushback' effect mentioned in Section 5.4.1. This results in the delayed engagement of the clamp springs in the simulation, most notable in Figure 6.10(b).

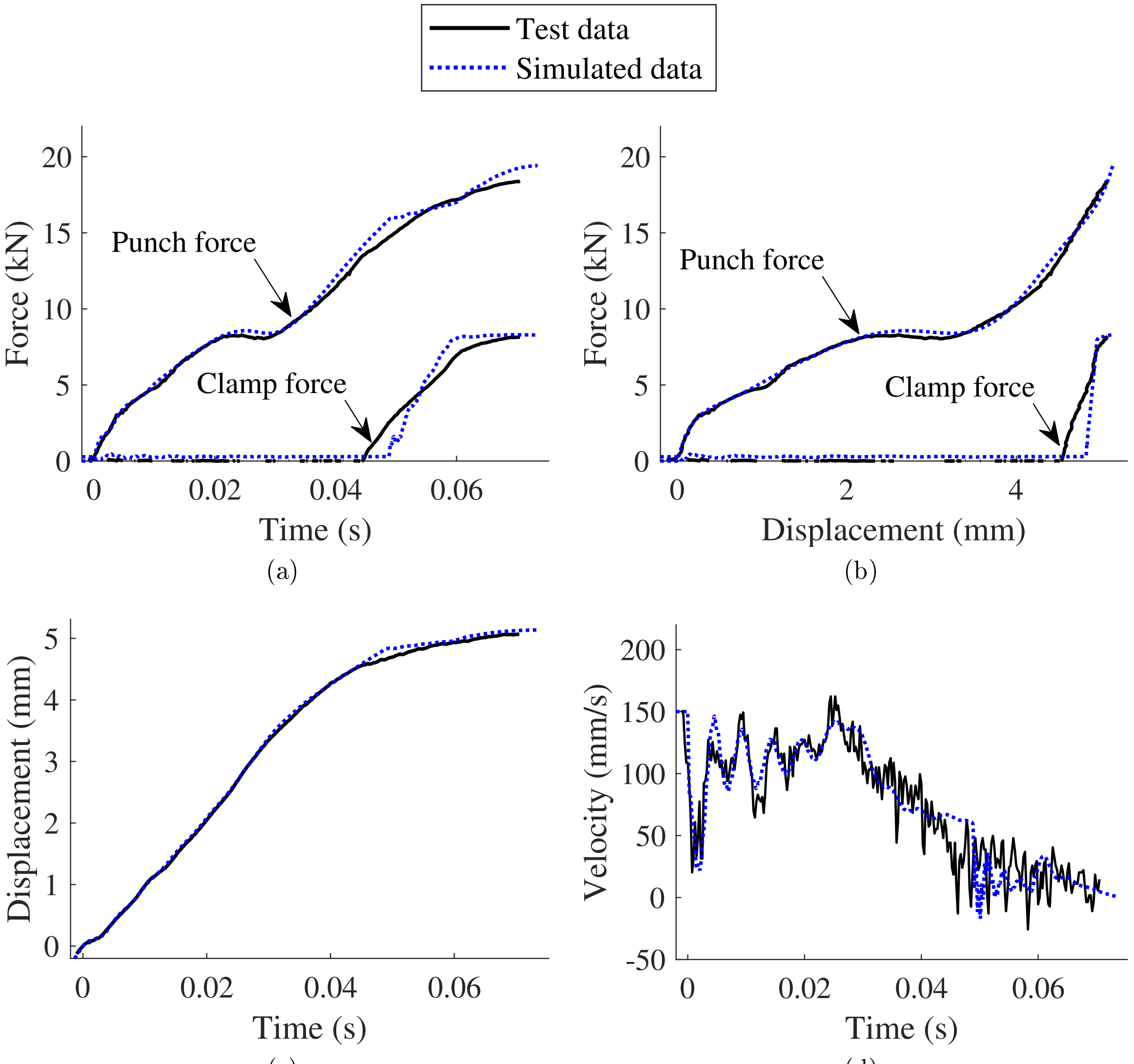

(a) (b)

(c) (d)

Figure 6.10: Comparison between experimental and simulated data. Training dataset: treatment 4. Validation dataset: treatment 1. (a) Force vs. time, (b) Force vs. relative displacement, (c) Relative displacement vs. time, (d) Relative velocity vs. time.

Although the accuracy of the model may be further improved with the inclusion of unmodelled dynamics such as the 'pushback' effect, the overall performance of the existing model suggests that a suitable balance is already achieved between model fidelity and complexity. Next, the performance of the model is assessed against all eight treatments.

The performance of the model in validation across all the treatments can be summarised via NRMSE values, as mentioned in Section 6.3.2. The punch force and head height are examined since these are directly related to the joint and therefore provide more insights into the performance of the model. Figure 6.11(a) and (b) show the NRMSE for the punch force and head height respectively. For each treatment labelled on the y-axis, the simulation output is validated against each individual replicate test result within the treatment. The errors are then averaged to obtain a mean root mean square error for each treatment. The individual bars in Figure 6.11(a) and (b) represent the mean NRMSE, and error bars are plotted at ±3 standard deviations either side of the mean. The definition of 5% as the error threshold relates to the limits used in the process monitoring of actual SPR applications, here it can be considered as a threshold below which the model errors are considered insignificant.

Alongside the NRMSE of the model-predicted head heights, the predicted values are shown in Figure 6.11(c). For the test data, each individual bar represents the mean measured head height of all five repeat joints for a given treatment, and the error bars are ±3 standard deviations from the mean. Furthermore, to put the accuracy of the simulation results into context, the absolute tolerances on the head height typically used in industry are indicated by the error bars on the x-axis with an upper limit of 0.3 mm and a lower limit of -0.5 mm [10]. This may also be considered as a tolerance of ±0.4 mm about a nominal value of -0.1 mm. In the current research the process parameters were not chosen with a specific target head height in mind, hence rather than using a single nominal value as reference across all treatments, the mean measured head height of each treatment can be considered as a reference, about which a tolerance band of ±0.4 mm can be applied. If the simulated head height corresponding to a particular treatment falls within ±0.4 mm of the measured value, it would indicate that the head height can be predicted to within the tolerances typically used in assessing joint quality in industry.

It is seen in Figure 6.11(a) that NRMSEs below 5% are achieved, and are therefore within the acceptable bounds. Good performance is in part attributed to the model of the joint, which allowed the restoring force to be computed accurately via interpolation when validating against most of the treatments. A model with a more complete force-displacement curve is better suited to simulating a wider range of input conditions. Interestingly, when validating against treatment 7 and 8, some extrapolation from the identified force-displacement curve would have been necessary as the simulated force and displacement exceeded the range of the

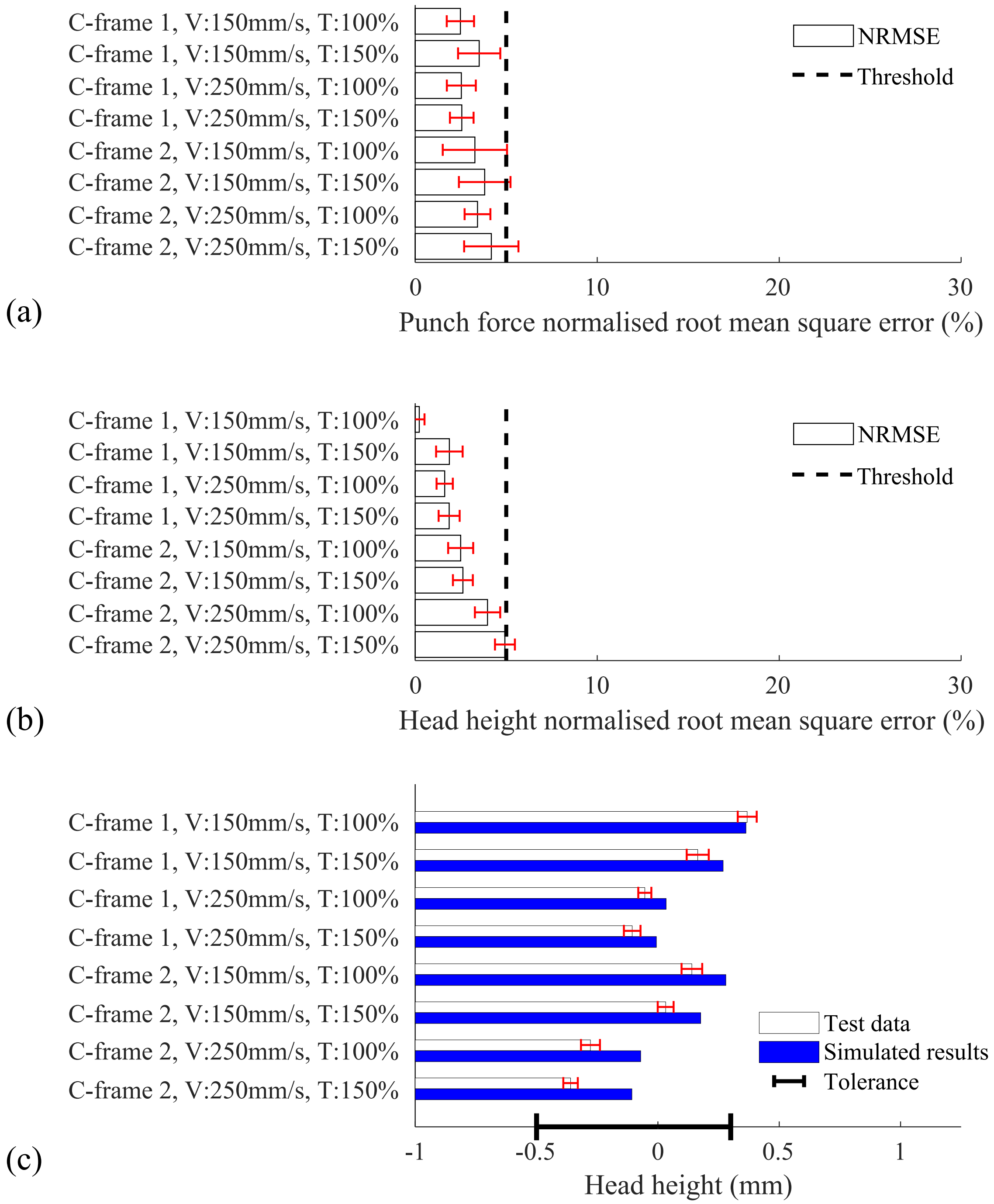

Figure 6.11: Evaluation of simulation outputs for the model of joint A trained on treatment 4. (a) Punch force NRMSE. (b) Head height NRMSE. (c) Comparison between measured and predicted head heights. V and T denote the setting velocity and motor current limit respectively. Error bars on training and validation data show the repeatability based on three standard deviations for five duplicate tests. The error bars on the x-axis denote the tolerance on acceptable head heights typically used in industry.

experimental data used in training the model of the joint. The low NRMSE values suggest that the extrapolated region was perhaps representative of the real behaviour of the joint.

In Figure 6.11(c), it can be seen that very good predictions are achieved; prediction errors of within ±0.3 mm are obtained across all the treatments. Although this level of error exceeds the standard deviation of the experimental measurements, it is within the tolerances used to judge joint quality in industry. The prediction accuracy is therefore considered to be acceptable.

6.3.3.3 Effect of C-frame type

Following on from previous comments about the difference in the force vs. relative displacement profiles in Figure 6.8(c), the effects of training the model of the joint on data obtained using different C-frame types is explored here.

To examine the performance of models trained on datasets associated with C-frame 2, the model of the joint was trained on the five replicates from treatment 8. Figure 6.12(a) shows the regression error in relation to model complexity (i.e. polynomial order). A polynomial of order 7 was fitted to the data, as shown in Figure 6.12(b). While higher orders gave lower RMSE values, the form of the fitted model was less stable with further increasing orders and therefore did not adequately represent the effective stiffness of the joint, which must be monotonically increasing with punch-die relative displacement.

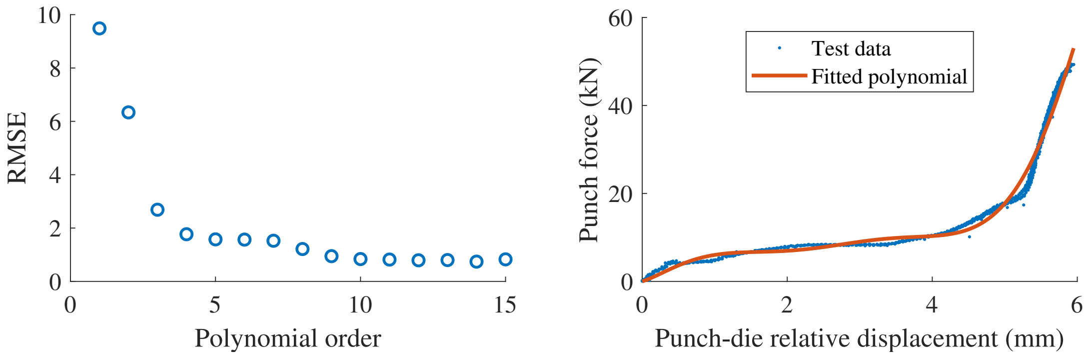

(a)

(b)

Figure 6.12: Training of the model of joint A on data from treatment 8. (a) Regression errors for models defined using each polynomial order. (b) Punch force vs. punch-die relative displacement, model of polynomial order 7. Fitted function: $y = -0.017x^7 + 0.337x^6 - 2.595x^5 + 9.504x^4 - 16.470x^3 + 9.855x^2 + 5.408x$, where y and x represent the punch force and punch-die relative displacement respectively.

The NRMSE for the punch force and head height are presented in Figure 6.13(a) and (b) respectively. Figure 6.13(c) shows the measured and predicted head height values. On the whole, punch force NRMSE values are in the region of 5% or lower, and the discrepancies in the predicted head heights are within ±0.2 mm across all the treatments. The magnitudes of the errors are on par with those seen in Figure 6.11, which suggests that the type of C-frame associated with the training data does not have a significant impact on the performance of the trained model, even when validating on data obtained on a different C-frame type. This implies that the aforementioned differences in the force vs. relative displacement profiles between the treatments in Figure 6.8(c) are insignificant when it comes to joint characterisation.

6.3.4 Joint B

Having assessed the performance of the models generated for joint A, a similar exercise was conducted for joint B in order to validate the modelling approach on an alternative joint configuration. The main motivation was to test the robustness of the approach.

As detailed in Figure 3.12, the material for joint B was a different grade of aluminium, the thickness of the material stack was twice that of joint A. The die cavity had a flat bottom surface rather than a raised central pip. The conditions described by the same eight treatments in Table 3.4 were also applicable to joint B.

6.3.4.1 Data overview

The punch force vs. punch-die relative displacement profiles between different treatments is shown in Figure 6.14. Data from treatments with different setting velocities, motor current limits, and C-frame types are compared in Figures 6.14(a), (b) and (c) respectively. The effect of the setting velocity, motor current limit and C-frame type on the force curve mirror the observations made in Section 6.3.3.1 regarding Figure 6.8; an increase in the setting velocity, motor current limit or stiffness of the C-frame leads to further rivet insertion.

Unlike in Figure 6.8(c) however, the difference between the loading part of the force curves in Figure 6.14(c) is negligible; both traces appear to lie on a single master curve. This suggests that joint B can be characterised using a single characteristic punch force vs. punch-die relative displacement curve regardless of the C-frame used in obtaining the experimental data. In view of this, data from treatment 8 were selected for training the model of the joint, as it made sense to train the model on the dataset which offered the most extensive punch force vs. punch-die relative displacement profile.

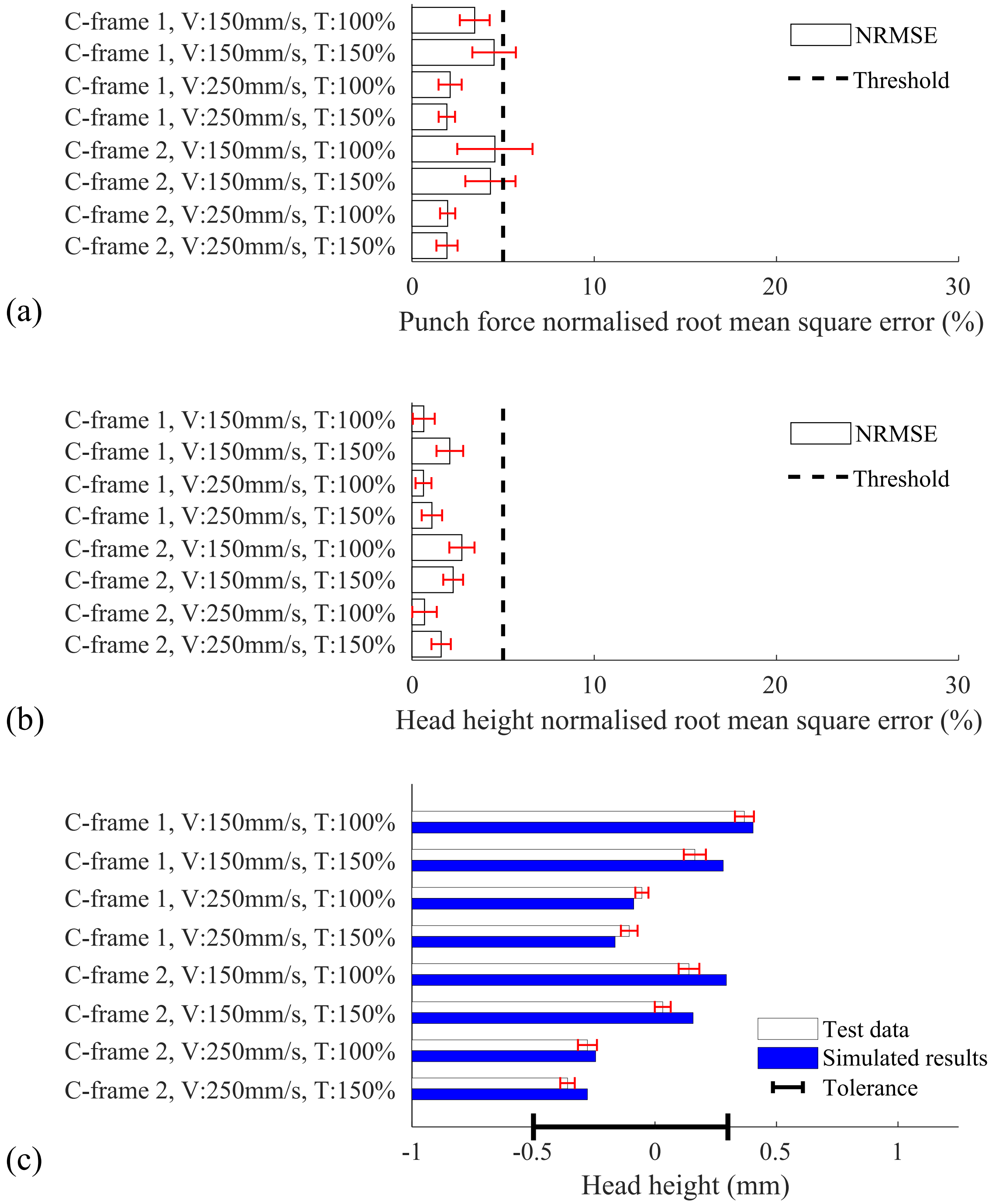

Figure 6.13: Evaluation of simulation outputs for the model of joint A trained on treatment 8. (a) Punch force NRMSE. (b) Head height NRMSE. (c) Comparison between measured and predicted head heights. V and T denote the setting velocity and motor current limit respectively. Error bars on training and validation data show the repeatability based on three standard deviations for five duplicate tests. The error bars on the x-axis denote the tolerance on acceptable head heights typically used in industry.

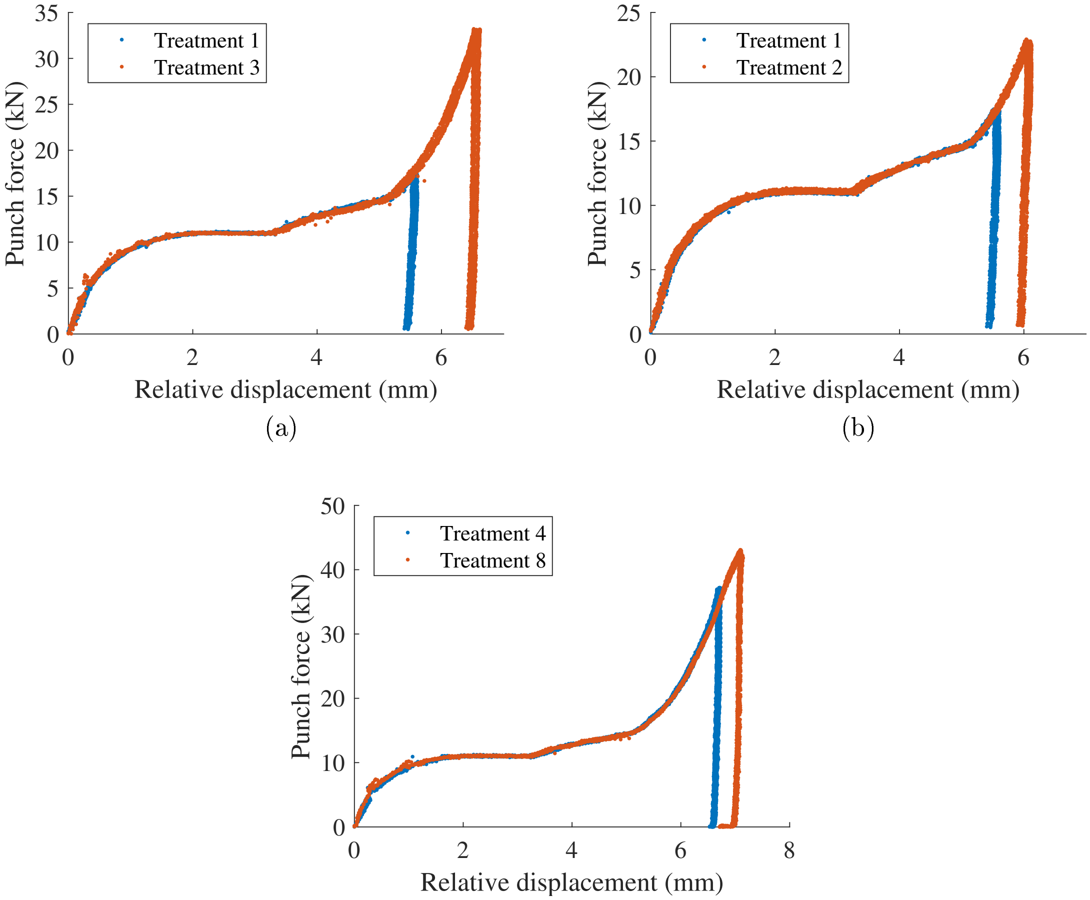

(a)

(b)

(c)

Figure 6.14: Joint B, punch force vs. punch-die relative displacement data from various treatments. (a) Comparing treatments 1 and 3 (i.e. setting velocities 150 and 250 mm/s respectively). (b) Comparing treatments 1 and 2 (i.e. motor current limits 100 and 150% respectively). (c) Comparing treatments 4 and 8 (i.e. C-frame types 1 and 2 respectively). Data from all five replicates for each treatment are overlaid in the figures.

6.3.4.2 Model evaluation

Data from treatment 8 was used to identify the model of the joint. Figure 6.15(a) shows the regression error in relation to the order of the fitted polynomial function. Figure 6.15(b) shows the fitted curve that represents the relationship between the punch force and rivet insertion distance. The polynomial curve in Figure 6.15(a) was of the 7th order, selected according to the root mean square error between the data and the fitted curve. The smoother profile of the experimental data allowed a lower order fit than that used for joint A.

In keeping with the format of the nominal case for joint A, here the model of joint B is identified using data from the five replicates in treatment 8 and validated against data from

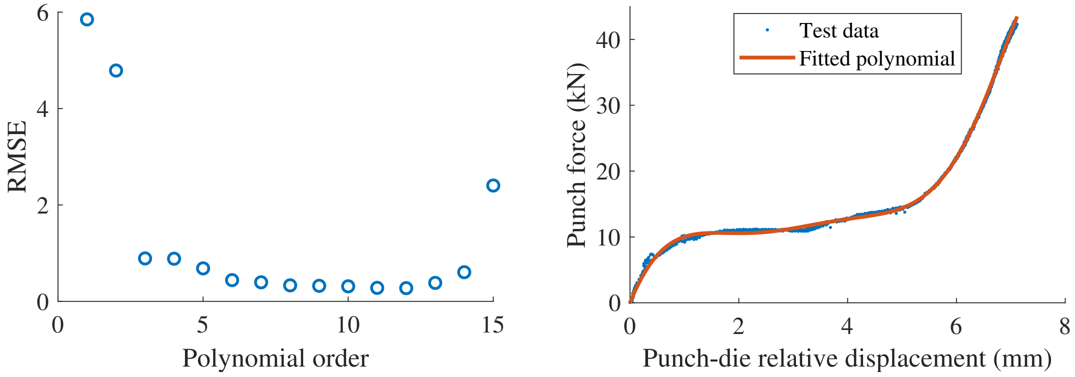

(a) (b)

Figure 6.15: Training of the model of joint B on data from treatment 8. (a) Regression errors for models defined using each polynomial order. (b) Punch force vs. punch-die relative displacement, model of polynomial order 7. Fitted function: $y = -0.002x^7 + 0.049x^6 - 0.329x^5 + 0.558x^4 + 2.789x^3 - 13.452x^2 + 20.409x$, where y and x represent the punch force and punch-die relative displacement respectively.

treatment 1. Figure 6.16 compares the experimentally acquired data with the simulated results. The overlay between the signals is indicative of good overall model performance. The clamping component of the force is not visible in Figure 6.16(a) and (b) as the clamping mechanism does not engage for the given input conditions. A slight over-prediction in the punch force can be noted in Figure 6.16(a) from 0.05 s onwards. Figure 6.16(b) shows that the profile of the punch force does not stray significantly from the characteristic force-displacement curve, which implies that the over-prediction in punch force vs. time may be attributed to an overestimation of the relative displacement in time. This is in fact observable in Figure 6.16(c), where the relative displacement can be seen to be over-predicted from 0.04 s onwards. Despite the said discrepancies, the relative velocity signal shown in Figure 6.16(d) is able to largely capture the transient response of the system.

Next, the training and validation approach is extended to all the eight treatments. The NRMSE for the punch force and head height are presented in Figure 6.17(a) and (b) respectively. Both the punch force and the head height NRMSEs satisfy the 5% threshold. Figure 6.17(c) shows the measured and predicted head height values, where it is seen that the predicted head height values are within ±0.4 mm of the mean measured head height, and are therefore within the tolerance band used to judge joint quality in industry.

In comparison to Figure 6.13, it would appear that the model for joint B performs better than that for joint A. This may be related to the punch force vs. punch-die relative displacement profile for joint B, which has less nonlinear features in contrast to that of joint A, and is therefore more suited to polynomial fitting. In support of this argument are Figures

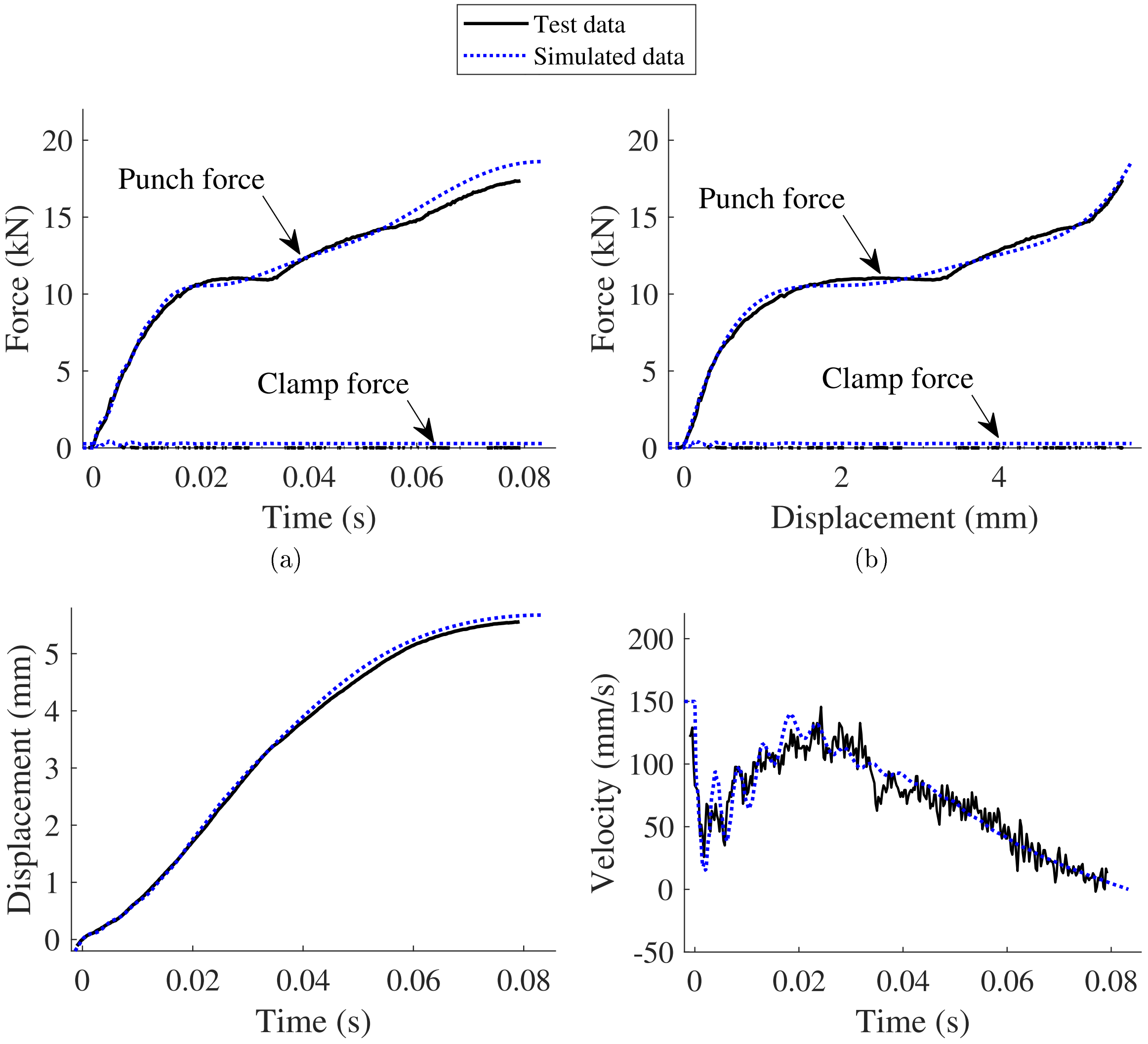

(a) (b) (c) (d)

Figure 6.16: Comparison between experimental and simulated data. Training dataset: treatment 8. Validation dataset: treatment 1. (a) Force vs. time, (b) Force vs. relative displacement, (c) Relative displacement vs. time, (d) Relative velocity vs. time.

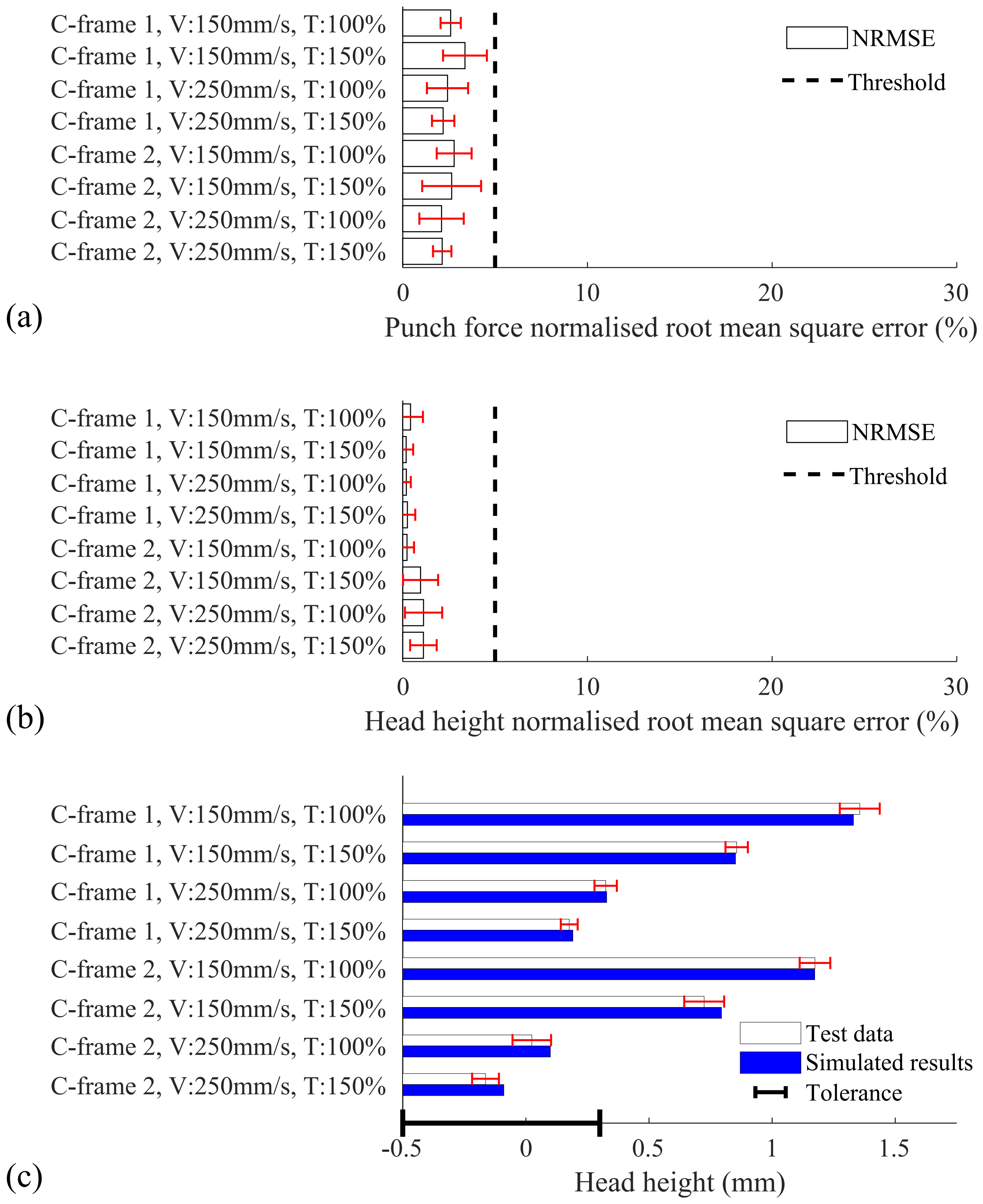

Figure 6.17: Evaluation of simulation outputs for the model of joint B trained on treatment 8. (a) Punch force NRMSE. (b) Head height NRMSE. (c) Comparison between measured and predicted head heights. V and T denote the setting velocity and motor current limit respectively. Error bars on training and validation data show the repeatability based on three standard deviations for five duplicate tests. The error bars on the x-axis denote the tolerance on acceptable head heights typically used in industry.

6.12 and 6.15, which indicate that the RMSE reduces faster with increasing polynomial order for joint B. A better fit would result in a more accurate model of the behaviour of the joint.

6.4 Discussion

6.4.1 Joint model identification

The predictive performance of the model for both joints A and B proves that the modelling approach is valid for both joint configurations, and that the behaviour of these joints can be suitably characterised by their force-displacement curves.

The current work serves as a basis for further verification of the model identification method in modelling joints made with other materials, as well as mixed-material joints. A potential challenge could be the strain-rate dependency of certain materials, for which the assumption of a nonlinear stiffness would not be adequate. In such a case, the use of a restoring force surface model rather than a restoring force curve may be required, with the inclusion of both relative displacement and relative velocity across the joint as independent variables that determine the restoring force.

6.4.2 Pushback effect

In contrast to joint A, joint B did not exhibit any noticeable material 'pushback' effects, which was likely influenced by the material properties as well as the thickness of the material coupons. Comparing Figures 6.18 and 6.19, differences in the response of the material stack before the application of the full clamping load are observed.

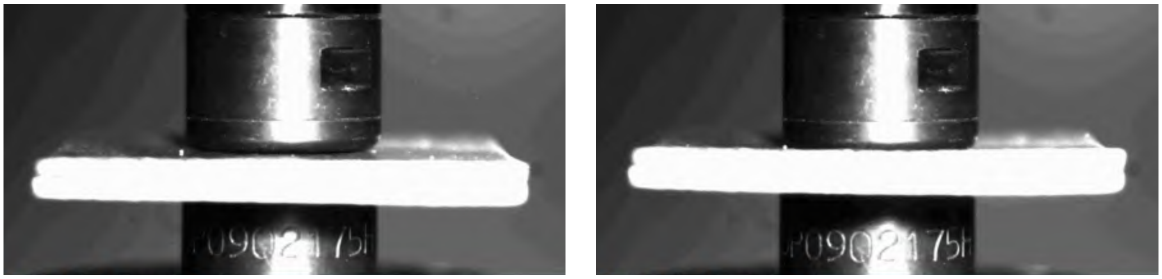

(a) (b)

Figure 6.18: Comparison of images from a riveting cycle for joint A. (a) Start of rivet insertion. (b) During rivet insertion, just before the engagement of the disc springs in the clamping mechanism.

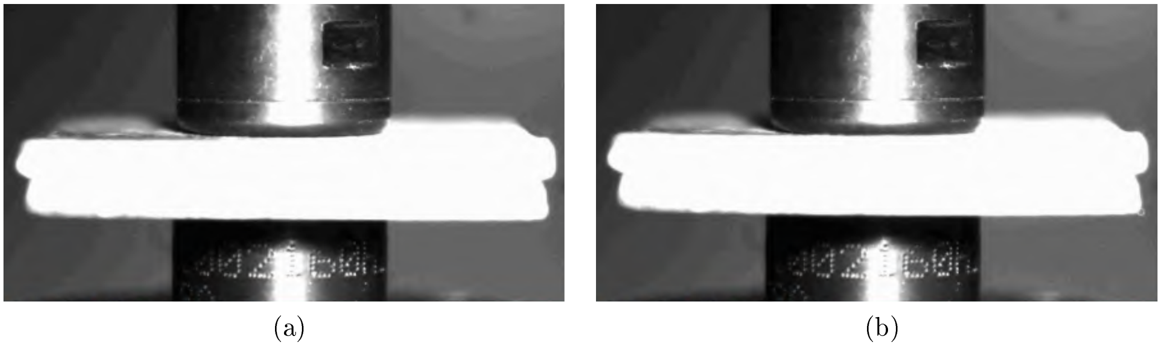

(a) (b)

Figure 6.19: Comparison of images from a riveting cycle for joint B. (a) Start of rivet insertion. (b) During rivet insertion, just before the engagement of the disc springs in the clamping mechanism.

In a real production process, the deformation of the material away from the immediate rivet insertion zone would have implications for the quality of the adjacent joints on the larger structure. Conversely, the pushback effect may be more prominent when joining material coupons, since these are unconstrained at the edges. The joining of larger and more complex parts may yield a different response as a result of the difference in geometry and also constraint conditions that apply around the riveting zone, depending on the way the parts are held in position. The impact of the pushback effect on the quality of the joint is yet to be determined, and would be an area of interest relating to the design of SPR joints.

6.4.3 Limitations

The root mean square error is associated with the variance of the error, which means that errors of a larger magnitude have a larger influence on its final value [113]. In contrast to an alternative error measure, such as the mean absolute error, the root mean square error may be seen as being unfairly weighted. On the other hand, the weighting of the root mean square error is such that errors of a larger magnitude contribute more to the calculated measure than smaller errors, thus it can be argued that an error measure which places harsher penalisation on larger errors can provide a more critical assessment of model performance. The evaluation of alternative error measures or other ways of quantifying the performance of the model may be an area for further work.

With a maximum of five replicates per treatment, the sample size is considered small. While the experimental data presented in this study generally appear to be repeatable, one must bear in mind that all the rivets and materials used in the testing were taken from their respective batches. Repeatable results obtained using consumables from the same batch are to be expected but are not necessarily a true reflection of a production line, where the material to be joined may come from different batches, or suppliers. In other words, more variability is expected in the joints produced on the production line. A related point is that the parts joined on a production line are not in the form of the coupons used in testing. As well as differences in geometry, the boundary conditions are unlikely to match; parts on an automotive production line are often firmly held in fixtures or clamped in place, while no such constraints are implemented in laboratory tests. The implication is that the behaviour of the joint may differ depending on how they are constrained, especially if the constraint is applied in proximity to the rivet insertion zone.

The aforementioned variability of the actual SPR processes and differences to the tests performed in the laboratory may detract from the predictive accuracy of a model which is trained on laboratory test data, and subsequently used to predict the outcomes of processes on the production line. In order to address this quantitatively, the model would need to be validated against the relevant data from site, such as the force-displacement curves for each joint. One approach would be to identify the true force-displacement characteristic by optically measuring the motion of the punch relative to the die, as was done in the current study. However, while this is feasible in a laboratory it may not be on a typical production line, where a high-speed camera may obstruct access to riveting locations or alternatively the view of the camera may be obstructed by the robot or tooling. Large scale collection of high quality data would require further thought and planning, but it is considered an essential step towards understanding the true behaviour as well as the variation in real SPR joints.

Conversely, high-speed video data from production lines may not be necessary; the variability of the process can also be inferred from the measured head heights of the produced joints, which would be much easier to obtain. Since the model is able to make predictions for the head height, it would be possible to replace the relevant deterministic parameters with stochastic ones in the model and quantify the resulting variability in the predicted head height. Comparison between the predicted and measured head heights from the field would provide insight into how well the model captures the variability in the process.

Stochastic parameters related to the riveting machine can be easily introduced to the current model, but variability in the rivet, material and die lie outside its scope. An option to improve the model could be to integrate FE simulations of the joining process with the simulation of the riveting machine, which would enable the full riveting process to be represented in greater detail. Furthermore, it would enable the assessment of how variations in the geometry or the properties of the rivet and material affect the produced joint.

Regarding the modelling of the joint, certain force-displacement profiles are more suited to the polynomial fitting method. A better fit at the modelling stage equates to a model of the joint which more capably captures the characteristics of the process, and consequently more accurate simulation results. One of the limitations of the current modelling approach is that the polynomial fit may not be adequate for characterising all joint configurations, particularly if the force-displacement profile contains sharp changes in gradient or highly nonlinear features. Other approaches which could generate more suitable models of the joint may be the use of piecewise polynomials, look-up tables, or other non-parametric methods. The modular structure of the developed model means that variant submodels can be easily implemented and assessed.

The levels of the motor current limit used in the investigation were chosen based on the range over which the torque-current characteristic of the motor was known to be approximately linear, as well as in consideration of the typical range of values used in the real SPR process. However, for the purpose of model validation, it can be argued that the levels were not wide enough to warrant a significant difference in the trained model. It may be worth using more distinctive levels in future work to validate the performance of the model for cases where the system is operated beyond the typical settings. It is also possible to identify the torque-current profile of the motor experimentally, which would help to extend the range of scenarios which the model can accurately predict.

6.5 Summary

This chapter has explained the steps taken to verify the model via custom simulation cases. The simulated behaviour of the motion control, motor and setter was assessed in consideration of the intended sequence of events in the mathematical model alongside the expected velocity, displacement and motor current traces. The simulated responses of the C-frame and clamping mechanism were verified against the associated parameter values assigned in the model. In addition, the convergence of the model solution was evaluated by checking the calculated head height over various time step sizes.

The performance of the full model relative to the real system has been examined via a series of training and validation scenarios. It has been seen that the setting velocity associated with the training dataset for the model of the joint has a notable impact on the predictive performance of the model. This is because the setting velocity determines to a large extent how much of the force-displacement characteristic curve is mapped out for subsequent use in model predictions. In contrast, the motor current limit and the C-frame type associated with the training dataset have little effect on the predictive performance of the trained model.

Model performance is quantified using the NRMSE. In consideration of the process monitoring and joint quality tolerances used by industry, excellent predictive accuracy is achieved. The results highlight the performance of the model in predicting the effects of making various changes to the system, including the type of C-frame, setting velocity, as well as the motor current limit. This gives confidence in its usage for subsequent model-based investigations.

In Chapter 7, a case study to explore the cycle time and energy consumption of the SPR process is carried out. The cycle time and energy usage are key indicators of the productivity and efficiency of the process, hence are two of the most important quantities in the joining industry. The case study serves to demonstrate the application of the model to solving industry-relevant problems.

Chapter 7

Case Study

7.1 Introduction

The cycle time of the SPR process refers to the time it takes to run through the sequence of steps involved in creating a single joint, as visualised in Figure 1.1. More specifically, it is the time elapsed between the start of the actuation of the punch and the moment at which it is retracted to its start position following rivet insertion.

On high-volume production lines in the automotive industry, even a small reduction in cycle time could have large implications for the overall productivity of the plant, assuming that the SPR process is on the critical path of the full production process. Here, the critical path refers to the sequence of processes which determines the overall productivity of a production line. If a particular process is on the critical path, any delays or breakdown in that process will delay the delivery of the final product. Likewise, a reduction in the time taken by that process would enhance the productivity of the line.

While a shortened cycle time for the SPR process may improve productivity, it can be associated with increased energy usage by the system. Energy expenditure and the associated costs play a significant role in the operation of any manufacturing facility. In a survey of nearly 50 UK manufacturers conducted by E.ON [114], it was noted that the cost of energy was the primary driver behind the energy policy of the large majority (78%) of the participating companies, with over 90% looking to bring down their energy consumption. This highlights the importance of assessing the energy demands of any proposed changes to an existing process.

The current case study aims to investigate how the cycle time or the energy consumption can be minimised by making changes to the system.

Two scenarios are considered:

1. Assuming the SPR system is on the critical path, minimise cycle time to increase productivity.
2. Assuming the SPR system is not on the critical path, minimise energy usage to reduce costs.

7.2 Scenario 1: minimise cycle time

7.2.1 Method

The model of the SPR system was used to estimate the potential reductions in cycle time achievable by changing the process factors: the stiffness of the C-frame, the stroke offset, the motor current limit and the setting velocity.

The stiffness of the C-frame exerts notable influence over the rivet insertion process, and while it is not a changeable process parameter over the life of a given system, understanding its influence on cycle time may aid the existing design process to better tailor a C-frame to the range of joints it is anticipated to make.

Stroke offset refers to the pre-defined distance between the end of the clamping mechanism and the workpiece, prior to the start of a riveting sequence. A smaller offset reduces the travel distance of the punch and therefore the cycle time on subsequent riveting cycles. Conversely, a larger offset facilitates access and transitions between joining locations. Its apparent influence on the cycle time made it a key parameter in the study.

The motor current limit controls the torque output of the motor during the rivet insertion phase and is therefore an important parameter in relation to the quality of the joint. The contribution of the applied torque in a predominantly inertia-based system is an understudied area.

Given the nature of the inertia-based process, the setting velocity is one of the most significant process parameters to the quality of the produced joint as well as cycle time.

The stroke offset, motor current limit and setting velocity were also parameters which were easily configurable on a real system without redesigning the system. This meant that the findings from the analysis could potentially be used to guide reconfigurations of existing systems as well as new ones.

Test cases were set up with joint A as the chosen joint configuration. Two levels of the motor current limit, three C-frame types corresponding to distinctive stiffness levels, and three levels for the stroke offset were defined, as shown in Table 7.1. The levels were selected according to the functional configurations of existing SPR systems. For the motor current limit, 50% represented a threshold level below which the ability of the system to maintain adequate velocity control up to the point of rivet insertion would be detrimentally affected. 100% was representative of the typical setting used in operation. The C-frame types 1, 2 and 3 represented the low, medium and high stiffness C-frames in existence, corresponding to effective stiffnesses of 13.7, 28.7 and 44 kN/mm respectively. The stroke offset values 20, 40 and 60 mm were typical of those used on automotive production lines. The motivation behind defining realistic values for each parameter was to investigate how a reconfiguration of existing systems may be used to reduce cycle time.

The underlying condition to be satisfied was that the resulting joint should arrive at the same final state across all the test cases. Hence, an optimisation problem was formulated to determine the setting velocity that would produce a flush head height. The setting velocity was chosen as the only design variable, on which a constraint was placed such that the maximum velocity was limited to 400 mm/s, corresponding to the operating limit on the real test system. The absolute value of the predicted head height would be minimised for each test case, in other words,

$$Objective:\ minimise\ |head\, height|$$

$$Constraint:\ 0 < setting\, velocity < 400\, mm/s$$

The optimisation algorithm is based on golden section search and parabolic interpolation [115].

Table 7.1 shows the list of test cases for which the setting velocity was optimised.

7.2.2 Results

The model-predicted results for the setting velocity and cycle time are illustrated in Figure 7.1. The total force required to produce a flush head height in joint A was 45 kN, this was the predicted peak force in all test cases.

The stroke offset has by far the largest influence on the cycle time. Reducing the stroke offset from 60 to 40 mm gives an average cycle time reduction of 12%. Likewise, changing the stroke offset from 40 to 20 mm yields an average of 14% reduction in cycle time. Since the time taken to traverse a distance at constant velocity is proportional to that distance, existing system configurations with large stroke offsets have potential for significant reductions in cycle time by shortening the stroke offset where practical.

For a given stroke offset, the cycle time appears to be closely related to the setting velocity: the larger the velocity, the shorter the cycle time. The appropriate setting velocity depends on the configuration of the system. A lower motor current limit requires an accord-

Table 7.1: Test cases for the case study.

Test case	Stroke offset (mm)	C-frame type	Motor current limit (%)
1	20	1	50
2	20	1	100
3	20	2	50
4	20	2	100
5	20	3	50
6	20	3	100
7	40	1	50
8	40	1	100
9	40	2	50
10	40	2	100
11	40	3	50
12	40	3	100
13	60	1	50
14	60	1	100
15	60	2	50
16	60	2	100
17	60	3	50
18	60	3	100

ingly higher setting velocity in order to produce a flush head height in the joint. Similarly, a more compliant C-frame requires an increase in the setting velocity, and vice versa.

With a view to reduce the cycle time, the problem is equivalent to maximising the setting velocity without compromising the head height of the resulting joint. This is attainable by selecting a C-frame of lower stiffness and reducing the motor current limit. Figure 7.1 shows that for a stroke offset of 20 mm, switching from C-frame 3 to 1 and changing the motor current limit from 100% to 50% would enable the setting velocity to be increased from 185 to 250 mm/s, resulting in a 10% reduction in cycle time. This could constitute a significant improvement in high-volume production scenarios.

7.3 Scenario 2: minimise energy consumption

7.3.1 Method

In this scenario, the primary concern was the energy usage of the system rather than the cycle time. Thus the problem was reframed to identify the configuration which yielded the lowest energy expenditure per cycle, without detriment to the resulting joint. Since the test cases from scenario 1 covered a broad range of system configurations, they were equally

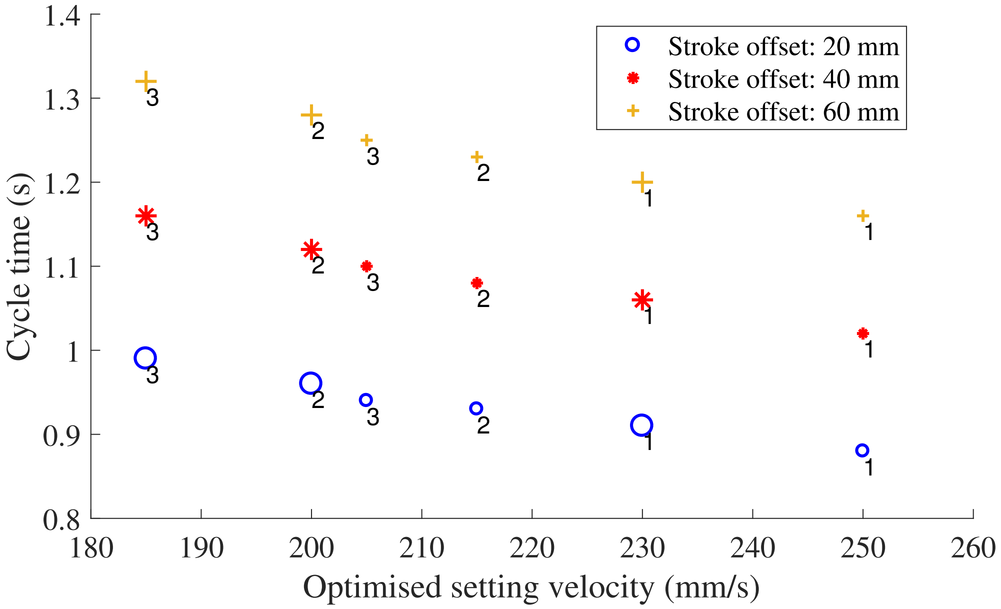

Figure 7.1: Predicted cycle time vs. setting velocity optimised to achieve a flush head height. Marker size represents the level of the motor current limit during rivet insertion, small: 50% limit, large: 100% limit. Marker labels denote the type of C-frame: 1, 2, and 3 correspond to C-frames with effective stiffness values of 13.7, 28.7 and 44 kN/mm respectively.

applicable for scenario 2, only the perspective of the analysis was adjusted to focus on energy consumption.

7.3.2 Results

The total electrical energy consumed by the modelled system over the course of a riveting cycle was computed from the time integral of the DC bus power. It was assumed that no energy was recovered from the braking phases of the motion sequence, in accordance with the configuration of the real system. The predicted energy consumption is presented in Figure 7.2.

The stroke offset is seen to have a substantial impact on the energy consumption of the system. Decreasing the stroke offset from 60 to 40 mm yields an average reduction of 8% in the energy usage, and from 40 to 20 mm the reduction is 9%. The results suggest that shortening the stroke offset is an effective way to reduce energy usage.

For a given stroke offset, the test cases which have the most contrasting energy consumption are those at either end of the velocity scale. A difference of 6% is noted between the energy usage at 185 and 250 mm/s. Although energy consumption appears to be positively correlated with setting velocity, the relationship is not monotonic, which could be an indication of interaction effects between the setting velocity, the motor current limit, and

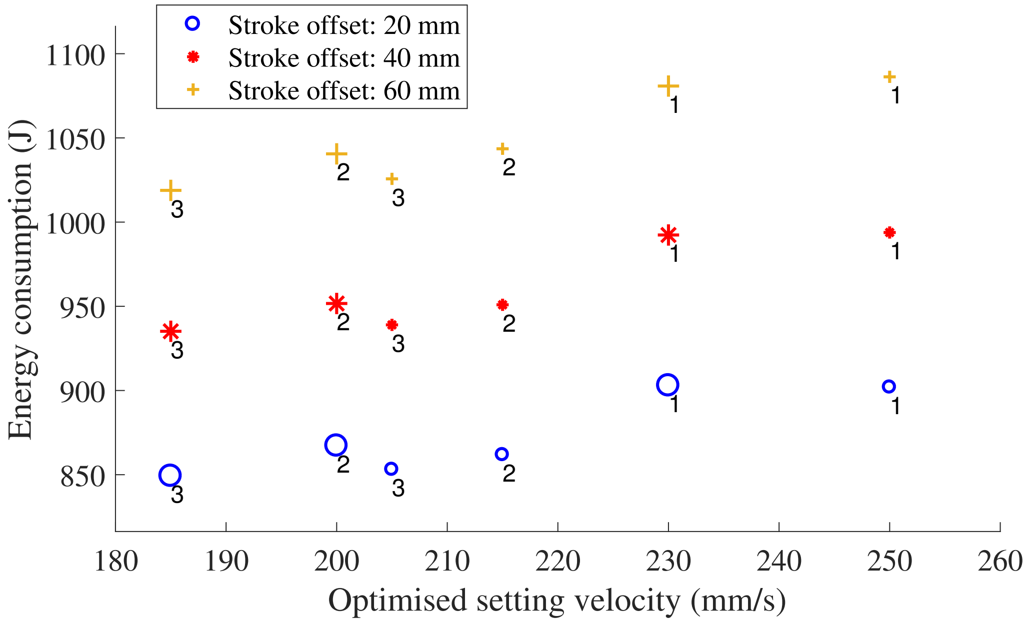

Figure 7.2: Predicted energy consumption vs. setting velocity optimised to achieve a flush head height. Marker size represents the level of the motor current limit during rivet insertion, small: 50% limit, large: 100% limit. Marker labels denote the type of C-frame: 1, 2, and 3 correspond to C-frames with effective stiffness values of 13.7, 28.7 and 44 kN/mm respectively.

the C-frame stiffness. These factors determine the work done by the motor torque and the recovery of energy due to springback of the C-frame, which influence the energy profile of a cycle.

A more detailed breakdown of the energy consumption is provided in Figure 7.3(a) and (b), corresponding to the simulated test cases at setting velocities of 185 and 250 mm/s respectively, for a fixed stroke offset of 20 mm.

E_{input} represents the total energy consumption of the system. The initial rising slope in E_{input} corresponds to the forward acceleration phase of the process, which is more prominent in Figure 7.3(b) than in Figure 7.3(a) due to the longer acceleration required to reach the higher setting velocity. In both cases, kinetic energy ($E_{kinetic}$) makes up a sizeable portion of the total input energy while the system is in motion. On rivet insertion, energy is dissipated in the plastic deformation of the joint, shown by the increase in E_{joint}. Strain energy (E_{strain}) is stored due to the elastic deformation of the components of the riveting system, which is subsequently recovered after rivet insertion. The energy dissipated due to friction ($E_{friction}$) is seen to be a major constituent of the total energy consumption, and larger frictional losses are incurred at a higher setting velocity.

$E_{w.regen}$ is the predicted energy consumption of an equivalent process which has regen-

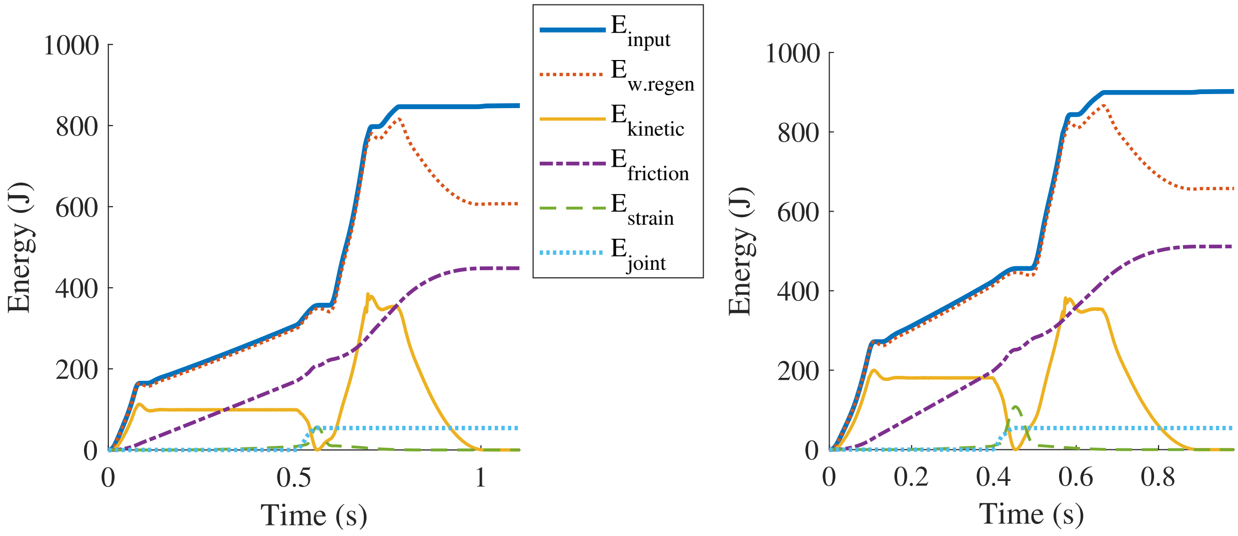

(a) (b)

Figure 7.3: Simulated energy vs. time, breakdown of components of the total energy consumption of the process. (a) Setting velocity: 185 mm/s. (b) Setting velocity: 250 mm/s

erative systems in place for energy recovery. During the controlled deceleration of the rivet setter, the motor acts as a generator and the kinetic energy of the system is converted into electrical energy. $E_{w.regen}$ is calculated on the assumption that this regenerated energy is stored in a supercapacitor bank such that the overall energy expenditure of the SPR system is reduced.

In the real system, the regenerated power is not stored but is instead dissipated as heat via a braking resistor. Therefore the difference between E_{input} and $E_{w.regen}$ gives an idea of the potential saving in energy if regenerative braking were implemented. Based on simulated results in Figure 7.3(a) and (b), the recoverable energy would be approximately 25% of the total energy consumption of a cycle without regenerative braking. This is a significant amount and is suggestive that the energy efficiency of the process can be notably improved with the integration of regenerative systems.

In the context of a large automotive plant, where the total number of SPR joints made may reach hundreds of millions per year, a reduction of 25% in the energy consumption of the SPR systems would have a non-trivial impact on the carbon footprint as well as the running costs of the facility. Although typically in high volume production, a shorter cycle time may be weighted more favourably than a lower energy consumption, a more energy-efficient approach may be preferred if the scheduling is such that the cycle time of the SPR system does not directly affect the wider manufacturing process.

7.4 Discussion

Via the case study, the model has been demonstrated as a capable tool for predicting the effects of making changes to the system, be it physical configurations or control settings, on the performance of the system. In industry, the head height and cycle time are two of the most important indicators of the performance of the process, hence the outputs of the model are intuitive to the end-users of SPR systems. The ability to predict the head height of the resulting joint could have substantial impact on the existing work processes within industry; the purpose of testing would be transformed from exploration to one of validation, and the number of experiments carried out would be considerably reduced.

7.4.1 Implications on joint quality

What is not apparent from the analysis so far is whether the robustness and performance of the joint, in terms of the static or fatigue strength, would be affected by the choice of process parameters, in particular at elevated setting velocities. While the predicted head heights suggest that distinctive process parameter sets may lead to the same resulting joint in terms of head height, the simulated response of the system at the machine-joint interface are markedly different, as illustrated in Figure 7.4. This suggests that the response of the system at the riveting interface depends strongly on the conditions associated with each process, which also implies that there may be differences in the actual joints that are unaccounted for by the current modelling approach.

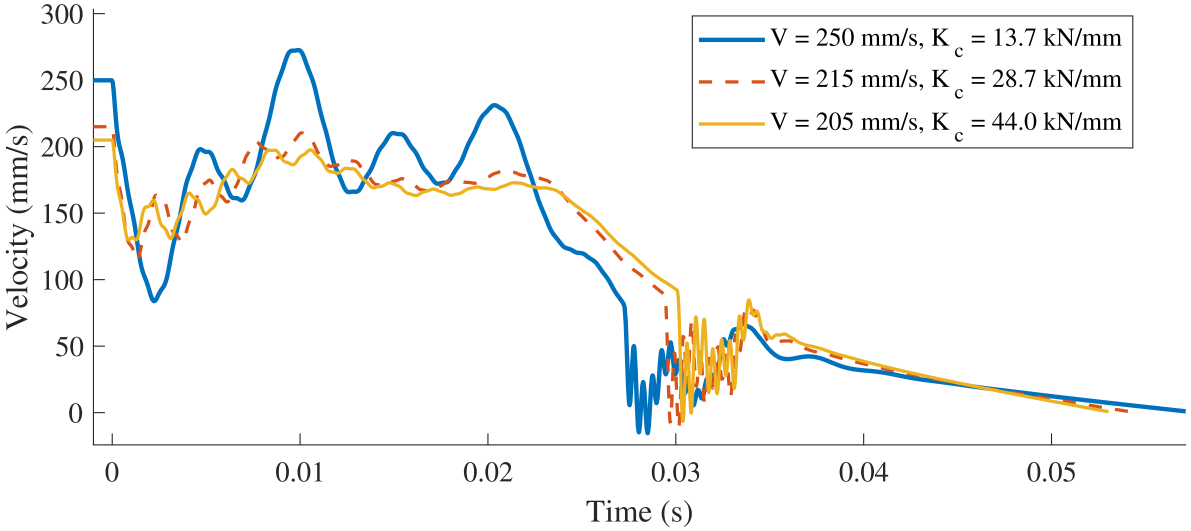

Figure 7.4: Simulated relative velocity vs. time during rivet insertion, effects of setting velocity V and C-frame stiffness K_c. Relative velocity is the velocity of the punch relative to the die, i.e. the velocity across the riveting interface.

In the case study, process parameters have been found with the intention of bringing the produced joints to a common final state in terms of the head height. The combination of simultaneously changing the setting velocity, motor current limit and the stiffness of the C-frame has not been addressed in published literature. There are, however, several studies which deal with the effects of setting velocity on the joint.

In an experimental study, Li et al. [15] noted a correlation between the head height and the T-peel strength of the SPR joint, and also between the interlock and the lap shear strength. Since the setting velocity was observed to have a large influence on both the head height and the interlock measurements, it was clear that the setting velocity had a substantial effect on the strength of the joint. In [23] Wang et al. investigated SPR joints made using a gunpowder-actuated system, which reached setting velocities of exceeding 5 m/s. The joints made were said to exhibit less variability and better lap-shear strength than those made with a hydraulic system. In their study of SPR with solid rivets as opposed to semi-tubular ones, Jäckel et al. [29] suggested that larger flow stresses would result from the higher strain rates at tool velocities of 5 to 10 m/s. The material may undergo both strain rate-dependent hardening and temperature-dependent softening during rivet insertion, which implied that there may be interactions between the two effects.

The published literature suggests that the setting velocity and therefore the strain rate can have significant effects on the form of the produced joint and its performance under load. Conversely, the range of strain rates in conventional inertia-based servo systems is much lower than those used in the referenced studies. Whether the typical range of strain rates seen on conventional SPR systems can have a substantial impact on the quality and the robustness of the process is an avenue to explore in future work.

7.4.2 Further implications

The implications of increased setting velocities on the life of the equipment is another area of interest. While the test cases in the current study were not predicted to generate larger process forces than the existing process, the increased setting velocities may affect the life of the belt drive, the roller screw mechanism, and other subsystems involved in the actuation of the punch.

In the simulations, in order to maintain the peak process forces at the same level, the stiffness of the C-frame was reduced in relation to the increase in the setting velocity. This is easily implemented in the model, but in practice, reducing the stiffness of a C-frame may involve targeted removal of material from the structure. The impact of such changes on the behaviour of the C-frame and also the quality of the produced joint may be worth considering in further work.

A related point is that alongside stiffness considerations, C-frames are designed with access in mind. The location of a joint on a given assembly largely determines the required height and depth of the throat of the C-frame, hence the geometry of the C-frame is not as freely configurable as the other process parameters. These dimensions also influence the mechanical properties of the C-frame; a C-frame with a large throat size may be more compliant than a smaller, more compact C-frame. Consequently, it may be argued that a C-frame corresponding to a given joint location can only take a certain form, and that this restricts its effective stiffness to within a specific range.

On the other hand, in view of these limitations the current work may serve as the impetus for a revolution in the design of the C-frame such that its effective stiffness can be modified to suit different objectives throughout its operational life. An adjustable-stiffness C-frame could allow the optimisation of the cycle time for a wide range of joints, or alternatively it could facilitate the reduction of energy consumption.

7.4.3 Assumptions

An assumption made in the study was that torque-current characteristic of the motor was linear. The true characteristic exhibits nonlinearity due to magnetic saturation. With the onset of saturation, more current would be required in order to generate the same level of torque, which means that more energy would be used. Although the assumption of linearity was an adequate approximation for the levels of motor current considered in the current work, changing the motor current limit to beyond the linear region may lead to unexpected results in terms of the predicted joint quality. Therefore, for future analyses which examine the performance of the system under more demanding motion profiles, a higher fidelity model of the torque-current relationship should be obtained.

7.5 Summary

Via a model-based case study, the work in this chapter has presented the potential benefits of making selected changes to the SPR system, either in terms of minimising cycle time or energy consumption.

For different settings of stroke offset distance, C-frame type and motor current limit, the appropriate setting velocity to achieve a flush head height was determined via optimisation. It was found that the cycle time could be minimised by minimising the stroke offset and effectively maximising the setting velocity. Choosing a C-frame of lower stiffness and reducing the motor current limit enabled the setting velocity to be increased to this end. Switching from C-frame 3 to 1, and reducing the motor current limit from 100% to 50% could potentially yield a 10% reduction in cycle time. While the impact of reducing the stroke offset on the cycle time reinforces existing understanding of the process, the minimisation of cycle time via tailored changes to a combination of factors constitutes a new contribution to knowledge. This has been possible only via a model-based analysis of the full SPR system.

Regarding the minimisation of energy consumption, results suggested that minimising the stroke offset, choosing a C-frame of high stiffness and increasing the motor current limit could enable a lower setting velocity to be used, which could minimise the energy consumption of the system without detrimentally affecting the quality of the produced joint. Further energy savings could be realised by incorporating regenerative systems into the process; simulated results suggest that as much as 25% reduction in the energy expenditure may by achievable.

The case study has considered the effects of changing selected factors which are either readily modifiable or customised as part of the design process for real systems. It may be thought of as a prelude to a more comprehensive sensitivity analysis which investigates how all the factors in the model affect the outcomes of the simulated process. The following chapter delves into this exact topic.

Chapter 8

Sensitivity Analysis

8.1 Introduction

Sensitivity and uncertainty analysis are techniques which provide an assessment of the influence of model inputs on the output, as well as how uncertainties are propagated through the model. In this chapter an introduction to the different types of sensitivity analysis is given, then the theory behind the analysis methods used in this study are described. Following that, the practical uses of sensitivity analysis methods are demonstrated via two examples:

1. Design exploration – to identify feasible changes to the system to improve the performance of the system
2. Uncertainty propagation – to understand how the uncertainties in the process inputs contribute to the variability of the produced joints

8.1.1 Literature review

Sensitivity analysis is a broad term which encompasses a host of different methods. The appropriate method to take depends on the goal of the analysis. One of the purposes of sensitivity analysis is to 'stress' the model to check its robustness when handling extreme or unusual input values.

In local sensitivity analysis the inputs to a model are varied around a nominal value. It is a one-at-a-time (OAT) method, in which the effect of a single parameter on the model output is evaluated with each analysis run. This method is derivative-based, i.e. the effect of a parameter is quantified via the partial derivative of the cost function with respect to the parameter. The approach of adjusting one parameter at a time is intuitive and the results are easy to interpret, which is what perhaps gives it a dominant presence in the body of published literature relating to sensitivity analysis [116]. However, the inadequacies of OAT methods are highlighted in [117], which lists the inability to identify interaction effects between parameters, insufficient exploration of the input space, etc. as evidence that a global approach to sensitivity analysis is necessary.

In contrast to local sensitivity analysis, global sensitivity analysis (GSA) examines the sensitivity over a larger domain by using inputs that are sampled across the full design space. This approach does not involve calculation of derivatives and is therefore suitable for complex models with nonlinearities. GSA can make use of either OAT or all-at-a-time strategies. The latter is where all inputs are simultaneously varied, which offers the advantage of better characterising the interactions between inputs, but at the expense of higher computational costs. Common types of GSA methods include correlation and regression analysis, the Morris screening method [118], the Sobol' method [119], etc.

Correlation and regression analysis methods derive measures of sensitivity from statistical analysis of the input and output samples. Coefficients such as the Pearson correlation coefficient and the partial correlation coefficient are useful for cases with a strong linear input-output relationship. In the case of nonlinear but monotonic relationships, the Spearman rank correlation coefficient or partial rank correlation coefficient are more suitable. On the other hand, such methods, can be unsuitable for highly nonlinear or non-monotonic input-output relationships [120].

The Morris screening method, also known as the Elementary Effects method, calculates sensitivities based on the perturbations in the output for multiple combinations of input levels. From one set of input values to the next, only the value of a single factor is changed, hence each individual perturbation in the output reflects a local sensitivity. However, the mean of the perturbations constitutes a measure of global sensitivity. The Morris screening method can be used to identify input factors which have negligible effects, linear effects, as well as nonlinear or interaction effects [121]. The Morris screening method will be examined in detail in Section 8.2.1.

The Sobol' method is a variance-based method. A variance-based sensitivity analysis quantifies how uncertainties in the inputs of a model affect its outputs. Via this approach, the input parameters are considered to be stochastic and each associated with a probability distribution. This distribution, when passed through the model, gives an output distribution, the variance of which is assumed to be representative of the output uncertainty. Variance-based methods are commonly realised using Monte Carlo simulations.

The effects of parameters on the model output are quantified using sensitivity measures or indices. Also referred to as Sobol' indices [119, 122], variance-based indices consist of the main effect index and the total effect index . The main effect index is the variance of the main effect for a given parameter, and is indicative of the potential reduction in the uncertainty of the model output if the true value of the parameter is known. The total effect index is the variance due to a particular parameter and its interactions, and represents the variance that would remain if the true values of all other parameters are known. The underlying idea is that gaining knowledge of an input parameter's true value would reduce the overall variance of the output, since that parameter's contribution to the output variance would become zero. For each input parameter, its percentage contribution to the output variance can be determined which then allows the parameters to be ranked in order of importance. Further details on variance-based methods will be provided in Section 8.2.2.

In addition to the aforementioned methods, an alternative is metamodelling, where a surrogate model is created which is computationally cheap yet captures the relationship between the inputs and the outputs of the original high-fidelity model. The surrogate model may also be referred to as a metamodel or emulator. The emulator can be computationally cheaper to run than the model, and can be used to derive the main effects, interaction effects, and the contribution of each input towards the output variance. GEM-SA [123] is a software tool which builds an emulator of a model. The Bayesian approach used in the software is said to be more efficient than conventional Monte-Carlo methods, in the sense that much fewer sample points are needed to build the emulator.

Studies which have examined the sensitivities of the SPR process are few in number.

In [28], Mucha used FE simulations to evaluate the impact of changing the geometry of the die on the appearance of the produced joint. Five different die designs were included in the study, where the differences between one die and the next appeared to be restricted to a single feature. The approach taken was essentially a OAT method where one factor was varied at a time, which meant that conclusions could only be made about the effects of changing individual features, rather than interaction effects between the features as well.

The work by Jäckel et al. [26] assessed the effects of the die geometry on the resulting joint via DOE and numerical simulation. Five features of the die were investigated: die depth, diameter, angle, height of the pip and diameter of the pip. From the results the authors were able to quantitatively assess the importance of each parameter on the interlock of the joint as well as the other measures, such as the risk of damage (i.e. cracking) in the material. A second sensitivity analysis was also performed to study the influence of the properties of the material on the joint.

Other works of relevance are experimental rather than numerical. Fu and Mallick [25] performed an experimental investigation of the effects of six process parameters on the static and fatigue strength of SPR joints. The parameters were: sheet thickness, rivet diameter, rivet length, rivet hardness, rivet coating and the pip height of the die. The relative contributions of each parameter to the static and fatigue strength of the joint were obtained via analysis of variance.

In the experimental study by Ma et al. [16], four factors were assessed with respect to their effects on the rivetability and strength of SPR joints: rivet hardness, rivet length, die width and the pip height of the die. The experiment design indicated a OAT approach.

Overall, it can be noted that GSA methods have not been rigorously applied to SPR systems. The studies that have used statistical methods to quantify the effects of parameters have focused solely on factors directly related to the rivet, material or die. The current work is therefore a new contribution to knowledge in considering the scope of the full riveting system.

In the examples from the wider literature on metal forming and joining processes such as [53, 51, 52, 55, 46], as previously mentioned in Section 3.2, the sensitivities of the processes of interest were explored using experiment designs involving a relatively small number of sample points. In contrast, GSA would offer a more comprehensive exploration of the parameter space. One of the underlying challenges of carrying out a variance-based sensitivity analysis is the computational cost of the problem. Performing many runs with high-fidelity models can become prohibitively expensive. This leads onto the topic of method selection for sensitivity analysis, which must take into account the complexity of the model as well as the aims of the investigation.

8.1.2 Method selection

Regarding the SPR system, the key questions to be answered were:

1. How might the design of the system be improved or optimised? Which parameters have the largest impact on the performance of the system?
2. For a given joining operation, what is the largest source of variation on the performance of the system? Which parameters, with their associated uncertainties, is the output of the system most sensitive to?

The first question was an exercise in design exploration and optimisation, to which the GSA approach was well-suited. While the second question related to uncertainty analysis.

GSA methods can be put into three main categories: screening, regression and variance-based methods. Screening methods are commonly accepted as qualitative, while variance-based methods are quantitative, meaning they provide a sensitivity index which can be interpreted in terms of the variance decomposition, i.e. how much of the variance in the output is due to a particular factor. Variance-based methods are particularly relevant for the assessment of how uncertainty in model parameters can affect the output of the SPR model. Provided that the model is a high-fidelity representation of the real system, the results would give insight into how variations in the system may affect the produced joint. Variability of the SPR process arising from manufacturing tolerances or fluctuations in environmental conditions have not been studied in the published literature, yet are known to influence the performance of the systems within industry.

In the published literature, a variety of problems have been tackled using different GSA methods, where the selection of the most appropriate method depended on the complexity of the model and the goals of the analysis. For models with a small number of parameters or a low running time, variance-based methods were directly implemented [51, 124]. For models with a large number of parameters or high computational cost, the approach was to first simplify the problem by either creating a metamodel or by screening out insignificant parameters, and then perform a variance-based analysis [125, 126, 127, 128, 129].

Regarding metamodelling, there are uncertainties associated with the evaluations made using the metamodel at points away from those used in building the metamodel. Iooss et al. [121] highlighted concerns relating to metamodel-related methods, such as the dependency of the quality of the metamodel on the experimental design, as well as the validation of the metamodel. While the metamodel may come close to the predictive performance of the high-fidelity model, some error is inevitable, which may influence the interpretation of the results of the sensitivity analysis. For these reasons, the metamodelling approach was not taken forward in this study.

To facilitate the selection of analysis methods, several useful aids exist in the form of diagrams, decision tables and classification charts thanks to various authors, some examples of which are found in [130], [121] and [131].

In the present study, the simulation time per run of the SPR system model was less than a minute, and the number of parameters in the model was between 20 and 100. Based on the aforementioned decision aids the Morris screening method was an appropriate first choice. Following screening, a variance-based method was suitable in the second stage of the analysis.

A screening analysis followed by a variance-based method is a robust approach to addressing complex models with large numbers of parameters. The screening stage identifies parameters whose contribution to the output of interest is negligible, such that they may be excluded from further analyses. This allows a more targeted analysis to be carried out using variance-based methods, which provides further insights into the relative contributions of each parameter. This is the recommended approach in [130] and [132]. Furthermore, even in the event that the variance-based results do not fully converge on the true sensitivities, conclusions can still be made about the relative importance of the parameters based on the outcomes of the screening analysis. Various works have shown that the Morris screening method offers a suitable qualitative approximation of the sensitivities obtained via the more comprehensive variance-based method [133, 134, 135].

8.2 Theory

8.2.1 Elementary Effects method

The Elementary Effects (EE) method is also known as the Morris screening method. It is a computationally efficient way of identifying the input factors to the model that have negligible, linear, and nonlinear or interaction effects on the model output [121].

The basis of the method is the elementary effect, which is an approximation of the local sensitivity of a parameter. Consider a model with a total of k independent input factors X (denoted X_i, $i = 1, \dots k$), and output Y. The elementary effect of the ith input parameter is calculated via:

$$EE_i = \frac{Y(X_1, X_2, ...X_i + \Delta_i, ...X_k) - Y(X_1, X_2, ...X_i, ...X_k)}{\Delta_0} \tag{8.1}$$

Where Δ_i is the change in the value of the ith input factor. For a parameter with a uniform distribution, Δ_i is defined as:

$$\Delta_i = \Delta_0(\mathit{Upper\,bound} - \mathit{Lower\,bound}) \tag{8.2}$$

Δ_0 is a value in the range [0, 1]. Saltelli et al. [132] recommends a value of $\Delta_0 = l/(2(l-1))$, where l is an integer number of levels chosen by the analyst, into which the input space of all parameters is to be discretised.

Note that in Equation 8.1 the numerator indicates how much the model output changes due to a specified change in the ith input factor, and in dividing the numerator by Δ_0 the calculated EE_i becomes a measure of the actual change in the model output per percentage change in the ith input factor. The larger the magnitude of EE_i, the more influential the ith input factor is said to be.

EE_i is essentially a local derivative approximation. A more global measure of sensitivity can be obtained by averaging over multiple local derivative approximations. The sequence of steps is as follows:

1. The parameters of interest are assigned a range and distribution. Assuming all parameters to be scalar, they may be considered as components of vector X. Let k be the total number of parameters.

2. An increment Δ_0 is chosen according to the specified number of discretisation levels l.

3. Each parameter is sampled randomly over the discretised levels. The samples constitute a vector of base values: x^*.

4. One or more components of x^* is incremented by Δ_i. The resulting vector is $x^{(1)}$, the first sample at which the model will be evaluated at.

5. The second sample is generated by incrementing or reducing one randomly selected component in $x^{(1)}$, i.e. $x^{(2)} = x^{(1)} + e_i\Delta_i$ or $x^{(1)} - e_i\Delta_i$, where e_i is a vector of zeros of the same dimensions as $x^{(1)}$ but with a value of 1 in the ith element, where i is randomly selected. Regarding the increment or reduction of the ith component, only the operation which gives a value within the pre-defined range for each parameter is permitted.

6. The third sample is generated by incrementing or reducing one randomly selected component in $x^{(2)}$, but this selected component must not have been selected before.

7. Further samples are selected in a similar fashion until $x^{(k+1)}$ is obtained. Within the set of $k+1$ samples, the value of each parameter should have been changed once. For a two or three-parameter problem, the samples can be plotted and connected with a straight line between each point. The resulting profile is referred to as a trajectory, and is a way of visualising the coverage of the input space. The same idea also applies for problems with more than three parameters.

8. The steps from 3 to 7 are repeated r number of times, producing r different trajectories. More trajectories generally lead to better coverage of the input space. The total number of samples is therefore $r(k+1)$.

9. The model is evaluated for all the generated samples, which may be thought of as being in groups corresponding to the trajectory to which they belong. Assume a scalar output is obtained per model evaluation.

10. On the jth trajectory, the ith component of all the samples corresponds to an input parameter. The elementary effect associated with that parameter is determined from

the model outputs at the two consecutive samples where the value of the ith parameter is changed. In mathematical form, this is expressed as:

$$EE_i^j(x^{(l)}) = \frac{Y(x^{(l+1)}) - Y(x^{(l)})}{\Delta_0} \tag{8.3}$$

Where l is in the set $\{1, \ldots k\}$, and assuming that $x^{(1)}$ is incremented to $x^{(l+1)}$. If instead a decrement was implemented, the calculation for the elementary effect is:

$$EE_i^j(x^{(l)}) = \frac{Y(x^{(l+1)}) - Y(x^{(l)})}{-\Delta_0} \tag{8.4}$$

11. Step 10 is repeated for all r trajectories, resulting in r elementary effects for each parameter.

12. Three sensitivity measures for each parameter are calculated using:

$$\mu_i = \frac{1}{r} \sum_{j=1}^{r} EE_i^j \tag{8.5}$$

$$\mu_i^* = \sum_{j=1}^{r} \left| EE_i^j \right| \tag{8.6}$$

$$\sigma_i^2 = \frac{1}{r-1} \sum_{j=1}^{r} (EE_i^j - \mu_i)^2 \tag{8.7}$$

Each trajectory generated in the input parameter space yields one elementary effect per parameter, hence each trajectory can be considered as sampling once from k distributions which encode the sensitivity behaviour associated with each of the k input parameters. Generating r trajectories is equivalent to randomly sampling r times, thus giving r elementary effects for each parameter. The mean and variance of the elementary effects quantify the sensitivity behaviour for the associated parameter.

The sample size depends strongly on the chosen method of sensitivity analysis and sampling technique. For the EE method, the number of samples are in the order of 10 times the number of inputs [132].

While it appears to be an extended version of the local derivative-based approach or OAT sampling, the trajectory design is able to overcome the limitations of OAT designs by exploring the entirety of the input space. In the event that a particular trajectory leads to unstable behaviour of the model, a sample point rather than the full design can simply be changed to one that the model handles better. Since each trajectory is independent to one another, trajectories may be replaced without invalidating the analysis.

In the current study, the trajectory design is initially chosen for ease of implementation and post-processing. The exact method used is as described in [134].

The software SimLab version 2.2.1 was used to set up and perform the sensitivity analysis. For more details on the software, readers are referred to [135].

8.2.1.1 Interpretation of the sensitivity measures

Two sensitivity measures are of particular interest:

- μ^*, the mean of the magnitude of the elementary effects. This represents the individual effect of an input parameter on the model output
- σ, the standard deviation of the elementary effects. This represents the combined effect of the input parameter due to nonlinear behaviour or interaction with other inputs, since a larger variance is suggestive of stronger dependence on the values of other parameters in the model

These provide a quantitative measure of the importance of a parameter relative to the others. Parameters with larger μ^* and σ are considered as having a larger effect on the output of the model, and vice versa. The parameters can therefore be ranked based on their relative influence on the model output.

In the published literature, a commonly made point is that the EE method is useful in identifying non-influential parameters, but no definite criteria is mentioned regarding what is considered influential or not. Qualitative assessment appears to be the dominant approach when it comes to selecting the parameters to be fixed in value on subsequent sensitivity analyses. In [135] it is mentioned that the EE method offers qualitative measures of sensitivity, rather than a quantitative evaluation of how much more important one factor is compared to another.

In the work by Morris [118], it is noted that whether a parameter is considered important or unimportant depends on the context of the problem, as well as the physical meaning behind the average change in the model output due to a change of Δ in the parameter of interest.

An example EE plot is shown in Figure 8.1, in which labels indicate the interpretation of μ^* and σ values depending on their location on the graph.

Consider a hypothetical case where two parameters A and B have similar values of σ, but μ^* for parameter B is twice as high as that of parameter A. It implies that a given percentage change in parameter B would incur twice the amount of change in the model output than the same percentage change in parameter A would. Parameter B can be said to be twice as important as parameter A.

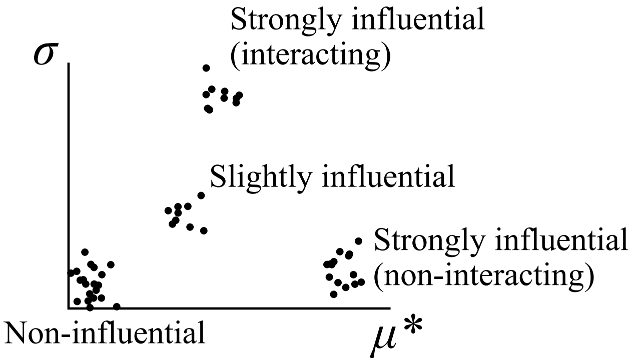

Figure 8.1: Illustration of the relative importance of parameters according to the location of their associated μ^* and σ values. Each point represents a parameter. Larger μ^* indicates stronger individual effects, while larger σ signifies stronger interaction effects, and vice versa.

It is clear that the computed sensitivity measures depend heavily on the distributions assigned to the parameters, since these determine the magnitude of Δ_i, or the sampling step by which the ith parameter is changed. Therefore, the designated distributions should be tailored to each unique problem to be addressed.

8.2.1.2 Limitations

While the sensitivity measures give an indication of the relative importance of the parameters, no further information is obtained about the interactions between them. The magnitude of the interactions are not quantified via the EE method. This prompts the use of another method, possibly variance-based, in order to identify the nature of the interactions and quantify their contribution to the output.

8.2.2 Variance-based method

Following on from the screening analysis, the subset of parameters identified as being unimportant are neglected in further analysis. The problem then becomes sufficiently simplified to be analysed via a more insightful, but computationally demanding approach: the variance-based method. This method sheds light on how variability in different parts of the system can affect the outcomes of the process.

Since the purpose of uncertainty analysis is to understand how much the variance in a given parameter contributes to the overall variance in the output, the parameters are defined with an updated set of distributions which represent the uncertainty in the system, due to manufacturing tolerances, variability in the dynamics of the system, or lack of knowledge.

By quantifying the uncertainty this way, the parameters with the largest contribution to the uncertainty of the output are identified. This can then be the basis of future assessments regarding the feasibility of reducing the uncertainty in the most influential parameters such that the most substantial reductions in the uncertainty of the process output can be minimised. This approach is also referred to as 'factor prioritisation' [135].

An interesting application of variance-based methods is to determine the minimum number of parameters that should be fixed in order to achieve a specified reduction in the variability of the output, i.e. 'variance cutting' [135]. Fully eliminating uncertainty in a real process is impossible, 'variance cutting' takes a more realistic approach of targeting a level of variability that is considered acceptable and identifying the least amount of change that would be required to achieve it.

Sobol' indices are sensitivity measures which provide the information of interest, and can be computed using Monte Carlo methods.

8.2.2.1 Sobol' indices

In [119], Sobol' proposed that the sensitivity of a function to an input factor could be characterised from the variances of the function evaluated over the distribution of the factor in question. The paper considered the case of grouping variables into two subsets, and determining the sensitivity of a function to those subsets. The idea of the sensitivity index was consolidated in [122]. It was noted that all first order indices were non-negative, and could be used to rank the input factors in order of importance provided that interaction effects did not dominate.

The method used in the current study is that described by Saltelli in [132]. Saltelli's method is an improved version of the Sobol' method, with the advantage of requiring much fewer model evaluations to obtain the sensitivity indices.

8.2.2.2 Main and interaction effects

Consider a given model where the model output y is a function of k independent random variables, in other words:

$$y = f(x_1, x_2, ...x_k) \tag{8.8}$$

The function f can be expanded into terms of increasing dimensions:

$$f = f_0 + \sum_i f_i + \sum_i \sum_{j>i} f_{ij} + ...f_{1,2,...k} \tag{8.9}$$

Where $f_i = f_i(x_i)$ and $f_{ij} = f_{ij}(x_i, x_j)$, which means that each term in the expanded equation is a function of its associated indices only, as denoted by the subscript.

Assuming that the mean of each term is zero, and all terms are orthogonal in pairs, the conditional expectation of the output can be determined. The first three terms are shown as follows:

$$f_0 = E(y) \tag{8.10}$$

$$f_i = E(y|x_i) - E(y) \tag{8.11}$$

$$f_{ij} = E(y|x_i, x_j) - f_i - f_j - E(y) \tag{8.12}$$

To compute $E(y|x_i)$, the x_i domain is divided into slices, and the average value of $(y|x_i)$ in each slice is obtained.

The variance of the conditional expectation, or $V[E(y|x_i)]$, represents the variance in the model output due to the uncertainty in x_i and is thus a measure of sensitivity. Subsequently dividing this variance by the total variance in the model output gives the proportion of the variance in the output that is attributable to the uncertainty in x_i. This is also known as the first order index or main effect index (MEI):

$$S_i = \frac{V[E(y|x_i)]}{V(y)} \tag{8.13}$$

The MEI describes the main effect of the associated parameter. It can be thought of as the expected reduction in the variance of the output if the ith input is fixed.

In addition to the main effects of individual parameters, the interaction effects between parameters are also of interest. The total variance in the output can be decomposed into the sum of main effects and interaction effects:

$$V(y) = \sum_i V_i + \sum_i \sum_{j>i} V_{ij} + ... + V_{1,2,...k} \tag{8.14}$$

where

$$V_i = V[f_i(x_i)] = V[E(y|x_i)] \tag{8.15}$$

$$V_{ij} = V[f_{ij}(x_i, x_j)] = V[E(y|x_i, y_i)] - V[E(y|x_i)] - V[E(y|x_j)] \tag{8.16}$$

V_i is the MEI as mentioned before. V_{ij} is the second order effect, which is the joint effect of both x_i and x_j without their individual main effects. The interaction effects can be thought of as the sum of all terms on the right-hand side of Equation 8.14 apart from V_i.

Equation 8.14 can be divided through by $V(y)$ to obtain:

$$1 = \sum_i S_i + \sum_i \sum_{j>i} S_{ij} + ... + S_{1,2,...k} \tag{8.17}$$

From Equation 8.17 it is seen that in the absence of interaction effects, the sum of all main effects would come to one.

The total effect index (TEI), or S_{Ti}, is defined as the contribution from the specified input factor and all its interactions with other factors.

$$S_{T_i} = \frac{E[V(y|x_{\sim i})]}{V(y)} = 1 - \frac{V[E(y|x_{\sim i})]}{V(y)} \tag{8.18}$$

The term $x_{\sim i}$ denotes all the input factors apart from the ith.

The difference between the TEI and the MEI for a given factor is a measure of how much that factor interacts with other factors. A factor which has a TEI of zero has no influence at all on the output, it is therefore a useful measure for factor fixing purposes. The sum of the TEIs for all input factors will generally exceed 1, unless no interaction effects are present, in which case the model is said to be 'additive'. For a perfectly additive model, the sum of all TEIs is exactly 1, as is the sum of all MEIs.

8.2.2.3 Computation

Details on the computation of the MEI and TEI are explained in [132], in which a Monte Carlo based procedure is used. The sequence of steps is summarised as follows:

1. Generate a matrix of random values of size (N,2k) and split this into two matrices A and B, each of size (N,k). N is referred to as the base sample, and k is the total number of input factors. Discussion on the choice of N is given in Section 8.2.3.

2. Create a matrix C_i, which is the same as B except the ith column is taken from the ith column of A.

3. Evaluate the model using A, B and C_i as inputs, such that three output vectors are obtained:

$$y_A = f(A) \tag{8.19}$$

$$y_B = f(B) \tag{8.20}$$

$$y_{C_i} = f(C_i) \tag{8.21}$$

4. The MEI for the ith factor X_i is estimated using:

$$S_i = \frac{V[E(Y|X_i)]}{V(Y)} = \frac{y_A \cdot y_{C_i} - f_0^2}{y_A \cdot y_A - f_0^2} = \frac{\frac{1}{N}\sum_{j=1}^{N} y_A^{(j)} y_C^{(j)} - f_0^2}{\frac{1}{N}\sum_{j=1}^{N} (y_A^{(j)})^2 - f_0^2} \tag{8.22}$$

   where

$$f_0^2 = (\frac{1}{N}\sum_{j=1}^{N} y_A^{(j)})^2 \tag{8.23}$$

5. The TEI for X_i is estimated from:

$$S_{T_i} = 1 - \frac{V[E(Y|X_{\sim i})]}{V(Y)} = 1 - \frac{y_B \cdot y_{C_i} - f_0^2}{y_A \cdot y_A - f_0^2} = 1 - \frac{\frac{1}{N}\sum_{j=1}^{N} y_B^{(j)} y_C^{(j)} - f_0^2}{\frac{1}{N}\sum_{j=1}^{N} (y_A^{(j)})^2 - f_0^2} \tag{8.24}$$

The computation of the MEI and TEI for all the k input factors to the model would require the model to be evaluated for matrix A, B and k different matrices for C_i. Hence, a total of $N + N + kN$ or $N(2 + k)$ model evaluations are required.

The dot product between y_A and y_{C_i} largely determines the value of the MEI. It is the multiplication of the model outputs computed from one matrix with that from another matrix in which all columns are resampled apart from the ith, i.e. all factors are resampled apart from X_i. Therefore the dot product represents the individual effect of X_i.

Consider the MEI equation: if factor X_i is influential, then the high values of y_A and y_{C_i} and also the low values would preferentially multiply, this would result in a larger value in the numerator and thus a higher MEI. If X_i is non-influential, then the high and low values of y_A and y_{C_i} would be randomly associated, which would lead to a smaller value in the numerator and therefore a lower MEI.

In the TEI equation, the dot product between y_B and y_{C_i} represents the main effect of all factors apart from X_i, so if the other factors are influential, it implies that X_i is less influential. In other words, preferential multiplication would lead to a larger value for the second term of the TEI equation, which in turn would result in a smaller value of TEI corresponding to X_i. If on the other hand the factors aside from X_i are non-influential, it would imply that X_i is more influential and thus a larger value of TEI would be produced.

8.2.3 Input parameter sampling

In order to sample the parameter space, the first step is to define a lower and upper limit for each parameter of interest and also its probability distribution. For uncertainty analysis it is crucial to be able to adequately represent the uncertainty in each parameter this way such that the uncertainty is propagated through the model.

When little is known about the distribution of a parameter, a conservative and common approach is to assign a uniform distribution [131]. From the perspective of design exploration and optimisation, the form of the distribution is not so critical, since the goal is to have sufficient coverage of the parameter space in order to explore a representative selection of scenarios. Therefore, a uniform distribution can be suitably assigned to each parameter.

For the purposes of uncertainty analysis, the propagation of small deviations in the process inputs to the output is of interest. In such a case, speculative ranges for the relevant parameters can be defined.

Regarding the selection of the input sample size, the general consensus in the published literature is that more samples are required for more input parameters. Low sensitivity factors typically converge faster than those of high sensitivity, and this needs to be accounted for in order to obtain stable sensitivity estimates across all input parameters.

The adequate choice of the base sample N is an open discussion. In [135] it is noted that N can be between a few hundred and one thousand. In [121] it is said that 10^4 model evaluations are necessary to estimate the sensitivity indices for a single input with an uncertainty of 10%. Pianosi et al. [131] place N at 1000 or above for variance-based methods, while emphasising that the number needed for convergence will likely vary according to the application.

Pianosi et al. [131] note that the convergence of the computed sensitivity indices in relation to the size of the sample should be checked. In the event of non-convergence, further simulations can be run and the results can be combined with the existing set to represent a larger sample. Methods such as subsampling and bootstrapping allow the assessment of convergence without having to run new simulations.

In the current study, $N = 5000$ was chosen as a starting point.

8.2.4 Choice of model outputs

The main outputs of interest are summarised as follows:

- Head height - Represents the final state of the workpiece at the end of the riveting process. It is one of the main measures of joint quality used in industry, and is easily obtained without destroying the joint.
- Kinetic energy of the system just before rivet insertion - Represents the main portion of the total energy input into the process. In inertia-based SPR, this may serve as a predictor for the success of the riveting process since a minimum threshold would need to be exceeded in order to produce an acceptable joint for a given setup.

Although much more data were generated per simulation run, the two outputs listed were considered as key indicators of the repeatability of the SPR process.

Following on, in order to address the two questions posed at the beginning of Section 8.1.2, two examples are presented to demonstrate the application of GSA methods in the design exploration of the SPR system, and subsequently the uncertainty analysis of the riveting process.

8.3 Example 1: design exploration

8.3.1 Problem definition

The aim was to explore how large changes to the design of the system can affect the SPR process. The sensitivity of the head height, the peak riveting force and that of the kinetic energy of the system were examined.

8.3.2 Method

All independent parameters in the model with a known direct or indirect influence on the produced joint were included in the analysis. For the purposes of design exploration, uniform distributions were assigned in order to sample the full design space indiscriminately. Lower and upper limits for each parameter were chosen based on the plausible design limits of the system, shown in Table 8.1. For example, the setting velocity (*veloSet*) is easily modified within the Bosch drive but has a practical maximum of 0.4 m/s due to the working limit of the PRSM. The insertion torque limit (*torqueLimRivet*) is another changeable setting (see Section 4.3), but is limited to an upper limit of 400% by the maximum current rating of the motor. The limits for the torque constant and other motor characteristics were based on the range of values specified for the IndraDyn S servomotor product line [136]. The limits for the stiffness of the C-frame were guided by the stiffnesses of the existing types of C-frames in production, estimated using FE analysis. For parameters such as the damping in the disc spring pack, little was known about the design limits, thus a wide range was assigned.

Table 8.1: Parameters and their assigned limits for design exploration purposes. The parameters and their roles in relation to the SPR process are defined in Chapter 4.

Parameter	Description	Units	Lower limit	Upper limit
veloSet	Setting velocity	(m/s)	0.05	0.4
torqueLimRivet	Insertion torque limit	(%)	0	400
Ra	Stator resistance	(Ω)	0.06	7.2

Table 8.1: Parameters and their assigned limits for design exploration purposes. The parameters and their roles in relation to the SPR process are defined in Chapter 4.

Parameter	Description	Units	Lower limit	Upper limit
Ld	Direct-axis inductance of motor	(H)	5.4×10^{-4}	0.0382
Lq	Quadrature-axis inductance of motor	(H)	5.4×10^{-4}	0.0382
Kt	Torque constant	(Nm/A)	0.29	3.94
Ke	EMF constant	$(V\,s/rad)$	0.171	2.31
Jm	Rotor inertia	$(kg\,m^2)$	10^{-5}	0.0138
$Rpulley1$	Motor pulley pitch circle radius	(m)	0.00357	0.05
$Rpulley2$	Actuator pulley pitch circle radius	(m)	0.00357	0.05
$Jpulley1$	Motor pulley inertia	$(kg\,m^2)$	2.94×10^{-6}	5.77×10^{-4}
$Kbelt$	Belt stiffness	(N/m)	10^5	3.4×10^6
$Cbelt$	Belt damping	$(N\,s/m)$	1	2×10^4
$Jsetter$	Flywheel and actuator inertia	$(kg\,m^2)$	7.06×10^{-4}	0.00859
Ph	PRSM lead	(m)	0.0024	0.006
d	Nominal diameter of screw shaft	(m)	0.018	0.048
mpc	Coupler mass	(kg)	0.1	0.4
$mplpu$	Plunger and punch mass	(kg)	0.215	0.86
$Kplpu$	Plunger-punch effective stiffness	(N/m)	2.51×10^7	10^8
mn	Nose mass	(kg)	0.9	3.6
$K1$	Stripper spring stiffness	(N/m)	1000	10^4
$K2$	Disc spring pack stiffness	(N/m)	10^4	4×10^6
$C2$	Disc spring pack damping	$(N\,s/m)$	1	2×10^4

Table 8.1: Parameters and their assigned limits for design exploration purposes. The parameters and their roles in relation to the SPR process are defined in Chapter 4.

Parameter	Description	Units	Lower limit	Upper limit
$preload$	Disc spring pack preload	(N)	500	2×10^4
$C3$	Coupler-hard stop contact damping	$(N\,s/m)$	1	2×10^4
mc	C-frame effective mass	(kg)	1	100
Kc	C-frame effective stiffness	(N/m)	8×10^7	4.4×10^8
Cc	C-frame effective damping	$(N\,s/m)$	1	2×10^4
$Z2$	Max distance between punch and flush-with-nose position	(m)	0.03	0.1
Zs	Maximum Spring Deflection	(m)	0.001	0.05

Using SimLab 2.2.1, sample generation for the Morris method was performed with the number of executions set to 320 and number of levels set to 8. In reference to Section 8.2.1, this was equivalent to $k = 31$, $r = 10$, and $l = 8$.

8.3.3 Results

8.3.3.1 Head height

For any given parameter the magnitude of μ^* represented the effect on the head height as the parameter in question was varied over the entire range of its plausible values. Considering the typical tolerances on head heights used in industry [10], a difference of 0.4 mm from the nominal flush head height was generally acceptable, hence parameters with a value of μ^* less than 0.4 mm may be considered unimportant. Likewise, a σ value less than 0.4 mm implied that interaction effects associated with a parameter were insignificant, and vice versa.

The computed sensitivity measures are shown in Figure 8.2(a). With μ^* in excess of 0.4 the following factors are clearly more important than the rest in terms of their influence on the head height of the joint:

- Radius of driven pulley ($Rpulley2$)
- Radius of driving pulley ($Rpulley1$)
- Setting velocity ($veloSet$)
- Back-EMF constant of the motor (Ke)
- Lead of roller screw (Ph)
- Torque level corresponding to the control signal for the motor current ($torqueLimRivet$)
- Torque constant of the motor (Kt)
- Inertia of the rivet setter ($Jsetter$)

It can be noted that the majority of the factors identified as being important are also related to the transmission ratios within the system. This is unsurprising given that the gearing directly influences the rivet setting velocity, and the effective stiffness of the system seen from the joint. These determine the kinetic energy delivered to the process and therefore exert strong influences over the head height of the joint.

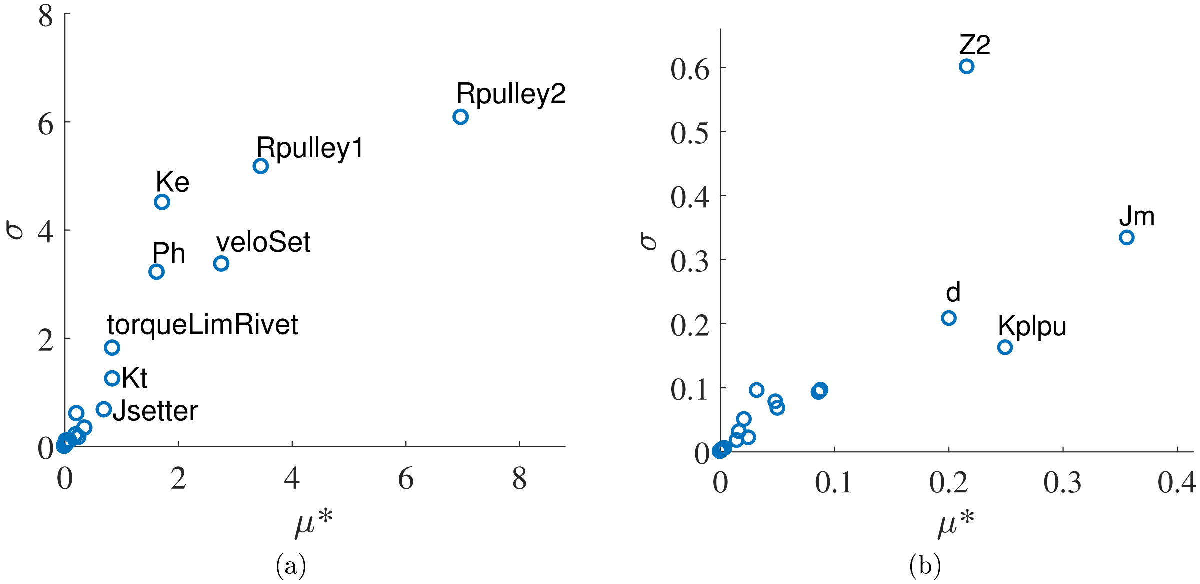

(a) (b)

Figure 8.2: Sensitivity measures obtained via the EE method, for the model output: head height. (a) Full view. (b) Zoomed in view.

In reference to the group of parameters clustered near the origin, a zoomed-in view is presented in Figure 8.2(b). Based the values for σ, $Z2$ or the maximum distance between the punch and the end of the clamp tube appears to be important in terms of nonlinear or interaction effects with other parameters. This particular parameter relates to the geometry of the clamping mechanism and affects the timing as well as the magnitude of the clamping force.

An alternative way to visualise the elementary effects is to rank them by μ or σ, as shown in Figures 8.3(a) and (b) respectively. Comparison of the two figures indicates that by and large, for the top 8 parameters, those with larger individual effects also have larger nonlinear or interaction effects. This suggests that none of the most important factors have a purely linear effect. The results show that while the parameters which directly influence the kinetic energy of the system are the most influential on the head height of the joint, the motor characteristics and the clamping also play an important role.

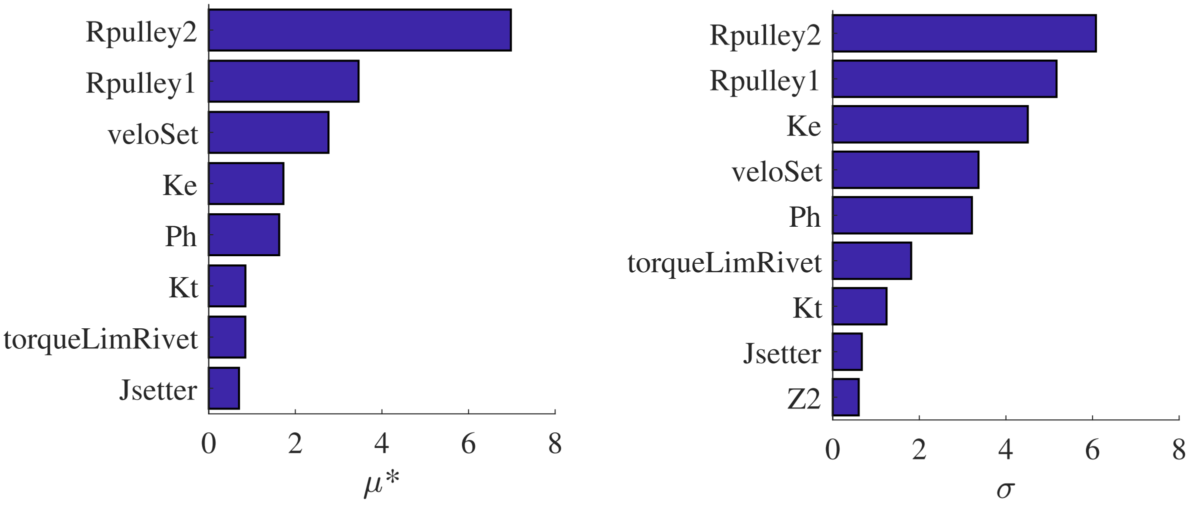

(a) (b)

Figure 8.3: Parameter ranking according to their importance to the head height, based on the EE sensitivity measures: (a) Individual effects (b) Nonlinear or interaction effects.

8.3.3.2 Kinetic energy

In Figure 8.4 the EE sensitivity measures are computed using the kinetic energy prior to rivet insertion as the model output.

Unlike head height, a threshold for the value of μ^* or σ for which a parameter is considered important does not exist. The impact of changes to the kinetic energy on the quality of the joint depends on a host of factors such as the compliances and losses within the riveting system. However, for the purposes of design exploration, it can be argued that since the energy dissipated in a joint is in the region of 50 J (see Appendix B.3), an increase or reduction of 50 J in the kinetic energy would be significant. In other words, parameters with μ^* or σ exceeding 50 are considered as important.

The most important factors to the kinetic energy are unsurprisingly those associated with the power transmission in the system. Pulley radii determine the transmission ratio which affect the kinetic energy in the system. The back-EMF constant of the motor governs the velocity the motor is able to reach, and the torque constant directly influences the acceleration as well as the velocity of the inertias.

The similarity of the results to those in Figure 8.2(a) confirm that the SPR process is predominantly kinetic energy-based. Such is the design of the system that the most influential factors to the joint are kinetic energy-related, even when considering the full scope of the plausible design space. An important parameter that features in Figure 8.2(a) but not Figure 8.4 is the motor current limit during rivet insertion (*torqueLimRivet*), which generally comes into effect during the process after the target setting velocity is reached and thus does not influence the velocity of the system prior to rivet insertion.

Figure 8.5(a) and (b) show the ranking of the parameters based on μ^* and σ respectively. It is noted that parameters with strong main effects also tend to have significant interaction effects, i.e. none of the important factors have a purely linear effect.

8.4 Example 2: uncertainty propagation

8.4.1 Problem definition

In contrast to design exploration, uncertainty analysis sought to answer a very different set of questions to those in design exploration. The aim was to understand how variations in the components of the system resulting from manufacturing tolerances or environmental factors could affect the quality of the process outputs, namely the head height of the joint.

8.4.2 Method

The analysis was composed of two parts:

1. Screening – to determine the most important parameters that contribute to the variability in the model output

2. Uncertainty analysis – to determine the contribution of the variability in each of the important parameters towards the variance in the model output

The first part would guide the reduction of the list of parameters to only the most important ones, in order to minimise the computational effort of the second part.

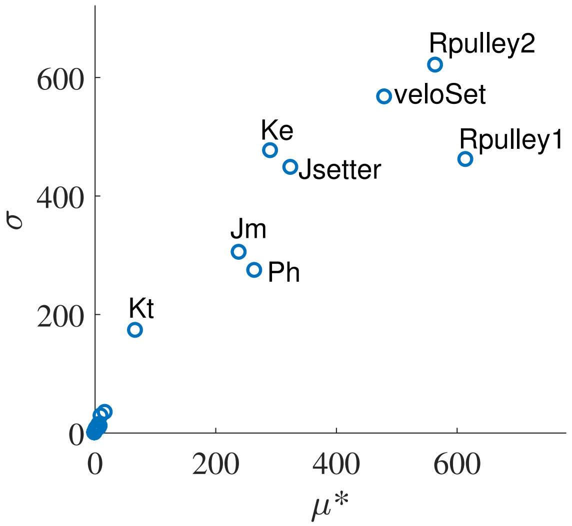

Figure 8.4: Sensitivity measures obtained via the EE method, for the model output: kinetic energy prior to rivet insertion.

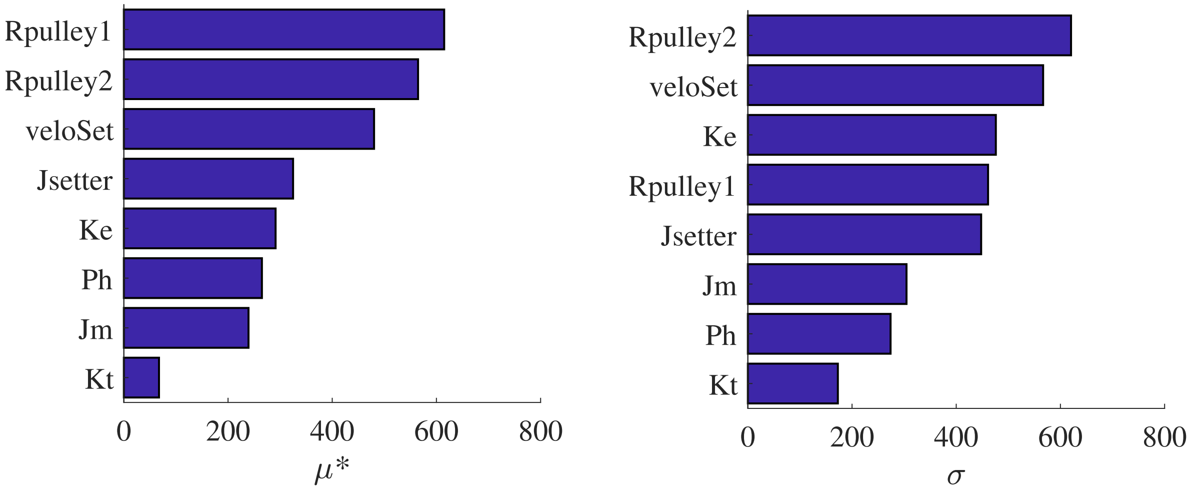

(a) (b)

Figure 8.5: Parameter ranking according to their importance to the kinetic energy prior to rivet insertion, based on the EE sensitivity measures: (a) Individual effects (b) Nonlinear or interaction effects.

Any parameter that could potentially affect head height were evaluated in the screening analysis, including those not-changeable by design. On a real joining process, the setting velocity and insertion torque are user-specified inputs. These are therefore excluded from the list of parameters evaluated.

Parameter sampling was more concerned with the coverage of the parameter space than the shape of the distribution of the samples. Therefore, all parameters were sampled from uniform distributions.

Table 8.2 shows the initial list of parameters as well as their lower and upper bounds used in the screening part of the analysis. The limits were defined based on the manufacturing tolerances where known, and best estimates of uncertainties otherwise.

Table 8.2: Parameters and their assigned limits for uncertainty analysis. The parameters and their roles in relation to the SPR process are defined in Chapter 4.

Parameter	Description	Units	Lower limit	Upper limit
Ra	Stator resistance	(Ω)	3.04	3.36
Ld	Direct-axis inductance of motor	(H)	0.00903	0.00998
Lq	Quadrature-axis inductance of motor	(H)	0.0102	0.0112
Kt	Torque constant	(Nm/A)	1.1	1.22
Ke	EMF constant	$(V\,s/rad)$	0.649	0.717
Jm	Rotor inertia	$(kg\,m^2)$	3.31×10^{-4}	3.47×10^{-4}
$Rpulley1$	Motor pulley pitch circle radius	(m)	0.0318	0.0319
$Rpulley2$	Actuator pulley pitch circle radius	(m)	0.0318	0.0319
$Kbelt$	Belt stiffness	(N/m)	2.6×10^5	2.8×10^5
$Jsetter$	Flywheel and actuator inertia	$(kg\,m^2)$	0.00309	0.00311
Ph	PRSM lead	(m)	0.00498	0.00502
$muprac$	Practical coefficient of friction		0.0184	0.00893
$coulomb$	PRSM Coulomb friction torque	(Nm)	0.72	0.88

Table 8.2: Parameters and their assigned limits for uncertainty analysis. The parameters and their roles in relation to the SPR process are defined in Chapter 4.

Parameter	Description	Units	Lower limit	Upper limit
$viscous$	PRSM viscous friction torque	$(Nm\,s/rad)$	0.00288	0.00352
Kr	PRSM effective stiffness	(N/m)	9×10^7	1.1×10^8
$Kplpu$	Plunger-punch effective stiffness	(N/m)	4.2×10^7	5.13×10^7
$K1$	Stripper spring stiffness	(N/m)	3600	4400
$K2$	Disc spring pack stiffness	(N/m)	1.8×10^6	2.2×10^6
$C2$	Disc spring pack damping	$(N\,s/m)$	6300	7700
$preload$	Disc spring pack preload	(N)	7000	8000
$Fc2$	Disc spring pack Coulomb friction	(N)	270	330
$K3$	Coupler-hard stop contact stiffness	(N/m)	9×10^7	1.1×10^8
$rivLength$	Rivet length	(m)	0.0054	0.0056
$matThickness$	Material stack thickness	(m)	0.00291	0.00309
$Kmat$	Material stack stiffness under compression	(N/m)	1.13×10^8	1.38×10^8
mc	C-frame effective mass	(kg)	7.74	9.46
Kc	C-frame effective stiffness	(N/m)	1.3×10^7	1.43×10^7
Cc	C-frame effective damping	$(N\,s/m)$	1350	1650

Table 8.2: Parameters and their assigned limits for uncertainty analysis. The parameters and their roles in relation to the SPR process are defined in Chapter 4.

Parameter	Description	Units	Lower limit	Upper limit
$Z2$	Max distance between punch and flush-with-nose position	(m)	0.0711	0.0712
Zs	Maximum Spring Deflection	(m)	0.00124	0.00186

For the uncertainty analysis part, parameter distributions were of importance since these would affect the calculated sensitivity indices. Given that little was known about the uncertainty in the parameters beyond their lower and upper limits, a uniform distribution was assigned to each parameter.

The SAFE toolbox [137] was used to implement the key steps of the variance-based sensitivity analysis, including sample generation, estimation of the sensitivity indices, and convergence checks.

8.4.3 Screening results

8.4.3.1 Head height

Figure 8.6(a) shows the sensitivity measures computed from the EE method. In terms of individual effects, the most important parameters according to μ^* are: rivet length, maximum available spring compression in the clamping mechanism, and Coulomb friction in the PRSM. In Figure 8.6(b), the 95% bootstrap confidence bounds are computed according to Appendix D and plotted in the form of boxes around the circular markers of their associated factors. The left and right edges of a box represent the lower and upper bounds of μ^* respectively. The top and bottom edges of a box represent the upper and lower bounds of σ respectively. In other words, the boxed area is indicative of the uncertainty in the estimated EE sensitivity measures. It is noted that despite some overlap between the confidence bounds of certain parameters, there is little doubt over the three most important parameters as ranked by μ^*.

The variability of the rivet length is defined according to the dimensional tolerance. The physical length of the rivet would logically affect its length in the deformed state, a slightly longer rivet would lead to a more protruded head height than a shorter one if both were inserted into the same material with the same amount of energy. Since the results indicate that it is the single largest contributor to the variability in the head height, it implies that

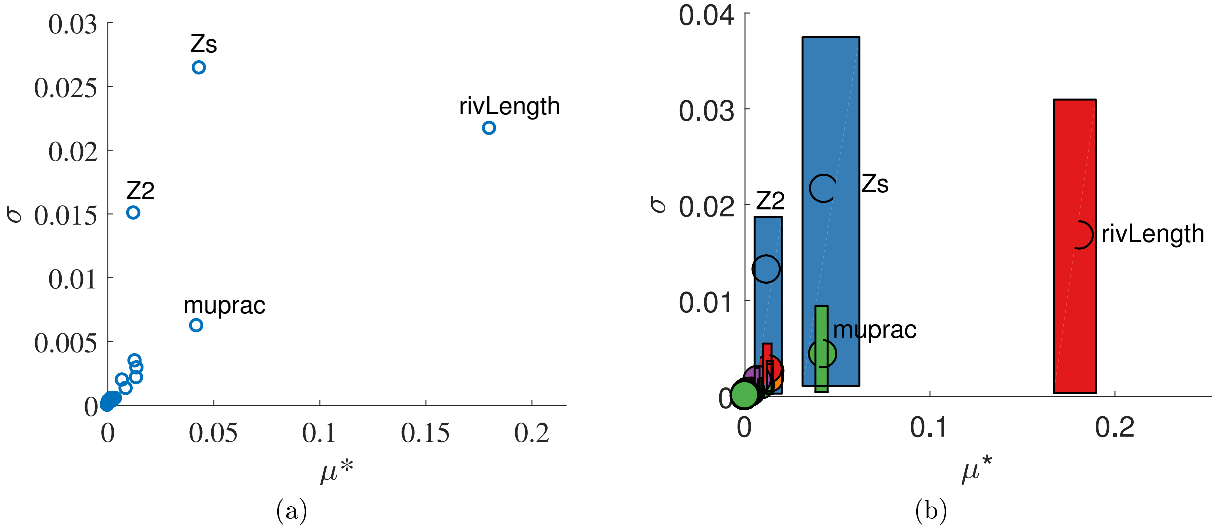

(a) (b)

Figure 8.6: EE sensitivity measures for the head height. (a) Standard view. (b) With confidence bounds shown as boxes.

the repeatability of the SPR process can be improved by narrowing the tolerance on the rivet length.

An alternative interpretation is that no changes to the process are necessary, given that the magnitude of μ^* for the most important parameter is no larger than 0.2 mm, and a 0.2 mm variation in the head height is within the tolerances typically used to assess the acceptability of the head height of a given joint [10]. It can be argued that although the aforementioned parameters may contribute towards the variance in the head height of the produced joints, their associated uncertainties are not severe enough to lead to unacceptable joints. The magnitude of σ also do not exceed 0.2 mm for all parameters, thus interaction effects are considered insignificant.

The results in Figure 8.6 provide insight into the sensitivities of a given process due to variability in a given system configuration, which is considerably more constrained than the plausible design limits assigned in Example 1. Accordingly, the importance of parameters in the current example are markedly different.

8.4.3.2 Kinetic energy

For interest, the variation in kinetic energy of the system prior to rivet insertion is also examined. Figure 8.7(a) shows the EE sensitivity measures for the kinetic energy of the system just before rivet insertion. The results highlight the importance of parameters relating directly to the computation of the kinetic energy. It is not surprising that variability in the inertias of the system should have a large impact on the kinetic energy. Similarly, the radii of the pulleys determine the transmission ratio of the belt drive, i.e. the angular velocity of the inertias, therefore they are important to the kinetic energy of the system.

Figure 8.7(b) shows the confidence bounds on the sensitivity measures. Aside from the radii of the driving and driven pulleys (i.e. Rpulley1 and Rpulley2), there is no overlap between the confidence bounds in μ^* for the most important parameters, meaning that there is no uncertainty about their relative ranking.

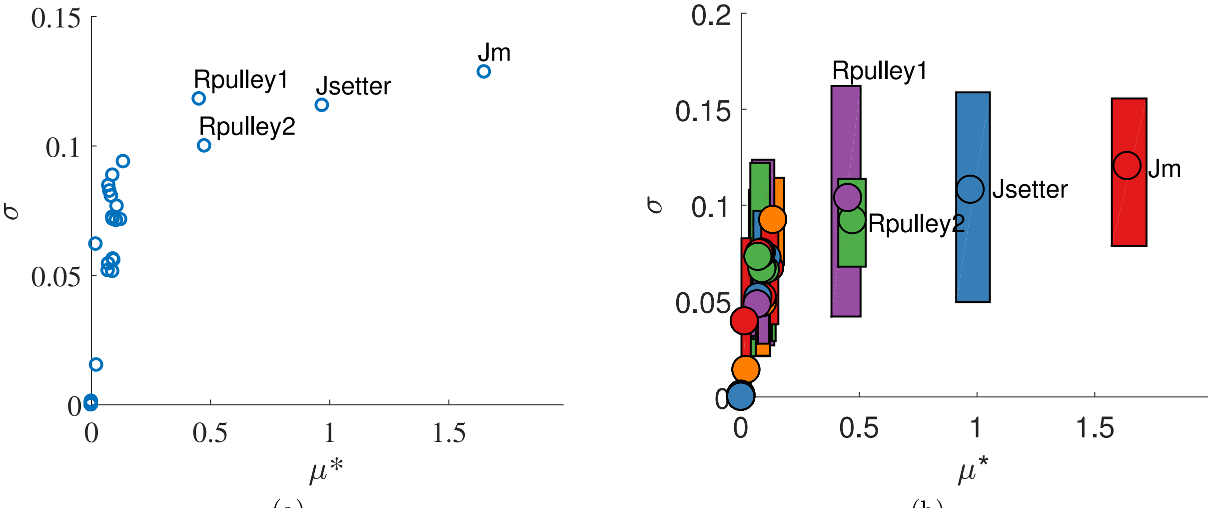

(a)

(b)

Figure 8.7: EE sensitivity measures for the kinetic energy prior to rivet insertion. (a) standard view. (b) with confidence bounds shown as boxes.

In terms of its impact on the resulting joint, the kinetic energy of the system prior to rivet insertion cannot be interpreted without knowledge of the configuration of the system and the joint to be made. The proportion of kinetic energy converted into work done on the joint, strain energy in the machine, or dissipated via friction losses, depends on the details of the exact setup and process. Consequently, there is no single definitive level of variation in the kinetic energy which may be considered significant.

The most important parameters in this case are all intuitive and expected. Calculations of variance-based sensitivity indices would offer little further insight. Therefore, it was decided not to pursue the sensitivities of the kinetic energy in further analyses.

8.4.3.3 Convergence analysis

A convergence check was necessary to validate the results of the screening stage. This step was key to preventing against possible misclassification of the importance of a parameter. The convergence of the EE sensitivity measures were evaluated via a bootstrap method (see Appendix D), using functions in the SAFE toolbox [137]. Sensitivity indices were calculated for samples of different sizes, from which the lower and upper bounds of the mean EEs were used as confidence bounds to indicate convergence. Narrowing bounds would indicate convergence, while widening bounds would represent divergence.

Figures 8.8 and 8.9 show the convergence plots for the EE sensitivity measures for the head height and the kinetic energy prior to rivet insertion respectively.

In Figure 8.8 the values of μ^* for the three most important factors do not appear to be fully converged. Overlap between the confidence intervals for Zs and $muprac$ suggests that their relative ranking may change with further model evaluations. However, the rank of $rivLength$ as the most influential factor is unlikely to change.

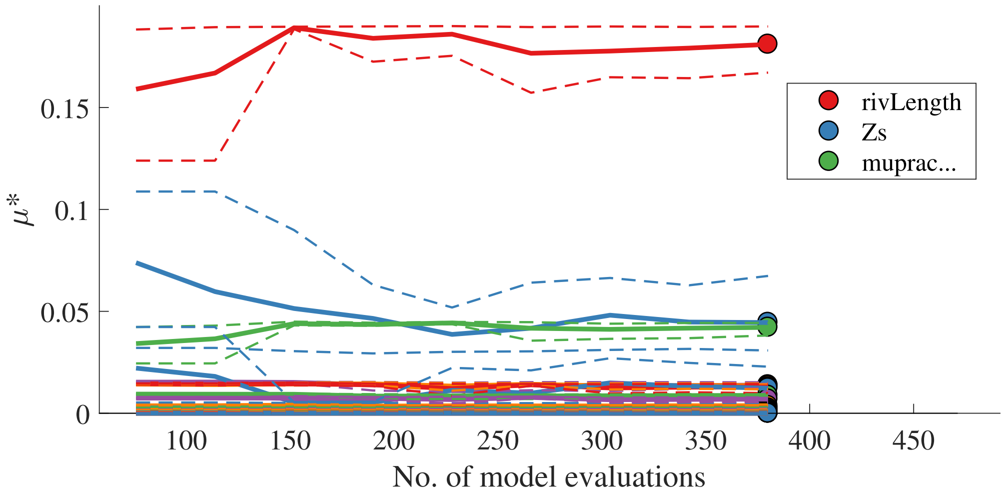

Figure 8.8: Convergence of the EE sensitivity measures for the head height.

In Figure 8.9, the results are sufficiently converged to fully support the relative ranking of the factors previously discussed with regards to Figure 8.7.

The results showed that although the EE indices had not fully converged for all of the outputs, the ranking of the most important parameters according to the value of μ^* were unlikely to undergo drastic changes even if more model evaluations were performed. Therefore the risk of misclassifying a significant parameter as an insignificant one was very low, meaning that the existing results could be reasonably used to screen out parameters and exclude them from further analyses. The alternative scenario of misidentifying an unimportant parameter as a significant one was equally unlikely, and would not have had major detrimental consequences besides incurring a larger computational cost in the variance-based analysis to follow.

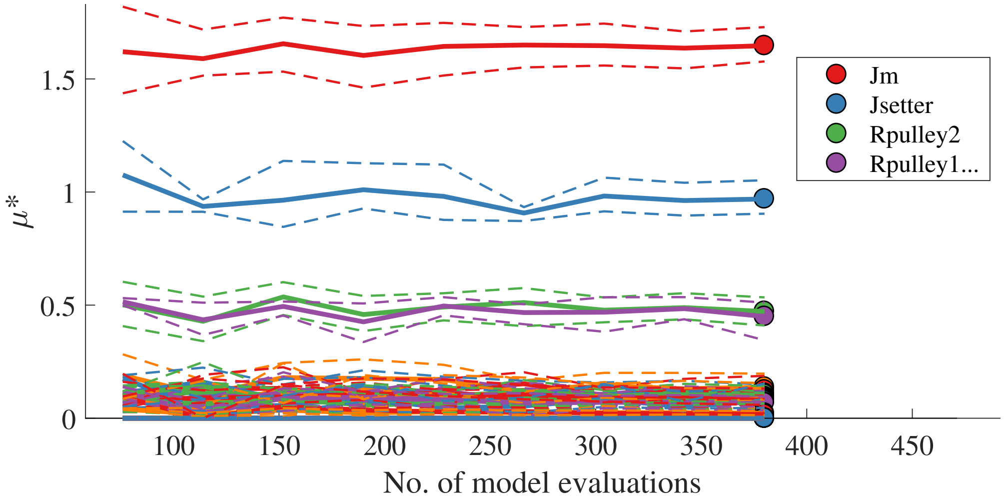

Figure 8.9: Convergence of the EE sensitivity measures for the kinetic energy prior to rivet insertion.

8.4.3.4 Shortlist of important parameters

In summary of the outcomes of the screening analysis, the parameters which were considered to be important to the head height and therefore included in the subsequent variance-based analysis were:

- Rivet length
- Maximum available spring compression in the clamping mechanism
- Coulomb friction coefficient in the PRSM

Given that the number of relevant parameters was reduced to three ($k = 3$), and the base random sample size was chosen to be 5000 ($N = 5000$), the number of model evaluations for calculating the Sobol' indices was $N(k + 2)$ or 25000.

Sample generation for the variance-based analysis was performed using functions from the SAFE toolbox. The same limits from Table 8.2 were assigned for each of the shortlisted parameters.

8.4.4 Uncertainty analysis results

8.4.4.1 Sobol' indices

The sensitivity indices for the head height are shown in Figure 8.10 . For a given factor, the central value is the bootstrap mean, and the lower and upper bounds are the 95% bootstrap confidence intervals.

From Figure 8.10 the rivet length is clearly the most influential parameter to the head height, as it has the highest MEI and TEI values of all the factors. Aside from the rivet length, one could argue that the Coulomb friction coefficient of the PRSM and the maximum available spring compression are similar in terms of their contribution to the variance in the head height. The mean values of the indices are largely in agreement with the screening results shown in Figure 8.6(a).

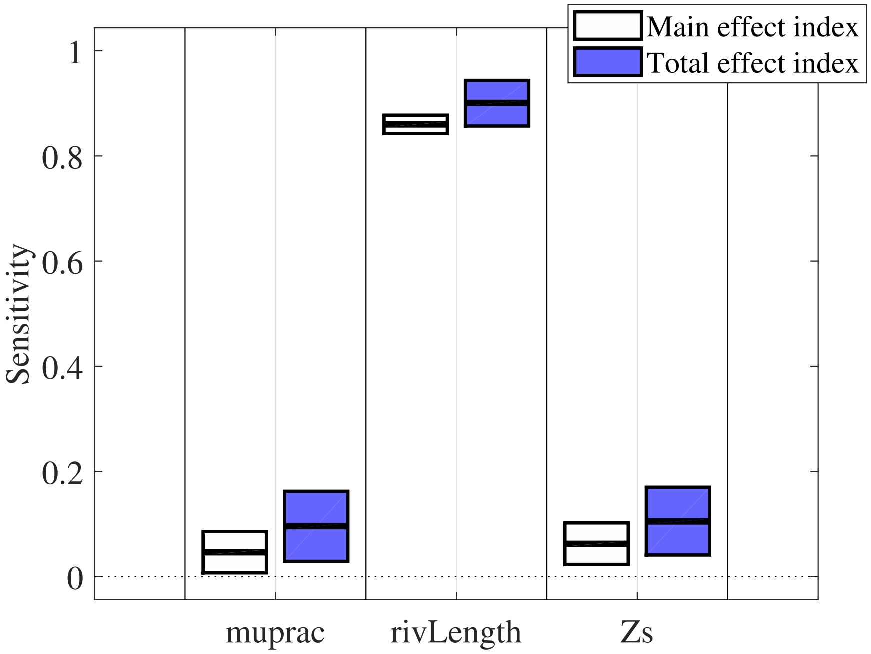

Figure 8.10: Sensitivity indices associated with the head height.

8.4.4.2 Convergence analysis

A convergence analysis was performed to verify whether the number of samples chosen was adequate, and whether a further increase in the number of model evaluations would yield significantly different results.

Figure 8.11 shows the convergence of the MEIs as well as the TEIs with regards to the head height. In Figure 8.11(a), the confidence bounds for the MEIs of all parameters appear to be converging with an increasing number of model evaluations. In Figure 8.11(b) the confidence bounds for the TEIs do not seem to be converging as quickly as those for the MEIs. There is significant overlap in the confidence bounds of both sensitivity measures for *Zs* and *muprac*. Further model evaluations may be necessary in order to obtain more precise values for the relative contributions of these two factors.

Confidence bounds on the sensitivity indices represent the estimation error. Estimation error results from the approximations used to estimate the sensitivity indices. According to

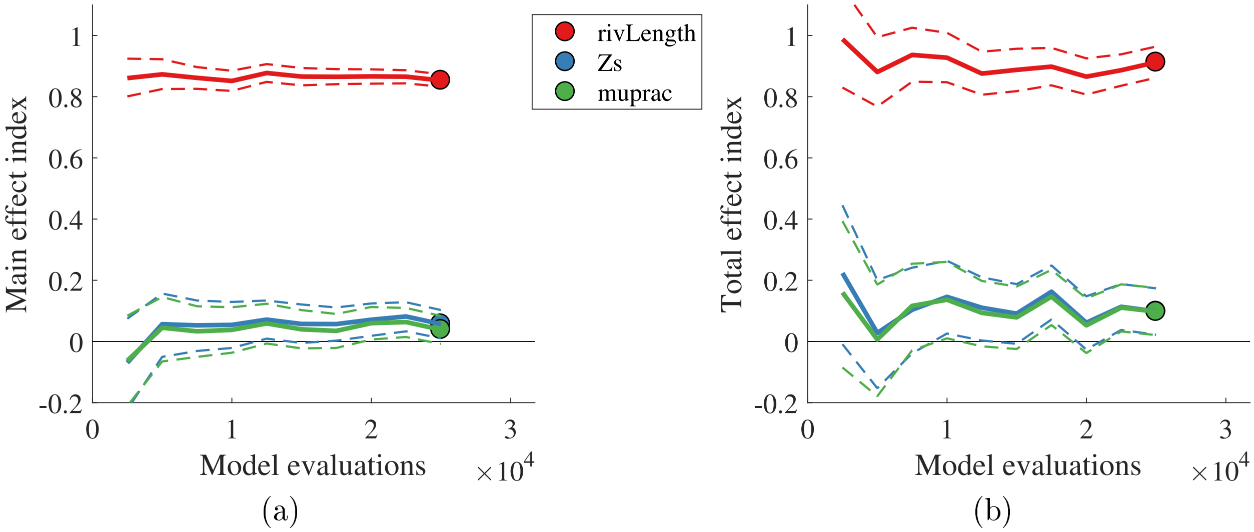

Figure 8.11: Convergence plots of sensitivity indices associated with the head height. (a) Main effect indices. (b) Total effect indices.

[131], one way to reduce the approximation error is to expand the sample size, and up to 10,000 or more samples per input factor may be required to achieve accurate estimations of the sensitivity indices. Considering the convergence plots in Figure 8.11, the number of samples may need to be increased substantially in order to achieve further reductions in the confidence intervals. However, this would not be necessary since the results are sufficiently converged to validate the results of the screening analysis, and to also give a quantitative assessment of how the uncertainties in the most important parameters affect the variability of the SPR process. The current results therefore satisfy the aims of the uncertainty analysis.

8.5 Discussion

8.5.1 Design exploration

The results from the design exploration example provide a view into a much broader design space than previously considered in the literature. As discussed in Section 2.1.3, existing literature concerning the effects of input parameters of the SPR process have tended to focus on the setting velocity or the properties relating to the rivet, material and die. In the current work, the influences of an extensive list of factors (shown in Table 8.1) spanning the full scope of the SPR system have been evaluated.

By sampling over the entire plausible range of values that the parameters can realistically take, the impact on the output of the model is drastic, as seen by the large magnitude of the main effects and interaction effects in Figures 8.2 and 8.4. One interpretation of Figure 8.2 is that by changing the radius of the driven pulley from one extreme to the other, the head height of the joint can vary by as much as 7 mm. This can be hard to grasp given that the full rivet length of the simulated joint configuration was only 5.5 mm. In view of this it can be argued that the results are too extreme to be realistic, and that assumptions regarding the behaviour of the joint beyond the nominal riveting loads may not necessarily reflect the behaviour of the real joint.

On the other hand, the counterargument can be made that the results should be interpreted in terms of the relative importance of the parameters to the output rather than the absolute values of the output. Regarding the assumptions of the behaviour of the joint, the modelled joint can also be considered as an object of known response under load, and the head height a measure of the compression undergone by that object. In this manner, the simulated joining event is abstracted to a more general process, one that exists only in the design space but is appropriate for the purposes of design exploration. After all, the behaviour of the joint has no bearing on the kinetic energy available to be input into the process. Therefore, the assumptions made do not invalidate the analysis, and are necessary for the effective exploration of the design space.

The simulated results offer answers to the ‘what if’ questions surrounding the design and operation of the system. From Figure 8.2(a) it could be seen that changing the radii of the pulleys would have a significant effect on the head height of the joint, more so than changing the inertias of the system. Such insights may inform future system designs which are required to make harder joints. Riveting these joints can be challenging due to the large amount of energy required. In light of the results from the current study, an effective solution could be to modify the transmission ratio of the belt drive to allow the motor to operate under optimum conditions while achieving the target velocities necessary to produce the joints.

Further to the joining of high strength materials, a past project undertaken in industry had looked into modifying the inertia of the flywheel as a means of tackling more challenging joints. However, the results of the current study suggest that while this approach would have some influence on the resulting joint, considering the amount of work to manufacture and fit a new flywheel to the system, a more cost effective solution would be to change the motor current limit (i.e. the level of torque applied by the motor during rivet insertion). The motor current limit is noted to be on par with the inertia of the system with regards to influence on the head height of the produced joint (Figure 8.2(a)), and importantly, can be adjusted via a software interface. This further highlights the potential applicability of the current analysis to real challenges faced in industry.

There is inherent value in the design exploration exercise as it offers an unrestricted overview of the possible designs of the system with direct visibility of the impact on the outputs of the process. The design of the existing systems have been iteratively refined over time, and are in a sense restricted by past experiences of what is known to work and what did not, and also uncertainties over what might work well. The example on design exploration shows that it is possible to assess the effects of significant design changes at no cost other than simulation time. The consequences of changing the belt transmission ratio, the inertia of the roller screw mechanism, or the stiffness of the C-frame are easily evaluated in the model, without the costs of designing test rigs or building prototypes. Thus, the example on design exploration also serves as a demonstration of the usefulness of the model and sensitivity analysis tools.

8.5.2 Uncertainty analysis

The findings from the screening analysis offer useful insight into the variability of the servo SPR process and thus address a gap in the published literature. In Chapter 2 there was a noted absence of studies which examined the variability of the SPR process; one of the few model-based sensitivity analyses on SPR was described in [26], but the work was configured for design optimisation rather than the assessment of variability for a given process.

In both the screening and variance-based stages of the analysis, the apparent importance of the rivet length, the clamping mechanism and the friction in the roller screw mechanism with regards to the head height of the joint is highlighted. Consequently, these are three distinct areas which can be targeted in the future development and refinement of the SPR system. For example, narrowing the tolerances on the rivet length could improve the repeatability of the head heights of the produced joints. This could have major implications for the rivet manufacturing process, since the narrowing of tolerances would inevitably lead to an increase in cost. Alternatively, tightening the tolerances in the clamping mechanism via a change in the design may be another option which could lead to improvements in the variability of the resulting joints.

Friction is to a large extent outside the control of the designer. However the effects of friction may be mitigated via some form of condition monitoring. Identification of changes in the friction characteristics would enable smarter maintenance or alternatively inform process control such that auto-adjustments are made to reduce the impact on the repeatability of the process.

Reducing the variability in the process not only improves the quality and strength of a single joint, but also has knock-on effects on the design of the parts which are joined together. For example, the flange length on parts to be riveted together is an important design variable which affects the weight and cost of the final product. Although minimising the flange length is beneficial with regards to weight and cost, common practice in the design process is in fact to increase the length requirement to allow for variations in the part, the prior processes and the riveting tool [138]. Reduced variation in the SPR system could help to alleviate design constraints on manufactured parts and thereby reduce costs, e.g. by enabling a shorter length requirement for the flange.

In automotive manufacturing, robustness to variation along with the availability of simulation tools in support of process design and parameter selection are some of the key factors considered in the selection of joining techniques [139]. The current work demonstrates that the model of the SPR system is a powerful tool which, when used in conjunction with publicly available sensitivity analysis software, can provide novel insights into the sensitivities of the physical joining process as well as highlight the main contributors to the variation in the process outputs.

8.5.3 Areas for improvement

In the context of a production line, the results of the uncertainty analysis may not be exactly representative of the actual variability in the produced joints. This is because the number of model evaluations corresponds to as many joints all made on different systems, each with a distinct combination of parameter values. In a real production plant the number of SPR systems are far fewer than the number of joints produced and therefore the actual variation in the factors specific to SPR systems may be less severe than that defined in the analysis.

On a given system, factors such as the maximum available disc spring compression are not expected to undergo any changes unless some form of damage were to occur, i.e. they can be considered as having fixed values. Friction on the other hand may vary with the temperature of the riveting system as it is operated through different duty cycles, or as the lubrication in the rivet setter is topped up as part of the maintenance schedule. Rivet length is not specific to a riveting system and thus the assumed distribution was justified. All this points at the need to tailor the sensitivity analysis to the details of the problem at hand. The approach taken in the current study is more suitable to understanding the process variability in large production plants with many SPR systems as opposed to smaller facilities with only a few systems.

Something not discussed so far is the ageing and wear of the equipment. The associated changes in the performance of a system is typically incremental over millions of cycles, which may be several months or years depending on the duty cycle of the system. To investigate the process variability due to this would prompt a very different set of configurations for the sensitivity analysis, a prerequisite of which would be the characterisation of the ageing and wear of riveting systems. To the author's knowledge, no studies within the SPR-related literature have looked into this topic. Existing work in the field of reliability modelling may serve as a reference point. In [140], Sun et al. argued that a model should include measures of product quality, tool degradation and tool failure in order to effectively model the reliability of a system. He et al. [141] suggested that system reliability can be overestimated if its interactions with the product quality are neglected, since component degradation can affect the process and vice versa. In the case of the SPR process, the reliability of the system and the repeatability of the resulting joints are intrinsically linked. The effect of ageing and degradation of electromechanical systems can consist of a reduction in the efficiency of the system, possibly via changes to the friction profile, or degradation of the motor characteristics. A model-based approach can be used to explore the potential impact of such changes on the quality of the produced joint without resorting to large experimental trials. Degradation and faults in the system may be modelled as changes to either the parameters or the model structure.

8.5.4 Process completion during simulation

In the first example relating to design exploration, it was clear from simulation data that under certain conditions the modelled system was unable to reach the target velocity before rivet insertion. Several factors may have contributed to this:

- The inertia of the system may have been too large to be accelerated up to the target speed in the distance available
- The motor characteristics may have been inadequate. Motor saturation may have been in effect
- The transmission ratios may have been inappropriate
- The springs in the clamping mechanism may have acted to significantly slow the motion of the punch
- The motor current limit may have been too restrictive in the lead-up to rivet insertion

From a design exploration perspective, identifying the exact conditions under which the system would no longer be able to complete the process would be a useful endeavour as it would help to establish some hard limits and guidelines regarding the plausible design of the system. However, the large number of parameters in the model means that this is far from straight forward. The identification of regions in the parameter space where the output is within a specified window is also known as 'factors mapping' [135]. The approach of Monte Carlo filtering and regionalised sensitivity analysis may be a potential candidate for tackling the problem in future work.

A separate unexplored topic is whether the sensitivity of the SPR process would depend on the joint configuration, i.e. the particular combination of rivet, material and die. This can also be considered as a question of how the characteristic force-displacement curves for a joint may affect the sensitivities of the model outputs. While the factors most important to the kinetic energy prior to rivet insertion will not be any different from those identified in the current study, the way in which the input factors affect the head height will certainly be influenced by the joint configuration. Thus, further sensitivity analyses using another joint configuration may provide insightful results.

8.5.5 Comments on the chosen GSA methods

It has been highlighted how the EE method and the variance-based method can be used in tackling two example problems: design exploration and uncertainty analysis. In view of the results, a critical assessment of each method must be made.

The EE method has played a key role in both the examples given. In design exploration it served to rank the parameters according to their relative importance, while in the second example, it allowed crucial decisions to be made about which parameters could be neglected in the subsequent variance-based sensitivity analysis. The variance-based method has provided a more accurate breakdown of the contribution of each parameter to the variance in the model output, but the conclusions from this quantitative analysis do not really differ from the qualitative results obtained with the EE method. This calls into question the cost vs. benefit of the variance-based method: if the same conclusions can be reached using a computationally cheaper method, why bother with the more expensive one?

Where the variance-based method comes into its own is perhaps in addressing a problem which requires a specific reduction in the variance of the output, i.e. choosing the factors to reduce the uncertainty of in order to achieve said goal. This approach is described as 'variance cutting' in [135]. In a scenario where multiple factors contribute significantly to the variance of the output, it would make sense to select the ones for which the reduction or elimination of uncertainty would incur the least cost. Such a decision cannot be made using a screening method alone, since it does not provide the breakdown of the contributions of the individual parameters. Therefore, both methods have their place in the uncertainty analysis of complex models.

8.6 Summary

In this chapter, two examples have been used to demonstrate the application of sensitivity analysis methods to the simulated SPR process.

The first example was motivated by the exploration of the plausible design space. The EE method was implemented to identify the factors in the model which had the largest effect on the model outputs: the head height and the kinetic energy prior to rivet insertion. It was found that the most important factors were those which directly related to the kinetic energy of the system: the pulley radii, setting velocity, back-EMF constant of the motor, transmission ratios, inertias, etc. as well as the motor current limit and torque constant of the motor. The results were logical in view of the inertia-based design of the system.

The second example studied the impact of uncertainties in the process inputs on the outputs, i.e. how variations in the SPR process could affect the resulting joint. The EE method was used to reduce the number of parameters to those that were important, subsequently a variance-based analysis was used to quantify the contribution of each remaining parameter towards the overall variability in the predicted head height. It was found that alongside the rivet length, other factors of note included the Coulomb friction coefficient in the PRSM and the maximum available spring compression in the clamping mechanism. The latter two are areas of the SPR system which traditionally have not been studied in the existing literature with regards to the quality of the joint. The findings from the current study can be used to inform more targetted improvements to the system such as condition monitoring to identify and mitigate the effects of variation in the friction in the system, or potential design changes to reduce the tolerances in the clamping mechanism, both of which should lead to a reduction in the process variability. Improvements to the repeatability of the SPR process could have significant implications for the design of automotive parts.

In the next chapter, a broader discussion of the contribution to knowledge and implications of the current work is presented, as well as avenues for further work.

Chapter 9

Discussion and Conclusions

SPR is a high-value joining technology which plays a significant role in the automotive industry. Making improvements to the technique as well as gaining a deeper understanding of the underlying physics form part of the same industry-wide drive. The current research is an industrial CASE project, run in collaboration with Atlas Copco IAS UK Limited. The applied nature of the current research reflects the demands of the industry, which is in need of a robust model of the SPR process in order to address some of the most pressing challenges it is facing.

This section elaborates on the relevance of the current work to the state of research on SPR as well as to the joining industry. Ideas for further work are also discussed.

9.1 Contribution to knowledge

From the literature review it was noted the simulation of the SPR process was predominantly focused on the rivet-material interaction during rivet insertion and the dynamics of the riveting tool was largely unaccounted for. In [9], Haque mentioned the need for the integration of knowledge across various sources including computer simulations and industrial trials, in order to gain a complete understanding of the relationships between the process variables and the output. Therefore, the main contribution of the current work is in addressing the gap in knowledge with regards to the influence of process inputs on the produced joint. Within this contribution four specific aspects are of particular note:

1. To the author's knowledge, the developed model is the first mechatronics system model of the inertia-based SPR system. The model is able to accurately predict the dynamic response of the riveting system as well as the head height of a given joint configuration, with very low computational expense. Prior to this work, such results would have had

to be obtained empirically. The model encapsulates all the insights gained over the course of this project and will facilitate further research into the SPR process.

2. A further contribution to knowledge is the detailed observation of the joining event using the high speed camera. Published works have made limited use of high speed videos in the analysis of the riveting process. Phenomenon such as the 'pushback' effect mentioned in Chapter 6 could only be identified using the approach taken in the current study.

3. The sensitivity analysis of the SPR system with respect to the variability of the head height of the produced joints has not be done before. While a few publications have investigated the sensitivity of the form of the final joint to various factors relating to the rivet, material and die [24, 25, 26], the current work is novel in that it is the first time the factors of the wider riveting system are evaluated via GSA methods. The finding of Chapter 8 can serve as a reference point for further investigations into the design optimisation of the riveting system.

4. A key contribution has been the use of the model to demonstrate two aspects of process improvement via a numerical optimisation study (Chapter 7). This has shown that significant cost or energy savings could be achieved in a production environment.

More generally, an important implication of this work is a broader view of the SPR technology; it will raise awareness of the complexities of the mechatronics system behind the riveting process, and the need to account for the dynamics of the machine to better simulate the riveting process.

Beyond SPR systems, the approach taken to model the process can also be applied to alternative joining techniques, such as clinching, single sided riveting [142], solid self pierce riveting [143], etc. The current work has proven that a complex process can be adequately represented using a combination of physics-based modelling of the machine, and empirical modelling of the workpiece. While there are distinct differences between the aforementioned joining methods, they are linked by the common mechanism of actuating a tool to create plastic deformation in a workpiece. Like SPR, techniques such as clinching see substantial usage in the automotive industry. In consideration of the insights gained into the SPR process in the current project, it is believed that alternative joining methods may also benefit from a similar modelling approach.

From a research strategy perspective, this direction is consistent with the current focus on concepts such as Digital Twins [144, 145, 146], Virtual Manufacturing [147, 148, 149, 150, 151], and so-called grey-box modelling [152, 153, 154, 155, 156, 157].

9.2 Implications for industry

First and foremost, the model facilitates the exchange of knowledge. Previously there was no single centralised source containing information or data regarding the dynamics of the system; relevant information was instead found in many separate sources, each offering a snippet of insight into the behaviour of the system. The current work has created a compact container of knowledge which brings together existing knowledge and builds on it, with the corresponding documentation to aid dissemination.

The system-level model of the SPR system plays a central role in the Industry 4.0 strategy of the industrial partner. Being the first of its kind, the current project is intended to be the base from which future projects will stem. The presentation of the current work to the management team has garnered positive feedback regarding the potential impact it could make to existing processes.

In a past project investigating the effects of changing the motor on an existing riveting system, the model was used to get an approximate idea of the suitable control gains, before performing the tuning on the actual system. On another occasion, a simplified model was written into a tool which estimated the minimum required travel distance for a system to reach the target setting velocity. The code was subsequently used by the company to assess the feasibility of reducing the stroke length on a list of existing systems on a production line. Isolated cases such as these have demonstrated the power of a model-based approach, but at the same time they have leveraged only partially the capabilities of the full model. Many more challenges can be addressed using the model.

One prominent challenge is that of finding the optimum setting velocity to achieve an acceptable joint. While the trials normally performed in the laboratory are useful for identifying the suitable rivet and die combination for joining a given material stack, the setting velocities recorded during this stage are not directly transferable to the systems on the production line due to differences in the type of rivet setter, the C-frame, and the size and fixture of the parts to be joined. The consequence is an additional cost incurred by the man hours and test samples used to find suitable setting velocities at the production facility, often via a trial and error approach. What is needed is a precise prediction of the appropriate setting velocities for the systems on the production line, such that the trials on site can be altogether eliminated. The developed model of the SPR system can be used to make such predictions provided that the systems are suitably characterised. The model can be run as part of an optimisation routine to find the suitable setting velocity for riveting on any system configuration, as demonstrated in Chapter 7. This has the potential to significantly reduce the amount of testing required on site, since much fewer tests would be required to validate the model prediction than in taking a trial and error approach. Therefore, the model could help to substantially lower the costs associated with the existing processes on site.

As well as predicting a single setting velocity for a given joint configuration, the model of the SPR system is a potential tool for identifying a multi-dimensional process window. Multi-objective optimisation could help to find the range of input parameter settings to produce acceptable joints and improve the process in terms of cycle time, energy consumption, or other metrics. Process input parameters which are presently fixed in value may become better utilised to this end.

Another area on which the model could have measurable impact is the design of SPR systems. For example, the model could help to determine the appropriate size and type of C-frame based on a list of joints that a proposed system is required to make. Rather than the existing process of testing on the system once it is fully assembled, it would be more cost-effective to be able to predict its performance and anticipate any potential issues at the design stage. By predicting the outcomes without having to make physical changes to the system, the purpose of testing would be transformed from exploration to one of validation, hence the scope of experiments carried out can be considerably reduced.

9.3 Further work

Following on from the discussion about the prediction of setting velocities, the accuracy of the prediction may be enhanced further with better modelling of the parts to be joined and their interaction with the SPR system. The parts on an automotive production line have undoubtedly very different dynamics to the coupons used in the laboratory tests. FE modelling would better capture the response of such parts when undergoing riveting. The complexities of machine-workpiece interactions can be tackled via a co-simulation setup, where the models of the SPR system and rivet insertion are run in parallel.

It is anticipated that future research will bring together the system-level model of the SPR system and the detailed FE simulations of the rivet-material interactions in co-simulation. The benefits would be a higher-fidelity representation of the full riveting process than previously achieved, resulting in even better predictive accuracy and greater insight into the sensitivities of the process. The implication to industry will certainly be greater savings in cost at the design stage. More importantly, there is immeasurable value in having the ability to evaluate novel designs or changes at the component level, and immediately visualise their impact on the final outputs of the full system.

Co-simulation could potentially address one of the shortcoming in the current work, which is that each identified model of the joint is specific to a particular joint configuration, since few inferences can be made from the experimental data regarding the physics of rivet-material interaction. In contrast, a detailed FE model of the joint would provide insight into the physics of rivet and material deformation. With every simulated joint and comparison to the corresponding test data, new or improved knowledge would be accumulated.

As well as improvements to the mechanical side of the model, there is demand within industry for the capability to evaluate the effects of changes to the PLC code on the performance of the system. This is motivated by potential time and cost savings in the software development cycle. With further improvements to the electronic and digital domains of the current model of the SPR system, such a demand is within reach.

Traditionally, software development for new products has been limited by the availability of a physical prototype of the hardware. The challenge of programming for hardware that does not yet exist can be addressed via a model-based approach, where a model of the hardware can be used as a target for software trials. The enabler for this is a representative plant model as well as an interface to interpret the programming code into the native simulation environment.

Improvements should also be made to electrical and electronic components in the model. A higher fidelity model of the control panel that captures the electrical characteristics of both the power and control sections of the drive unit would allow more representative predictions of the power profile of the unit. A particular point of interest is the effect of different motion profiles and duty cycles on the temperature of the drive, which is a key factor to consider when sizing the cooling system for the control panel.

9.4 Conclusions

To summarise, the thesis describes a programme of work that has implemented a novel mechatronics or systems-level model of self-pierce riveting. The model has been rigorously validated, used to propose optimal process parameters, and explore system-level sensitivity from both a design and operational perspective.

The specific conclusions of the research are as follows:

1. It can be concluded that a systems-level model of self-pierce riveting is able to successfully capture the mechanics and dynamics of the joining process without relying on finite element approaches.

2. The rivet insertion process can be adequately characterised using two separate empirical models, one representing the rivet-material interaction, and the other representing the material stack under clamping.

3. The setting velocity associated with the dataset that is used to train the model of the joint is highly important to the performance of the trained model, since the setting velocity directly affects the extent of the characteristic force-displacement curves that are identified.

4. On the other hand, the motor current limit or the C-frame associated with the training dataset for the model of the joint have little effect on the overall performance of the model. This is because the extent to which the characteristic force-displacement curves are mapped out during testing is not as sensitive to these factors as it is to the setting velocity.

5. The ‘pushback’ effect, where the material being riveted undergoes deflection prior to the engagement of the clamping force, may be an important phenomenon to consider in the modelling of the process.

6. The minimisation of the stroke offset on a SPR system can yield substantial savings in cycle time and energy consumption. Incorporation of regenerative systems may enable reduction in the energy usage of up to 25%.

7. Cycle time can be further reduced by maximising the setting velocity, although corresponding reductions would be necessary for the motor current limit and the C-frame stiffness to avoid compromising the quality of the produced joint. Alternatively, the energy consumption can be lowered by minimising the setting velocity, which would need to be balanced with increases in the motor current limit and the C-frame stiffness to maintain joint quality.

8. From a design exploration perspective, it is evident that the factors directly related to the kinetic energy of the system have the largest influence on the process outputs. This is in line with the inertia-based design of the system.

9. From an uncertainty analysis perspective, it can be concluded that the rivet length, the friction in the planetary roller screw mechanism, and the maximum available spring compression in the clamping mechanism are primary factors that contribute to the variability of the process, i.e. variability in the head height.

Bibliography

[1] R. Heuss, N. Müller, W. von Sintern, A. Starke, and A. Tschiesner. Lightweight, heavy impact. McKinsey & Company, 2012.

[2] S. Pagerit, P. Sharer, and A. Rousseau. Fuel economy sensitivity to vehicle mass for advanced vehicle powertrains. In *SAE 2006 World Congress & Exhibition*. SAE International, April 2006.

[3] E. R. H. Fuchs, F. R. Field, R. Roth, and R. E. Kirchain. Strategic materials selection in the automobile body: Economic opportunities for polymer composite design. *Composites science and technology*, 68(9):1989–2002, 2008.

[4] J. Mortimer. Jaguar uses X350 car to pioneer use of self-piercing rivets. *Industrial Robot: An International Journal*, 28(3):192–198, 2001.

[5] European Aluminium Association. Body structures. The Aluminium Automotive Manual, 2013. [Online; accessed: 01-Jun-2019]. Available from: https://www.european-aluminium.eu/resource-hub/aluminium-automotive-manual/.

[6] A. Weber. Assembling Ford's aluminum wonder truck, 2015. [Online; accessed 01-May-2019]. Available from: https://www.assemblymag.com/articles/92728-assembling-fords-aluminum-wonder-truck/.

[7] EPSRC. New projects to harness UK's digital manufacturing potential, 2018. [Online; accessed 31-May-2019]. Available from: https://epsrc.ukri.org/newsevents/news/ukdigitalmanufacturing/.

[8] D. Li, A. Chrysanthou, I. Patel, and G. Williams. Self-piercing riveting - a review. *The International Journal of Advanced Manufacturing Technology*, 92(5-8):1777–1824, 2017.

[9] R. Haque. Quality of self-piercing riveting (SPR) joints from cross-sectional perspective: A review. *Archives of Civil and Mechanical Engineering*, 18(1):83–93, 2018.

[10] L. Han, M. Thornton, D. Li, and M. Shergold. Effect of setting velocity on self-piercing riveting process and joint behaviour for automotive applications. In *SAE 2010 World Congress & Exhibition*. SAE International, 04 2010.

[11] P. R. King. *Analysis and quality monitoring self-pierce riveting process*. PhD thesis, University of Hertfordshire, 1997.

[12] X. Sun and M. A. Khaleel. Strength estimation of self-piercing rivets using lower bound limit load analysis. *Science and Technology of Welding and Joining*, 10(5):624–635, September 2005.

[13] P.-O. Bouchard, T. Laurent, and L. Tollier. Numerical modeling of self-pierce riveting–from riveting process modeling down to structural analysis. *Journal of materials processing technology*, 202(1):290–300, 2008.

[14] S. Fayolle, P. O. Bouchard, and K. Mocellin. Modelling the strength of self-piercing riveted joints. In *Self-Piercing Riveting*, pages 79–107. Woodhead Publishing, 2014.

[15] D. Li, L. Han, A. Chrysanthou, M. Shergold, and G. Williams. The effect of setting velocity on the static and fatigue strengths of self-piercing riveted joints for automotive applications. In *TMS 2014: 143rd Annual Meeting & Exhibition*, pages 557–564, Cham, 2016. Springer International Publishing.

[16] Y. Ma, M. Lou, Y. Li, and Z. Lin. Effect of rivet and die on self-piercing rivetability of AA6061-T6 and mild steel CR4 of different gauges. *Journal of Materials Processing Technology*, 251:282–294, 2018.

[17] R. Porcaro, A. G. Hanssen, M. Langseth, and A. Aalberg. Self-piercing riveting process: An experimental and numerical investigation. *Journal of materials processing technology*, 171(1):10–20, 2006.

[18] G. Casalino, A. Rotondo, and A. Ludovico. On the numerical modelling of the multiphysics self piercing riveting process based on the finite element technique. *Advances in Engineering Software*, 39(9):787–795, 2008.

[19] K. Mori, T. Kato, Y. Abe, and Y. Ravshanbek. Plastic joining of ultra high strength steel and aluminium alloy sheets by self piercing rivet. *CIRP Annals*, 55(1):283 – 286, 2006.

[20] E. Atzeni, R. Ippolito, and L. Settineri. Experimental and numerical appraisal of self-piercing riveting. *CIRP Annals-Manufacturing Technology*, 58(1):17–20, 2009.

[21] M. Grujicic, J. Snipes, S. Ramaswami, and F. Abu-Farha. Process modeling, joint-property characterization and construction of joint connectors for mechanical fastening by self-piercing riveting. *Multidiscipline Modeling in Materials and Structures*, 10(4):631–658, 2014.

[22] O. Hahn, C. Kraus, G. Leuschen, R. Mauermann, and R. Neugebauer. Research in impulse joining of self pierce riveting. 2008.

[23] B. Wang, C. Hao, J. Zhang, and H. Zhang. A new self-piercing riveting process and strength evaluation. *Journal of Manufacturing Science and Engineering*, 128(2):580–587, 2005.

[24] S. A. Westgate, R. Doo, F. Liebrecht, S. Braeunling, T. Mattsson, and K.-O. Strömberg. The development of lightweight self-piercing riveting equipment. In *SAE 2001 World Congress*. SAE International, March 2001.

[25] M. Fu and P.K. Mallick. Effect of process variables on the static and fatigue properties of self-piercing riveted joints in aluminum alloy 5754. In *SAE 2001 World Congress*. SAE International, March 2001.

[26] M. Jäckel, T. Falk, and D. Landgrebe. Concept for further development of self-pierce riveting by using cyber physical systems. *Procedia CIRP*, 44:293–297, 2016.

[27] Y. Abe, T. Kato, and K. Mori. Self-piercing riveting of high tensile strength steel and aluminium alloy sheets using conventional rivet and die. *Journal of materials processing technology*, 209(8):3914–3922, 2009.

[28] J. Mucha. A study of quality parameters and behaviour of self-piercing riveted aluminium sheets with different joining conditions. *Strojniški vestnik-Journal of Mechanical Engineering*, 57(4):323–333, 2011.

[29] M. Jäckel, C. Kraus, and T. Kropp. Effects of increased tool velocity on mechanical joining of steel and aluminum sheet metals. *Procedia CIRP*, 23:24–28, 2014.

[30] R. Neugebauer, K.-D. Bouzakis, B. Denkena, F. Klocke, A. Sterzing, A. E. Tekkaya, and R. Wertheim. Velocity effects in metal forming and machining processes. *CIRP Annals-Manufacturing Technology*, 60(2):627–650, 2011.

[31] R. Haque, J. H. Beynon, and Y. Durandet. Characterisation of force-displacement curve in self-pierce riveting. *Science and Technology of Welding and Joining*, 17(6):476–488, 2012.

[32] R. Haque and Y. Durandet. Investigation of self-pierce riveting (SPR) process data and specific joining events. *Journal of Manufacturing Processes*, 30:148–160, 2017.

[33] R. Haque. *Residual stress and deformation in SPR joints of high strength materials.* PhD thesis, Swinburne University of Technology, 2014.

[34] R. Haque, N. S. Williams, S. E. Blacket, and Y. Durandet. A simple but effective model for characterizing SPR joints in steel sheet. *Journal of materials processing technology*, 223:225–231, 2015.

[35] R. Haque and Y. Durandet. Strength prediction of self-pierce riveted joint in cross-tension and lap-shear. *Materials & Design*, 108:666–678, 2016.

[36] C. Brecher, M. Esser, and S. Witt. Interaction of manufacturing process and machine tool. *CIRP Annals-Manufacturing Technology*, 58(2):588–607, 2009.

[37] B.-A. Behrens, A. Bouguecha, M. Vucetic, and A. Chugreev. Advanced wear simulation for bulk metal forming processes. volume 80, page 4003. Les Ulis: EDP Sciences, 2016.

[38] K. Swidergal, C. Lubeseder, I. von Wurmb, A. Lipp, J. Meinhardt, M. Wagner, and S. Marburg. Experimental and numerical investigation of blankholder's vibration in a forming tool: a coupled MBS-FEM approach. *Production Engineering*, 9(5-6):623–634, 2015.

[39] M. Franzke, S. Puchhala, and H. Dackweiler. Modeling the interaction effects between tools and the work piece for metal forming processes. In *AIP Conference Proceedings*, volume 908, pages 1489–1494. AIP, 2007.

[40] C. Brecher, W. Klein, and M. Tannert. Optimization of multi-stage closed-die forging processes by coupled simulation of the machine and the forging processes. *Production Engineering*, 4(2-3):279–286, 2010.

[41] W. G. Frazier, E. A. Medina, J. C. Malas, and R. D. Irwin. Modeling and simulation of metal forming equipment. *Journal of materials engineering and performance*, 6(2):153–160, 1997.

[42] T. Kroiß, U. Engel, and M. Merklein. Comprehensive approach for process modeling and optimization in cold forging considering interactions between process, tool and press. *Journal of Materials Processing Technology*, 213(7):1118–1127, 2013.

[43] P. Groche, F. Hoppe, and J. Sinz. Stiffness of multipoint servo presses: Mechanics vs. control. *CIRP Annals*, 66(1):373–376, 2017.

[44] C.-C. Schenke, H. Wiemer, and K. Großmann. Analysis of servo-mechanic drive concepts for forming presses. *Production Engineering*, 6(4-5):467–474, 2012.

[45] J. Antony. *Design of experiments for engineers and scientists.* Elsevier, 2014.

[46] S. Elangovan, K. Prakasan, and V. Jaiganesh. Optimization of ultrasonic welding parameters for copper to copper joints using design of experiments. *The International Journal of Advanced Manufacturing Technology*, 51(1):163–171, Nov 2010.

[47] H. Pashazadeh, Y. Gheisari, and M. Hamedi. Statistical modeling and optimization of resistance spot welding process parameters using neural networks and multi-objective genetic algorithm. *Journal of Intelligent Manufacturing*, 27(3):549–559, Jun 2016.

[48] M. D. McKay, R. J. Beckman, and W. J. Conover. Comparison of three methods for selecting values of input variables in the analysis of output from a computer code. *Technometrics*, 21(2):239–245, 1979.

[49] F. Moroni, A. Pirondi, and F. Kleiner. Experimental analysis and comparison of the strength of simple and hybrid structural joints. *International Journal of Adhesion and Adhesives*, 30(5):367–379, 2010.

[50] A. Faria Neto, A. F. Branco Costa, and M. F. de Lima. Use of factorial designs and the response surface methodology to optimize a heat staking process. *Experimental Techniques*, 42(3):319–331, Jun 2018.

[51] Z. Allam, E. Becker, C. Baudouin, R. Bigot, and P. Krumpipe. Forging process control: Influence of key parameters variation on product specifications deviations. *Procedia Engineering*, 81:2524–2529, 2014.

[52] S.-Y. Kim, K. Tsuruoka, and T. Yamamoto. Effect of forming speed in precision forging process evaluated using CAE technology and high performance servo-press machine. *Procedia Engineering*, 81:2415–2420, 2014.

[53] M. Gao, H. Huang, Q. Wang, Z. Liu, and X. Li. Energy consumption analysis on sheet metal forming: focusing on the deep drawing processes. *The International Journal of Advanced Manufacturing Technology*, 96(9-12):3893–3907, 2018.

[54] P. Muñoz-Escalona and P. Maropoulos. Integrated optimisation of surface roughness and tool performance when face milling 416 ss. *International Journal of Computer Integrated Manufacturing*, 23(3):248–256, 2010.

[55] M. Oudjene and L. Ben-Ayed. On the parametrical study of clinch joining of metallic sheets using the taguchi method. *Engineering Structures*, 30(6):1782 – 1788, 2008.

[56] X. Wang, X. Li, Z. Shen, Y. Ma, and H. Liu. Finite element simulation on investigations, modeling, and multiobjective optimization for clinch joining process design accounting for process parameters and design constraints. *The International Journal of Advanced Manufacturing Technology*, 96(9):3481–3501, Jun 2018.

[57] NIST/SEMATECH. e-Handbook of Statistical Methods, 2012. [Online; accessed 03-Jun-2019]. Available from: https://www.itl.nist.gov/div898/handbook/pri/section3/pri334.htm.

[58] G. P. Cipriano, L. Blaga, J. F. dos Santos, P. Vilaça, and S. T. Amancio-Filho. Fundamentals of force-controlled friction riveting: Part i - joint formation and heat development. *Materials*, 11(11):2294, 2018.

[59] G. P. Cipriano, L. Blaga, J. F. dos Santos, P. Vilaça, and S. T. Amancio-Filho. Fundamentals of force-controlled friction riveting: Part ii - joint global mechanical performance and energy efficiency. *Materials*, 11(12):2489, 2018.

[60] S. Kumar and M. Tobin. Design of experiment is the best way to optimize a process at minimal cost. In *Ninth IEEE/CHMT International Symposium on Electronic Manufacturing Technology,Competitive Manufacturing for the Next Decade*, pages 166–173, Feb 1990.

[61] R. L. Plackett and J. P. Burman. The design of optimum multifactorial experiments. *Biometrika*, 33(4):305–325, 1946.

[62] M. Tiegelkamp and K.-H. John. *IEC 61131-3: Programming industrial automation systems*. Springer, 1995.

[63] JCGM. Evaluation of measurement data - guide to the expression of uncertainty in measurement, September 2008. [Online; accessed 01-Aug-2020]. Available from: https://www.iso.org/sites/JCGM/GUM/JCGM100/C045315e-html/C045315e.html.

[64] M. Palmer. Propagation of uncertainty through mathematical operations, 2003. [Online; accessed 22-Aug-2020]. Available from: http://web.mit.edu/fluids-modules/www/exper_techniques/2.Propagation_of_Uncertaint.pdf.

[65] NI. Calculating absolute accuracy or system accuracy, 2020. [Online; accessed 22-Aug-2020]. Available from: https://www.ni.com/en-gb/support/documentation/supplemental/18/calculating-absolute-accuracy-or-system-accuracy.html.

[66] NI. NI 9215 Datasheet, 2020. [Online; accessed 22-Aug-2020]. Available from: http://www.ni.com/pdf/manuals/373779a_02.pdf.

[67] J. Muelaner. Calculating an uncertainty budget for a measurement, 2020. [Online; accessed 31-May-2020]. Available from: https://www.muelaner.com/uncertainty-budget/.

[68] L. Wang, S. Chai, D. Yoo, L. Gan, and K. Ng. Modeling of AC drives and power converter. pages 1–26. John Wiley & Sons Singapore Pte. Ltd, 2014.

[69] D. W. Novotny and T. A. Lipo. *Vector control and dynamics of AC drives*, volume 1. Oxford university press, 1996.

[70] J.-C. Maré. Friction modelling and simulation at system level: Considerations to load and temperature effects. *Proceedings of the Institution of Mechanical Engineers, Part I: Journal of Systems and Control Engineering*, 229(1):27–48, 2015.

[71] SKF. Roller screws, SKF technical publication 14489 EN, 2014.

[72] C. H. Kim and J. S. Arora. Nonlinear dynamic system identification for automotive crash using optimization: A review. *Structural and Multidisciplinary Optimization*, 25(1):2–18, 2003.

[73] L. Ljung. Approaches to identification of nonlinear systems. In *Proceedings of the 29th Chinese Control Conference*, pages 1–5. IEEE, 2010.

[74] G. Kerschen, K. Worden, A. F. Vakakis, and J.-C. Golinval. Past, present and future of nonlinear system identification in structural dynamics. *Mechanical systems and signal processing*, 20(3):505–592, 2006.

[75] J.-P. Noël and G. Kerschen. Nonlinear system identification in structural dynamics: 10 more years of progress. *Mechanical Systems and Signal Processing*, 83:2–35, 2017.

[76] K. Runesson, P. Steinmann, M. Ekh, and A. Menzel. Constitutive modeling of engineering materials - theory and computation, 2006. Lecture notes, Chalmers University of Technology, Göteborg.

[77] H. Yukawa, K. Kobayashi, and S. Kawamura. Identification of viscoelastic model for long pile synthetic turf by using multi-intensity impact test. *Procedia Engineering*, 34:849–854, 2012.

[78] M. Kulisiewicz. The evaluation of some mechanical properties of materials by means of an identification method of a nonlinear dynamical system. *Archives of Civil and Mechanical Engineering*, 16(3):380–386, 2016.

[79] T. Naraghi and A. S. Nobari. Identification of the dynamic characteristics of a viscoelastic, nonlinear adhesive joint. *Journal of sound and vibration*, 352:92–102, 2015.

[80] S. M. S. Sadati, A. S. Nobari, and T. Naraghi. Identification of a nonlinear joint in an elastic structure using optimum equivalent linear frequency response function. *Acta Mechanica*, 223(7):1507–1516, 2012.

[81] K. Jamroziak. Analysis of a degenerated standard model in the piercing process. *Journal of Achievements in Materials and Manufacturing Engineering*, 22(1):49–52, 2007.

[82] J.-L. Chenot, L. Fourment, R. Ducloux, and E. Wey. Finite element modelling of forging and other metal forming processes. *International journal of material forming*, 3(1):359–362, 2010.

[83] C. C. António, C. F. Castro, and L. C. Sousa. Optimization of metal forming processes. *Computers & structures*, 82(17-19):1425–1433, 2004.

[84] H. Marouani, A. Ben Ismail, E. Hug, and M. Rachik. Rate-dependent constitutive model for sheet metal blanking investigation. *Materials Science and Engineering: A*, 487(1):162–170, 2008.

[85] J. K. Sønstabø, D. Morin, and M. Langseth. Macroscopic modelling of flow-drill screw connections in thin-walled aluminium structures. *Thin-Walled Structures*, 105:185–206, 2016.

[86] L. Huang, J. F. C. Moraes, D. G. Sediako, J. B. Jordon, H. Guo, and X. Su. Finite-element and residual stress analysis of self-pierce riveting in dissimilar metal sheets. *Journal of Manufacturing Science and Engineering*, 139(2):021007, 2016.

[87] S. F. Masri and T. K. Caughey. A nonparametric identification technique for nonlinear dynamic problems. *Journal of Applied Mechanics*, 46(2):433–447, 1979.

[88] S. F. Masri, J. P. Caffrey, T. K. Caughey, A. W. Smyth, and A. G. Chassiakos. Identification of the state equation in complex non-linear systems. *International Journal of Non-Linear Mechanics*, 39(7):1111–1127, 2004.

[89] C. Surace, K. Worden, and G. R. Tomlinson. An improved nonlinear model for an automotive shock absorber. *Nonlinear Dynamics*, 3(6):413–429, 1992.

[90] R. C. Ehrgott and S. F. Masri. Modeling the oscillatory dynamic behaviour of electrorheological materials in shear. *Smart Materials and Structures*, 1(4):275, 1992.

[91] S. F. Masri, R. Kumar, and R. C. Ehrgott. Modeling and control of an electrorheological device for structural control applications. *Smart Materials and Structures*, 4(1A):A121, 1995.

[92] H. P. Gavin, R. D. Hanson, and F. E. Filisko. Electrorheological dampers, part II: testing and modeling. *Journal of Applied Mechanics*, 63(3):676–682, 1996.

[93] E. F. Crawley and A. C. Aubert. Identification of nonlinear structural elements by force-state mapping. *AIAA journal*, 24(1):155–162, 1986.

[94] M. A. Al-Hadid and J. R. Wright. Developments in the force-state mapping technique for non-linear systems and the extension to the location of non-linear elements in a lumped-parameter system. *Mechanical Systems and Signal Processing*, 3(3):269–290, 1989.

[95] E. F. Crawley and K. J. O'Donnell. A procedure for calculating the damping in multi-element space structures. *Acta Astronautica*, 15(12):987–996, 1987.

[96] E. F. Crawley and K. J. O'Donnell. Force-state mapping identification of nonlinear joints. *AIAA journal*, 25(7):1003–1010, 1987.

[97] B. D. Ferney and S. L. Folkman. Force-state characterization of struts using pinned joints. *Shock and Vibration*, 4(2):103–113, 1997.

[98] S. Duym. An alternative force state map for shock absorbers. *Proceedings of the Institution of Mechanical Engineers, Part D: Journal of Automobile Engineering*, 211(3):175–179, 1997.

[99] K. Worden, W. J. Staszewski, and J. J. Hensman. Natural computing for mechanical systems research: A tutorial overview. *Mechanical Systems and Signal Processing*, 25(1):4–111, 2011.

[100] S. F. Masri, A. G. Chassiakos, and T. K. Caughey. Identification of nonlinear dynamic systems using neural networks. *Journal of Applied Mechanics*, 60(1):123–133, 1993.

[101] D. J. Kim and B. M. Kim. Application of neural network and fem for metal forming processes. *International Journal of Machine Tools and Manufacture*, 40(6):911–925, 2000.

[102] R. Teti and D. D'Addona. Intelligent classification of neural network models for mild steel behaviour in hot forming. *Proceedings of the Institution of Mechanical Engineers, Part B: Journal of Engineering Manufacture*, 218(6):619–630, 2004.

[103] Ł. Sztangret, D. Szeliga, J. Kusiak, and M. Pietrzyk. Application of inverse analysis with metamodelling for identification of metal flow stress. *Canadian Metallurgical Quarterly*, 51(4):440–446, 2012.

[104] I. Zohourkari, S. Assarzadeh, and M. Zohoor. Modeling and analysis of hot extrusion metal forming process using artificial neural network and anova. In *ASME 2010 10th Biennial Conference on Engineering Systems Design and Analysis*, pages 831–839. American Society of Mechanical Engineers, 2010.

[105] I. Babuska and J. T. Oden. Verification and validation in computational engineering and science: basic concepts. *Computer methods in applied mechanics and engineering*, 193(36):4057–4066, 2004.

[106] C. J. Roy and W. L. Oberkampf. A comprehensive framework for verification, validation, and uncertainty quantification in scientific computing. *Computer Methods in Applied Mechanics and Engineering*, 200(25):2131 – 2144, 2011.

[107] W. L. Oberkampf and T. G. Trucano. Verification and validation in computational fluid dynamics. *Progress in Aerospace Sciences*, 38(3):209 – 272, 2002.

[108] C. Gräbner. How to relate models to reality? an epistemological framework for the validation and verification of computational models. *Journal of Artificial Societies and Social Simulation*, 21(3), 2018.

[109] M. Kumar and A. S. Whittaker. Cross-platform implementation, verification and validation of advanced mathematical models of elastomeric seismic isolation bearings. *Engineering Structures*, 175:926–943, 2018.

[110] J. P. C. Kleijnen. Verification and validation of simulation models. *European journal of operational research*, 82(1):145–162, 1995.

[111] P. Bogacki and L. F. Shampine. A 3(2) pair of Runge-Kutta formulas. *Applied Mathematics Letters*, 2(4):321 – 325, 1989.

[112] T. Chai and R. R. Draxler. Root mean square error (RMSE) or mean absolute error (MAE)?-Arguments against avoiding RMSE in the literature. *Geoscientific model development*, 7(3):1247–1250, 2014.

[113] H. Madsen, P. Pinson, G. Kariniotakis, H. A. Nielsen, and T. S. Nielsen. Standardizing the performance evaluation of short-term wind power prediction models. *Wind Engineering*, 29(6):475–489, 2005.

[114] E.ON. The value of energy, 2019. [Online; accessed 25-Apr-2019]. Available from: https://www.themanufacturer.com/reports-whitepapers/do-uk-manufacturers-understand-the-value-of-energy/.

[115] G. E. Forsythe, M. A. Malcolm, and C. B. Moler. *Computer methods for mathematical computations*, volume 259. Prentice-hall Englewood Cliffs, NJ, 1977.

[116] F. Ferretti, A. Saltelli, and S. Tarantola. Trends in sensitivity analysis practice in the last decade. *Science of the Total Environment*, 568:666–670, 2016.

[117] A. Saltelli and P. Annoni. How to avoid a perfunctory sensitivity analysis. *Environmental Modelling & Software*, 25(12):1508–1517, 2010.

[118] M. D. Morris. Factorial sampling plans for preliminary computational experiments. *Technometrics*, 33(2):161–174, 1991.

[119] I. M. Sobol. Sensitivity estimates for nonlinear mathematical models. *Mathematical modelling and computational experiments*, 1(4):407–414, 1993.

[120] J. C. Helton and F. J. Davis. Illustration of sampling-based methods for uncertainty and sensitivity analysis. *Risk Analysis: An International Journal*, 22(3):591 – 622, 2002.

[121] B. Iooss and P. Lemaître. A review on global sensitivity analysis methods. In *Uncertainty management in simulation-optimization of complex systems*, pages 101–122. Springer, 2015.

[122] I. M. Sobol. Global sensitivity indices for nonlinear mathematical models and their monte carlo estimates. *Mathematics and computers in simulation*, 55(1-3):271–280, 2001.

[123] A. O'Hagan and M. Kennedy. The GEM software, 2017. [Online; accessed 02-May-2019]. Available from: http://www.tonyohagan.co.uk/academic/GEM/.

[124] N. Bilal. Implementation of Sobol's method of global sensitivity analysis to a compressor simulation model. In *International Compressor Engineering Conference*. Purdue University, 2014.

[125] D. C. Batterbee, N. D. Sims, W. Becker, K. Worden, and J. Rowson. Computational model of an infant brain subjected to periodic motion simplified modelling and bayesian sensitivity analysis. *Proceedings of the Institution of Mechanical Engineers, Part H: Journal of Engineering in Medicine*, 225(11):1036–1049, 2011.

[126] M. Scott, P. L. Green, D. O'Driscoll, K. Worden, and N. D. Sims. Sensitivity analysis of an advanced gas-cooled reactor control rod model. *Nuclear Engineering and Design*, 305:514–523, 2016.

[127] L. C. Astfalck, E. J. Cripps, J. P. Gosling, and I. A. Milne. Emulation of vessel motion simulators for computationally efficient uncertainty quantification. *Ocean Engineering*, 172:726–736, 2019.

[128] B. Wetenhall, J. M. Race, H. Aghajani, and J. Barnett. The main factors affecting heat transfer along dense phase CO2 pipelines. *International Journal of Greenhouse Gas Control*, 63:86–94, 2017.

[129] S. Martínez, A. Erkoreka, P. Eguía, E. Granada, and L. Febrero. Energy characterization of a PASLINK test cell with a gravel covered roof using a novel methodology: Sensitivity analysis and Bayesian calibration. *Journal of Building Engineering*, 22:1–11, 2019.

[130] J. Cariboni, D. Gatelli, R. Liska, and A. Saltelli. The role of sensitivity analysis in ecological modelling. *Ecological modelling*, 203(1-2):167–182, 2007.

[131] F. Pianosi, K. Beven, J. Freer, J. W. Hall, J. Rougier, D. B. Stephenson, and T. Wagener. Sensitivity analysis of environmental models: A systematic review with practical workflow. *Environmental Modelling & Software*, 79:214–232, 2016.

[132] A. Saltelli, M. Ratto, T. Andres, F. Campolongo, J. Cariboni, D. Gatelli, M. Saisana, and S. Tarantola. *Global sensitivity analysis: the primer*. John Wiley & Sons, 2008.

[133] F. Sarrazin, F. Pianosi, and T. Wagener. Global sensitivity analysis of environmental models: convergence and validation. *Environmental Modelling & Software*, 79:135–152, 2016.

[134] F. Campolongo, J. Cariboni, and A. Saltelli. An effective screening design for sensitivity analysis of large models. *Environmental modelling & software*, 22(10):1509–1518, 2007.

[135] A. Saltelli, S. Tarantola, F. Campolongo, and M. Ratto. Sensitivity analysis in practice: a guide to assessing scientific models. *Chichester, England*, 2004.

[136] Bosch Rexroth AG. Rexroth IndraDyn S MSK synchronous motors, project planning manual, 2006.

[137] F. Pianosi, F. Sarrazin, and T. Wagener. A Matlab toolbox for global sensitivity analysis. *Environmental Modelling & Software*, 70:80–85, 2015.

[138] M. W. Danyo. Self-piercing riveting (SPR) in the automotive industry: an overview. In *Self-Piercing Riveting*, pages 171–180. Woodhead Publishing, 2014.

[139] R. Hewitt. Self-piercing riveting (SPR) in automated vehicle construction. In *Self-Piercing Riveting*, pages 181–207. Woodhead Publishing, 2014.

[140] J. Sun, L. Xi, E. Pan, S. Du, and B. Ju. Integration of product quality and tool degradation for reliability modelling and analysis of multi-station manufacturing systems. *International Journal of computer integrated manufacturing*, 22(3):267–279, 2009.

[141] Y. He, Z. He, L. Wang, and C. Gu. Reliability modeling and optimization strategy for manufacturing system based on RQR chain. *Mathematical Problems in Engineering*, 2015, 2015.

[142] Y. Liu, L. Zhang, W. Liu, and P. C. Wang. Single-sided piercing riveting for adhesive bonding in vehicle body assembly. *Journal of Manufacturing Systems*, 32(3):498–504, 2013.

[143] V. Sartisson and G. Meschut. Self-locking self-pierce riveting: a new self-pierce riveting technology for multi-material applications in lightweight car body structures. *Welding in the World*, pages 1–8, 2017.

[144] DigiTwin. Digital twins for improved dynamic design, 2019. [Online; accessed 29-Apr-2019]. Available from: http://digitwin.ac.uk/.

[145] M. Sharma. Role of digital twin in automotive industry, 2018. [Online; accessed 31-May-2019]. Available from: https://www.smmt.co.uk/2018/12/role-of-digital-twin-in-automotive-industry/.

[146] EPSRC. EPSRC manufacturing the future theme regional meetings 2018/19 - workshop report, May 2019. [Online; accessed 31-May-2019]. Available from: https://epsrc.ukri.org/newsevents/pubs/mtfregionalmeetingsreport201819/.

[147] A. A. Kadir, X. Xu, and E. Hämmerle. Virtual machine tools and virtual machining - a technological review. *Robotics and computer-integrated manufacturing*, 27(3):494–508, 2011.

[148] N. Anh Vu, T. Lin, A. Azamatov, T. Lwin, and J.-W. Lee. Development of integrated rotorcraft design and virtual manufacturing framework. *Aircraft Engineering and Aerospace Technology*, 83(3):171–185, 2011.

[149] G. Pohit and K. Kumar. Virtual manufacturing of various types of gears and validation of the technique using rapid prototype. *Virtual and Physical Prototyping*, 7(2):153–171, 2012.

[150] D. K. Lee, Y. Kim, I. H. Hwang, D. K. Oh, and J. G. Shin. Study on a process-centric modeling methodology for virtual manufacturing of ships and offshore structures in shipyards. *The International Journal of Advanced Manufacturing Technology*, 71(1-4):621–633, 2014.

[151] M. Armendia, D. Euhus, and F. Peysson. Twin-control: a new concept towards machine tool health management. In *3rd European Conference of the Prognostics and Health Management Society. Bilbao, Spain*, pages 5–8, 2016.

[152] X. Bao, X. Chen, X. Luo, and H. Zuo. Gray-box modeling and QFT control for precision servo transmission systems. *Frontiers of Mechanical Engineering*, 6(4):442–448, 2011.

[153] A. J. Isaksson. Some aspects of industrial system identification. *IFAC Proceedings Volumes*, 46(32):153–159, 2013.

[154] M. Gebhardt, J. Mayr, N. Furrer, T. Widmer, S. Weikert, and W. Knapp. High precision grey-box model for compensation of thermal errors on five-axis machines. *CIRP annals*, 63(1):509–512, 2014.

[155] R. Caponetto, S. Graziani, F. Pappalardo, and F. Sapuppo. Identification of IPMC nonlinear model via single and multi-objective optimization algorithms. *ISA transactions*, 53(2):481–488, 2014.

[156] J.-P. Noël and J. Schoukens. Grey-box state-space identification of nonlinear mechanical vibrations. *International Journal of Control*, 91(5):1118–1139, 2018.

[157] A. Vargas, M. D. Iqbal, J. S. Erickson, and K. P. Bennett. Grey-box process control mining for anomaly monitoring and deconstruction. *arXiv preprint arXiv:1808.03709*, 2018.

Appendix A

Experimental Setup

Additional details on the experimental system are provided here. Figures A.1(a) and (b) show the configuration screens for the primary and secondary load cells respectively.

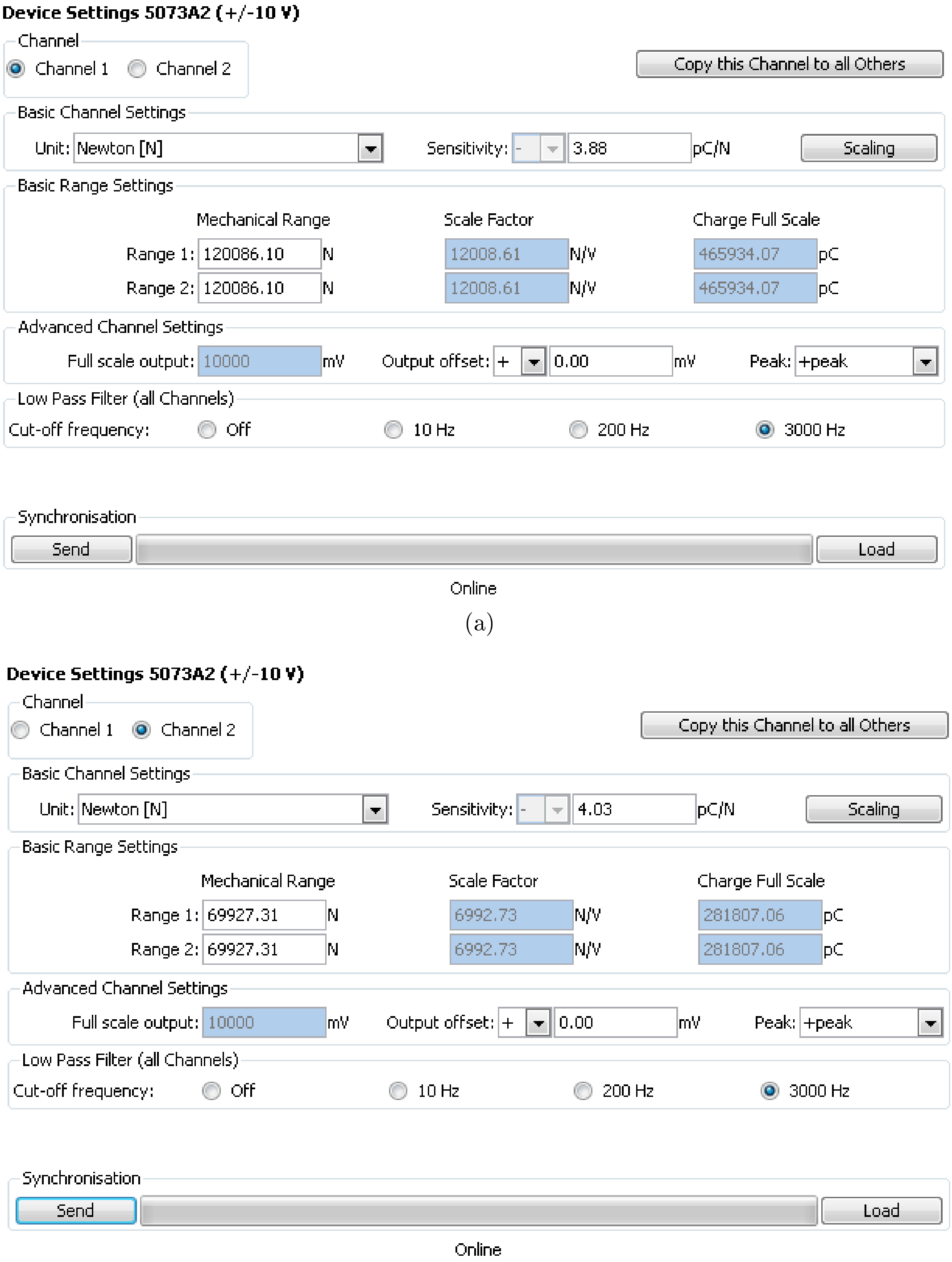

Device Settings 5073A2 (+/-10 V)

Channel: ● Channel 1 ○ Channel 2

Basic Channel Settings

Unit: Newton [N]
Sensitivity: - 3.88 pC/N

Basic Range Settings

	Mechanical Range	Scale Factor	Charge Full Scale
Range 1:	120086.10 N	12008.61 N/V	465934.07 pC
Range 2:	120086.10 N	12008.61 N/V	465934.07 pC

Advanced Channel Settings

Full scale output: 10000 mV
Output offset: + 0.00 mV
Peak: +peak

Low Pass Filter (all Channels)

Cut-off frequency: ○ Off ○ 10 Hz ○ 200 Hz ● 3000 Hz

Synchronisation

Online

(a)

Device Settings 5073A2 (+/-10 V)

Channel: ○ Channel 1 ● Channel 2

Basic Channel Settings

Unit: Newton [N]
Sensitivity: - 4.03 pC/N

Basic Range Settings

	Mechanical Range	Scale Factor	Charge Full Scale
Range 1:	69927.31 N	6992.73 N/V	281807.06 pC
Range 2:	69927.31 N	6992.73 N/V	281807.06 pC

Advanced Channel Settings

Full scale output: 10000 mV
Output offset: + 0.00 mV
Peak: +peak

Low Pass Filter (all Channels)

Cut-off frequency: ○ Off ○ 10 Hz ○ 200 Hz ● 3000 Hz

Synchronisation

Online

(b)

Figure A.1: Configuration of the charge amplifier using Manuware. (a) Channel 1, primary load cell. (b) Channel 2, secondary load cell.

Appendix B

Experimental Results

Here the results from the experimental investigation described in Chapter 3 are presented. The results are split into two sections corresponding to the two joint configurations studied, with eight subsections under each corresponding to the eight treatments from Table 3.4.

B.1 Joint A

B.1.1 Treatment 1: C-frame 1, setting velocity 150 mm/s, motor current limit 100%

Table B.1: Summary of results for joint A, treatment 1.

	Mean	Standard deviation
Peak punch force (kN)	18.45	0.10
Peak clamp force (kN)	8.18	0.04
Head height (mm)	0.37	0.01
Estimated rivet insertion distance using camera data (mm)	5.10	0.02
Energy dissipated in joint (J)	42.3	0.28

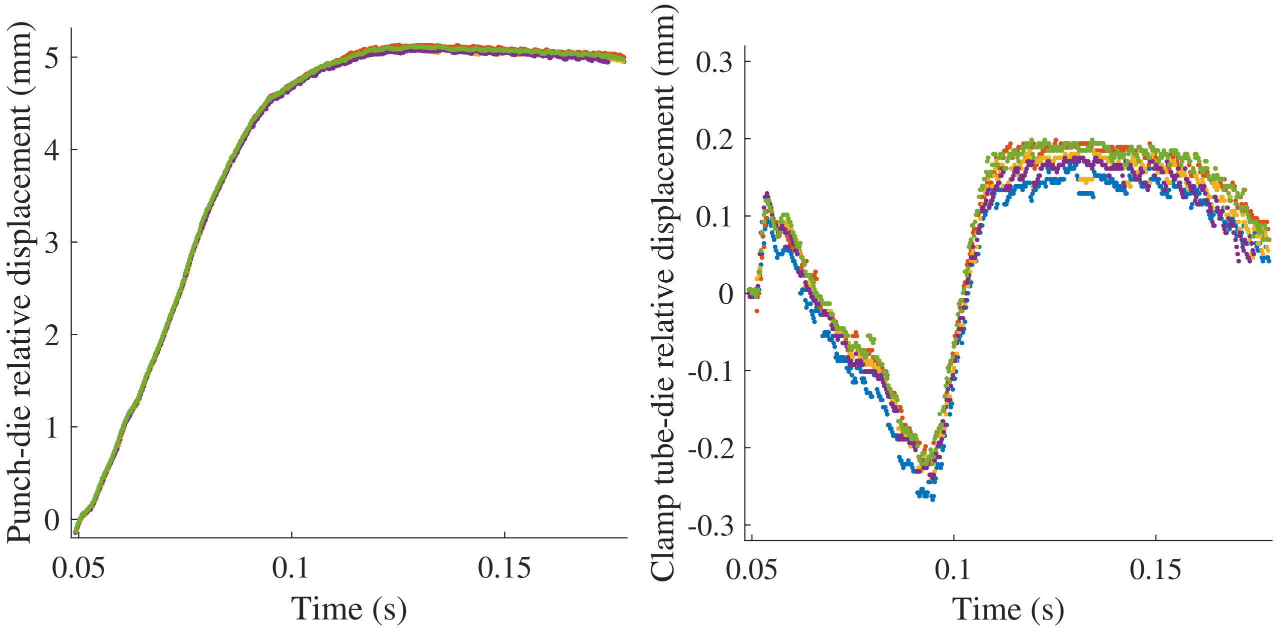

(a)

(b)

Figure B.1: (a) Relative displacement between the punch and the die vs. time. (b) Relative displacement between the clamping tube and the die vs. time.

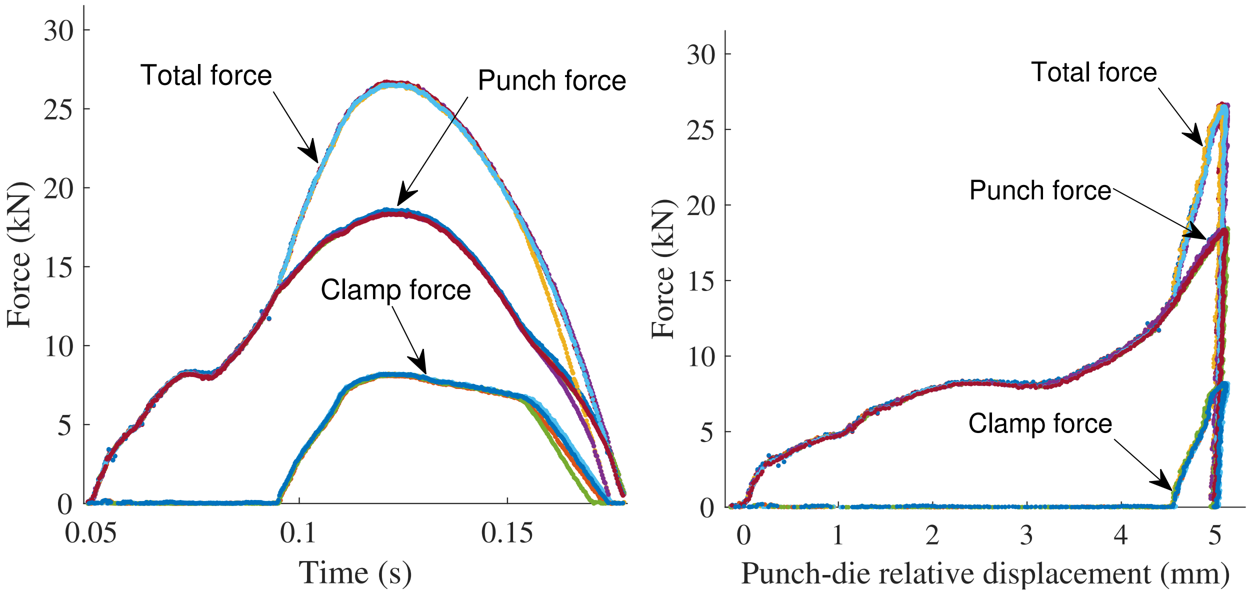

(a)

(b)

Figure B.2: (a) Process forces vs. time. (b) Process forces vs. relative displacement between the punch and the die.

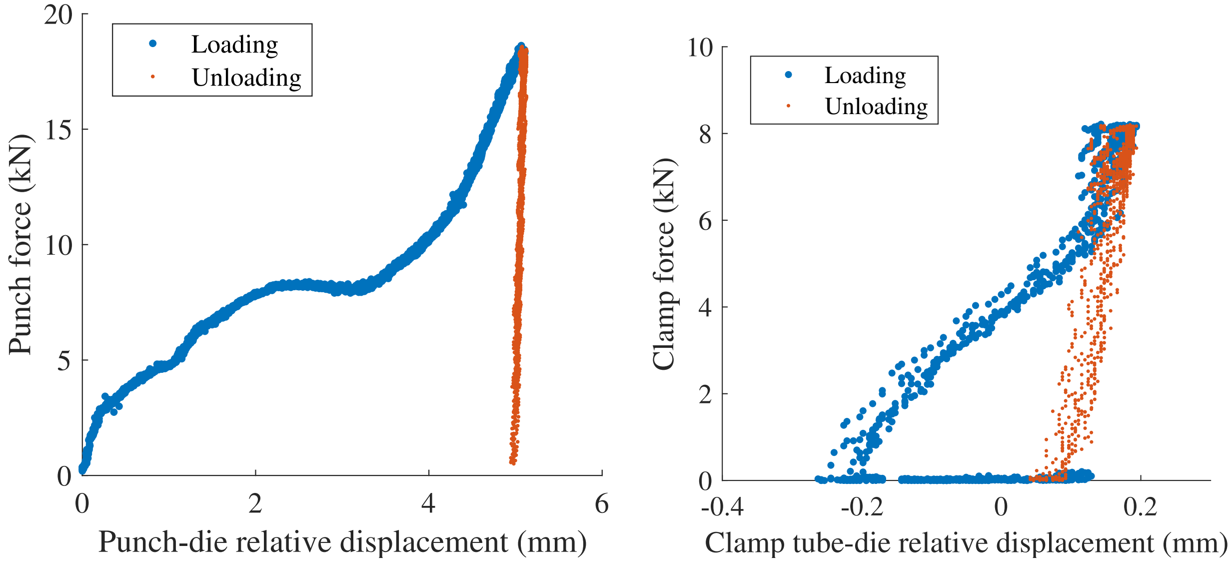

(a) (b)

Figure B.3: (a) Punch force vs. relative displacement between the punch and the die. (b) Clamp force vs. relative displacement between the clamp tube and the die.

B.1.2 Treatment 2: C-frame 1, setting velocity 150 mm/s, motor current limit 150%

Table B.2: Summary of results for joint A, treatment 2.

	Mean	Standard deviation
Peak punch force (kN)	21.79	0.16
Peak clamp force (kN)	8.71	0.08
Head height (mm)	0.16	0.02
Estimated rivet insertion distance using camera data (mm)	5.34	0.01
Energy dissipated in joint (J)	46.86	0.25

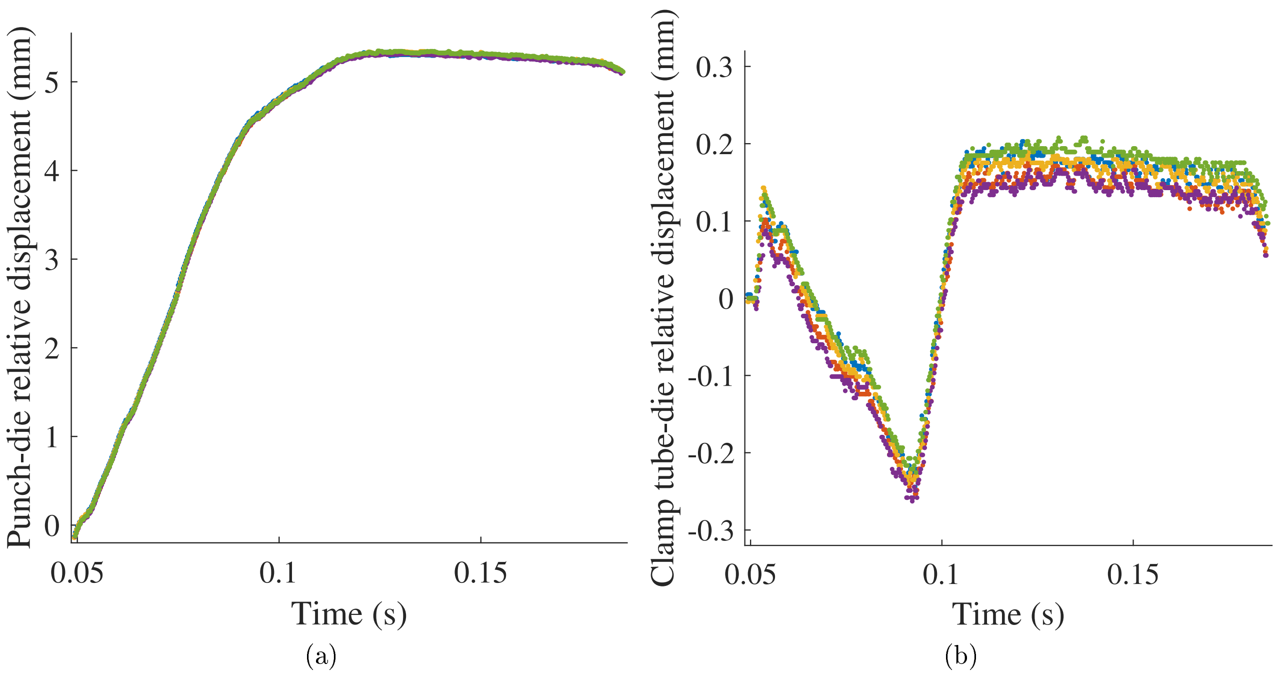

Figure B.4: (a) Relative displacement between the punch and the die vs. time. (b) Relative displacement between the clamping tube and the die vs. time.

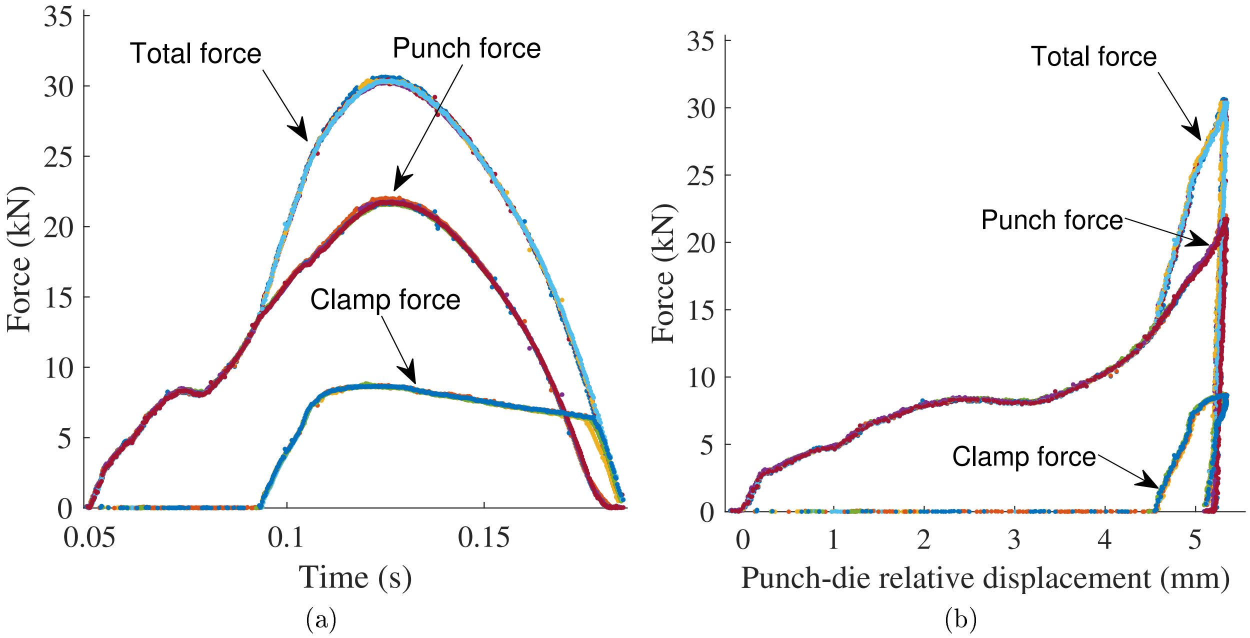

Figure B.5: (a) Process forces vs. time. (b) Process forces vs. relative displacement between the punch and the die.

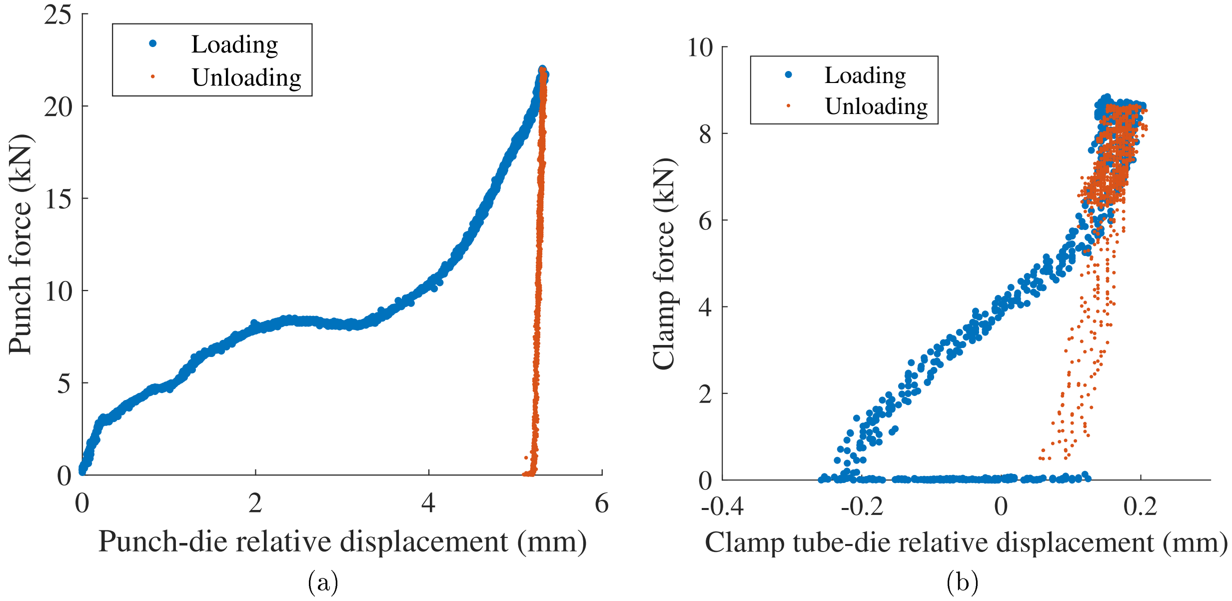

(a) (b)

Figure B.6: (a) Punch force vs. relative displacement between the punch and the die. (b) Clamp force vs. relative displacement between the clamp tube and the die.

B.1.3 Treatment 3: C-frame 1, setting velocity 250 mm/s, motor current limit 100%

Table B.3: Summary of results for joint A, treatment 3.

	Mean	Standard deviation
Peak punch force (kN)	38.10	0.10
Peak clamp force (kN)	9.66	0.02
Head height (mm)	-0.05	0.01
Estimated rivet insertion distance using camera data (mm)	5.52	0.03
Energy dissipated in joint (J)	52.80	0.88

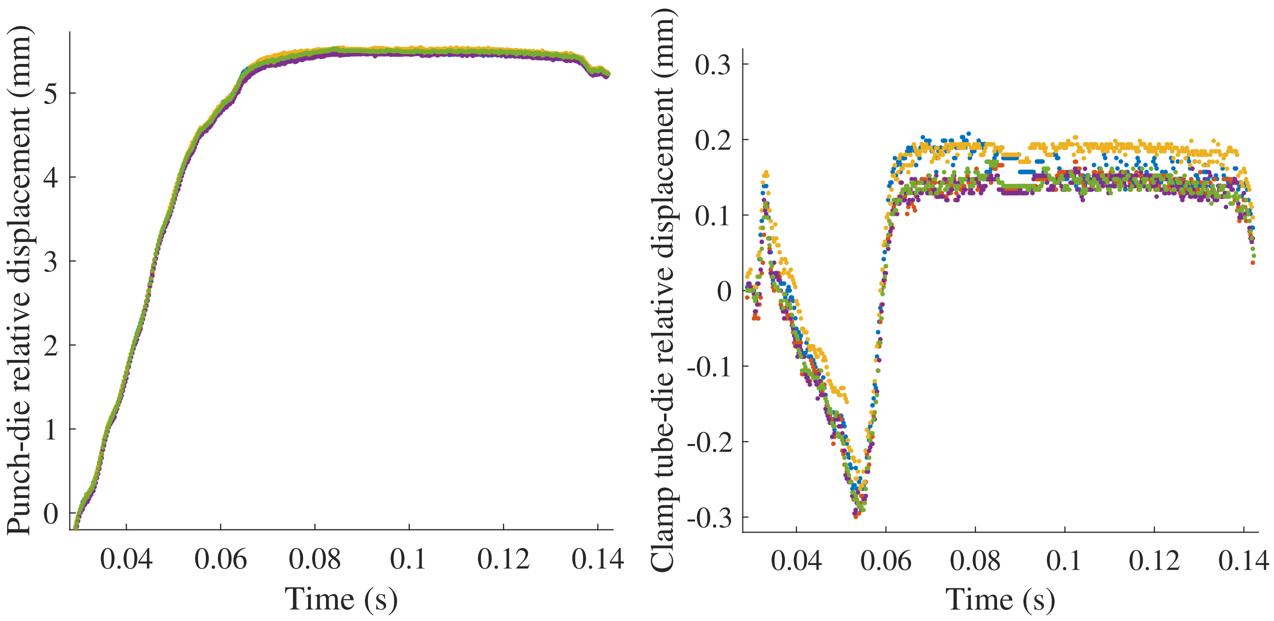

(a) (b)

Figure B.7: (a) Relative displacement between the punch and the die vs. time. (b) Relative displacement between the clamping tube and the die vs. time.

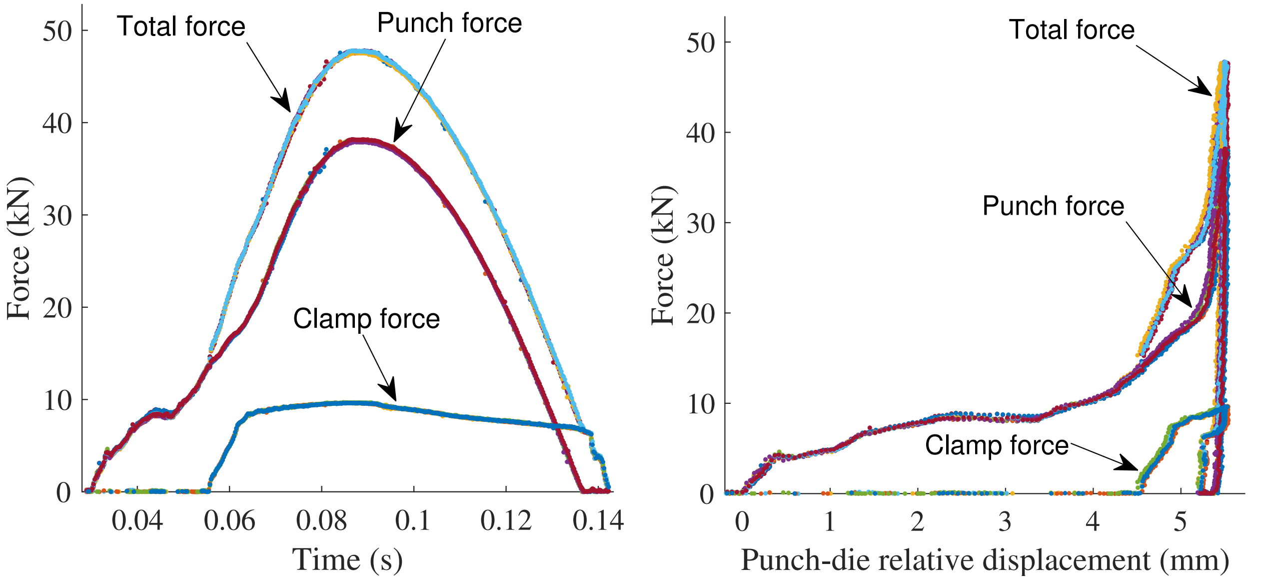

(a) (b)

Figure B.8: (a) Process forces vs. time. (b) Process forces vs. relative displacement between the punch and the die.

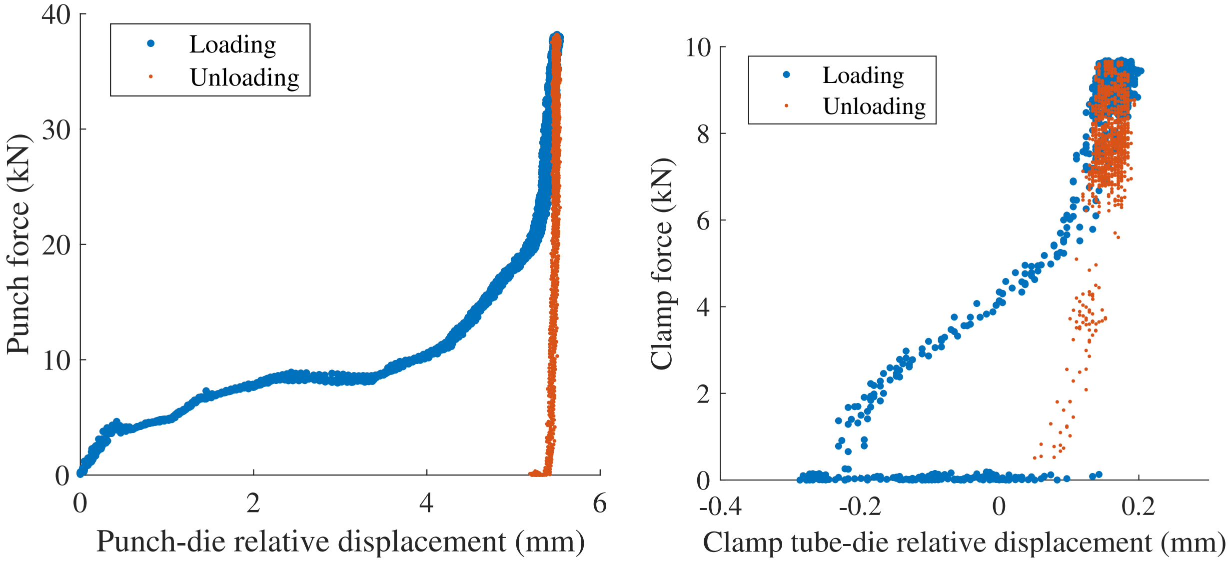

(a) (b)

Figure B.9: (a) Punch force vs. relative displacement between the punch and the die. (b) Clamp force vs. relative displacement between the clamp tube and the die.

B.1.4 Treatment 4: C-frame 1, setting velocity 250 mm/s, motor current limit 150%

Table B.4: Summary of results for joint A, treatment 4.

	Mean	Standard deviation
Peak punch force (kN)	41.49	0.07
Peak clamp force (kN)	9.90	0.03
Head height (mm)	-0.11	0.01
Estimated rivet insertion distance using camera data (mm)	5.57	0.02
Energy dissipated in joint (J)	54.72	0.78

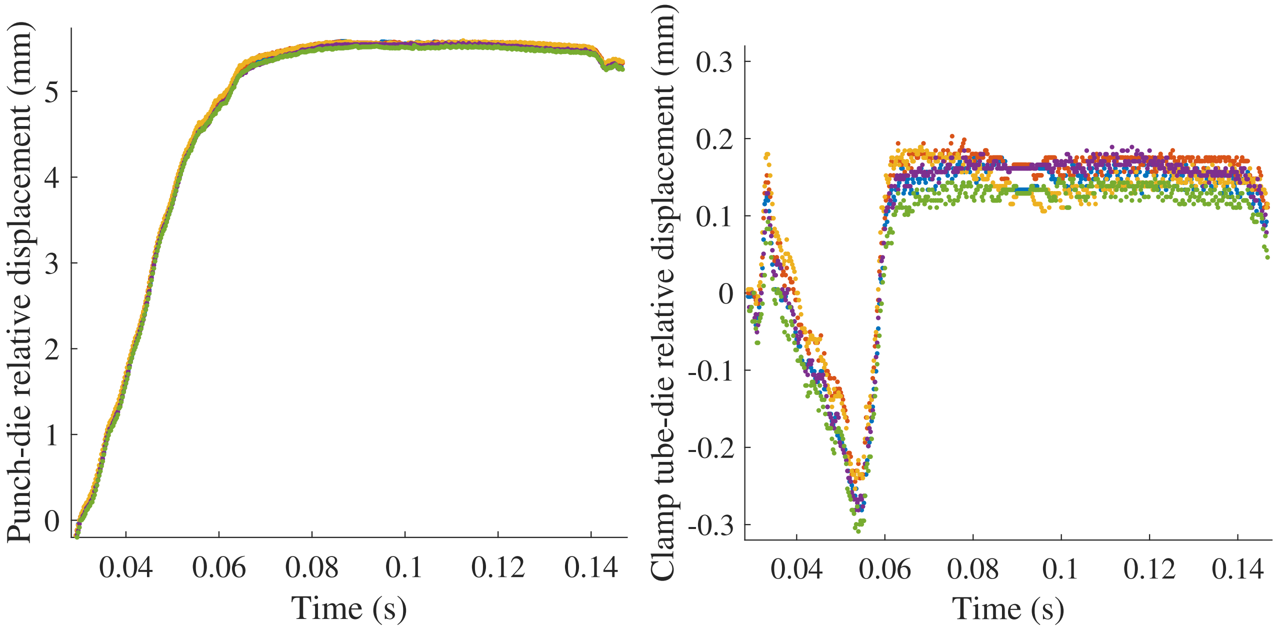

(a) (b)

Figure B.10: (a) Relative displacement between the punch and the die vs. time. (b) Relative displacement between the clamp tube and the die vs. time.

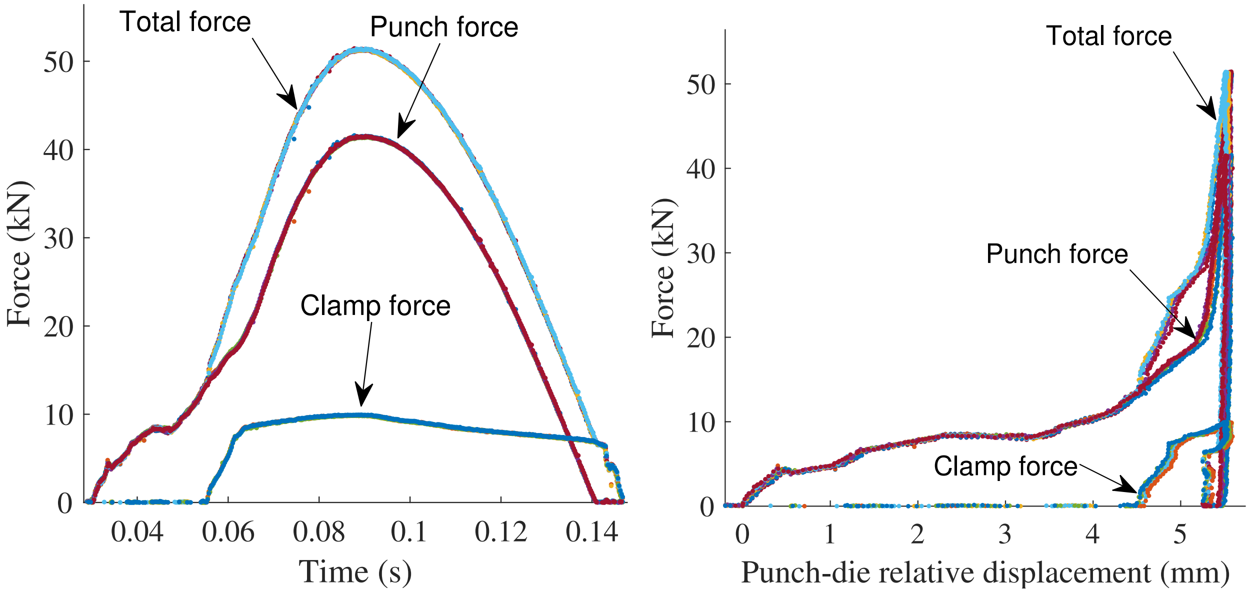

(a) (b)

Figure B.11: (a) Process forces vs. time. (b) Process forces vs. relative displacement between the punch and the die.

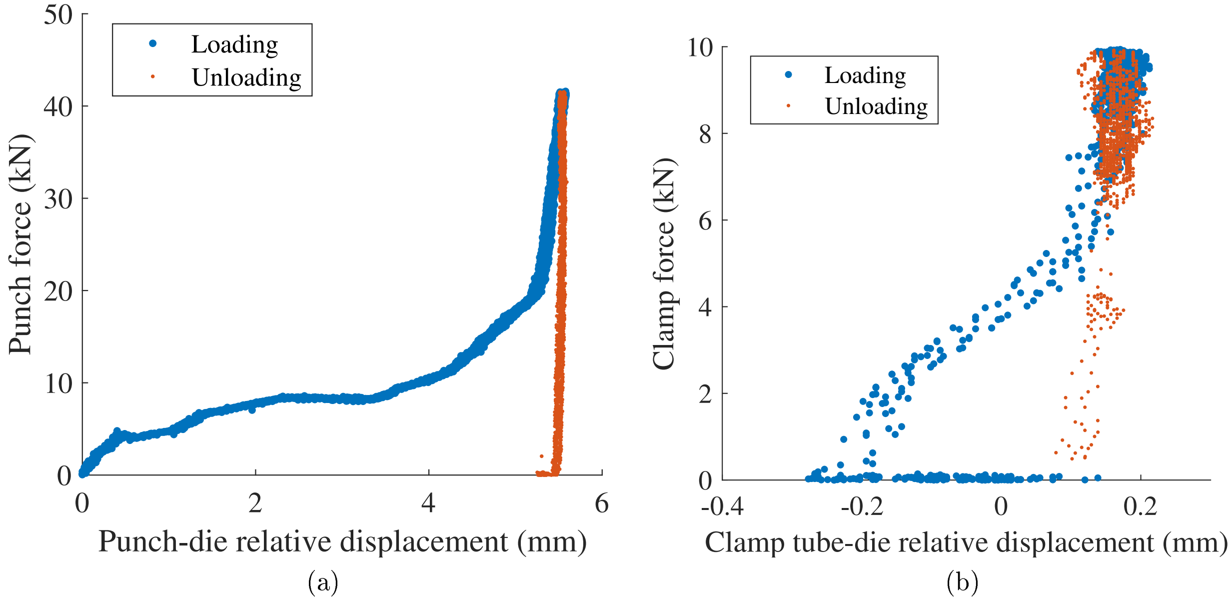

(a) (b)

Figure B.12: (a) Punch force vs. relative displacement between the punch and the die. (b) Clamp force vs. relative displacement between the clamp tube and the die.

B.1.5 Treatment 5: C-frame 2, setting velocity 150 mm/s, motor current limit 100%

Table B.5: Summary of results for joint A, treatment 5.

	Mean	Standard deviation
Peak punch force (kN)	21.47	0.39
Peak clamp force (kN)	8.62	0.15
Head height (mm)	0.14	0.01
Estimated rivet insertion distance using camera data (mm)	5.28	0.03
Energy dissipated in joint (J)	47.36	0.57

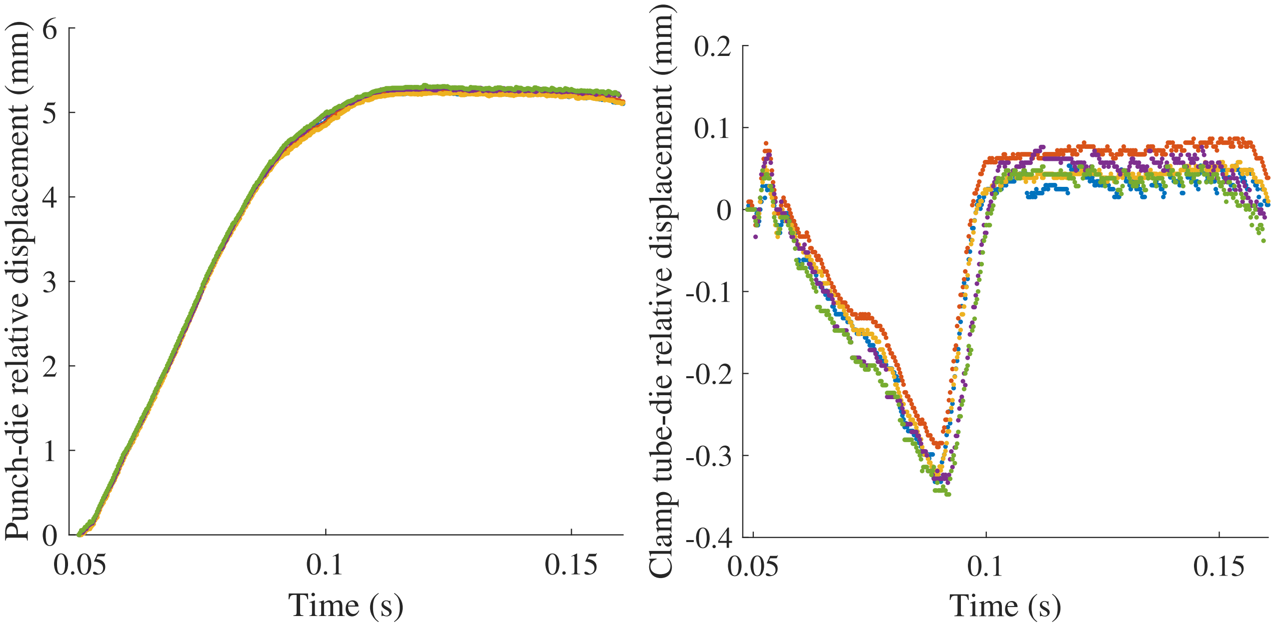

(a) (b)

Figure B.13: (a) Relative displacement between the punch and the die vs. time. (b) Relative displacement between the clamping tube and the die vs. time.

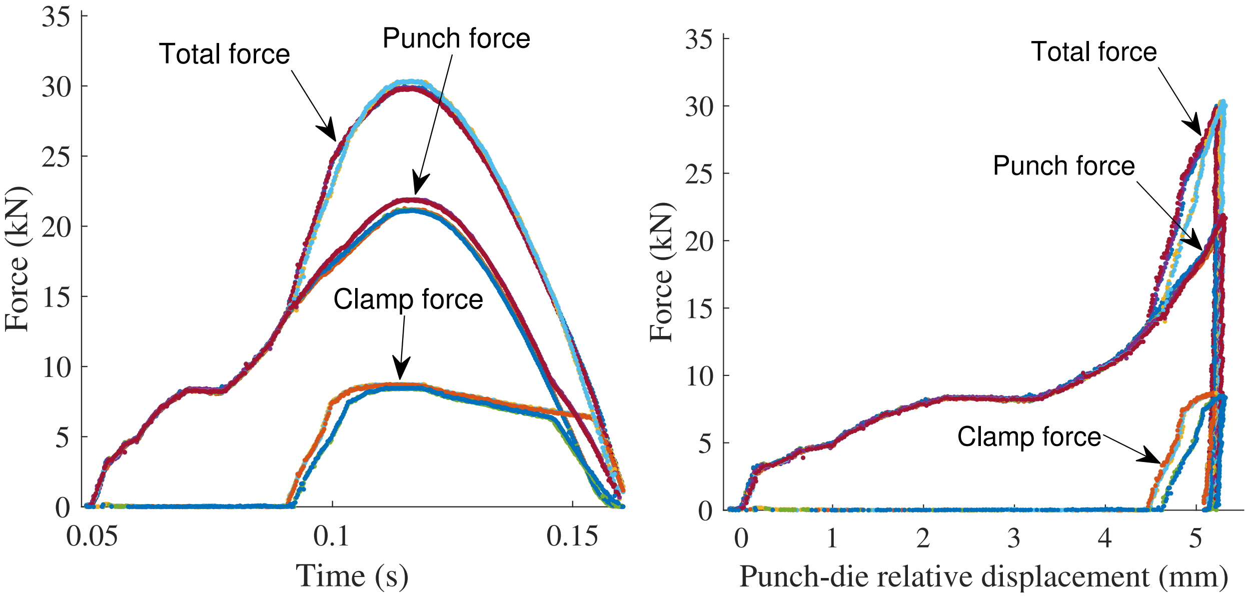

(a) (b)

Figure B.14: (a) Process forces vs. time. (b) Process forces vs. relative displacement between the punch and the die.

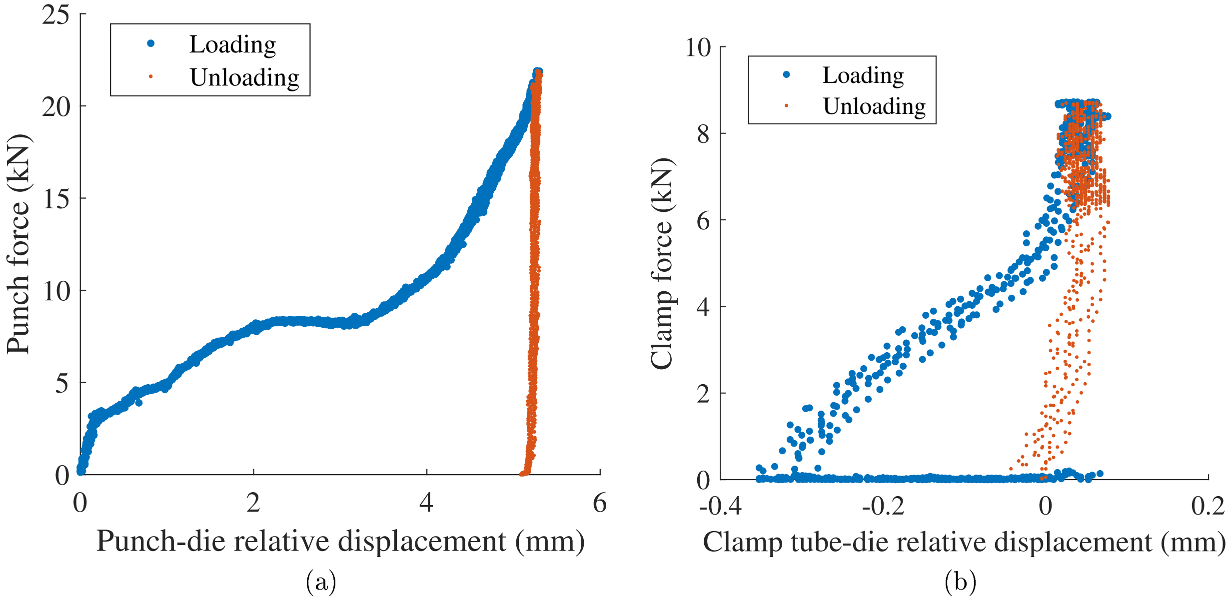

(a) (b)

Figure B.15: (a) Punch force vs. relative displacement between the punch and the die. (b) Clamp force vs. relative displacement between the clamp tube and the die.

B.1.6 Treatment 6: C-frame 2, setting velocity 150 mm/s, motor current limit 150%

Table B.6: Summary of results for joint A, treatment 6.

	Mean	Standard deviation
Peak punch force (kN)	26.96	0.28
Peak clamp force (kN)	9.02	0.09
Head height (mm)	0.03	0.01
Estimated rivet insertion distance using camera data (mm)	5.42	0.01
Energy dissipated in joint (J)	50.28	0.59

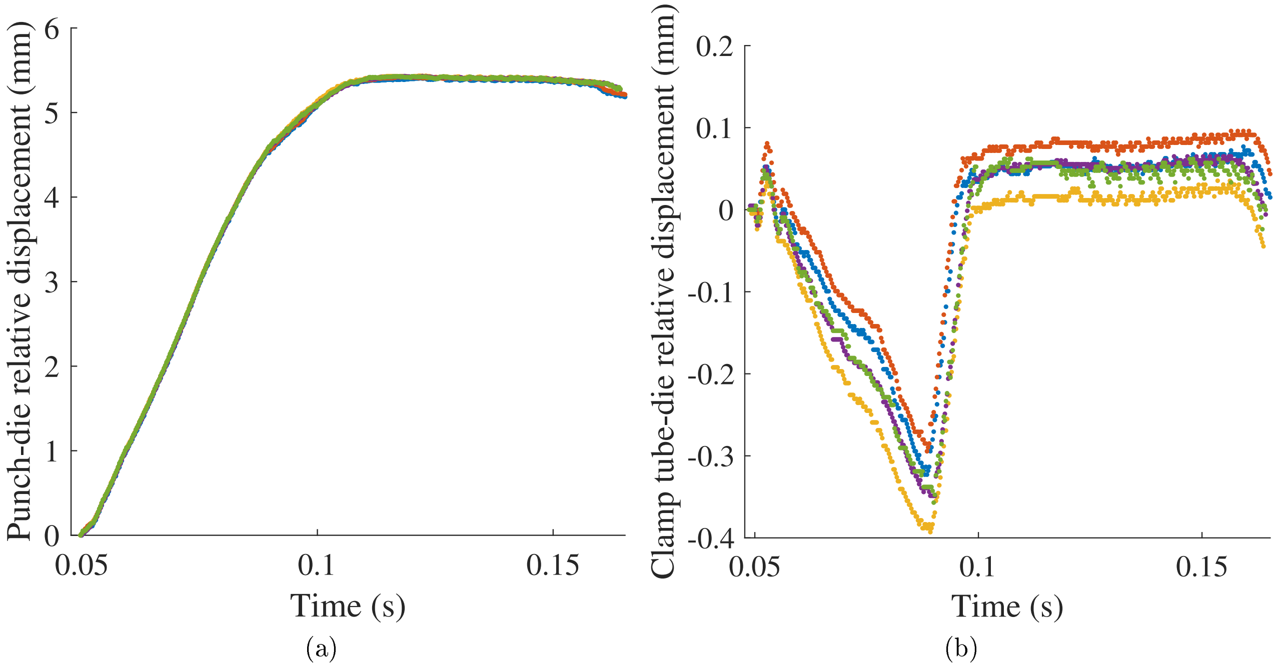

Figure B.16: (a) Relative displacement between the punch and the die vs. time. (b) Relative displacement between the clamping tube and the die vs. time.

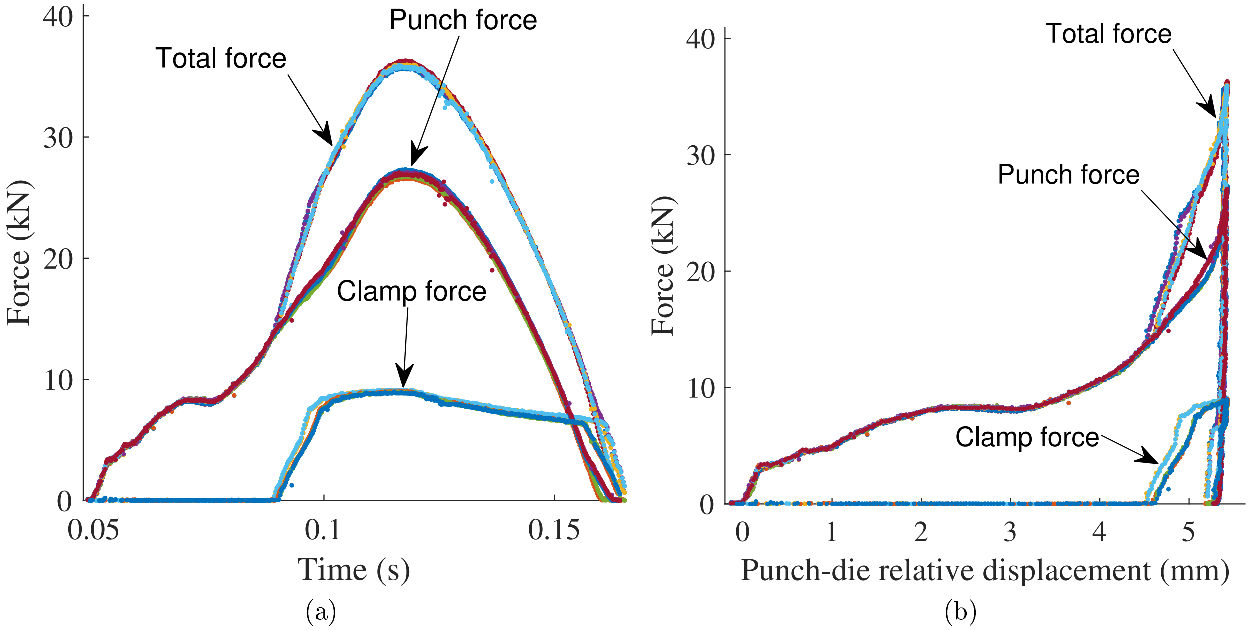

Figure B.17: (a) Process forces vs. time. (b) Process forces vs. relative displacement between the punch and the die.

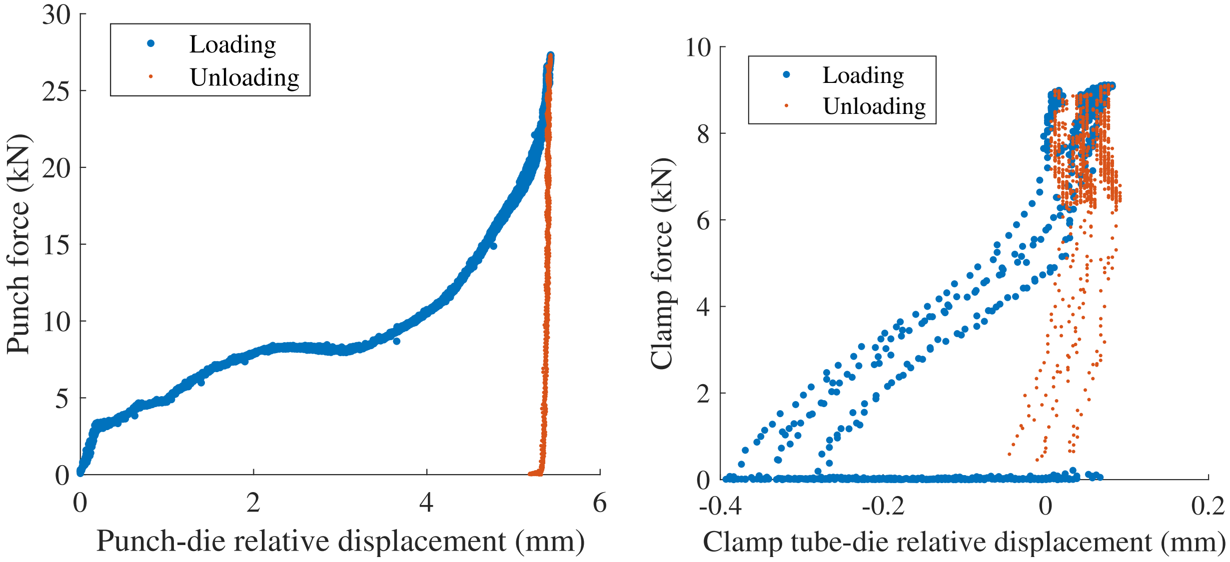

(a) (b)

Figure B.18: (a) Punch force vs. relative displacement between the punch and the die. (b) Clamp force vs. relative displacement between the clamp tube and the die.

B.1.7 Treatment 7: C-frame 2, setting velocity 250 mm/s, motor current limit 100%

Table B.7: Summary of results for joint A, treatment 7.

	Mean	Standard deviation
Peak punch force (kN)	46.35	0.18
Peak clamp force (kN)	10.45	0.17
Head height (mm)	-0.28	0.01
Estimated rivet insertion distance using camera data (mm)	5.80	0.03
Energy dissipated in joint (J)	62.20	0.53

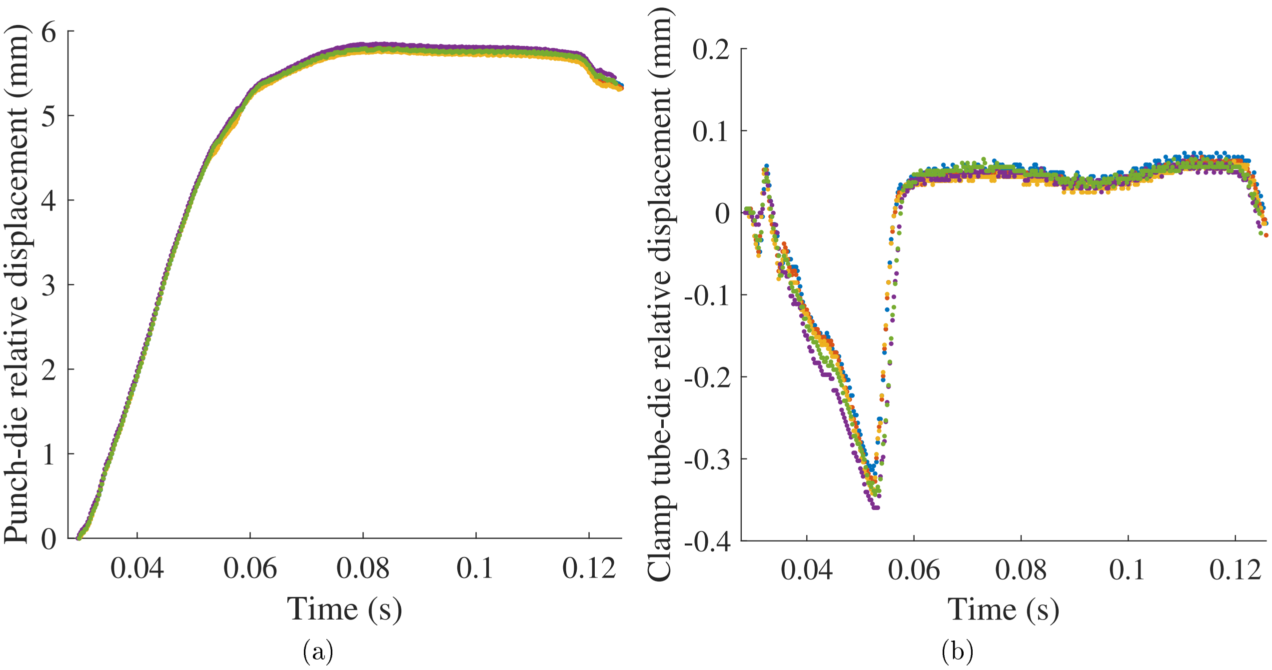

(a) (b)

Figure B.19: (a) Relative displacement between the punch and the die vs. time. (b) Relative displacement between the clamping tube and the die vs. time.

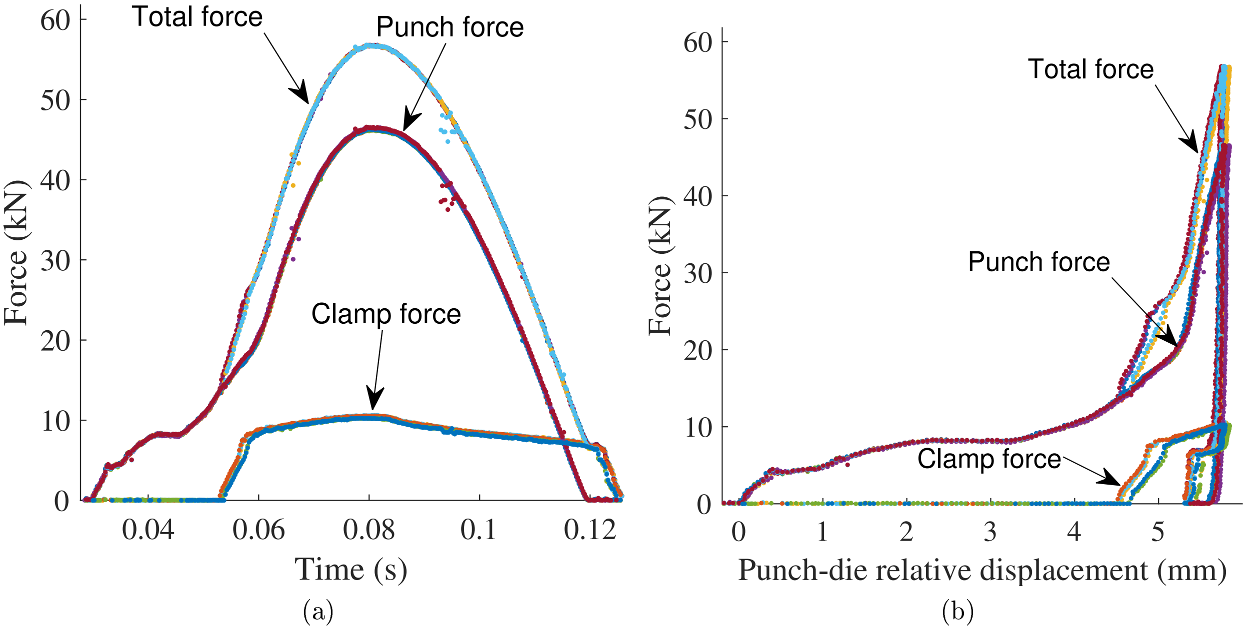

(a) (b)

Figure B.20: (a) Process forces vs. time. (b) Process forces vs. relative displacement between the punch and the die.

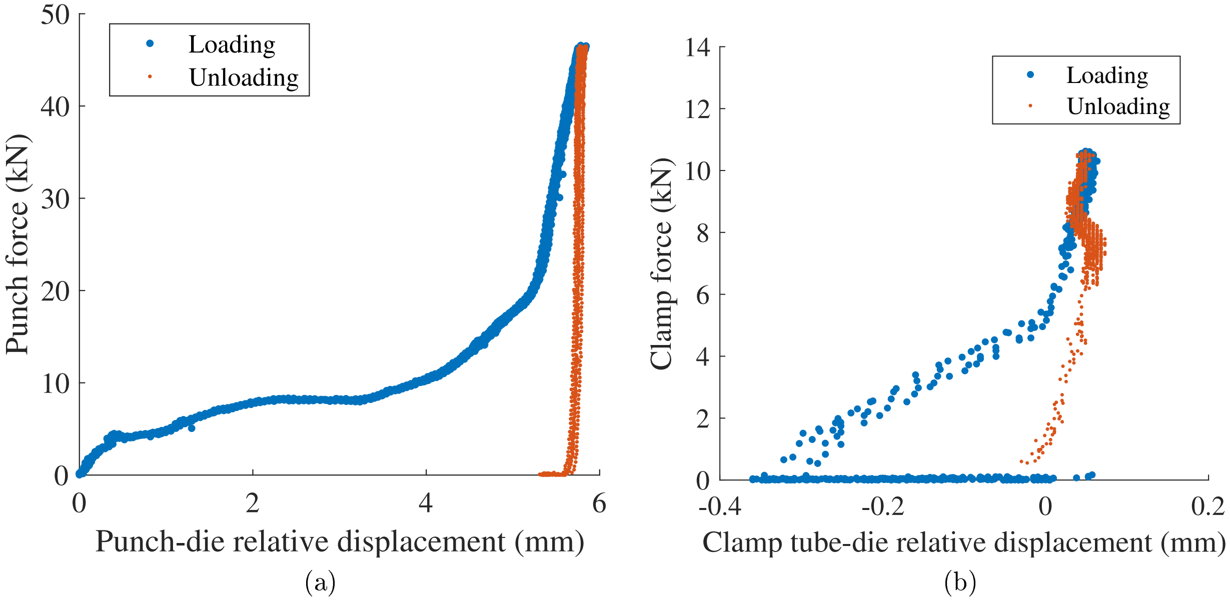

(a) (b)

Figure B.21: (a) Punch force vs. relative displacement between the punch and the die. (b) Clamp force vs. relative displacement between the clamp tube and the die.

B.1.8 Treatment 8: C-frame 2, setting velocity 250 mm/s, motor current limit 150%

Table B.8: Summary of results for joint A, treatment 8.

	Mean	Standard deviation
Peak punch force (kN)	48.51	0.77
Peak clamp force (kN)	12.26	1.54
Head height (mm)	-0.36	0.01
Estimated rivet insertion distance using camera data (mm)	5.91	0.04
Energy dissipated in joint (J)	67.18	1.61

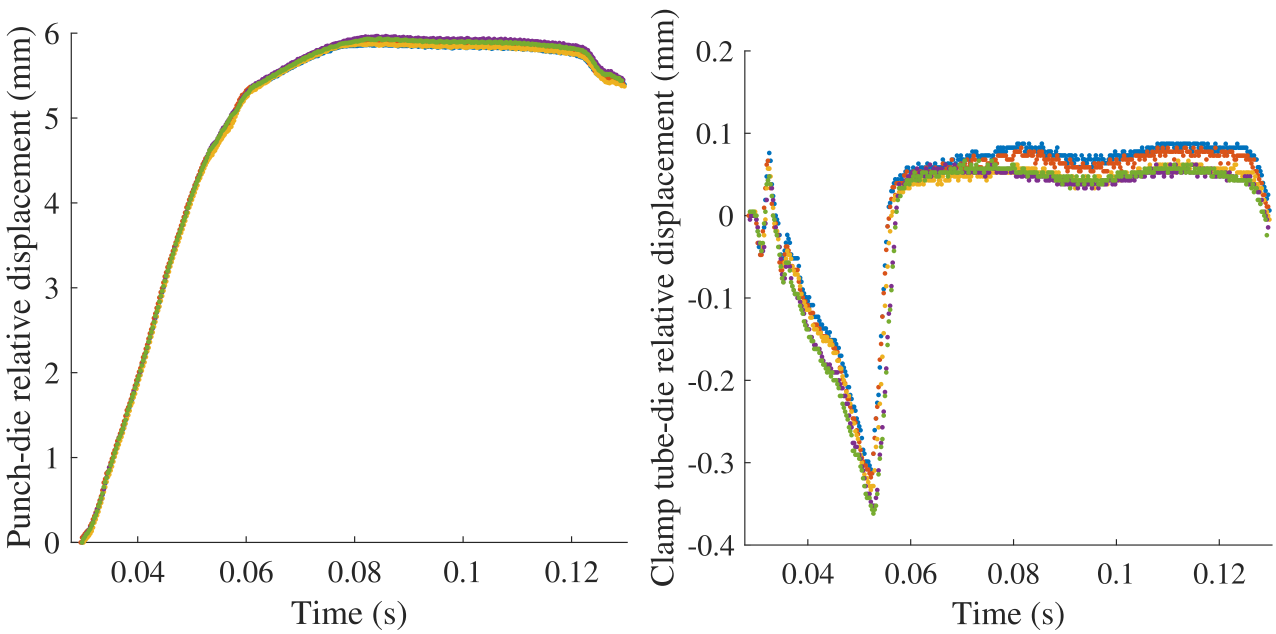

(a) (b)

Figure B.22: (a) Relative displacement between the punch and the die vs. time. (b) Relative displacement between the clamping tube and the die vs. time.

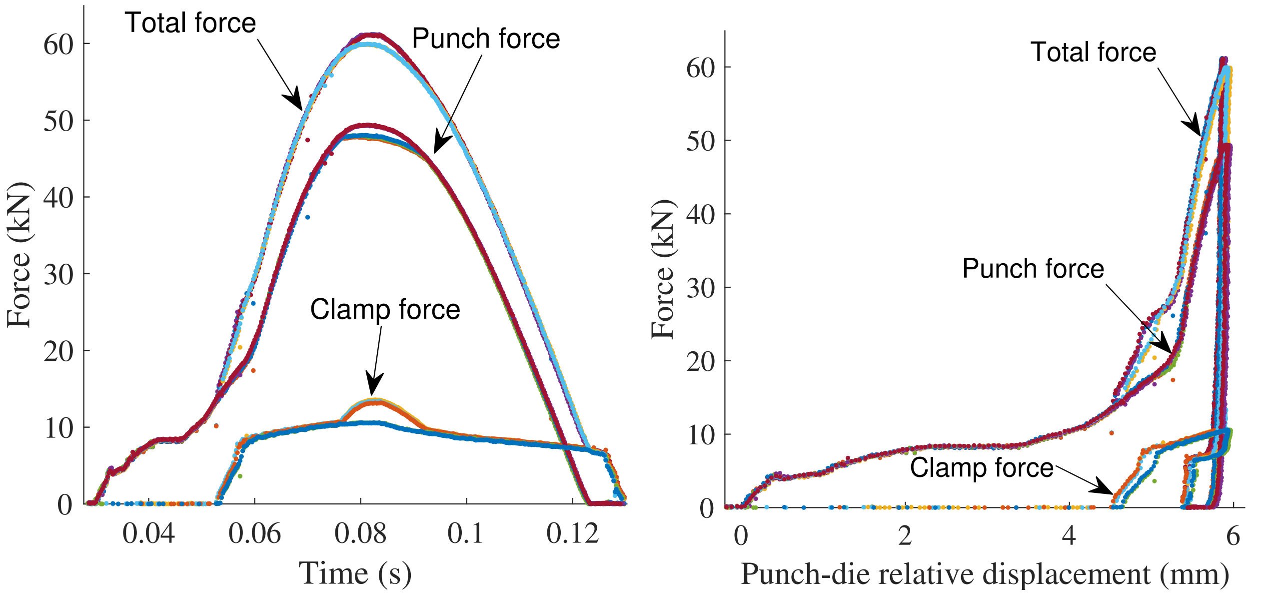

(a) (b)

Figure B.23: (a) Process forces vs. time. (b) Process forces vs. relative displacement between the punch and the die.

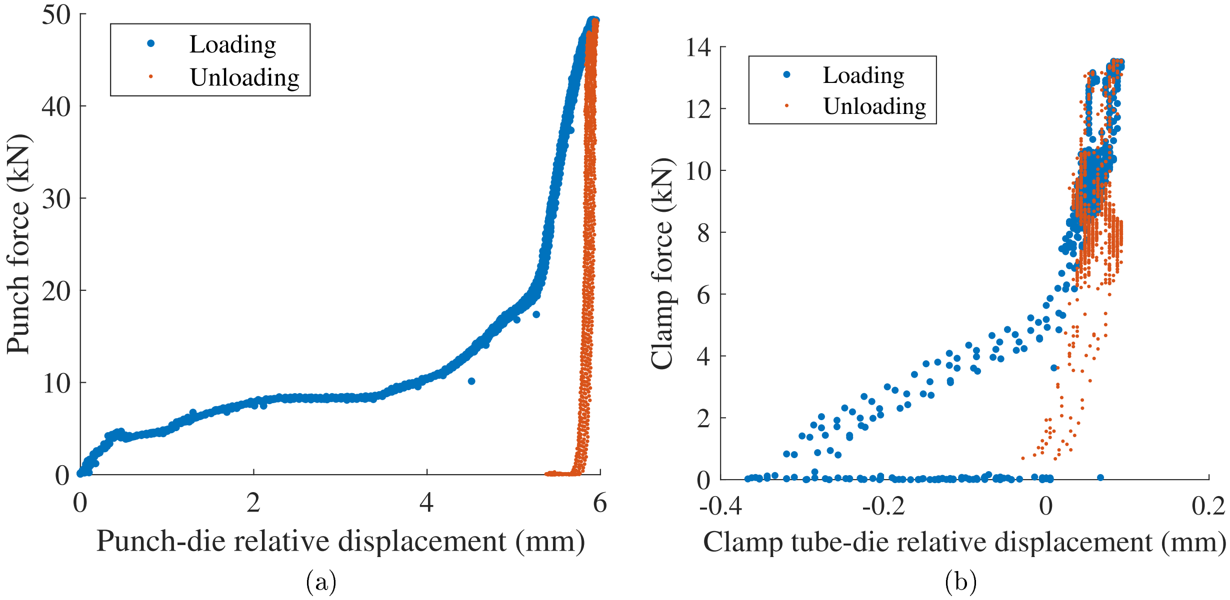

(a) (b)

Figure B.24: (a) Punch force vs. relative displacement between the punch and the die. (b) Clamp force vs. relative displacement between the clamp tube and the die.

B.2 Joint B

B.2.1 Treatment 1: C-frame 1, setting velocity 150 mm/s, motor current limit 100%

Table B.9: Summary of results for joint B, treatment 1.

	Mean	Standard deviation
Peak punch force (kN)	17.44	0.12
Peak clamp force (kN)	0.14	0.04
Head height (mm)	1.36	0.03
Estimated rivet insertion distance using camera data (mm)	5.58	0.03
Energy dissipated in joint (J)	60.78	0.31

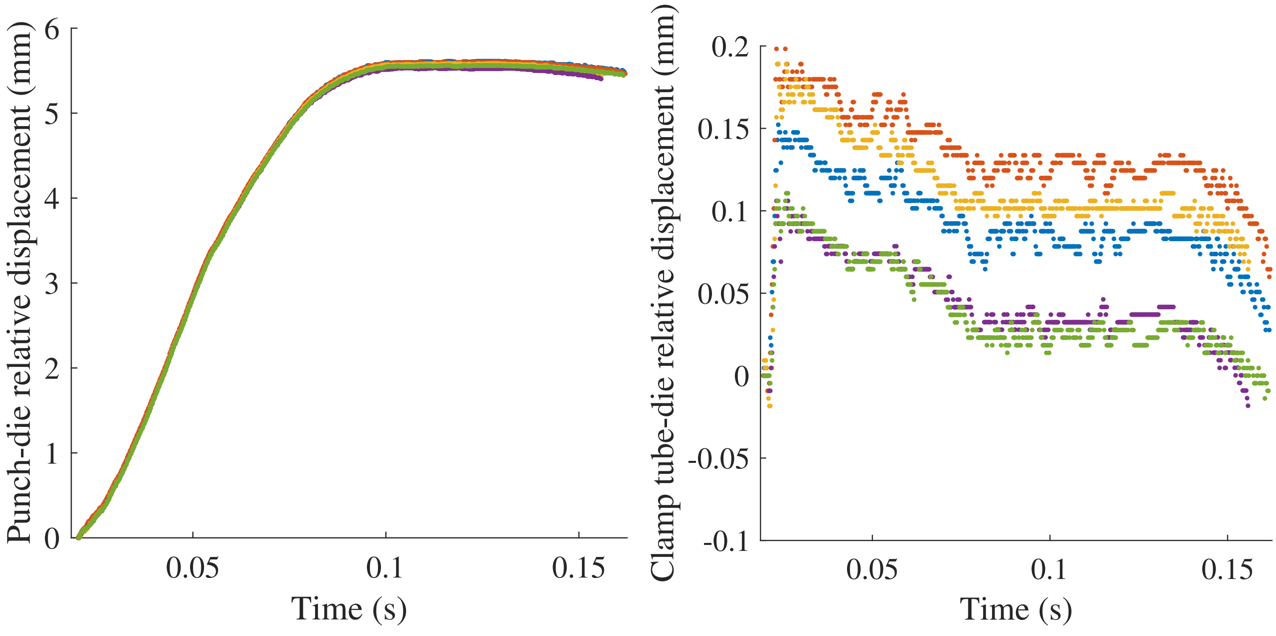

(a) (b)

Figure B.25: (a) Relative displacement between the punch and the die vs. time. (b) Relative displacement between the clamping tube and the die vs. time.

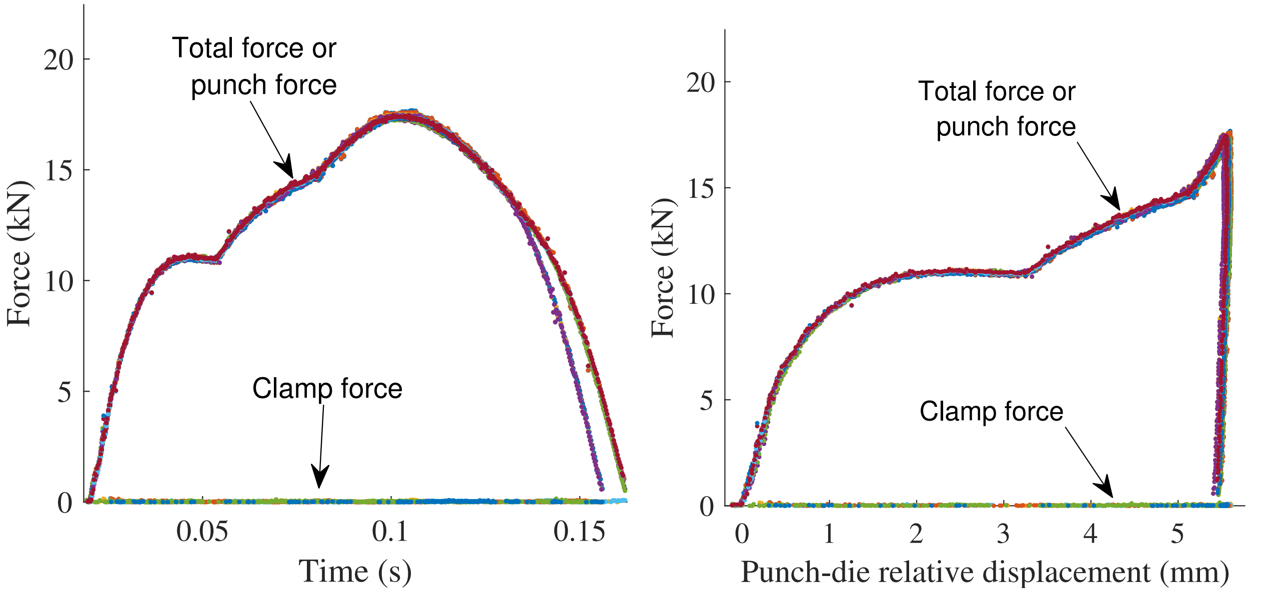

(a) (b)

Figure B.26: (a) Process forces vs. time. (b) Process forces vs. relative displacement between the punch and the die.

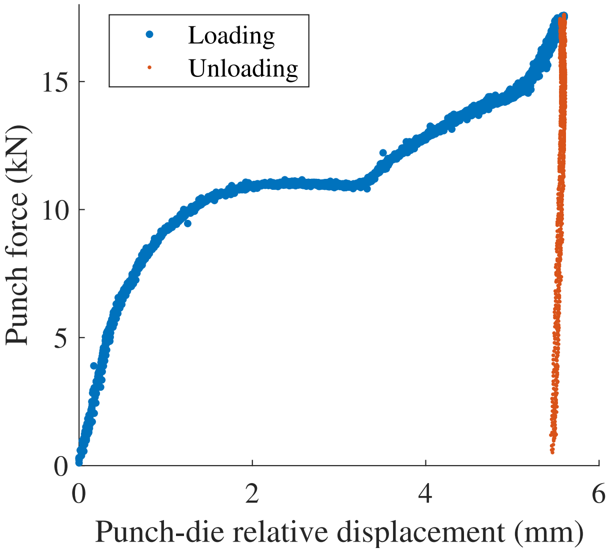

Figure B.27: Punch force vs. relative displacement between the punch and the die.

B.2.2 Treatment 2: C-frame 1, setting velocity 150 mm/s, motor current limit 150%

Table B.10: Summary of results for joint B, treatment 2.

	Mean	Standard deviation
Peak punch force (kN)	22.67	0.21
Peak clamp force (kN)	0.10	0.04
Head height (mm)	0.86	0.02
Estimated rivet insertion distance using camera data (mm)	6.07	0.03
Energy dissipated in joint (J)	70.80	0.28

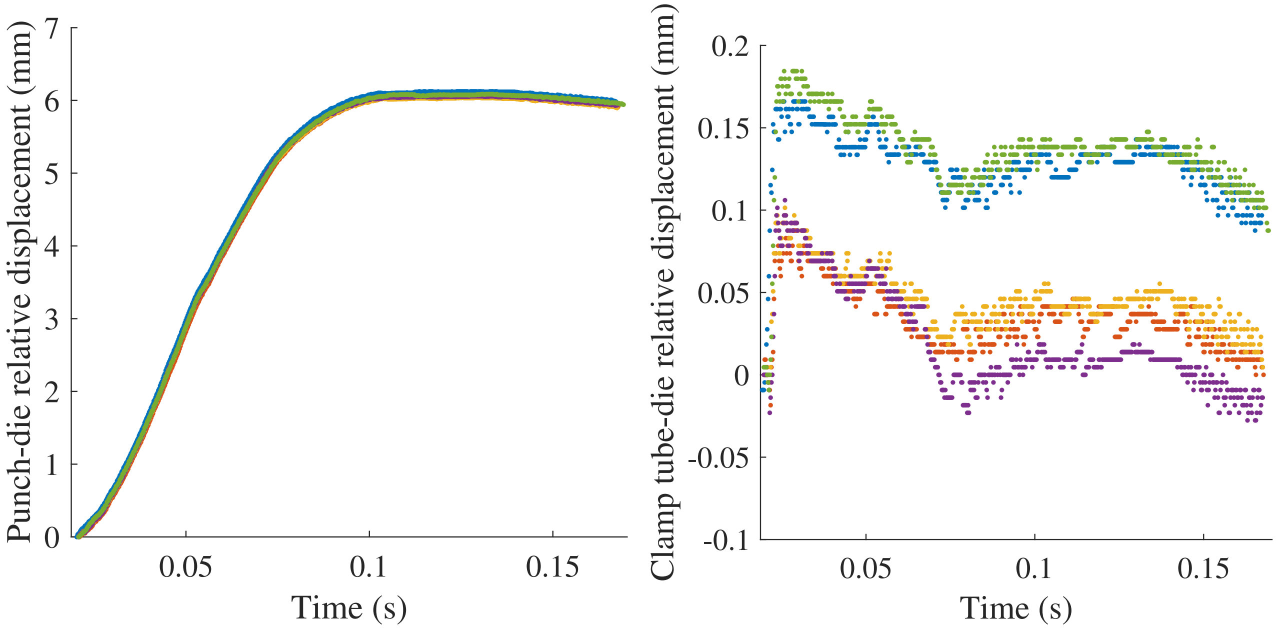

(a) (b)

Figure B.28: (a) Relative displacement between the punch and the die vs. time. (b) Relative displacement between the clamping tube and the die vs. time.

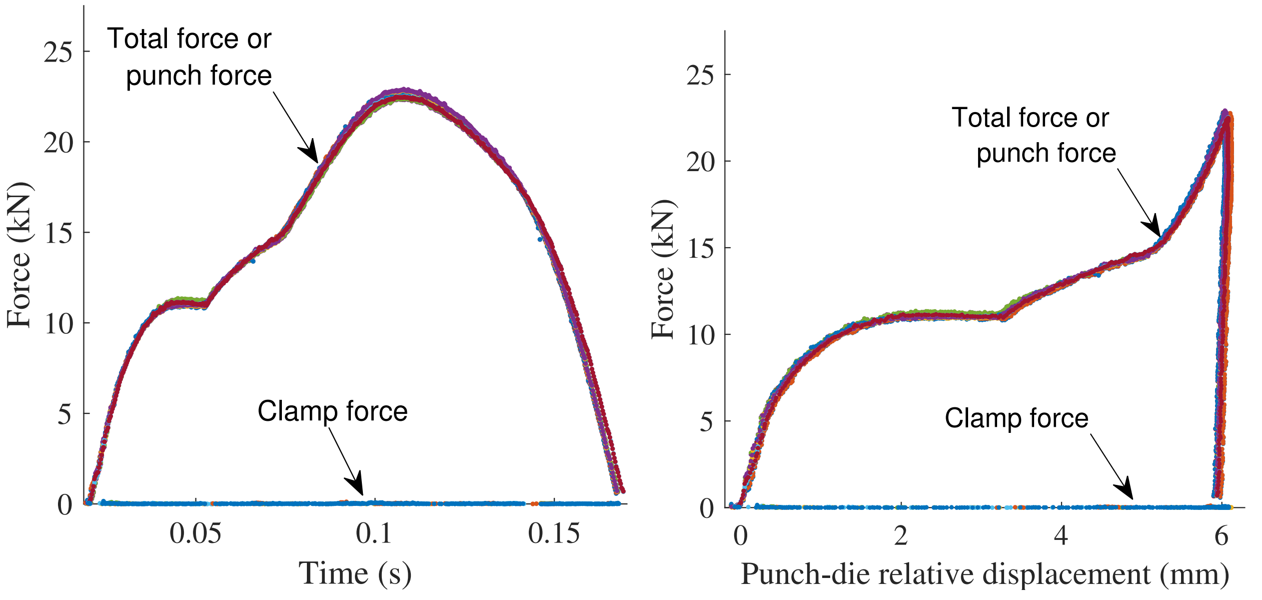

(a) (b)

Figure B.29: (a) Process forces vs. time. (b) Process forces vs. relative displacement between the punch and the die.

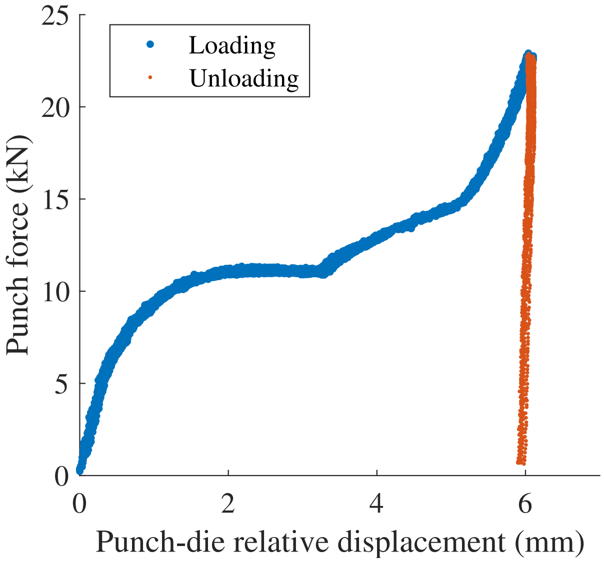

Figure B.30: Punch force vs. relative displacement between the punch and the die

B.2.3 Treatment 3: C-frame 1, setting velocity 250 mm/s, motor current limit 100%

Table B.11: Summary of results for joint B, treatment 3.

	Mean	Standard deviation
Peak punch force (kN)	33.13	0.07
Peak clamp force (kN)	8.83	0.04
Head height (mm)	0.32	0.02
Estimated rivet insertion distance using camera data (mm)	6.58	0.04
Energy dissipated in joint (J)	84.18	0.16

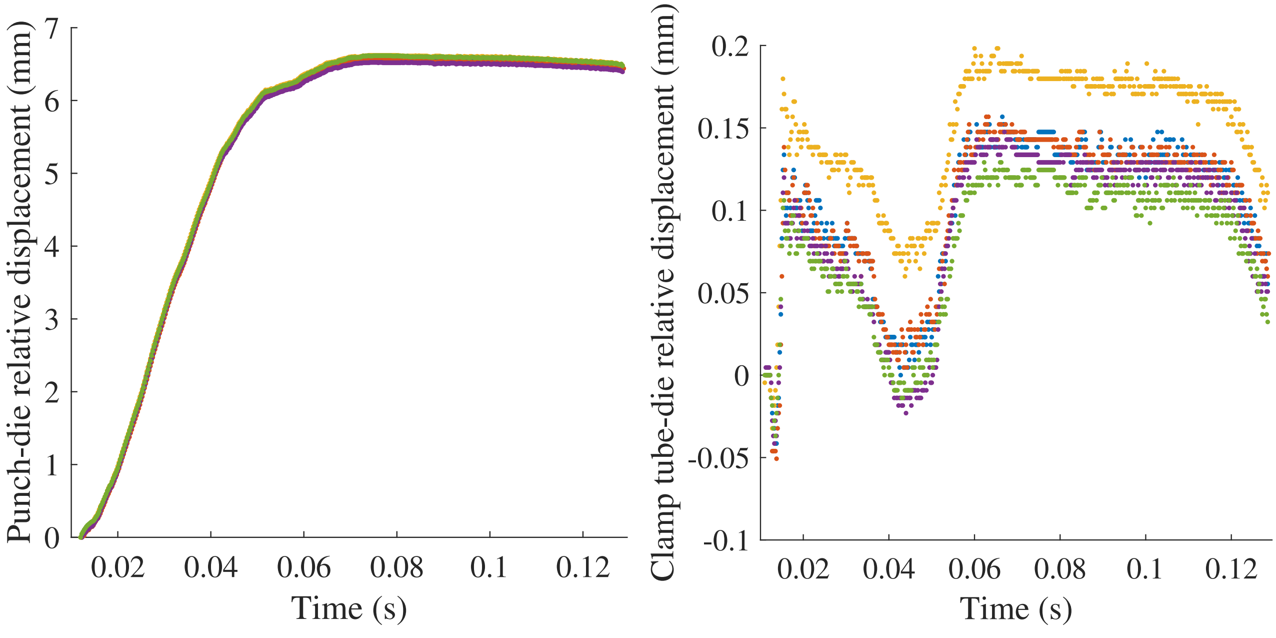

(a) (b)

Figure B.31: (a) Relative displacement between the punch and the die vs. time. (b) Relative displacement between the clamping tube and the die vs. time.

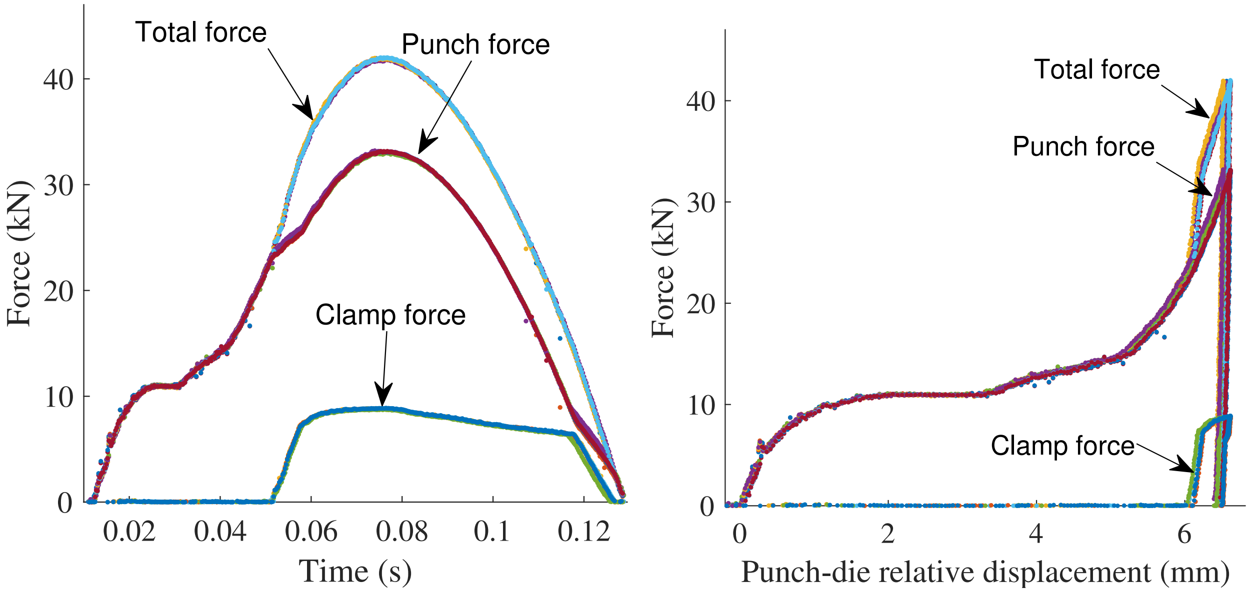

(a) (b)

Figure B.32: (a) Process forces vs. time. (b) Process forces vs. relative displacement between the punch and the die.

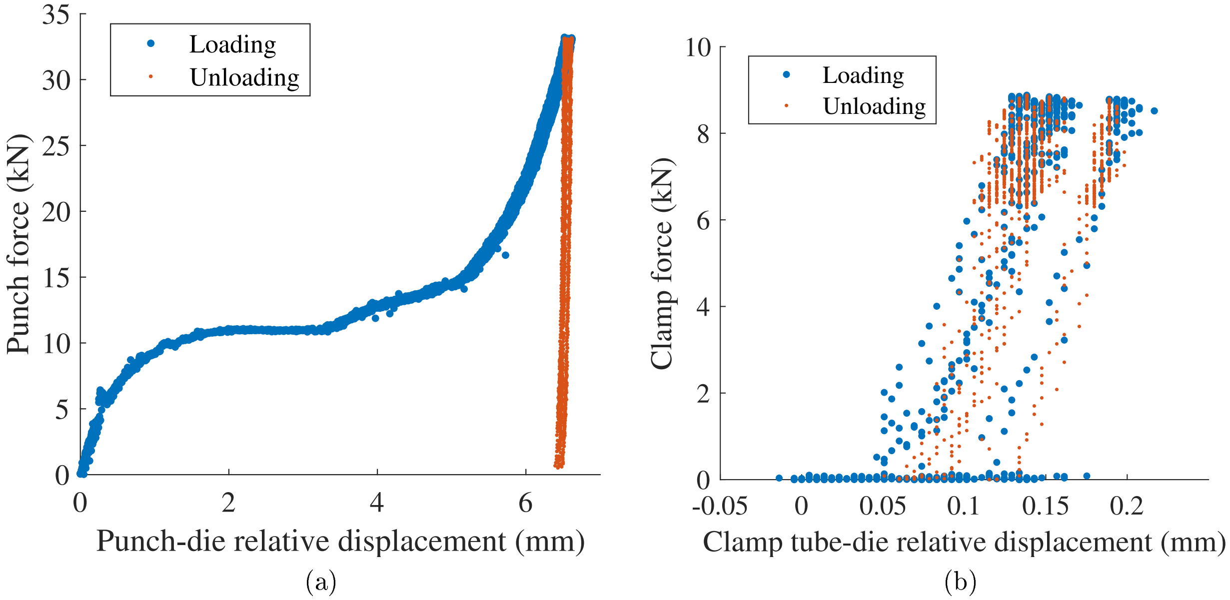

(a)

(b)

Figure B.33: (a) Punch force vs. relative displacement between the punch and the die. (b) Clamp force vs. relative displacement between the clamp tube and the die.

B.2.4 Treatment 4: C-frame 1, setting velocity 250 mm/s, motor current limit 150%

Table B.12: Summary of results for joint B, treatment 4.

	Mean	Standard deviation
Peak punch force (kN)	37.09	0.10
Peak clamp force (kN)	9.17	0.03
Head height (mm)	0.18	0.01
Estimated rivet insertion distance using camera data (mm)	6.72	0.02
Energy dissipated in joint (J)	88.70	0.31

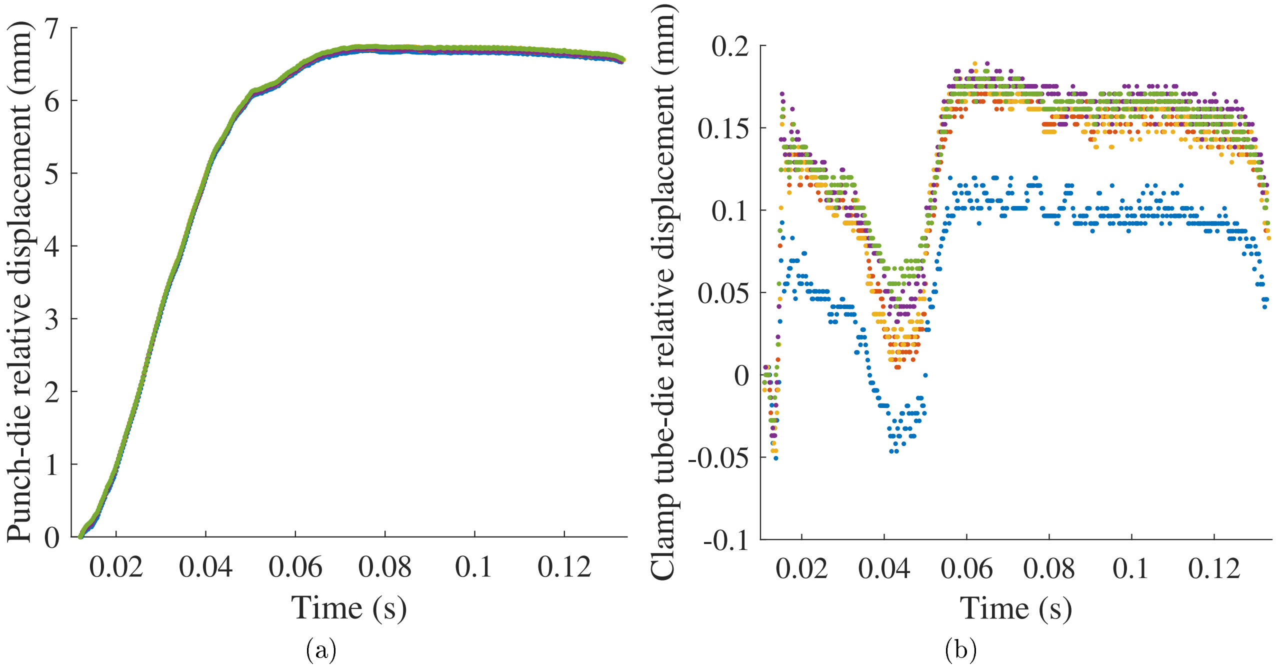

Figure B.34: (a) Relative displacement between the punch and the die vs. time. (b) Relative displacement between the clamping tube and the die vs. time.

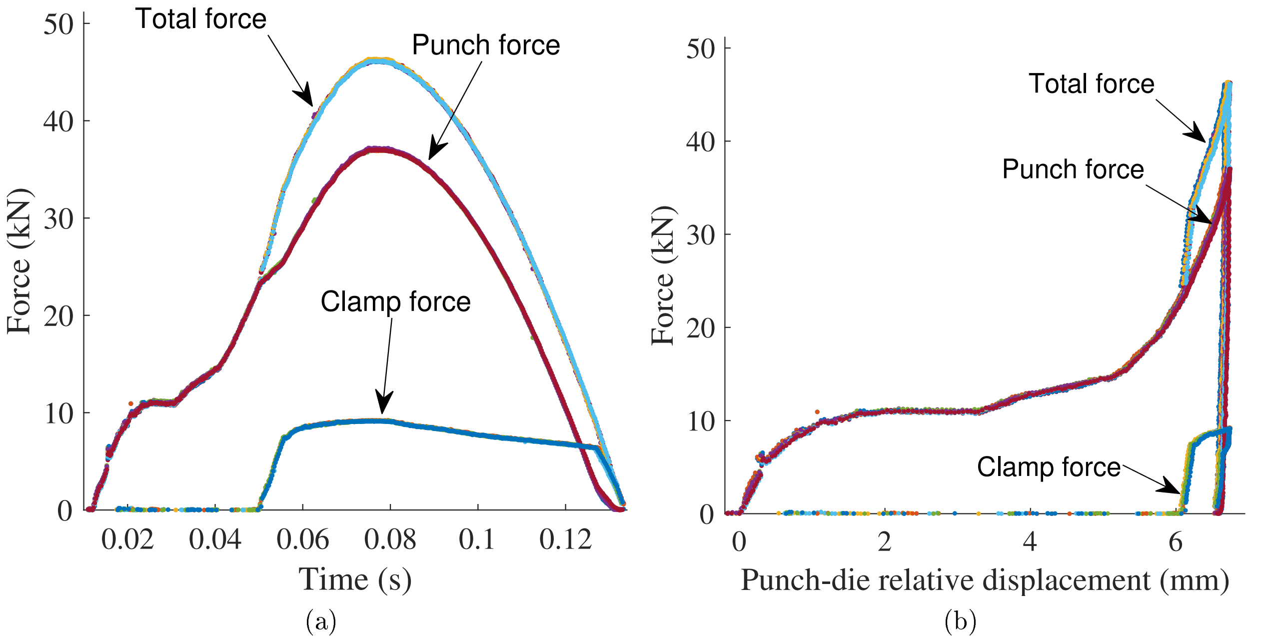

Figure B.35: (a) Process forces vs. time. (b) Process forces vs. relative displacement between the punch and the die.

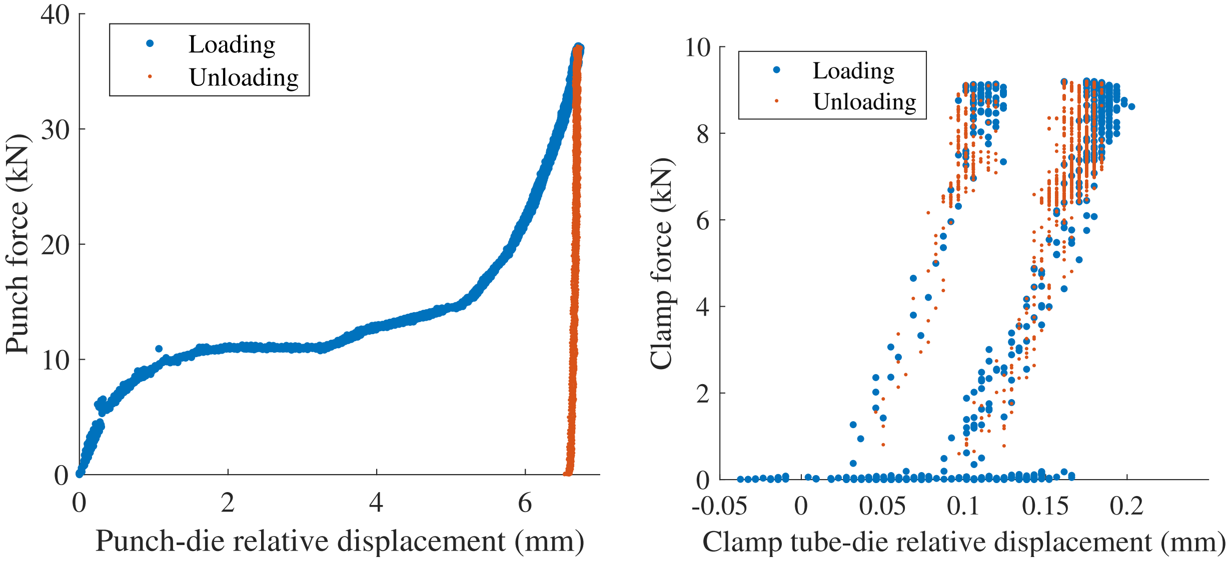

(a) (b)

Figure B.36: (a) Punch force vs. relative displacement between the punch and the die. (b) Clamp force vs. relative displacement between the clamp tube and the die.

B.2.5 Treatment 5: C-frame 2, setting velocity 150 mm/s, motor current limit 100%

Table B.13: Summary of results for joint B, treatment 5.

	Mean	Standard deviation
Peak punch force (kN)	18.82	0.12
Peak clamp force (kN)	0.09	0.05
Head height (mm)	1.17	0.02
Estimated rivet insertion distance using camera data (mm)	5.70	0.03
Energy dissipated in joint (J)	64.64	0.42

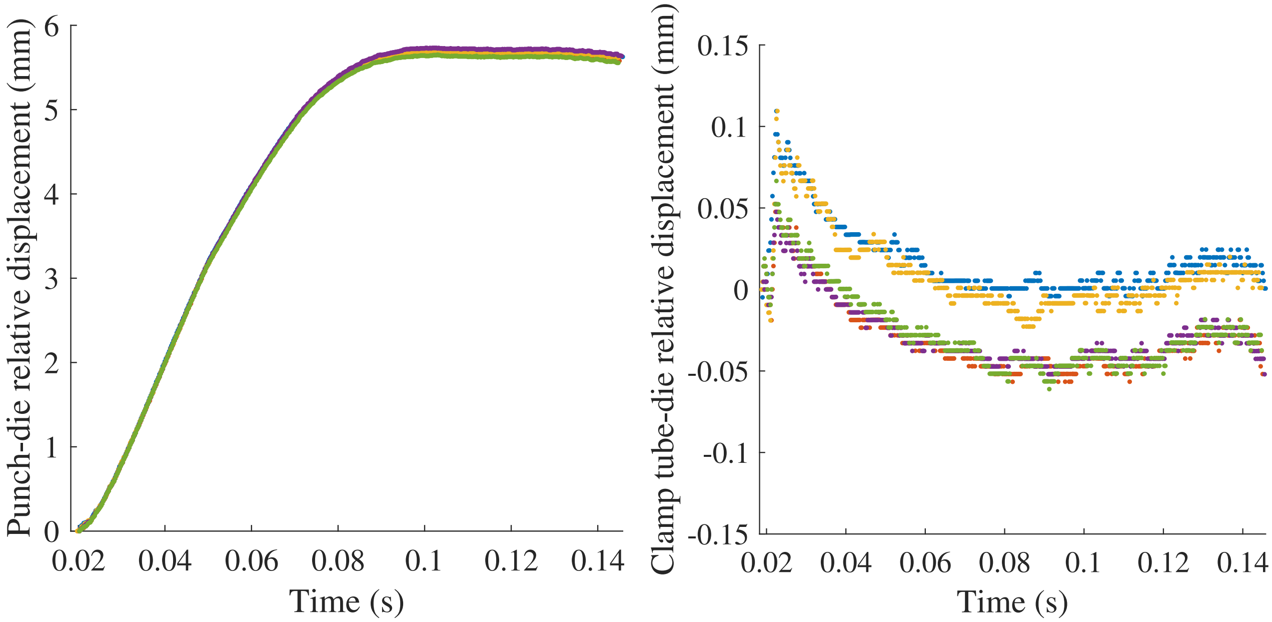

(a) (b)

Figure B.37: (a) Relative displacement between the punch and the die vs. time. (b) Relative displacement between the clamping tube and the die vs. time.

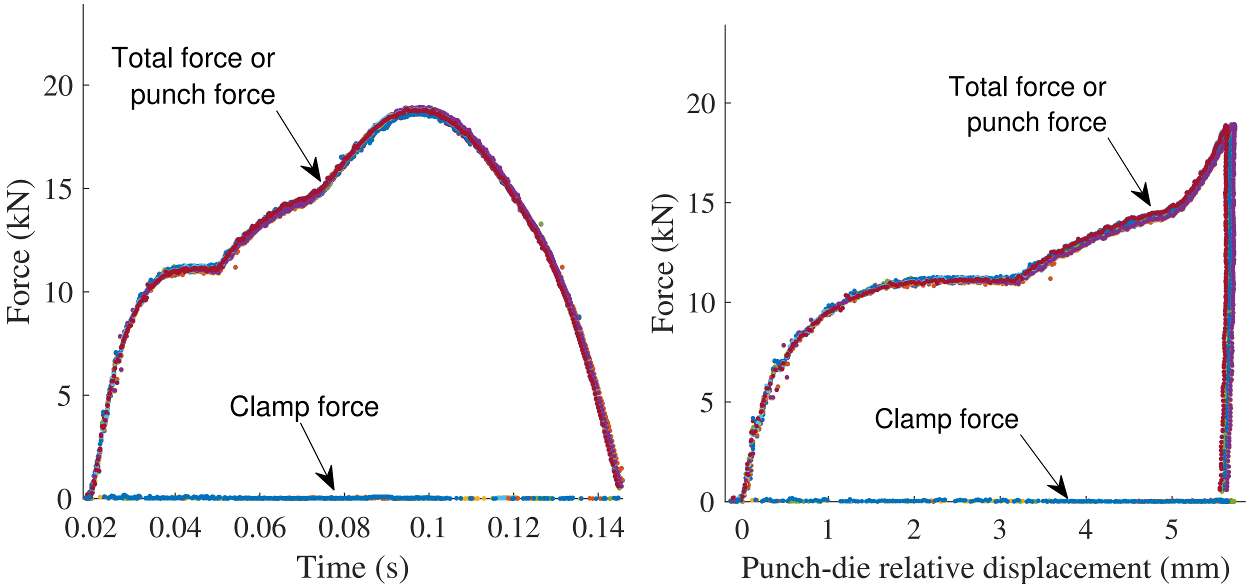

(a) (b)

Figure B.38: (a) Process forces vs. time. (b) Process forces vs. relative displacement between the punch and the die.

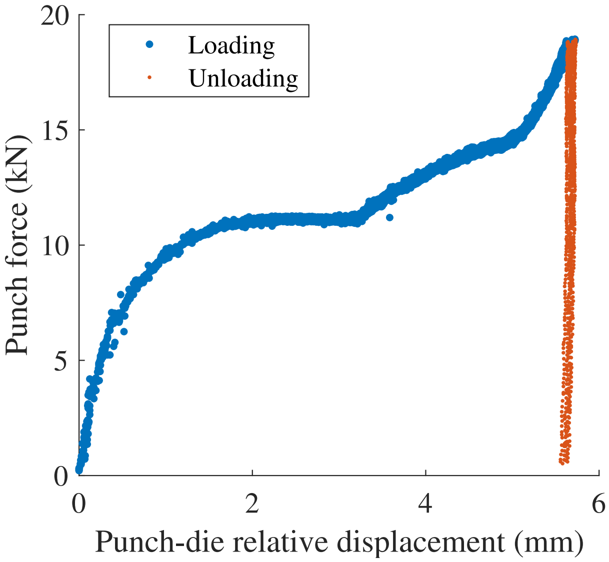

Figure B.39: Punch force vs. relative displacement between the punch and the die.

B.2.6 Treatment 6: C-frame 2, setting velocity 150 mm/s, motor current limit 150%

Table B.14: Summary of results for joint B, treatment 6.

	Mean	Standard deviation
Peak punch force (kN)	24.56	0.54
Peak clamp force (kN)	1.72	1.56
Head height (mm)	0.72	0.03
Estimated rivet insertion distance using camera data (mm)	6.17	0.03
Energy dissipated in joint (J)	74.20	0.67

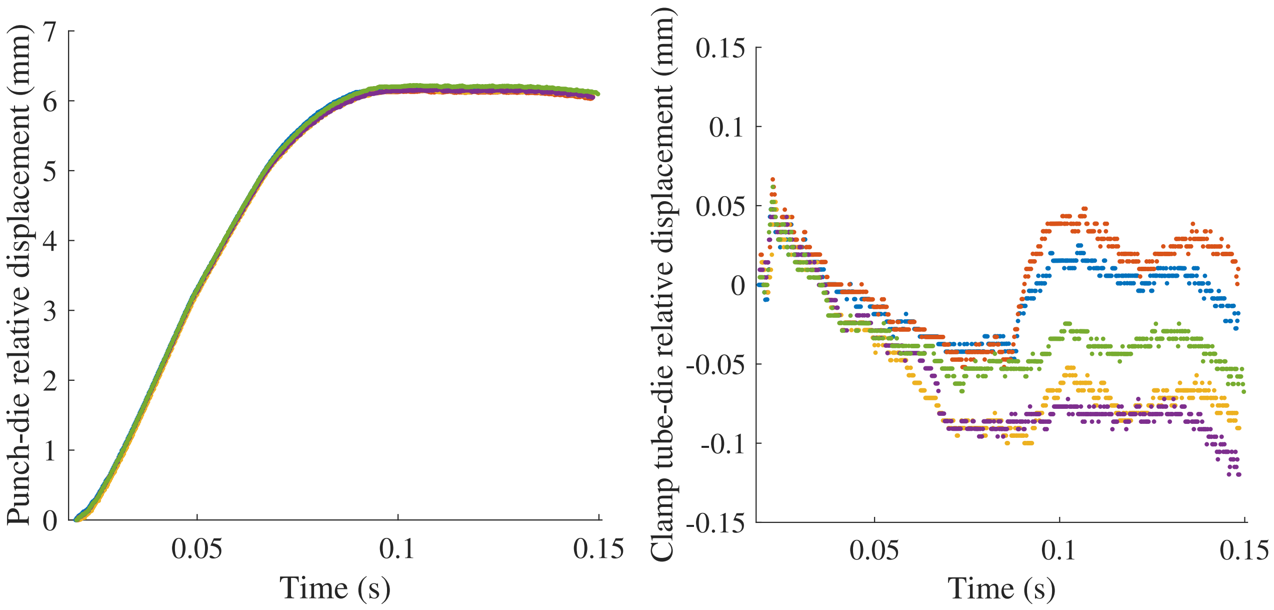

(a) (b)

Figure B.40: (a) Relative displacement between the punch and the die vs. time. (b) Relative displacement between the clamping tube and the die vs. time.

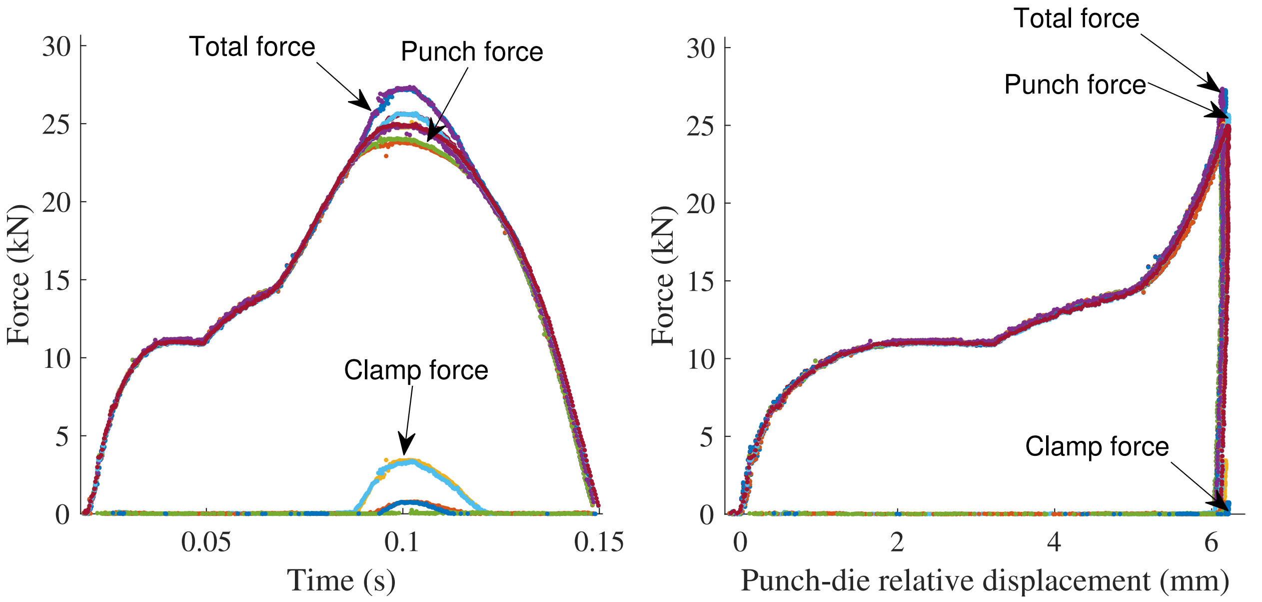

(a) (b)

Figure B.41: (a) Process forces vs. time. (b) Process forces vs. relative displacement between the punch and the die.

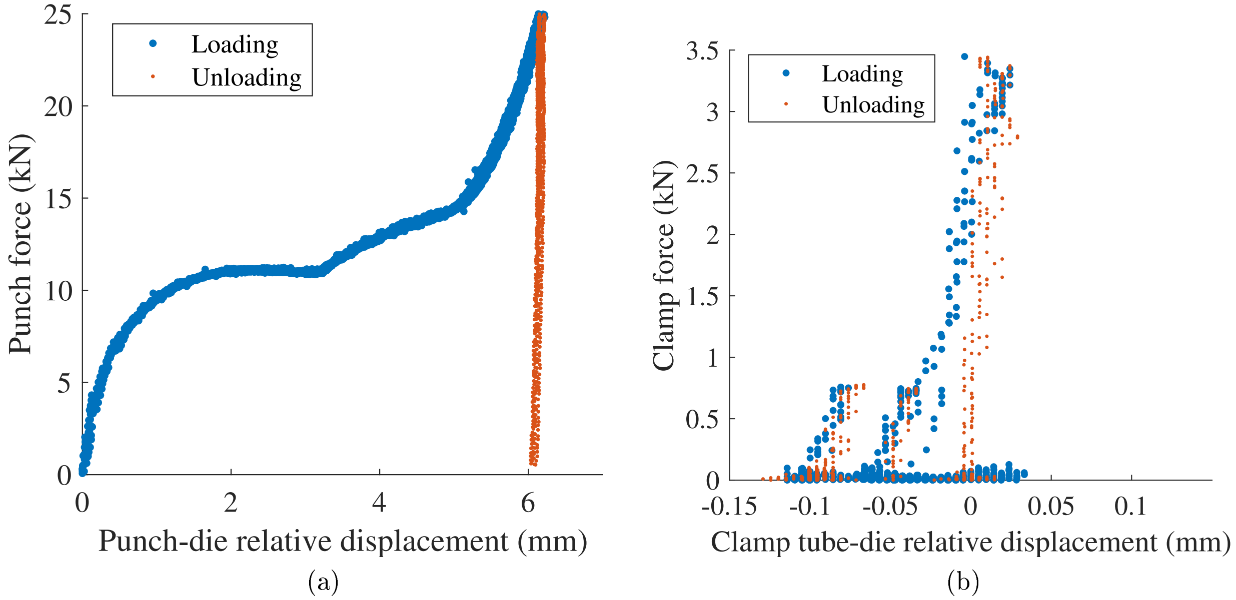

Figure B.42: (a) Punch force vs. relative displacement between the punch and the die. (b) Clamp force vs. relative displacement between the clamp tube and the die.

B.2.7 Treatment 7: C-frame 2, setting velocity 250 mm/s, motor current limit 100%

Table B.15: Summary of results for joint B, treatment 7.

	Mean	Standard deviation
Peak punch force (kN)	39.29	0.18
Peak clamp force (kN)	9.48	0.10
Head height (mm)	0.02	0.03
Estimated rivet insertion distance using camera data (mm)	6.93	0.05
Energy dissipated in joint (J)	95.66	0.68

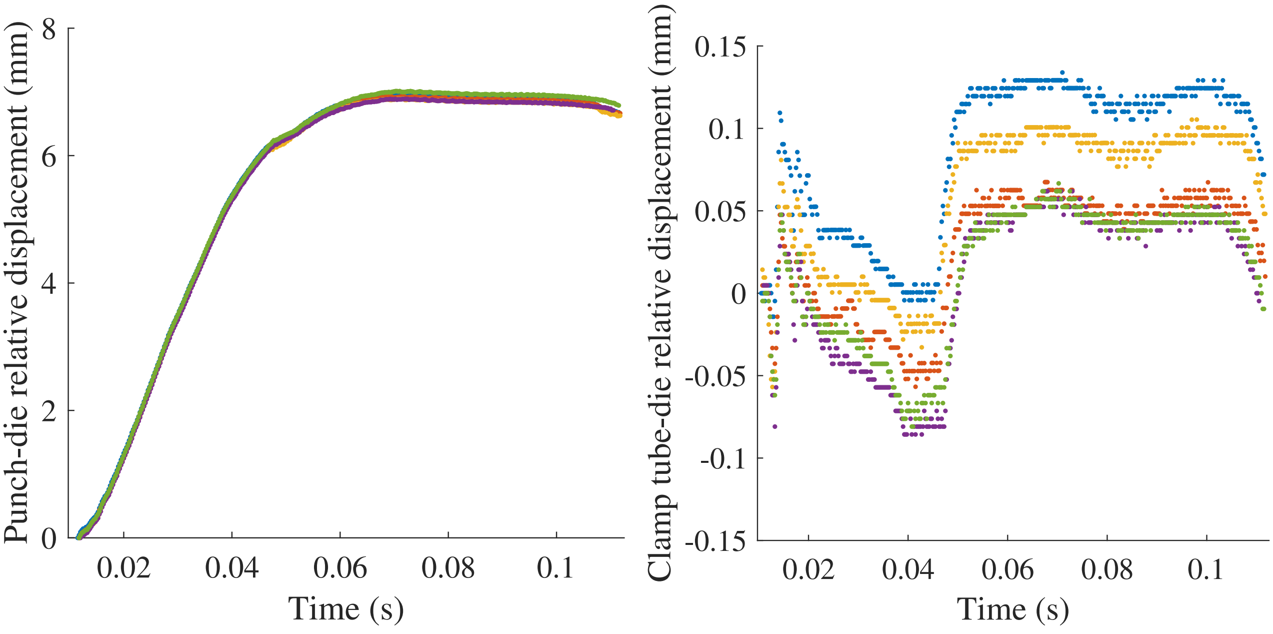

(a) (b)

Figure B.43: (a) Relative displacement between the punch and the die vs. time. (b) Relative displacement between the clamping tube and the die vs. time.

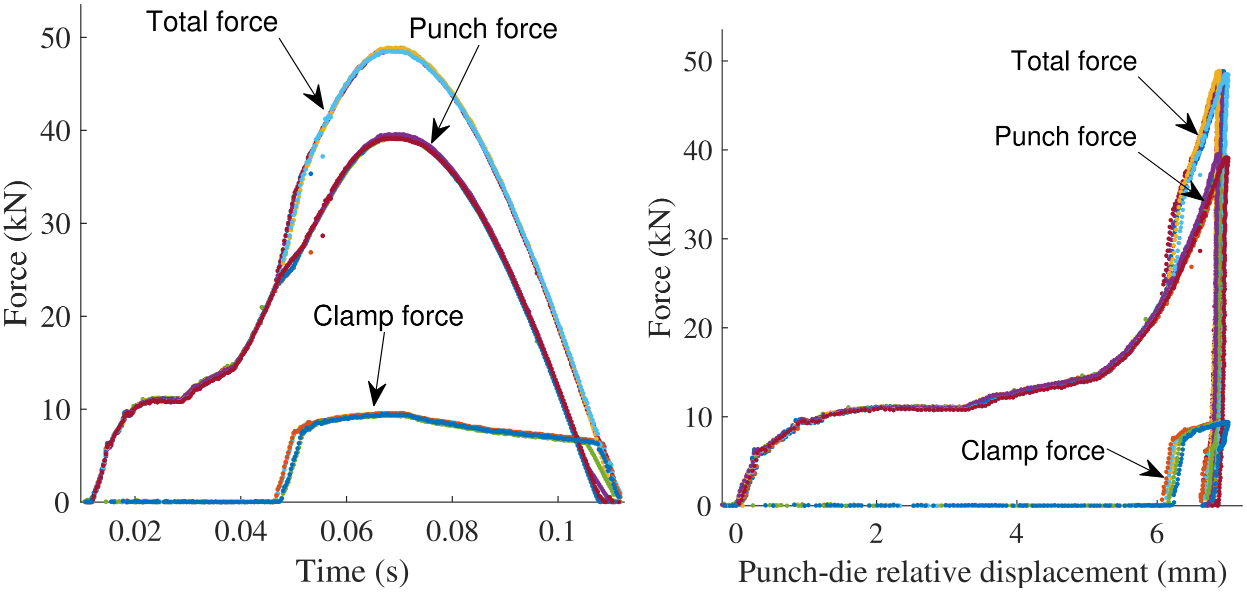

(a) (b)

Figure B.44: (a) Process forces vs. time. (b) Process forces vs. relative displacement between the punch and the die.

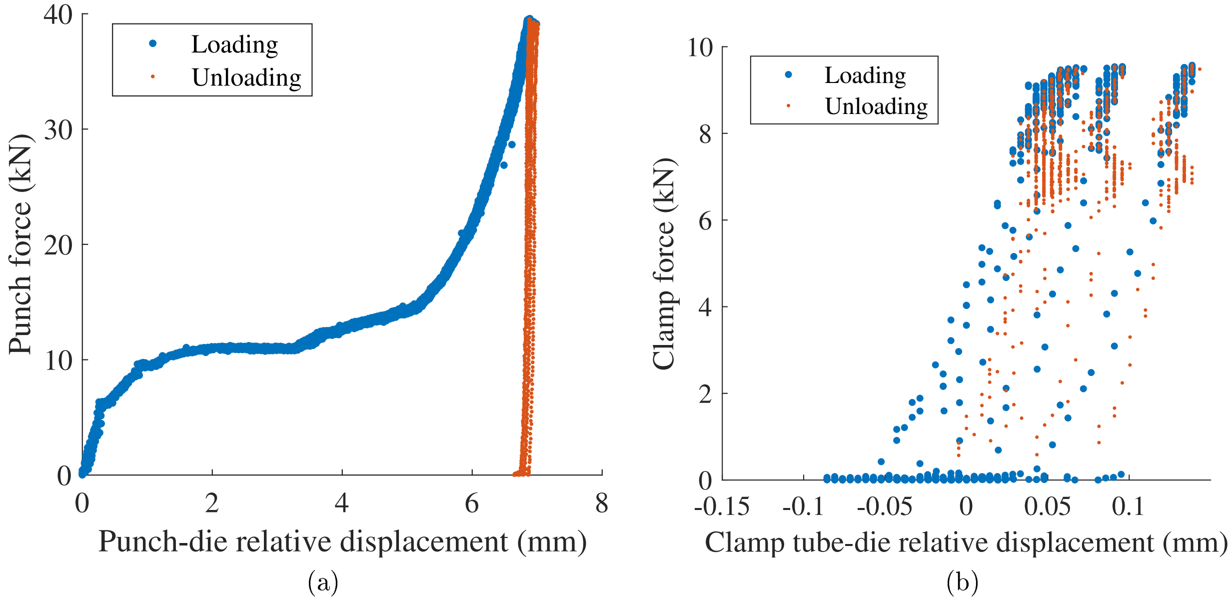

Figure B.45: (a) Punch force vs. relative displacement between the punch and the die. (b) Clamp force vs. relative displacement between the clamp tube and the die.

B.2.8 Treatment 8: C-frame 2, setting velocity 250 mm/s, motor current limit 150%

Table B.16: Summary of results for joint B, treatment 8.

	Mean	Standard deviation
Peak punch force (kN)	42.57	0.32
Peak clamp force (kN)	10.01	0.14
Head height (mm)	-0.16	0.02
Estimated rivet insertion distance using camera data (mm)	7.11	0.02
Energy dissipated in joint (J)	103.62	0.36

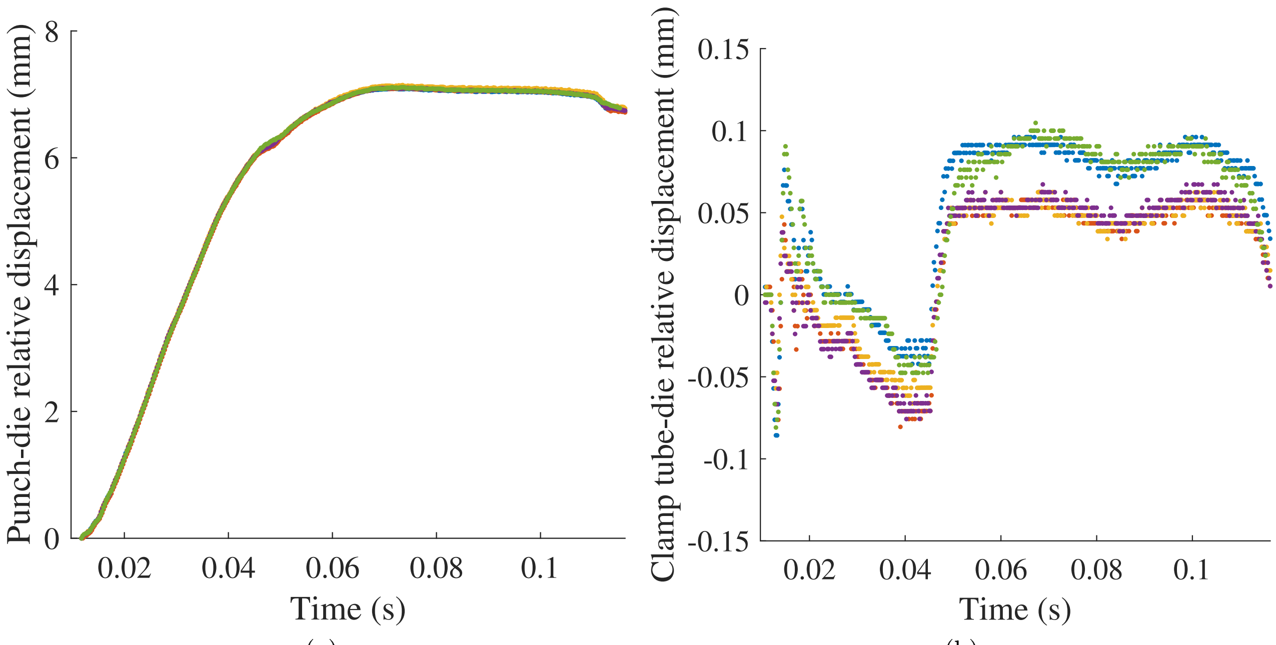

(a)

(b)

Figure B.46: (a) Relative displacement between the punch and the die vs. time. (b) Relative displacement between the clamping tube and the die vs. time.

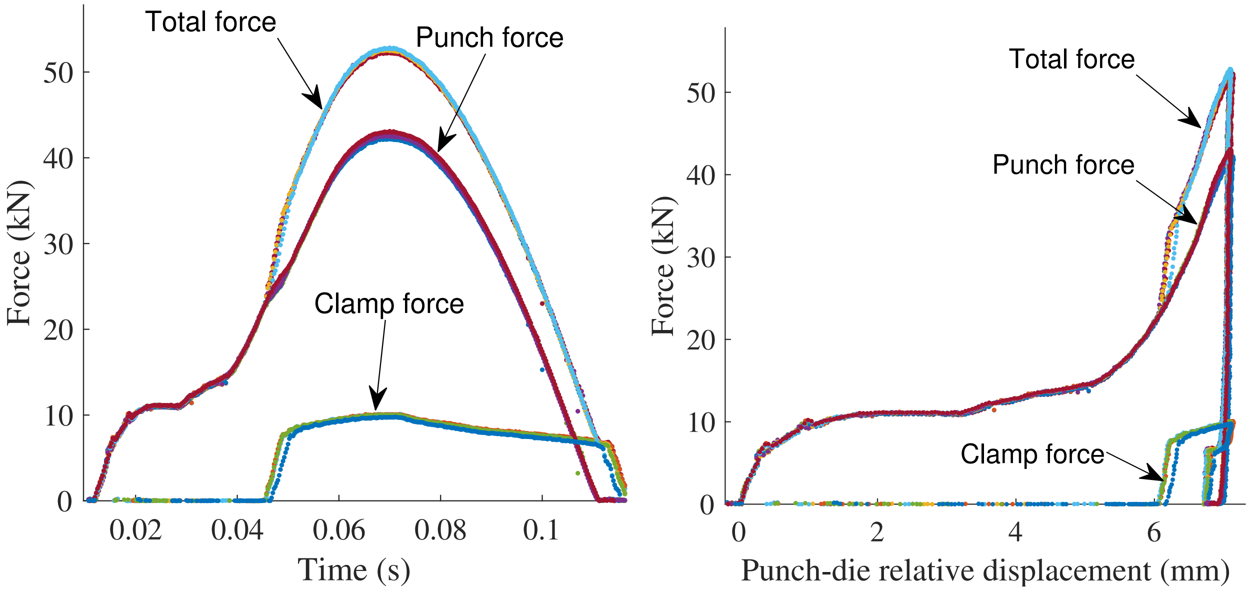

(a)

(b)

Figure B.47: (a) Process forces vs. time. (b) Process forces vs. relative displacement between the punch and the die.

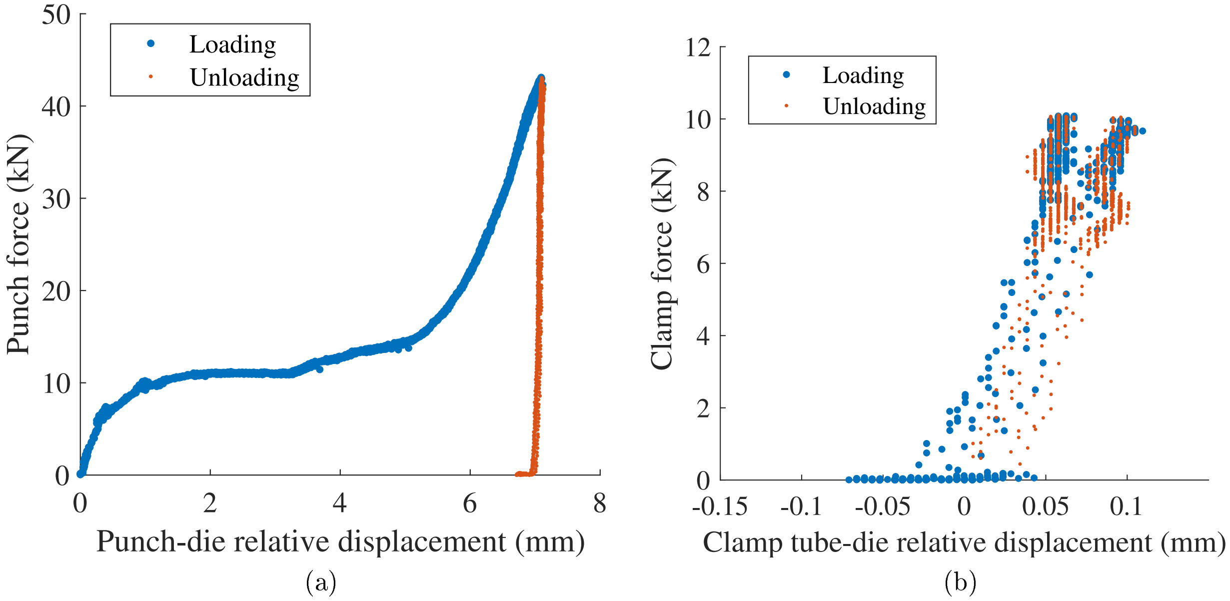

(a) (b)

Figure B.48: (a) Punch force vs. relative displacement between the punch and the die. (b) Clamp force vs. relative displacement between the clamp tube and the die.

B.3 Tables of experimental runs

Tables B.17 and B.18 describe the conditions in the runs performed on C-frames 1 and 2 respectively. The run number denotes the sequence in which the runs were performed.

Table B.17: Test runs and head height measurements for testing on C-frame 1

Run	Velocity (mm/s)	Motor current limit (%)	Rivet	Material	Die	Head height (mm)
1	250	150	C50G41A	1.5mm RC5754 + 1.5mm RC5754	DP09-175	-0.09
2	150	150	K50742A	3mm AC600 + 3mm AC600	DG10-160	0.85
3	150	150	K50742A	3mm AC600 + 3mm AC600	DG10-160	0.86
4	250	150	K50742A	3mm AC600 + 3mm AC600	DG10-160	0.18
5	250	100	C50G41A	1.5mm RC5754 + 1.5mm RC5754	DP09-175	-0.06

Table B.17: Test runs and head height measurements for testing on C-frame 1

Run	Velocity (mm/s)	Motor current limit (%)	Rivet	Material	Die	Head height (mm)
6	250	100	K50742A	3mm AC600 + 3mm AC600	DG10-160	0.31
7	250	150	C50G41A	1.5mm RC5754 + 1.5mm RC5754	DP09-175	-0.12
8	150	100	C50G41A	1.5mm RC5754 + 1.5mm RC5754	DP09-175	0.37
9	150	100	K50742A	3mm AC600 + 3mm AC600	DG10-160	1.32
10	150	150	K50742A	3mm AC600 + 3mm AC600	DG10-160	0.88
11	150	100	C50G41A	1.5mm RC5754 + 1.5mm RC5754	DP09-175	0.35
12	250	150	K50742A	3mm AC600 + 3mm AC600	DG10-160	0.19
13	250	150	C50G41A	1.5mm RC5754 + 1.5mm RC5754	DP09-175	-0.11
14	250	150	K50742A	3mm AC600 + 3mm AC600	DG10-160	0.16
15	150	150	C50G41A	1.5mm RC5754 + 1.5mm RC5754	DP09-175	0.19
16	250	150	K50742A	3mm AC600 + 3mm AC600	DG10-160	0.17
17	150	150	K50742A	3mm AC600 + 3mm AC600	DG10-160	0.84
18	150	100	C50G41A	1.5mm RC5754 + 1.5mm RC5754	DP09-175	0.38
19	250	100	C50G41A	1.5mm RC5754 + 1.5mm RC5754	DP09-175	-0.05
20	250	100	K50742A	3mm AC600 + 3mm AC600	DG10-160	0.32

Table B.17: Test runs and head height measurements for testing on C-frame 1

Run	Velocity (mm/s)	Motor current limit (%)	Rivet	Material	Die	Head height (mm)
21	250	150	C50G41A	1.5mm RC5754 + 1.5mm RC5754	DP09-175	-0.1
22	150	150	C50G41A	1.5mm RC5754 + 1.5mm RC5754	DP09-175	0.16
23	250	100	K50742A	3mm AC600 + 3mm AC600	DG10-160	0.32
24	250	100	C50G41A	1.5mm RC5754 + 1.5mm RC5754	DP09-175	-0.04
25	150	100	K50742A	3mm AC600 + 3mm AC600	DG10-160	1.36
26	150	100	C50G41A	1.5mm RC5754 + 1.5mm RC5754	DP09-175	0.38
27	250	150	K50742A	3mm AC600 + 3mm AC600	DG10-160	0.18
28	250	100	K50742A	3mm AC600 + 3mm AC600	DG10-160	0.35
29	150	150	C50G41A	1.5mm RC5754 + 1.5mm RC5754	DP09-175	0.16
30	250	100	C50G41A	1.5mm RC5754 + 1.5mm RC5754	DP09-175	-0.06
31	150	150	K50742A	3mm AC600 + 3mm AC600	DG10-160	0.85
32	150	100	C50G41A	1.5mm RC5754 + 1.5mm RC5754	DP09-175	0.36
33	150	150	C50G41A	1.5mm RC5754 + 1.5mm RC5754	DP09-175	0.16
34	250	150	C50G41A	1.5mm RC5754 + 1.5mm RC5754	DP09-175	-0.11
35	150	100	K50742A	3mm AC600 + 3mm AC600	DG10-160	1.37

Table B.17: Test runs and head height measurements for testing on C-frame 1

Run	Velocity (mm/s)	Motor current limit (%)	Rivet	Material	Die	Head height (mm)
36	150	100	K50742A	3mm AC600 + 3mm AC600	DG10-160	1.39
37	250	100	K50742A	3mm AC600 + 3mm AC600	DG10-160	0.32
38	150	100	K50742A	3mm AC600 + 3mm AC600	DG10-160	1.34
39	150	150	C50G41A	1.5mm RC5754 + 1.5mm RC5754	DP09-175	0.15
40	250	100	C50G41A	1.5mm RC5754 + 1.5mm RC5754	DP09-175	-0.06

.

Table B.18: Test runs and head height measurements for testing on C-frame 2

Run	Velocity (mm/s)	Motor current limit (%)	Rivet	Material	Die	Head height (mm)
41	150	100	C50G41A	1.5mm RC5754 + 1.5mm RC5754	DP09-175	0.13
42	250	150	K50742A	3mm AC600 + 3mm AC600	DG10-160	-0.17
43	150	100	C50G41A	1.5mm RC5754 + 1.5mm RC5754	DP09-175	0.13
44	250	100	C50G41A	1.5mm RC5754 + 1.5mm RC5754	DP09-175	-0.29
45	150	100	K50742A	3mm AC600 + 3mm AC600	DG10-160	1.17
46	250	150	C50G41A	1.5mm RC5754 + 1.5mm RC5754	DP09-175	-0.36

Table B.18: Test runs and head height measurements for testing on C-frame 2

Run	Velocity (mm/s)	Motor current limit (%)	Rivet	Material	Die	Head height (mm)
47	250	100	C50G41A	1.5mm RC5754 + 1.5mm RC5754	DP09-175	-0.28
48	250	100	C50G41A	1.5mm RC5754 + 1.5mm RC5754	DP09-175	-0.29
49	250	100	K50742A	3mm AC600 + 3mm AC600	DG10-160	0.03
50	250	150	K50742A	3mm AC600 + 3mm AC600	DG10-160	-0.18
51	150	100	K50742A	3mm AC600 + 3mm AC600	DG10-160	1.18
52	250	150	C50G41A	1.5mm RC5754 + 1.5mm RC5754	DP09-175	-0.35
53	150	150	C50G41A	1.5mm RC5754 + 1.5mm RC5754	DP09-175	0.02
54	250	150	C50G41A	1.5mm RC5754 + 1.5mm RC5754	DP09-175	-0.35
55	150	100	C50G41A	1.5mm RC5754 + 1.5mm RC5754	DP09-175	0.13
56	150	100	K50742A	3mm AC600 + 3mm AC600	DG10-160	1.19
57	250	150	K50742A	3mm AC600 + 3mm AC600	DG10-160	-0.15
58	250	100	K50742A	3mm AC600 + 3mm AC600	DG10-160	0.03
59	250	150	K50742A	3mm AC600 + 3mm AC600	DG10-160	-0.18
60	150	150	K50742A	3mm AC600 + 3mm AC600	DG10-160	0.74
61	150	150	K50742A	3mm AC600 + 3mm AC600	DG10-160	0.75

Table B.18: Test runs and head height measurements for testing on C-frame 2

Run	Velocity (mm/s)	Motor current limit (%)	Rivet	Material	Die	Head height (mm)
62	150	150	C50G41A	1.5mm RC5754 + 1.5mm RC5754	DP09-175	0.02
63	250	100	K50742A	3mm AC600 + 3mm AC600	DG10-160	0.03
64	150	100	K50742A	3mm AC600 + 3mm AC600	DG10-160	1.14
65	150	100	K50742A	3mm AC600 + 3mm AC600	DG10-160	1.19
66	150	150	K50742A	3mm AC600 + 3mm AC600	DG10-160	0.69
67	150	150	K50742A	3mm AC600 + 3mm AC600	DG10-160	0.74
68	250	100	C50G41A	1.5mm RC5754 + 1.5mm RC5754	DP09-175	-0.27
69	150	150	C50G41A	1.5mm RC5754 + 1.5mm RC5754	DP09-175	0.04
70	250	150	C50G41A	1.5mm RC5754 + 1.5mm RC5754	DP09-175	-0.37
71	250	150	C50G41A	1.5mm RC5754 + 1.5mm RC5754	DP09-175	-0.37
72	250	100	C50G41A	1.5mm RC5754 + 1.5mm RC5754	DP09-175	-0.26
73	150	150	C50G41A	1.5mm RC5754 + 1.5mm RC5754	DP09-175	0.04
74	250	150	K50742A	3mm AC600 + 3mm AC600	DG10-160	-0.14
75	250	100	K50742A	3mm AC600 + 3mm AC600	DG10-160	0.05
76	150	150	K50742A	3mm AC600 + 3mm AC600	DG10-160	0.7

Table B.18: Test runs and head height measurements for testing on C-frame 2

Run	Velocity (mm/s)	Motor current limit (%)	Rivet	Material	Die	Head height (mm)
77	250	100	K50742A	3mm AC600 + 3mm AC600	DG10-160	-0.02
78	150	100	C50G41A	1.5mm RC5754 + 1.5mm RC5754	DP09-175	0.16
79	150	100	C50G41A	1.5mm RC5754 + 1.5mm RC5754	DP09-175	0.15
80	150	150	C50G41A	1.5mm RC5754 + 1.5mm RC5754	DP09-175	0.04

Appendix C

Parameter Identification - Friction Profile

The identification of the friction characteristics of the PRSM was performed on the same test system described in Figure 3.1. The motivation behind the work was the need for accurate predictions of the dynamic response of the system throughout the riveting process.

Since it was not practical to test the PRSM in isolation from the rest of the system, any experimentally observed friction characteristics would be that of the overall rivet setter rather than the PRSM alone. However, to simplify the model, the friction in the rivet setter was assumed to act only as a friction torque which resisted the rotational motion of the PRSM. The model proposed in Section 4.2.3 was an effort to break down this friction torque into its constituent parts.

C.1 Method

In order to identify the velocity-dependent and static friction components, a relationship had to be determined between the torque acting on the PRSM and its angular velocity.

The system was hence run through a series of simple displacement motions, each at a different nominal velocity. For each nominal velocity, the motor current over the constant velocity phase of the motion was averaged to obtain a mean value.

The motor current was considered to be directly proportional to the electromagnetic torque generated by the motor, related by the torque constant K_t. The underlying assumption was that the torque-current relationship was linear over the range of motor currents investigated, i.e. that K_t was a constant value, neglecting potential motor saturation effects. This was a reasonable assumption given that the level of the motor currents during the constant velocity stage of the motion did not exceed the nominal rating of the motor.

C.2 Results and discussion

Figure C.1(a) shows an example dataset from a test run at 150 mm/s. During the constant velocity phase of the motion from 0.2 s onwards, the motor current is seen to be relatively stable, meaning that the torque generated by the motor was more or less constant and in balance with the viscous losses in the system.

Figure C.1(b) shows the summary of all the tests. At low velocities, the losses in the system were expected to be dominated by static rather than viscous friction, hence the torque required to maintain very low velocities was considered more representative of the static friction.

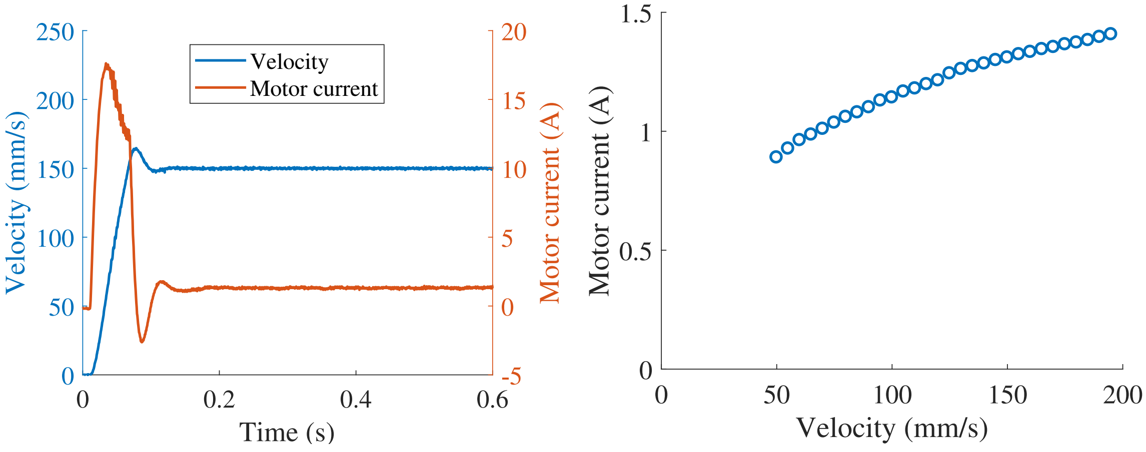

(a) (b)

Figure C.1: (a) Example data from a test run at a nominal velocity of 150 mm/s. (b) Motor current vs. nominal linear velocity of the PRSM.

By plotting the estimated torque against the nominal velocity, the viscous friction coefficient (B_r) could be obtained from the gradient of the line of best fit, as shown in Figure C.2. Additionally, the static friction (T_{cr}) could be obtained from the intercept of the fitted line with the y-axis. The values for B_r and T_{cr} were estimated as 0.0032 Nm/(rad/s) and 0.9 Nm respectively.

The fitted line was a linear approximation of the true characteristics. Due to programmed constraints on the test system, it was not possible to obtain data for velocities lower than 50 mm/s, and the assumption was made that the identified torque-velocity relationship would equally apply at lower velocities. However, this could be an oversimplification of the true dynamics. Future work should be carried out to investigate the friction characteristics in this region to gain a better understanding of the friction in the system.

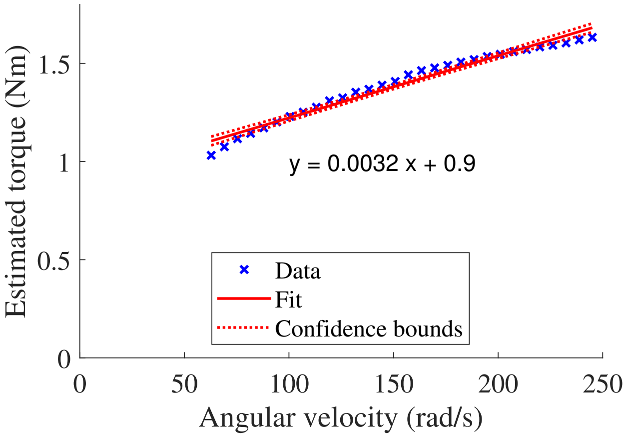

Figure C.2: Estimated torque vs. nominal angular velocity of the PRSM. Labels indicate the identified components of the friction characteristics.

Appendix D

Bootstrap method

The confidence intervals in Chapter 8 give an indication of the accuracy of the estimated sensitivity indices and the confidence in the estimates. A 95% confidence interval of a sensitivity index means that there is 95% confidence that the true value of the sensitivity index lies within the specified bounds of the interval.

Typically, the calculation of confidence intervals makes the assumption that the sampling distribution is normal, i.e. the distribution of the sensitivity index is normal. In the sensitivity analysis however, due to time and computational restraints, the number of simulation runs was limited and the true sampling distribution was unknown. If simulated outputs from all the runs were used in calculating the sensitivity index for a given parameter, the result would be a single value which would reveal nothing about the distribution. Bootstrap is a way to approximate the sampling distribution.

The method involves taking smaller sample many times, say N_{res} times, from the original full sample, each of which is referred to as a 'resample'. The sensitivity measures are computed for each resample, generating a total of N_{res} sets of sensitivity indices. Subsequently the mean (μ_{si}) and standard deviation (σ_{si}) of the sensitivity indices are calculated, which are then used to define the confidence intervals as

$$\mu_{si} \pm 1.96 \frac{\sigma_{si}}{\sqrt{N_{res}}}$$

For a given sensitivity index of a parameter, the distribution of the N_{res} values is an approximation of what would be obtained if N_{res} samples were taken from the true distribution, i.e. from the outcomes of an infinite number of sensitivity analyses. Therefore, the confidence intervals computed this way are a valid indication of the confidence in the sensitivity indices.

In the study, 500 resamples were taken in the calculation of the confidence intervals for the uncertainty analysis.